

Stable Barium Isotopes
Biogeochemical Cycling and Palaeoceanographic Applications

Dissertation

zur Erlangung des Doktorgrades

Dr. rer. nat.

der Mathematisch-Naturwissenschaftlichen Fakultät
der Christian-Albrechts-Universität zu Kiel

vorgelegt von

Yang Yu

Kiel, 2021

Erster Gutachter und Betreuer: Prof. Dr. Martin Frank

Zweiter Gutachter: Dr. Tristan J. Horner

Eingereicht am: 26. Mai 2021

Tag der Disputation: 06. Juli 2021

Zum Druck genehmigt: 06. Juli 2021

Gez. Prof. Dr. Frank Kempken, Dekan

Erklärung

Hiermit erkläre ich des Eides statt, dass ich die vorliegende Abhandlung, abgesehen von der Beratung durch meine Betreuer, nach Inhalt und Form selbstständig erarbeitet habe und keine anderen als die von mir aufgeführten Quellen und Hilfsmittel verwendet wurden.

Diese Arbeit ist unter Einhaltung der Regeln guter wissenschaftlicher Praxis der Deutschen Forschungsgemeinschaft entstanden und wurde weder in Auszügen noch in ganzer Form an einer anderen Stelle im Rahmen eines Prüfungsverfahrens eingereicht.

Teile dieser Arbeit wurden zur Veröffentlichung in einer Fachzeitschrift eingereicht oder sind in Vorbereitung eingereicht zu werden.

Es wurde kein akademischer Grad entzogen.

Kiel, den 26. Mai 2021

Yang Yu

Abstract

Stable barium (Ba) isotopes have received increasing attention in the past decade as a result of improved analytical precision and their potential as a tracer for ocean circulation and for palaeoceanographic reconstructions. However, challenges exist regarding the isotope analysis and interpretation of this emerging isotopic tracer. The first major challenge is the accurate and precise determination of the natural stable Ba isotope fractionation ($\delta^{138}\text{Ba}$) in various samples matrices, such as seawaters, river waters, carbonates, sulphates and sediments. Multi-collector inductively-coupled plasma mass spectrometry (MC-ICP-MS) offers rapid sample throughput for stable Ba isotope analysis, but suffers from severe matrix effects caused by changes in matrix load and instrumental mass bias variations during the measurements. While significant efforts have been invested into improving chemical purification and refining the models of mass bias correction, the impact of plasma conditions has rarely been considered. In this thesis, a detailed investigation of non-spectral matrix effects on the accuracy and precision of stable Ba isotope analysis has been carried out under different plasma conditions quantified by the Normalised Argon Index (NAI). Based on the results of our experiments, a new approach is proposed to address how the matrix effects can be attenuated by optimising the NAI, which minimises and stabilises the instrumental mass fractionation. The improved understanding of the behaviour of the matrix-induced mass bias allows us to define a matrix tolerance state for stable Ba isotope analysis with MC-ICP-MS.

The second challenge in the study of oceanic Ba isotope systematics is a lack of constraints on the dissolved Ba isotope composition of endmember water masses in the high-latitude oceans. The modern deep ocean circulation system is largely driven by the sinking of cold, saline water masses in high latitudes, where North Atlantic Deep Water (NADW) and Antarctic Bottom Water (AABW) acquire their respective Ba isotope compositions. In this thesis, we characterise the $\delta^{138}\text{Ba}$ signatures of NADW and AABW by analysing a suite of depth profiles from the Nordic Seas, the Labrador Sea, and the Weddell Sea. The contrasting $\delta^{138}\text{Ba}$ signals between these northern and southern endmembers are most likely the result of the Ba isotope fractionation signatures introduced into the return path of the thermohaline circulation by barite formation in the Southern Ocean. In combination with the previously reported low and mid-latitude $\delta^{138}\text{Ba}$

profiles, we are able to better constrain the meridional Ba transport and mixing processes across the entire Atlantic Ocean. The systematic variation in the meridional $\delta^{138}\text{Ba}$ profiles provides valuable insights into the biogeochemical cycling of Ba in the modern ocean and thus builds the framework for potential applications of stable Ba isotopes in palaeoceanography.

Applying stable Ba isotope signatures extracted from shallow-water corals as a novel tracer for river runoff constitutes the third primary topic of this thesis. Coral-based reconstructions of riverine inputs are critical for the understanding of local and global elemental budgets in the context of climate change and anthropogenic land use. The elemental ratios of Ba/Ca in corals are the commonly used tracer for riverine runoff. However, coral Ba/Ca records at different locations show contrasting behaviour, which hinders the use of Ba/Ca as a reliable tracer for past river runoff in coastal regions. Stable Ba isotope compositions in shallow-water corals may reflect the ambient seawater Ba isotope signatures and have great potential to provide important constraints on seasonal changes in riverine inputs and to validate coral Ba/Ca records. Our results of a monthly resolved coral record from the Andaman Islands (India) show that coral $\delta^{138}\text{Ba}$ values are generally light during the South Asian Summer Monsoon characterised by enhanced rainfall and regional river discharge suggesting that coral $\delta^{138}\text{Ba}$ may act as a novel runoff proxy. This inference is supported by the stable Ba isotope compositions of local seawater samples, with a significantly light $\delta^{138}\text{Ba}$ value of $+0.29 \pm 0.04\text{‰}$ during the summer monsoon periods compared to heavy $\delta^{138}\text{Ba}$ values of $+0.44 \pm 0.05\text{‰}$ during other times of the year. In addition, we estimate the Ba isotope fractionation between corals and seawater, which sheds light on the effects of mineral growth kinetics and biomineralization controlling the process of Ba incorporation into coral skeletons.

In summary, this thesis addresses three important objectives, which are the establishment of a matrix tolerance state for stable Ba isotope analysis with MC-ICP-MS, the characterisation of the dissolved Ba isotope distributions in water masses in the modern deep ocean, and the application of seasonal Ba isotope changes recorded by shallow-water corals to reconstruct past river runoff.

Kurzfassung

Stabile Barium (Ba)-Isotope haben im letzten Jahrzehnt aufgrund verbesserter analytischer Präzision und ihres Potenzials als Indikator für Ozeanzirkulation und paläozeanographische Rekonstruktionen zunehmende Bedeutung erlangt. Allerdings gibt es Herausforderungen sowohl in Bezug auf die Isotopenanalytik als auch auf die Interpretation dieses relativ neuen isotopischen Indikators. Eine große Herausforderung ist die genaue und präzise Bestimmung der natürlichen stabilen Ba-Isotopenfraktionierung ($\delta^{138}\text{Ba}$) in verschiedenen Proben-Materialien (z.B. Meerwasser, Flusswasser, Karbonate, Sulfate und Sedimente). Induktiv gekoppelte Multikollektor-Plasma-Massenspektrometrie (MC-ICP-MS) erlaubt einen schnellen Probendurchsatz für die Analyse stabiler Ba-Isotope, kann bedingt durch die chemische Zusammensetzung der Proben (Matrix) zu Artefakten führen. Diese werden durch Veränderungen in der Matrixlast und der daraus resultierenden instrumentellen Massenfraktionierung während der Messungen verursacht. Während in der Literatur vorwiegend über erhebliche Anstrengungen in die Verbesserung der chemischen Aufbereitung und die Verbesserung der Modelle zur Korrektur der instrumentellen Massenfraktionierung berichtet wurde, wurde der Einfluss von Plasmabedingungen nur selten berücksichtigt. In dieser Arbeit wurde eine detaillierte Untersuchung von nicht-spektralen Matrixeffekten auf die Genauigkeit und Präzision der Analyse von stabilen Ba-Isotopen unter verschiedenen Plasmabedingungen durchgeführt, die durch den "Normalisierten Argon-Index"(NAI) quantifiziert werden können. Basierend auf den Ergebnissen unserer Experimente können Matrixeffekte durch Optimierung des NAI abgeschwächt werden, wodurch die instrumentelle Massenfraktionierung minimiert und stabilisiert wird. Das verbesserte Verständnis der matrixbedingten Massenfraktionierung ermöglicht es uns, einen Matrix-Toleranzzustand für die Analyse stabiler Ba-Isotope mit der MC-ICP-Massenspektrometrie zu definieren.

Ein weiteres Problem in der ozeanischen Ba-Isotopensystematik ist die unzureichende Datenbasis der gelösten Ba-Isotopenzusammensetzung der Wassermassen in den Ozeanen hoher Breiten. Das moderne Zirkulationssystem des tiefen Ozeans wird größtenteils durch das Absinken von kalten, salzhaltigen Wassermassen in hohen Breiten angetrieben, wo auch das Nordatlantische Tiefenwasser (NADW) und das Antarktische

Bodenwasser (AABW) ihre jeweilige Ba-Isotopenzusammensetzung erhalten. In dieser Studie charakterisieren wir die $\delta^{138}\text{Ba}$ -Signaturen von NADW und AABW durch die Analyse einer Reihe von Tiefenprofilen aus dem Nordmeer, der Labradorsee und dem Weddellmeer. Die Ergebnisse zeigen unterschiedliche $\delta^{138}\text{Ba}$ -Signale für die Wassermassen der nördlichen und südlichen Breiten. Die Unterschiede sind wahrscheinlich das Ergebnis der Ba-Isotopenfraktionierung durch Barytbildung im Südozean. Diese veränderte Isotopensignatur wird daraufhin mit der thermohalinen Zirkulation nach Norden transportiert. In Kombination mit den besser bekannten $\delta^{138}\text{Ba}$ -Verteilungen der niedrigen und mittleren Breiten können wir den meridionalen Ba-Transport und die Mischungsprozesse im gesamten Atlantik besser bestimmen. Die beobachtete systematische Variation der meridionalen $\delta^{138}\text{Ba}$ -Profile liefert wertvolle Einblicke in den biogeochemischen Kreislauf von Ba im modernen Ozean und schafft somit die Voraussetzungen für mögliche Anwendungen von stabilen Ba-Isotopen in der Paläozeanographie.

Die Anwendung stabiler Ba-Isotopensignaturen in Flachwasserkorallen als neuartiger Indikator für die Stärke des Flusseintrags in die Ozeane ist das dritte Hauptthema dieser Studie. Korallenbasierte Rekonstruktionen von Flusseinträgen sind entscheidend für das Verständnis lokaler und globaler Elementbudgets im Kontext von Klimawandel und anthropogener Landnutzung. Häufig genutzte Indikatoren für diesen Flusseintrag sind die elementaren Ba/Ca-Verhältnisse in Korallen, die aber an verschiedenen Standorten kein einheitliches Bild zeigen. Dies erschwert die Verwendung von Ba/Ca als zuverlässigen Indikator für Paläo-Flusseinträge in Küstenregionen. Stabile Ba-Isotopenzusammensetzungen in Flachwasserkorallen können die Ba-Isotopensignaturen des umgebenden Meerwassers widerspiegeln und haben daher großes Potential, wichtige Hinweise auf saisonale Veränderungen der Flusseinträge zu liefern und korallenbasierte Ba/Ca-Aufzeichnungen zu validieren. Monatlich aufgelöste Ba-Isotopenanalysen an einer Koralle, die auf den Andamanen (Indischer Ozean) beprobt wurde, zeigen, dass die $\delta^{138}\text{Ba}$ -Werte der Koralle während des südasiatischen Sommermonsuns, der durch verstärkte Regenfälle und erhöhte regionale Flusseinträge gekennzeichnet ist, generell leichter sind. Dies deutet darauf hin, dass die $\delta^{138}\text{Ba}$ -Signatur von Korallen als neuer Indikator für Flusseinträge herangezogen werden könnte. Diese Schlussfolgerung wird durch die stabile Ba-Isotopenzusammensetzung lokaler Meerwasserproben gestützt, die einen leichten $\delta^{138}\text{Ba}$ -Wert von $+0.29 \pm 0.04\%$ während der Sommermonsun-Perioden

zeigen. Im Vergleich dazu sind die $\delta^{138}\text{Ba}$ -Werte zu anderen Jahreszeiten signifikant schwerer ($+0.44 \pm 0.05\%$). Darüber hinaus können wir eine erste Abschätzung der Ba-Isotopenfraktionierung zwischen Korallen und Meerwasser erzielen. Dies erlaubt uns Rückschlüsse auf die Kinetik des Mineralwachstums und der Biomineralisation, die den Prozess des Ba-Einbaus in Korallenskelette kontrollieren.

Zusammenfassend lässt sich sagen, dass in dieser Doktorarbeit drei wichtige Fragestellungen der Ba-Isotopengeochemie adressiert werden. Dies sind die Etablierung eines Matrix-Toleranzzustands für die Analyse stabiler Ba-Isotope mit MC-ICP-MS, die Charakterisierung der Verteilungen gelöster Ba-Isotope in Wassermassen im modernen tiefen Ozean und die Anwendung saisonaler Ba-Isotopenveränderungen, die von Flachwasserkorallen aufgezeichnet wurden, um Flusseinträge in die Ozeane zu rekonstruieren

Contents

Abstract	i
Kurzfassung.....	iii
1 Introduction.....	1
1.1 Barium and its stable isotopes	1
1.2 Barium isotope fractionation in seawater	2
1.3 Sources of barium in the global ocean	6
1.4 Barium isotopes as new proxies for palaeoceanography.....	7
1.4.1 Barium isotopes in shallow and cold-water corals.....	7
1.4.2 Barium isotopes in marine sediments	9
1.5 Outline of the thesis	10
1.6 Declaration of my own contributions.....	12
2 Extended Methodology.....	13
2.1 Chemical separation of Ba from matrices.....	13
2.1.1 Barium pre-concentration from seawater	14
2.1.2 Ion exchange chromatography	15
2.2 Principle of the isotope dilution technique	16
2.3 Double spike data reduction	18
3 Scientific Chapter I.....	23
The impact of MC-ICP-MS plasma conditions on the accuracy and precision of stable isotope measurements evaluated for barium isotopes.....	23
Abstract	23
3.1 Introduction.....	24
3.2 Experimental setup.....	28
3.2.1 Instrumental setups and data reduction	28
3.2.2 The NIST SRM 3014a Ba solutions doped with matrix elements	30
3.2.3 Seawater reference sample and chemical purification	30
3.2.4 Carbonate sample preparation and chemical purification	31
3.3 Results and discussion	32
3.3.1 Sensitivity	32
3.3.2 Oxide formation rate.....	34
3.3.3 Non-spectral matrix effects.....	36
3.3.4 Effects on instrumental mass fractionation correction methods	40
3.3.5 Ba isotopic compositions of SAFe D2 and JCp-1.....	46
3.4 Conclusion.....	48

4	Scientific Chapter II	49
	High-latitude controls on dissolved barium isotope distributions in the Atlantic Meridional Overturning Circulation	49
	Abstract.....	49
4.1	Introduction.....	50
4.2	Materials and methods.....	51
4.2.1	Hydrography.....	51
4.2.2	Sampling and pre-treatment.....	55
4.2.3	Ba concentration analyses.....	56
4.2.4	Stable Ba isotope analyses.....	56
4.3	Results.....	57
4.4	Discussion.....	60
4.4.1	Origin of the $\delta^{138}\text{Ba}$ signature of NADW.....	60
4.4.2	Origin of the $\delta^{138}\text{Ba}$ signature of AABW.....	62
4.4.3	High-latitude controls on Ba isotope distributions in the deep ocean...63	
4.4.4	Ba isotope fractionation in the upper ocean.....	65
4.4.5	Palaeoceanographic prospects.....	69
4.5	Conclusions.....	70
5	Scientific Chapter III	71
	Monthly resolved coral $\delta^{138}\text{Ba}$ record of increased riverine inputs during the South Asian Summer Monsoon at the Andaman Islands, NE Indian Ocean	71
	Abstract.....	71
5.1	Introduction.....	72
5.2	Materials and Methods.....	74
5.2.1	Study area.....	74
5.2.2	Coral and seawater samples collection and preparation.....	76
5.2.3	Geochemical analysis.....	78
5.2.4	Coral age model.....	81
5.2.5	Methodology of seawater $\delta^{18}\text{O}$ ($\delta^{18}\text{O}_{\text{SW}}$) reconstruction.....	83
5.2.6	Environmental data sources and statistical analysis.....	84
5.3	Results.....	84
5.3.1	Interview Island coral (AND-2-B) time series.....	84
5.3.2	Mayabunder coral (AND-3-A II) time series.....	87
5.3.3	Surface seawater Ba concentrations ($[\text{Ba}]_{\text{SW}}$) and isotope compositions ($\delta^{138}\text{Ba}_{\text{SW}}$).....	88
5.4	Discussion.....	91

5.4.1	Monthly variations in $\delta^{18}\text{O}_{\text{SW}}$ and palaeosalinity estimates	91
5.4.2	$\delta^{138}\text{Ba}_{\text{coral}}$ as a novel proxy for riverine inputs	92
5.4.3	Constraints on coral Ba isotope compositions	97
5.5	Conclusions.....	103
6	Summary, Conclusions and Outlook	105
6.1	Summary and Conclusions	105
6.2	Outlook.....	108
	Acknowledgements.....	111
	References.....	113
	Appendix	129

1 Introduction

1.1 Barium and its stable isotopes

Barium (Ba) is one of the alkaline earth metals and has seven stable isotopes, ^{130}Ba , ^{132}Ba , ^{134}Ba , ^{135}Ba , ^{136}Ba , ^{137}Ba and ^{138}Ba with relative abundances of 0.106%, 0.101%, 2.417%, 6.592%, 7.854%, 11.232% and 71.698%, respectively (Fig. 1.1, Meija et al., 2016). The isotope composition of Ba is commonly reported in the delta-notation (δ) relative to the National Institute of Standards and Technology (NIST) standard reference material (SRM) 3104a as $\delta^x\text{Ba} (\text{‰}) = \left(\frac{{}^x\text{Ba}_{\text{sample}}}{{}^x\text{Ba}_{\text{NIST SRM 3104a}}} - 1 \right) \times 1000$, where x represents the Ba isotope mass 137 or 138. Under mass-dependent isotope fractionation, $\delta^{137}\text{Ba}$ can be directly converted to $\delta^{138}\text{Ba}$ by multiplication with a factor of ~ 1.33 (Horner et al., 2015). This simple conversion is generally valid given that any systematic errors introduced are significantly smaller than current analytical uncertainties.

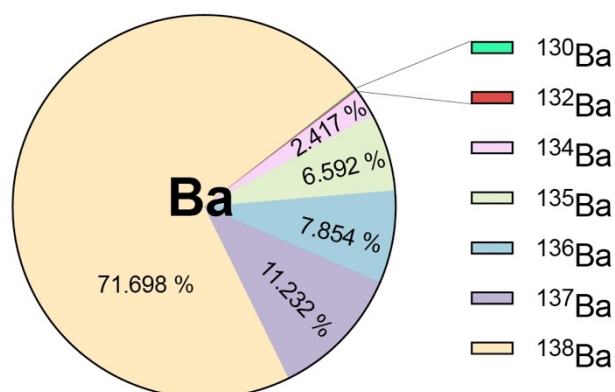


Fig. 1.1: The relative abundance of stable barium isotopes (Meija et al., 2016).

The magnitude of Ba isotope fractionation has been thought to be negligible for many decades. The first Ba isotope analysis was conducted as early as 1938 (Nier, 1938). Eugster et al. (1969) subsequently improved the precision significantly by using a double-spike technique but found no statistical difference in the Ba isotope compositions between terrestrial and meteoritic samples measured on a single-focusing thermal ionisation mass spectrometer (TIMS). Recent improvements in multi-collector inductively coupled plasma mass spectrometry (MC-ICP-MS) and TIMS have decreased the analytical uncertainties of the measurements and brought a new dimension to the field of stable Ba isotope analysis in that differences in Ba isotope compositions as small as 0.01‰ amu^{-1}

can now be resolved (Horner and Crockford, 2021). Since 2010, the interest in mass-dependent Ba isotope fractionation has increased substantially and significant variations in Ba isotope compositions have been observed for a variety of sample materials, such as seawater (Bates et al., 2017; Cao et al., 2020a, 2016; Horner et al., 2015; Hsieh and Henderson, 2017; Yu et al., 2020), river water (Cao et al., 2020b; Charbonnier et al., 2020; Gou et al., 2020; Hsieh and Henderson, 2017), groundwater (Mayfield et al., 2021), marine carbonates (Geyman et al., 2019; Hemsing et al., 2018; Liu et al., 2019; Pretet et al., 2015), marine sediments (Bridgestock et al., 2019, 2018; Crockford et al., 2019), sulphates (Böttcher et al., 2018; Tian et al., 2020; von Allmen et al., 2010), as well as terrestrial and extra-terrestrial materials (Gong et al., 2020; Hsieh et al., 2021; Li et al., 2020; Moynier et al., 2015; Nan et al., 2018; Nielsen et al., 2020, 2018; Tieman et al., 2020; van Zuilen et al., 2016b).

1.2 Barium isotope fractionation in seawater

The biogeochemical cycling of dissolved Ba ($[Ba]$) and its isotopes ($\delta^{138}Ba$) in the modern ocean has been extensively studied over the past five years (e.g., Cao et al., 2020, 2016; Horner et al., 2015; Hsieh and Henderson, 2017). Water column concentrations of dissolved Ba show a nutrient-like depth profile in the oceans (Fig. 1.2a), with $[Ba]$ depletion in surface waters resulting from removal with biogenic particles and $[Ba]$ enrichment at depth due to particulate matter decomposition and remineralisation (Bacon and Edmond, 1972; Lea and Boyle, 1989). Similarly, vertical distribution of $\delta^{138}Ba$ (Fig. 1.2b) shows that in the uppermost water column, Ba isotope fractionation is largely induced by preferential adsorption of the light isotopes to biogenic particles (Cao et al., 2020a, 2016). Below the surface ocean, the microbial oxidation of sinking organic matter can develop a microenvironment in which Ba^{2+} and SO_4^{2-} ions from both respired organic matter and ambient seawater accumulate and reach an oversaturated state for $BaSO_4$ (barite), despite that the vast majority of ocean is undersaturated with respect to barite (Bishop, 1988; Dehairs et al., 1980; Horner et al., 2017). This pelagic barite formation preferentially assimilates light Ba isotopes, which leads to heavy dissolved $\delta^{138}Ba$ values in subsurface seawater (Bates et al., 2017; Horner et al., 2015). As a result, there is an increase in dissolved $\delta^{138}Ba$ values between ~ 200 and ~ 600 m water depth supporting earlier findings that most barite precipitation occurs at these depths (Bates et al., 2017; Horner et al., 2015). Below the subsurface ocean, barite dissolution slowly releases light

Ba isotopes to intermediate and deep waters. The fractionated Ba isotope compositions observed in the deep waters, in contrast to that of surface and subsurface waters, are mainly controlled by barite dissolution and large scale mixing. This vertical cycling of barite leads to a strong negative correlation between [Ba] and $\delta^{138}\text{Ba}$, with the upper ocean being depleted in [Ba] and featuring heavier $\delta^{138}\text{Ba}$ values, and the deep ocean being enriched in [Ba] and featuring lighter $\delta^{138}\text{Ba}$ values (Fig. 1.2, Bates et al., 2017; Bridgestock et al., 2018; Cao et al., 2020b; Hemsing et al., 2018; Horner et al., 2015; Hsieh and Henderson, 2017).

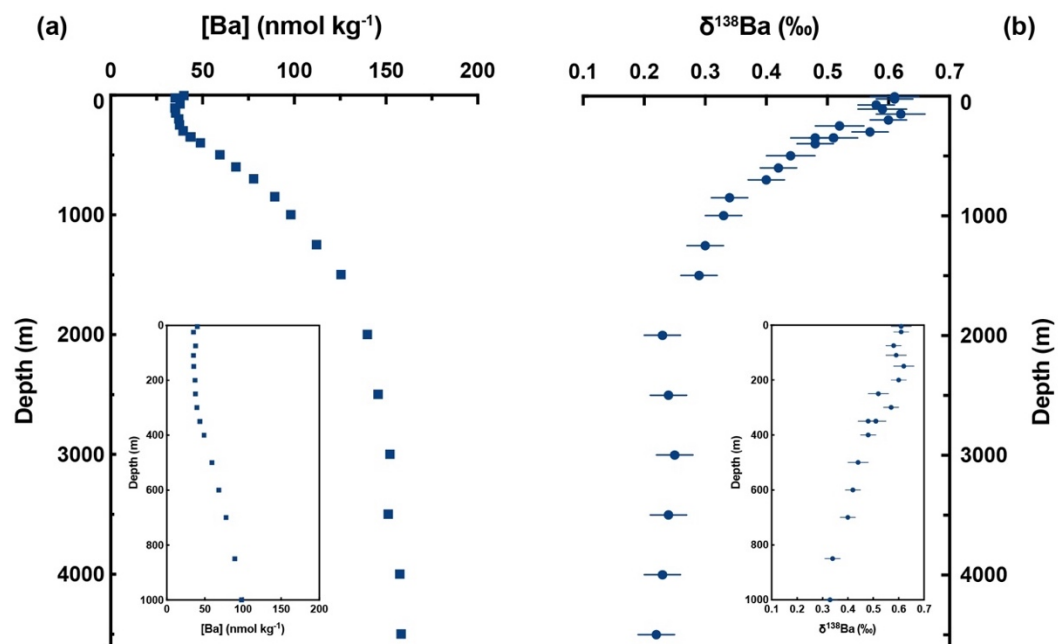


Fig. 1.2: Profiles of dissolved (a) [Ba] and (b) $\delta^{138}\text{Ba}$ from the North Pacific Ocean at the “SAFE” station (Geyman et al., 2019).

In a global context, Ba isotope compositions of open ocean seawater are mainly governed by large-scale ocean circulation. Given that the oceanic residence time of dissolved Ba (7–21 kyr, Horner and Crockford, 2021) is comparable to the global ocean mixing time, stable Ba isotopes can be used as a novel tracer for water masses and their mixing. In the Atlantic Ocean, the distribution of $\delta^{138}\text{Ba}$ in deep waters clearly follow the two endmember mixing between North Atlantic Deep Water (NADW) and Antarctic Bottom Water (AABW, Fig. 1.3, Bates et al., 2017; Hsieh and Henderson, 2017). The Southern Ocean plays a key role in setting the preformed Ba isotope compositions in the global ocean, in which the well ventilated Circumpolar Deep Water (CDW) supplies waters with

high [Ba] ($\sim 90 \text{ nmol kg}^{-1}$) and light $\delta^{138}\text{Ba}$ signatures ($\sim +0.35\text{‰}$) to the surface ocean (Hsieh and Henderson, 2017).

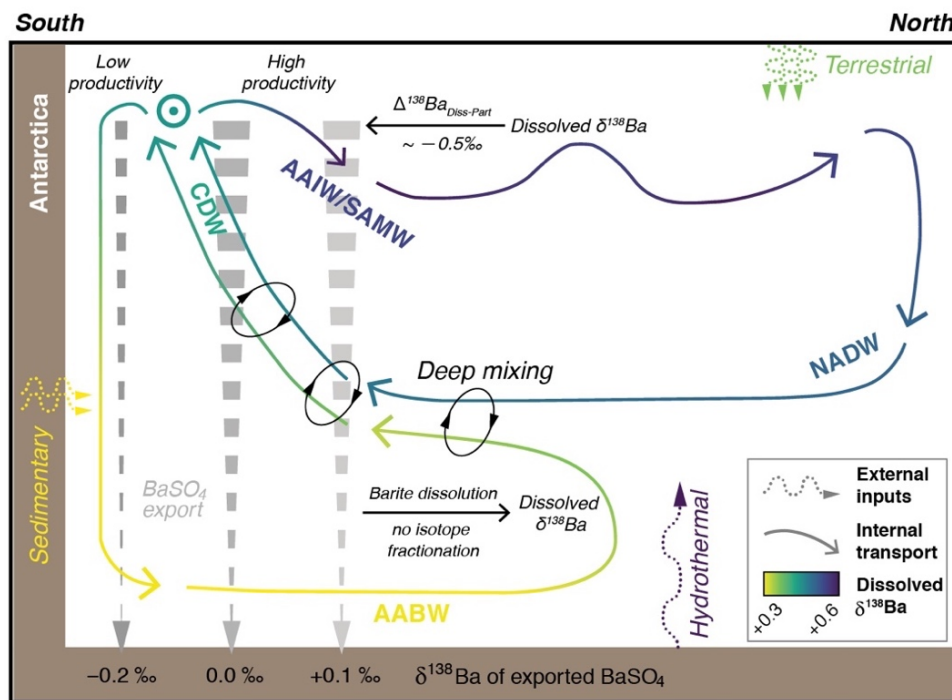


Fig. 1.3: A conceptual model of Ba cycling in the Atlantic Ocean. The rising intrusion of CDW onto the Antarctic continental shelves is accompanied by little Ba isotope fractionation in the low-productivity Weddell Gyre. In contrast, the northward ventilation of CDW that passes the high-productivity zones undergoes extensive Ba isotope fractionation, presumably as a result of barite formation and mixing. The variations in dissolved $\delta^{138}\text{Ba}$ values are indicated by the colour shading. This figure is modified from Horner and Crockford (2021).

The rising intrusion of CDW onto the Antarctic continental shelves in the low-productivity Weddell Gyre experiences little Ba isotope fractionation before subsequently mixing with cold shelf waters resulting in the formation of AABW (Fig. 1.3). Given that the $\delta^{138}\text{Ba}$ signature of AABW ($+0.26\text{‰}$, Hsieh and Henderson, 2017) is about 0.07‰ lighter than upwelled CDW ($\sim +0.33\text{‰}$, Hsieh and Henderson, 2017), and that terrestrial $\delta^{138}\text{Ba}$ values are isotopically light ($\sim +0.20\text{‰}$, Cao et al., 2020b; Charbonnier et al., 2020; Gou et al., 2020; Hsieh and Henderson, 2017), weathering inputs from the grounded glaciers of Antarctica likely contribute to the light $\delta^{138}\text{Ba}$ value of AABW. In contrast, the northward ventilation of CDW that enters the high-productivity Antarctic Circumpolar Current (ACC) undergoes extensive Ba isotope fractionations, presumably

as a result of enhanced productivity and associated barite precipitation (Horner and Crockford, 2021). As the waters transit northward away from the ACC, surface dissolved [Ba] values decrease from ~ 90 to ~ 50 nmol kg^{-1} , associated with an increase in $\delta^{138}\text{Ba}$ values from $\sim +0.3$ to $\sim +0.5\text{‰}$ (Bates et al., 2017; Hsieh and Henderson, 2017). The northward flowing Subantarctic Mode Water (SAMW) and Antarctic Intermediate Water (AAIW) are considered as one of the major sources of heavy $\delta^{138}\text{Ba}$ to the North Atlantic (Horner and Crockford, 2021). Another potential source of heavy $\delta^{138}\text{Ba}$ delivery to the high-latitude North Atlantic are the Nordic Seas Overflow Waters ($+0.52\text{‰}$, Yu et al., unpublished), which eventually merge into NADW and constitutes the northern-deep limb of the Atlantic Meridional Overturning Circulation (AMOC, Talley, 2013).

Taken together, differences in primary productivity and barite precipitation determine the preformed $\delta^{138}\text{Ba}$ signatures of the AABW and NADW end-members. The AMOC, on the other hand, generally governs the meridional distributions of Ba isotopes in the Atlantic Ocean. In the Pacific Ocean, old deep water masses (e.g., Pacific Deep Water, PDW) have relatively high [Ba] value of ~ 150 nmol kg^{-1} due to continuing barite dissolution along the oceanic conveyor belt, but retain a light $\delta^{138}\text{Ba}$ value of $\sim +0.23\text{‰}$ (Geyman et al., 2019) similar to that of AABW ($+0.26\text{‰}$, Fig 1.4, Hsieh and Henderson, 2017).

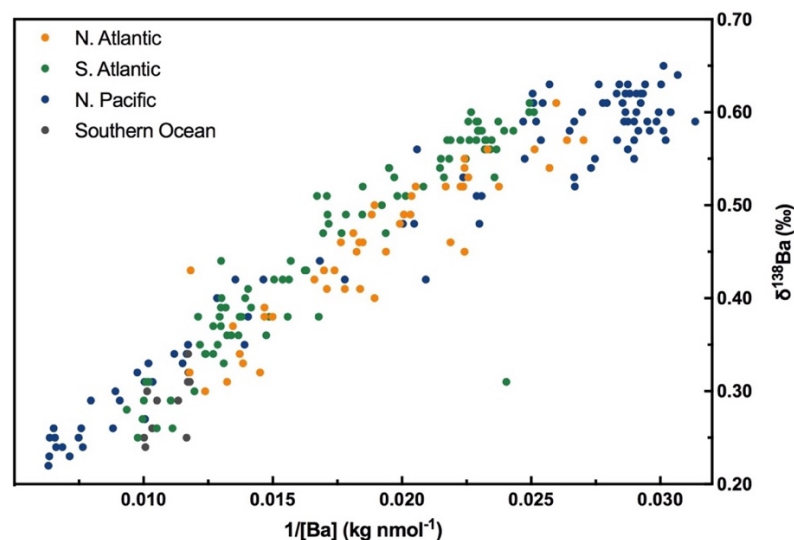


Fig. 1.4: A global compilation of dissolved $\delta^{138}\text{Ba}$ against $1/[\text{Ba}]$ (Bates et al., 2017; Bridgestock et al., 2018; Cao et al., 2020a, 2020b; Geyman et al., 2019; Horner et al., 2015; Hsieh and Henderson, 2017).

1.3 Sources of barium in the global ocean

The supply of Ba to the open ocean mainly originates from riverine and groundwater discharge of weathered, crustal silicate minerals (Paytan and Kastner, 1996). The annual flux of riverine and groundwater Ba to the global ocean was estimated at range between 7–10 Gmol yr⁻¹ (Das and Krishnaswami, 2006; Gaillardet et al., 2003), with groundwater accounting for 6–36% of the total flux (Mayfield et al., 2021). As shown in Fig. 1.5, the Ba isotope compositions in rivers (between ~ +0.2 and ~ +0.3‰, Cao et al., 2020b; Charbonnier et al., 2020; Gou et al., 2020; Hsieh and Henderson, 2017) and groundwater (~ +0.1‰, (Mayfield et al., 2021) are heavier than those of the upper continental crust (0.00 ± 0.04‰, (Nan et al., 2018), but lighter than those in surface oceans (between ~ +0.3 and ~ +0.6‰, Bates et al., 2017; Cao et al., 2020a, 2016; Horner et al., 2015; Hsieh and Henderson, 2017). In addition, benthic Ba inputs from hydrothermal vent fluids contribute isotopically heavy $\delta^{138}\text{Ba}$ (+1.7 ± 0.7‰) to the deep ocean (Hsieh et al., 2021).

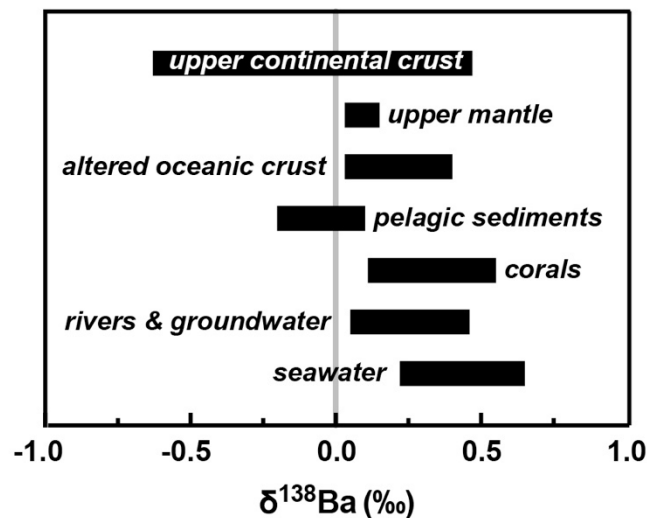


Fig. 1.5: Summary of Ba isotope compositions ($\delta^{138}\text{Ba}$) of different reservoirs. Data source: (Bates et al., 2017; Bridgestock et al., 2019, 2018; Cao et al., 2020a, 2020b; Charbonnier et al., 2020; Geyman et al., 2019; Gou et al., 2020; Hemsing et al., 2018; Horner et al., 2015; Hsieh and Henderson, 2017; Liu et al., 2019; Mayfield et al., 2021; Nan et al., 2018; Nielsen et al., 2020, 2018; Pretet et al., 2015).

Recent investigations of combined [Ba] and $\delta^{138}\text{Ba}$ signatures of river waters and estuarine samples showed significant Ba isotope fractionation at low salinities that mainly result from fluvial particle adsorption-desorption processes (Gou et al., 2020; Cao et al.,

unpublished data). Generally, dissolved [Ba] in river waters increases from a relatively low value at zero salinity to the [Ba] maxima at low salinity, associated with the salinity-induced desorption of Ba from suspended fluvial particles (e.g., Coffey et al., 1997; Joung and Shiller, 2014). In contrast, dissolved [Ba] at intermediate and high salinities is characterised by conservative two-endmember mixing between low salinity waters at the [Ba] maxima and seawater (e.g., Guay and Falkner, 1997; Samanta and Dalai, 2016). Similarly, the $\delta^{138}\text{Ba}$ value of the river water endmember at zero salinity is significantly elevated due to preferential removal of light Ba isotopes by adsorption onto particles, and subsequently drop to a minimum value at a slightly higher salinity indicating desorption of isotopically light Ba isotopes from particles (Cao et al., unpublished data). Towards the open ocean, conservative mixing dominates $\delta^{138}\text{Ba}$ distributions along salinity gradients in river estuaries (Cao et al., unpublished data). As a consequence, reported data from coastal regions show that riverine inputs significantly lower near-shore $\delta^{138}\text{Ba}$ signatures in the East China Sea and the South Atlantic, respectively (Cao et al., 2020b; Hsieh and Henderson, 2017). In addition, Ba isotope compositions in the upstream freshwater of the Yellow River exhibit strong seasonality, mainly resulting from variations in suspended particulate matter fluxes during different monsoon periods (Gou et al., 2020). Therefore, the seasonal variations in monsoon circulation and related changes in river discharge are expected to result in significant $\delta^{138}\text{Ba}$ variability in near-shore seawater and thus in temporal variations of $\delta^{138}\text{Ba}$ in coastal carbonates. Extending the use of Ba isotopes into reconstructions of past environments will be discussed below in section 1.4.

1.4 Barium isotopes as new proxies for palaeoceanography

1.4.1 Barium isotopes in shallow and cold-water corals

The ratio of barium to calcium (Ba/Ca) in shallow-water coral skeletons has been widely used as a proxy for river discharge in coastal regions (e.g., McCulloch et al., 2003). However, a number of studies have reported “anomalous” signals of coral Ba/Ca that are decoupled from peak river discharge, suggesting that this proxy is not solely controlled by river runoff (e.g., Jupiter et al., 2008; Lewis et al., 2007; Sinclair, 2005). Other factors, such as coastal upwelling (Lea et al., 1989) and dust inputs (Bryan et al., 2019), can potentially have a significant effect on the temporal variability of the coral Ba/Ca proxy.

As discussed in section 1.3, river waters have light Ba isotope compositions relative to the surface ocean and can significantly modify the $\delta^{138}\text{Ba}$ signatures of coastal seawaters (Cao et al., 2020b; Hsieh and Henderson, 2017). Therefore, if corals living in shallow waters reliably record the ambient seawater $\delta^{138}\text{Ba}$ signatures, coral $\delta^{138}\text{Ba}$ records could serve as a complementary proxy to Ba/Ca ratios for the reconstruction of riverine inputs. Similarly, Ba isotopes in cold-water corals harbour great potential to provide new insights into the past oceanic Ba cycle and deep ocean circulation over a range of timescales (Geyman et al., 2019; Hemsing et al., 2018).

Recent studies have explored how Ba isotopes are fractionated during Ba incorporation into coral skeletons. Based on first-principal calculations, heavy Ba isotopes are enriched in aragonites ($\Delta^{138/134}\text{Ba}_{\text{aragonite-solution}} \approx +0.4\text{‰}$) due to the much stronger Ba-O bonds if growing aragonites are in thermodynamic equilibrium with the aqueous solutions (Mavromatis et al., 2020; Wang et al., 2021). However, Ba isotopic exchange equilibrium is unlikely to be achieved during coral growth in the natural environment. Recently, a precipitation experiment of inorganic aragonite showed a reversed relationship between Ba isotope fractionation ($\Delta^{138/134}\text{Ba}_{\text{aragonite-solution}}$) and aragonite growth rate during Ba incorporation (Mavromatis et al., 2020). The precipitated aragonite that is formed at low growth rates ($\leq 10^{-8.1}$ mol/m²/s) is enriched in isotopically heavier Ba isotopes, while the newly formed aragonite becomes progressively enriched in lighter Ba isotopes when growth rates exceed $10^{-8.0}$ mol/m²/s (Mavromatis et al., 2020). However, given that this precipitation experiment was conducted under a chemical steady-state condition, the mineral growth rate may have different effects on Ba isotope fractionation during natural coral calcification.

Contrary to theoretical calculations and inorganic precipitation experiments, Pretet et al. (2015) demonstrated that Ba isotope compositions of bulk samples from cultured, aragonitic corals (between +0.21‰ and +0.55‰) are isotopically identical or lighter than those of the ambient Mediterranean surface seawater ($+0.56 \pm 0.09\text{‰}$). Another study of natural coral skeletons suggested that annually-resolved $\delta^{138}\text{Ba}$ records ($+0.33 \pm 0.08\text{‰}$) from diverse oceanic settings display negative offsets ($\sim -0.30\text{‰}$) from the typical Pacific surface seawater $\delta^{138}\text{Ba}$ values (Liu et al., 2019). The magnitude of Ba isotope fractionation between coral and seawater has been suggested to be relatively constant and largely unaffected by biomineralization processes and sea surface temperature (Liu et al.,

2019). In addition, two comprehensive assessments of depth-dependent variations of $\delta^{138}\text{Ba}$ in cold-water corals (aragonite and calcite) showed constant shift in isotope ratios towards lighter values than ambient seawater (Geyman et al., 2019; Hemsing et al., 2018). Within their reported uncertainties, no significant correlation between the extent of Ba isotope fractionation and species, temperature, salinity, pH or depth has been observed (Geyman et al., 2019; Hemsing et al., 2018). Overall, the direction and magnitude of Ba isotope fractionation ($\Delta^{138/134}\text{Ba}_{\text{coral-seawater}}$ between -0.02‰ and -0.37‰ , Geyman et al., 2019; Hemsing et al., 2018; Liu et al., 2019; Pretet et al., 2015) in both shallow and cold-water corals are generally comparable with fractionation during precipitation of aragonite-structured witherite (BaCO_3 , between -0.09‰ and -0.33‰ , Mavromatis et al., 2016; von Allmen et al., 2010) and double carbonate $\text{BaMn}(\text{CO}_3)_2$ (-0.23‰ , Böttcher et al., 2012).

1.4.2 Barium isotopes in marine sediments

The accumulation of non-detrital Ba or barite (BaSO_4) in marine sediments is considered to be a robust proxy for past export production and has been used to reconstruct past biogeochemical processes in the ocean (Dymond et al., 1992; Eagle et al., 2003; Paytan et al., 1996; Paytan and Griffith, 2007). In comparison to other sedimentary components (e.g., organic carbon, calcium carbonates and opal) that are used to reconstruct primary productivity and export production, barite preservation in deep-sea sediments is relatively high (Dehairs et al., 1980; Paytan et al., 1996). However, diagenetic processes in sulphate-depleted sediments and changes in bulk sedimentation rates can compromise the reliability of sedimentary barite as a reliable proxy for export production (McManus et al., 1998; Riedinger et al., 2006; Torres et al., 1996).

The Ba isotope composition of marine sediments has recently been proposed as a novel tool to provide insights into past changes in export production (Bridgestock et al., 2019, 2018). The inferred isotope composition of excess Ba is $\delta^{138}\text{Ba} = +0.09 \pm 0.01\text{‰}$, which likely represents the $\delta^{138}\text{Ba}$ contribution from authigenic barite formed in the upper ocean (Bridgestock et al., 2018). In addition, Crockford et al. (2019) measured a mean $\delta^{138}\text{Ba}$ value of isolated pelagic barites from core-top sediments of $+0.04 \pm 0.06\text{‰}$. Assuming that the precipitation of barite predominantly occurs in the upper 500 m of the water column, the magnitude of the isotope fractionation ($\Delta^{138/134}\text{Ba}_{\text{barite-dissolved}}$) accompanying

Ba removal from the upper ocean was estimated to be between -0.4 and -0.5% (Bridgestock et al., 2018; Crockford et al., 2019). This range of isotope fractionation is comparable with the average Ba isotope offsets between the marine particulate and total dissolved Ba in the South Atlantic ($\Delta^{138/134}\text{Ba}_{\text{particle-dissolved}} = -0.53 \pm 0.04\%$, Horner et al., 2015), the Lake Superior ($\Delta^{138/134}\text{Ba}_{\text{particle-dissolved}} = -0.41 \pm 0.09\%$, Horner et al., 2017), and the South China Sea ($\Delta^{138/134}\text{Ba}_{\text{particle-dissolved}} = -0.46 \pm 0.11\%$, Cao et al., 2020a). In contrast to field-based estimates of $\Delta^{138/134}\text{Ba}_{\text{barite-dissolved}}$, results from two experimental studies of barite precipitation suggested that the Ba isotope fractionation effect ($\Delta^{138/134}\text{Ba}_{\text{barite-dissolved}}$) is between -0.25% and -0.35% (Böttcher et al., 2018; von Allmen et al., 2010). Addressing the discrepancy between field and experiment-based estimates of $\Delta^{138/134}\text{Ba}_{\text{barite-dissolved}}$ clearly needs more modern process studies in diverse environments (Horner and Crockford, 2021).

Nevertheless, if the $\delta^{138}\text{Ba}$ signature of excess Ba accumulated in marine sediments solely depends on the isotope composition of the dissolved Ba in the upper ocean, the sedimentary excess $\delta^{138}\text{Ba}$ can track changes in the balance between Ba supply (e.g., riverine inputs) and removal (e.g., barite precipitation), which in turn is closely related to export production (Bridgestock et al., 2018). Results from $\delta^{138}\text{Ba}$ measurements of bulk sediments in the South Atlantic and the Southern Ocean indicated that the increase in barite accumulation rates coincides with increased sedimentary $\delta^{138}\text{Ba}$ values, suggesting enhanced export production during the Palaeocene-Eocene thermal maximum (PETM) recovery (Bridgestock et al., 2019). This study highlighted the great potential of using sedimentary Ba isotopes to assess the potential controls on non-detrital Ba accumulation rates in marine sediments and to reconstruct export production.

1.5 Outline of the thesis

This dissertation addresses three primary objectives, starting from establishing a matrix tolerance state for stable Ba isotope analysis with MC-ICP-MS (chapter 3), then examining the factors controlling dissolved Ba isotope distributions in the high-latitude oceans (chapter 4), and finally extending the use of Ba isotopes into palaeoceanographic applications in combination with other proxies in tropical coral skeletons (chapter 5). These three main chapters are presented in the form of independent scientific articles, with chapter 3 already published, chapter 4 to be submitted and chapter 5 in review.

Chapter 1 introduces the systematics of stable Ba isotope fractionations in seawater, rivers, groundwater, corals and marine sediments. The research background including previous applications of Ba isotopes in oceanographic and palaeoceanographic studies are also discussed.

Chapter 2 outlines the principal analytical procedures for the measurement of stable Ba isotope compositions in seawater and coral skeletons. In particular, this chapter concentrates on the chemical purification of Ba from sample matrices and the description of Ba isotopic data reduction using the isotope-dilution and the double-spike techniques.

Chapter 3 addresses how instrumental mass bias change as a function of MC-ICP-MS plasma conditions as well as of impurity concentrations in Ba isotope analysis. The results show that the effect of matrix elements on instrumental mass fractionation is highly variable despite the application of a double-spike but can be significantly attenuated by optimising plasma conditions. This study opens a new window for understanding the instrumental mass fractionation in response to different but quantifiable plasma conditions and thus for improving stable isotope analysis with MC-ICP-MS.

Chapter 4 assesses the systematics of dissolved seawater Ba concentrations and isotope compositions in the Nordic Seas, the Labrador Sea and the Weddell Sea. This study underscores the high-latitude controls of dissolved Ba isotopes in the water masses of the Atlantic Meridional Overturning Circulation (AMOC) and enhances our current understanding of the mechanisms governing marine Ba isotope fractionation in the upper ocean.

Chapter 5 presents a monthly resolved stable Ba isotope record of a young fossil coral from the Andaman Islands, India. This is the first study to test the applicability of coral $\delta^{138}\text{Ba}$ as a new proxy for past riverine inputs on seasonal timescales against other coral proxies and external environmental drivers. In addition, the Ba isotope fractionation between coral skeletons and local seawater is estimated, which sheds light on the effects of mineral growth kinetics and biomineralization on the process of coral calcification.

Chapter 6 summarises this dissertation and sets a framework for future studies.

1.6 Declaration of my own contributions

Chapter 3 declaration: Christopher Siebert, Jan Fietzke and I proposed the study. I carried out the Ba concentration and isotope measurements in the laboratory and wrote the manuscript. Tyler Goepfert and Ed Hathorne assisted in the analyses of the Ba concentration and isotope data. All co-authors contributed to the discussions and improved the text of the manuscript. This chapter has already been published in the journal *Chemical Geology*, authored by Yang Yu, Christopher Siebert, Jan Fietzke, Tyler Goepfert, Ed Hathorne, Zhimian Cao and Martin Frank under the title: The impact of MC-ICP-MS plasma conditions on the accuracy and precision of stable isotope measurements evaluated for barium isotopes.

Chapter 4 declaration: Martin Frank, Ed Hathorne proposed the study. Georgi Laukert, Marcus Gutjahr and Genna Patton collected the samples. I conducted the Ba concentration and isotope analyses including sample preparations and chemical purifications. I interpreted the data and wrote the manuscript, which was improved by discussions with all co-authors. This chapter will soon be submitted and will be authored by Yang Yu, Ruifang C. Xie, Marcus Gutjahr, Georgi Laukert, Zhimian Cao, Ed Hathorne, Christopher Siebert, Genna Patton and Martin Frank under the title: High-latitude controls on dissolved barium isotope distributions in the Atlantic Meridional Overturning Circulation.

Chapter 5 declaration: Ed Hathorne, Thomas Felis and Martin Frank proposed the study. Ed Hathorne, Thomas Felis and C.P. Rajendran collected the samples. I conducted the geochemical analyses including sample preparations and chemical purifications. I interpreted the data and wrote the manuscript, which was improved by discussions with all co-authors. This chapter has been submitted to the journal *Geochimica et Cosmochimica Acta*, authored by Yang Yu, Ed Hathorne, Christopher Siebert, Thomas Felis, C.P. Rajendran and Martin Frank under the title: Monthly resolved coral $\delta^{138}\text{Ba}$ record of increased riverine inputs during the South Asian Summer Monsoon at the Andaman Islands, NE Indian Ocean.

2 Extended Methodology

This chapter concentrates on the chemical purifications of Ba, the principles of the isotope dilution technique and a detailed description of double-spike data reduction. Further details concerning sample materials, sampling campaigns and analyses of other geochemical records, especially the instrumental operational conditions, are extensively discussed and presented in the respective chapters.

2.1 Chemical separation of Ba from matrices

To determine accurate and precise Ba isotope ratios with MC-ICP-MS, separation of the analyte from the sample matrix is preferred to minimise any possible spectral interferences and non-spectral matrix effects. Barium suffers from a number of isobaric interferences across its mass range (Table 2.1). In addition to xenon (Xe) isobaric interferences in the argon (Ar) gas used for MC-ICP-MS, a range of molecular interferences can also affect Ba isotope signals. On the other hand, although the very high temperature of the plasma allows a high ionisation efficiency and rapid sample throughput, the non-spectral matrix effects can interfere with the ionisation and transmission of the analyte, which may lead to systematic deviations and errors in isotope analysis (Gillson et al., 1988; Tan and Horlick, 1987). Therefore, the Ba purification was achieved by application of a pre-concentration method from seawater in conjunction with the ion exchange chromatography described below.

Table 2.1: Possible isobaric interferences for Ba isotope analysis with MC-ICP-MS

m/z	130	131	132	134	135	136	137	138
Ba isotopes	^{130}Ba		^{132}Ba	^{134}Ba	^{135}Ba	^{136}Ba	^{137}Ba	^{138}Ba
Isobaric interferences	^{130}Xe ^{130}Te $^{90}\text{Zr}^{40}\text{Ar}$	^{131}Xe $^{91}\text{Zr}^{40}\text{Ar}$	^{132}Xe $^{92}\text{Zr}^{40}\text{Ar}$ $^{92}\text{Mo}^{40}\text{Ar}$	^{134}Xe $^{94}\text{Zr}^{40}\text{Ar}$ $^{94}\text{Mo}^{40}\text{Ar}$	$^{95}\text{Mo}^{40}\text{Ar}$	^{136}Ce $^{96}\text{Zr}^{40}\text{Ar}$	$^{97}\text{Mo}^{40}\text{Ar}$	^{138}La ^{138}Ce $^{98}\text{Mo}^{40}\text{Ar}$

2. Extended Methodology

2.1.1 Barium pre-concentration from seawater

To reduce the amount of major matrix elements (e.g., Mg, Sr and Ca), Ba is precipitated from seawater as a carbonate prior to ion exchange chromatography, based on the procedure described by Foster et al. (2004) and Horner et al. (2015). To minimise Ba contamination and blank contributions from the powder reagent sodium carbonate (Na_2CO_3 , Lot No. F13Z022), a 1.1M solution of Na_2CO_3 was cleaned from Ba by stepwise addition of a 1.0 M solution of calcium chloride (CaCl_2 , Lot No. 23152) to induce carbonate precipitation. The amount of CaCl_2 added was calculated to achieve a residual Na_2CO_3 solution with a final concentration of 1.0 M. The resulting precipitate was removed by centrifuging and the residual “Ba-free” Na_2CO_3 solution (pH ~ 12) was transferred into a clean Teflon bottle.

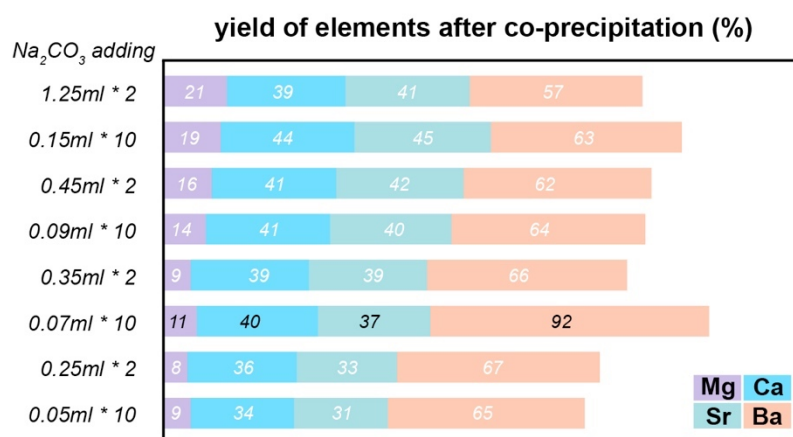


Fig. 2.1: The co-precipitation experiments from 10 mL of seawater. The yield of each element after co-precipitation is calculated based on their respective concentrations and is reported as percent (%).

Aliquots of 5 or 10 mL of acidified seawater were appropriately spiked with an ^{130}Ba - ^{135}Ba double-spike in 7 mL of Teflon vials. After an equilibration period of 24 hours, seawater samples were transferred to acid-cleaned 15 mL centrifuge tubes for Ba pre-concentration. The prepared “Ba-free” Na_2CO_3 solution was added stepwise (35 or 70 μL) to each sample with vigorously shaking at intervals, which led to co-precipitation of the dissolved Ba with the calcium carbonate (CaCO_3). The total amount of Na_2CO_3 added and the yield of this protocol were tested on an aliquot of 10 mL of laboratory seawater reference material, which indicated a yield of 11% for Mg, 40% for Ca, 37% for Sr and

92% for Ba (Fig. 2.1). After settling of the milky precipitate (> 8 hours), most of the supernatant was decanted with a clean pipette tip and discarded. The residual precipitate was dissolved in 2 mL of 1 M HCl and transferred back into its respective Teflon vial for ion exchange chromatography.

2.1.2 Ion exchange chromatography

Ion exchange chromatography was conducted using the cation exchange resin (BIORAD® AG50W-X8 resin, 200-400 μm mesh-size, 1.4 mL resin bed) to further purify Ba from residual sample matrices. The chemical procedures of ion exchange chromatography were adopted and modified from the protocols described in Cao et al. (2016) and Horner et al. (2015). The cation exchange resin was pre-cleaned with 10 mL of 6 M HNO_3 and 5 mL of 6 M HCl before conditioning with 5 mL of 1 M HCl. The column elution curve was calibrated to estimate which element is washed out of the cation resin with defined amounts of specific acids. Fig. 2.2 shows that the major cation Mg is eluted first when using 1 M HCl. With the molarity of HCl increased to 3 M, the major matrix elements Ca and Sr can be quantitatively washed out with 8 mL of 3 M HCl. Subsequently, Ba cuts were collected with 10 mL of 2 M HNO_3 . This ion exchange chromatography procedure was repeated in full to quantitatively isolate Ba from seawater sample matrices. Finally, the purified Ba was dried down and dissolved in 2% (v/v) HNO_3 for Ba isotope analysis.

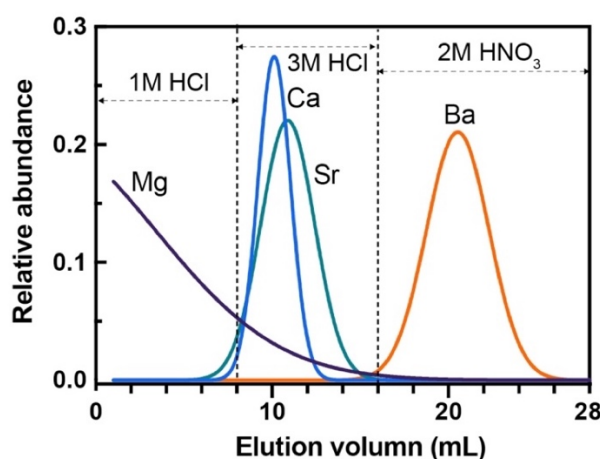


Fig. 2.2: Elution curves of Ba purification procedures on columns containing AG50W-X8 resin and using different reagents.

2.2 Principle of the isotope dilution technique

The ability of isotope dilution method to correct for matrix effects and instrumental mass bias contributes to the fact that isotope dilution is recognised as one of the benchmark methods of elemental concentration determination (Heumann, 1992; Klinkhammer and Chan, 1990). In the case of Ba, the principle of isotope dilution is shown in Fig. 2.3 by the schematic mass spectrum of Ba with two stable isotopes at masses 135 and 138.

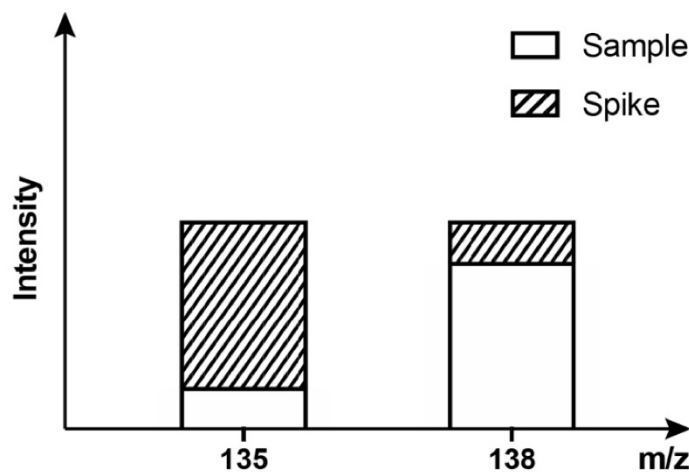


Fig. 2.3: The principle of the isotope dilution technique shown by the schematic mass spectrum of Ba with two isotopes ^{135}Ba and ^{138}Ba .

In this case ^{138}Ba is more abundant in the sample and the spike is enriched in ^{135}Ba . The amount of enrichment and spike addition to the sample must be well known to determine the Ba concentration of the analyte. Once the spike and the sample have been completely mixed and the mixed ratio (R_{mix}) has been measured, concentrations can be calculated using the following equations:

$$[Ba]_{sample} (ng\ g^{-1}) = [Ba]_{spike} \cdot \frac{W_{spike}}{W_{sample}} \cdot \frac{M_{natural}}{M_{spike}} \cdot \frac{A^{135}Ba_{spike}}{A^{135}Ba_{natural}} \cdot \frac{\left(\frac{A^{138}Ba_{spike}}{A^{135}Ba_{spike}} - R_{mix} \right)}{\left(R_{mix} - \frac{A^{138}Ba_{natural}}{A^{135}Ba_{natural}} \right)} \quad (2.1)$$

or

$$[Ba]_{sample} (nmol g^{-1}) = \frac{[^{135}Ba]_{spike}}{A^{138}Ba_{natural}} \cdot \frac{W_{spike}}{W_{sample}} \cdot \frac{\left(\frac{A^{138}Ba_{spike}}{A^{135}Ba_{spike}} - R_{mix} \right)}{\left(R_{mix} - \frac{A^{138}Ba_{natural}}{A^{135}Ba_{natural}} \right)} \quad (2.2)$$

$[Ba]_{sample}$: sample total Ba concentration in ng g⁻¹ or nmol g⁻¹;

$[Ba]_{spike}$, $[^{135}Ba]_{spike}$: total Ba concentration and the concentration of ¹³⁵Ba isotope in the spike;

W_{spike} , W_{sample} : weight in g of the spike and the sample;

$M_{natural}$, M_{spike} : sample natural atomic mass and spike atomic mass;

$A^{135}Ba_{spike}$, $A^{135}Ba_{natural}$, $A^{138}Ba_{spike}$, $A^{138}Ba_{natural}$: natural and spike relative abundances of Ba isotopes 135 and 138;

R_{mix} : mass bias corrected measured ratios of ¹³⁸Ba/¹³⁵Ba in the sample-spike mixture.

The uncertainty of Ba concentration measurements applying the isotope dilution technique mainly originates from errors in the amount of spike added, the concentration and relative isotope abundances in the spike as well as the measurement of the R_{mix} . Errors in relative abundances of Ba isotopes are commonly be minimised by calibrated measurements against a Ba standard solution with natural isotopic abundances. Therefore, they can be neglected for further consideration and the standard deviation (σ) of $[Ba]_{sample}$ can be approximated by the law of error propagation:

$$\sigma([Ba]_{sample}) \approx \sqrt{\sigma^2([Ba]_{spike}) + \varphi^2(R_{mix}) \cdot \sigma^2(R_{mix})} \quad (2.3)$$

where $\varphi(R_{mix})$ is the error multiplication factor of the measured R_{mix} values, which is smallest when the optimum ratio (R_{opt}) is reached under the following equation:

$$R_{opt} = \sqrt{^{138/135}Ba_{natural} \cdot ^{138/135}Ba_{spike}} \quad (2.4)$$

This ideal R_{opt} ratio is close to 1 for highly enriched spikes. For the spike used in this study, 0.64 is the optimum ratio. Of course, the range of acceptable R_{opt} depends on the accuracy required but is also inversely related to the precision of the measurement. In

practical terms, an experiment is required to determine this range. Alternatively, a realistic estimate of sample Ba concentration helps to reach the R_{opt} , which can be achieved by a calibration curve from measuring external Ba concentration standards with natural isotopic compositions.

2.3 Double spike data reduction

The double spike technique is a well-established method to correct measurements of stable isotope ratios for instrumental mass fractionation (Dodson, 1963; Galer, 1999; Rudge et al., 2009; Siebert et al., 2001), which involves measuring the relative amounts of four isotopes, two of which are elevated by the addition of enriched isotope spikes to the sample. A schematic diagram of this technique is shown in Fig. 2.4.

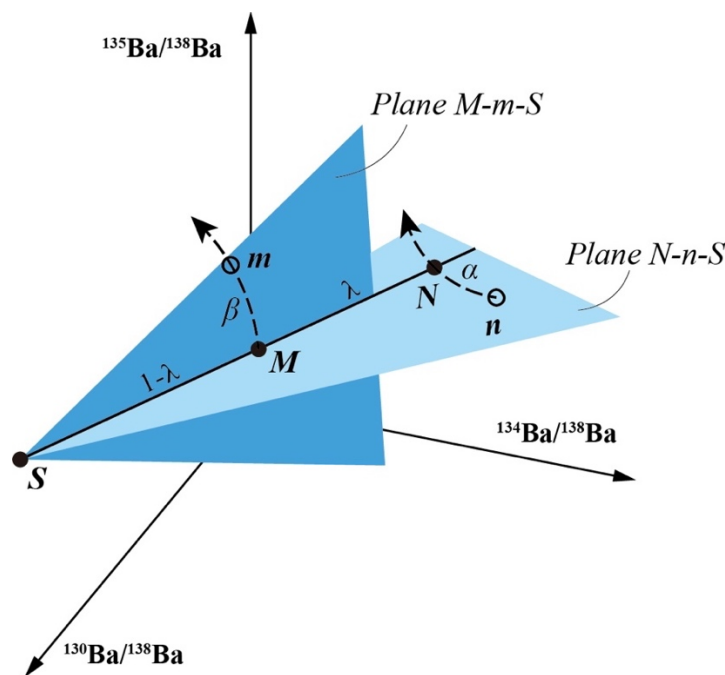


Fig. 2.4: Schematic diagram showing the principle of the double spike technique. In four-isotope space, the double spike (S) is added to a natural sample (N) and the resulting mixture (M) is only dependent on the mixing proportion (λ). As a consequence of the IMF, the measured mixture (m) is displaced along the IMF vector $M-m$ as a function of the instrumental fractionation factor (β). The natural sample (N) is displaced along mass dependent natural fractionation vector $N-n$ with the natural fractionation factor (α). Since the isotopic compositions of S and n are known, a single measurement of m is sufficient to calculate the other three unknown variables α , β and N .

The double spike (S) is added to a natural sample (N) and the resulting mixture (M) is only dependent on the mixing proportion (λ), which leads to a mixing equation as:

$$\left(\frac{{}^i Ba}{{}^{138} Ba} \right)_M = \lambda \cdot \left(\frac{{}^i Ba}{{}^{138} Ba} \right)_N + (1 - \lambda) \cdot \left(\frac{{}^i Ba}{{}^{138} Ba} \right)_S \quad (2.5)$$

where i represents isotopes 130, 134 and 135. As a consequence of instrumental mass bias, the measured mixture (m) is displaced along the instrumental mass fractionation vector $M-m$ with an instrumental fractionation factor (β). Assuming that the mass bias follows an exponential law, this instrumental fractionation can be expressed as:

$$\left(\frac{{}^i Ba}{{}^{138} Ba} \right)_m = \left(\frac{{}^i Ba}{{}^{138} Ba} \right)_M \cdot \left(\frac{i}{138} \right)^\beta \quad (2.6)$$

Similarly, the natural sample (N) is displaced along mass dependent natural fractionation vector $N-n$ with the natural fractionation factor (α), which can be expressed as:

$$\left(\frac{{}^i Ba}{{}^{138} Ba} \right)_n = \left(\frac{{}^i Ba}{{}^{138} Ba} \right)_N \cdot \left(\frac{i}{138} \right)^\alpha \quad (2.7)$$

In contrast to radiogenic isotope systems (e.g., Nd), for stable isotope systems which undergo mass dependent natural fractionation, the additional measurements of un-spiked samples (n) is not necessary as n is the composition of a standard or a reference. Given that the isotopic compositions of S and n are known, a single measurement of m is sufficient to calculate the other three unknown variables α , β and N by using the above three equations. It is particularly noted that the results of the inversion are independent of the choice of denominator isotope (e.g., ${}^{137}Ba$ or ${}^{138}Ba$).

A three-dimensional data reduction procedure similar to that described by Siebert et al. (2001) is carried out using a MATLAB-based script and presented in detail as follows:

2. Extended Methodology

(1) Definition of the plane N - n - S

The isotope compositions of sample N , standard n and spike (S) define a plane N - n - S with the equation $z = ax + by + c$, in which parameters a , b and c can be obtained with a assumed value of natural fractionation factor α by the following equations:

$$\begin{aligned}
 a &= \frac{\left(\frac{^{135}\text{Ba}}{^{138}\text{Ba}}\right)_n \cdot \left[\left(\frac{^{134}\text{Ba}}{^{138}\text{Ba}}\right)_N - \left(\frac{^{134}\text{Ba}}{^{138}\text{Ba}}\right)_S\right] + \left(\frac{^{135}\text{Ba}}{^{138}\text{Ba}}\right)_N \cdot \left[\left(\frac{^{134}\text{Ba}}{^{138}\text{Ba}}\right)_S - \left(\frac{^{134}\text{Ba}}{^{138}\text{Ba}}\right)_n\right] + \left(\frac{^{135}\text{Ba}}{^{138}\text{Ba}}\right)_S \cdot \left[\left(\frac{^{134}\text{Ba}}{^{138}\text{Ba}}\right)_n - \left(\frac{^{134}\text{Ba}}{^{138}\text{Ba}}\right)_N\right]}{\left(\frac{^{135}\text{Ba}}{^{138}\text{Ba}}\right)_n \cdot \left[\left(\frac{^{130}\text{Ba}}{^{138}\text{Ba}}\right)_N - \left(\frac{^{130}\text{Ba}}{^{138}\text{Ba}}\right)_S\right] + \left(\frac{^{135}\text{Ba}}{^{138}\text{Ba}}\right)_N \cdot \left[\left(\frac{^{130}\text{Ba}}{^{138}\text{Ba}}\right)_S - \left(\frac{^{130}\text{Ba}}{^{138}\text{Ba}}\right)_n\right] + \left(\frac{^{135}\text{Ba}}{^{138}\text{Ba}}\right)_S \cdot \left[\left(\frac{^{130}\text{Ba}}{^{138}\text{Ba}}\right)_n - \left(\frac{^{130}\text{Ba}}{^{138}\text{Ba}}\right)_N\right]} \\
 b &= \frac{\left(\frac{^{130}\text{Ba}}{^{138}\text{Ba}}\right)_n \cdot \left[\left(\frac{^{134}\text{Ba}}{^{138}\text{Ba}}\right)_N - \left(\frac{^{134}\text{Ba}}{^{138}\text{Ba}}\right)_S\right] + \left(\frac{^{130}\text{Ba}}{^{138}\text{Ba}}\right)_N \cdot \left[\left(\frac{^{134}\text{Ba}}{^{138}\text{Ba}}\right)_S - \left(\frac{^{134}\text{Ba}}{^{138}\text{Ba}}\right)_n\right] + \left(\frac{^{130}\text{Ba}}{^{138}\text{Ba}}\right)_S \cdot \left[\left(\frac{^{134}\text{Ba}}{^{138}\text{Ba}}\right)_n - \left(\frac{^{134}\text{Ba}}{^{138}\text{Ba}}\right)_N\right]}{\left(\frac{^{130}\text{Ba}}{^{138}\text{Ba}}\right)_n \cdot \left[\left(\frac{^{135}\text{Ba}}{^{138}\text{Ba}}\right)_N - \left(\frac{^{135}\text{Ba}}{^{138}\text{Ba}}\right)_S\right] + \left(\frac{^{130}\text{Ba}}{^{138}\text{Ba}}\right)_N \cdot \left[\left(\frac{^{135}\text{Ba}}{^{138}\text{Ba}}\right)_S - \left(\frac{^{135}\text{Ba}}{^{138}\text{Ba}}\right)_n\right] + \left(\frac{^{130}\text{Ba}}{^{138}\text{Ba}}\right)_S \cdot \left[\left(\frac{^{135}\text{Ba}}{^{138}\text{Ba}}\right)_n - \left(\frac{^{135}\text{Ba}}{^{138}\text{Ba}}\right)_N\right]} \\
 c &= \left(\frac{^{134}\text{Ba}}{^{138}\text{Ba}}\right)_n - a \cdot \left(\frac{^{130}\text{Ba}}{^{138}\text{Ba}}\right)_n - b \cdot \left(\frac{^{135}\text{Ba}}{^{138}\text{Ba}}\right)_n
 \end{aligned} \tag{2.8}$$

(2) Definition of the instrumental mass fractionation vector M - m

The instrumental mass fractionation vector M - m is defined by two equations: $z = dx + e$ and $z = fy + g$, in which parameters d , e , f and g can be obtained with a assumed value of instrumental fractionation factor β by the following equations:

$$\begin{aligned}
 d &= \frac{\left(\frac{^{134}\text{Ba}}{^{138}\text{Ba}}\right)_m - \left(\frac{^{134}\text{Ba}}{^{138}\text{Ba}}\right)_M}{\left(\frac{^{130}\text{Ba}}{^{138}\text{Ba}}\right)_m - \left(\frac{^{130}\text{Ba}}{^{138}\text{Ba}}\right)_M} \\
 e &= \left(\frac{^{134}\text{Ba}}{^{138}\text{Ba}}\right)_m - d \cdot \left(\frac{^{134}\text{Ba}}{^{138}\text{Ba}}\right)_M \\
 f &= \frac{\left(\frac{^{134}\text{Ba}}{^{138}\text{Ba}}\right)_m - \left(\frac{^{134}\text{Ba}}{^{138}\text{Ba}}\right)_M}{\left(\frac{^{135}\text{Ba}}{^{138}\text{Ba}}\right)_m - \left(\frac{^{135}\text{Ba}}{^{138}\text{Ba}}\right)_M} \\
 g &= \left(\frac{^{134}\text{Ba}}{^{138}\text{Ba}}\right)_m - f \cdot \left(\frac{^{135}\text{Ba}}{^{138}\text{Ba}}\right)_M
 \end{aligned} \tag{2.9}$$

(3) *Definition of the intersection between the vector M-m and the plane N-n-S*

This defined instrumental mass fractionation vector $M-m$ intercepts the defined plane $N-n-S$ and the coordinates x_{int} , y_{int} and z_{int} of the intersection are calculated by:

$$\begin{aligned}x_{int} &= \frac{bg - be + ef - cf}{af + bd - df} \\y_{int} &= \frac{ae - ag + dg - cd}{af + bd - df} \\z_{int} &= ax_{int} + by_{int} + c\end{aligned}\tag{2.10}$$

(4) *Refining the instrumental mass fractionation factor β by iteration:*

These intercept values (x_{int} , y_{int} , z_{int}) are assigned to the values of $(^{130}\text{Ba}/^{138}\text{Ba})_M$, $(^{135}\text{Ba}/^{138}\text{Ba})_M$ and $(^{134}\text{Ba}/^{138}\text{Ba})_M$, respectively. Based on the equation 2.9, a new instrumental fractionation factor β can be obtained. With this new value of β , the calculations (steps 2-4) are reiterated and results (e.g., factor β) converge after three iterations.

(5) *Definition of the plane M-m-S in analogy to step 1.*

(6) *Definition of the natural mass fractionation vector N-n in analogy to step 2.*

(7) *Definition of the intersection between the vector N-n and the plane M-m-S in analogy to step 3.*

(8) *Refining the natural mass fractionation factor α in analogy to step 4.*

(9) *Repetition of the whole procedure (steps 1-8) once and the final results converge.*

3 Scientific Chapter I

The impact of MC-ICP-MS plasma conditions on the accuracy and precision of stable isotope measurements evaluated for barium isotopes

Published as: Yu, Y., Siebert, C., Fietzke, J., Goepfert, T., Hathorne, E., Cao, Z., Frank, M., 2020. The impact of MC-ICP-MS plasma conditions on the accuracy and precision of stable isotope measurements evaluated for barium isotopes. *Chemical Geology*. 549. <https://doi.org/10.1016/j.chemgeo.2020.119697>

Abstract

Stable barium isotope measurements with multi-collector inductively coupled plasma mass spectrometry (MC-ICP-MS) remain an analytical challenge and can be considerably affected by the presence of matrix elements, even when applying double spiking. Therefore significant efforts were invested in previous studies to develop efficient barium purification methods. However, due to the high variability in matrix/barium ratios for diverse sample matrices, potential matrix effects can still not be excluded. While a lot of effort has been invested into improving the chemical separation protocols, the impact of plasma conditions on the accuracy and precision of stable isotope measurements has rarely been considered. Here we present a systematic investigation of the relationship between plasma conditions, instrumental mass fractionation (IMF) and impurity (i.e. matrix) concentrations. The Normalised Argon Index (NAI) and Matrix-Argon Index (MA) are used to quantify MC-ICP-MS plasma conditions and plasma mass loading, respectively. Our results show that the effect of matrix elements on IMF is largely linked to plasma conditions (i.e. NAI) and behaves as a linear function of mass loading (i.e. MA). Accordingly, the matrix effects can be significantly attenuated by increasing the NAI thereby minimising the risk of plasma “over-loading”. The improved understanding of the behaviour of the matrix-induced IMF allows us to define a matrix tolerance plasma state for barium isotope analysis. The accuracy of this recommended method is further assessed by analyses of two well-studied reference materials, the GEOTRACES seawater reference sample SAFe D2 and the carbonate reference material JCp-1. We expect that the analytical protocol described in this study is applicable not only to barium isotope

analysis, but also to a wide range of other stable isotope measurements with MC-ICP-MS.

3.1 Introduction

In recent years, stable barium (Ba) isotope compositions have been developed as a novel tool to study marine productivity, water mass mixing, riverine Ba flux to the oceans and tectonic processes (e.g., Bridgestock et al., 2019; Cao et al., 2020a, 2016; Gou et al., 2020; Horner et al., 2015; Hsieh and Henderson, 2017; Nan et al., 2018). Experimental studies have revealed significant and consistent Ba isotopic fractionations between minerals and solutions, and the light isotopes were found to be enriched in Ba precipitates compared to the aqueous phase in most cases (Böttcher et al., 2018, 2012; Mavromatis et al., 2020, 2016; Pretet et al., 2015; von Allmen et al., 2010). In the modern ocean, substantial variations in Ba isotope signatures with water depth and large-scale ocean circulation were found. The marine upper waters are systematically enriched in heavy Ba isotopes as a consequence of preferential adsorption of the lighter isotopes onto biogenic particles as well as barite formation in subsurface microenvironments. In comparison, the dynamics of dissolved Ba isotopes in the intermediate and deep waters of open ocean are thought to be primarily controlled by physical mixing between water masses of different origins (Bates et al., 2017; Bridgestock et al., 2018; Cao et al., 2016; Horner et al., 2015; Hsieh and Henderson, 2017). Ba isotopes in shallow and deep-water corals have been used to reconstruct the Ba isotope compositions of past ambient seawater (Geyman et al., 2019; Hemsing et al., 2018; Liu et al., 2019). Moreover, interest in stable Ba isotope compositions of different terrestrial and meteoritic materials has increased in recent years (Gong et al., 2019; Li et al., 2020; Moynier et al., 2015; Nan et al., 2018; Nielsen et al., 2020, 2018; van Zuilen et al., 2016a).

Although Nier (1938) already analysed Ba isotopes, only recently significant progress was made in the development of high accuracy and precision methods for the determination of stable Ba isotope ratios in various sample matrices. Ba isotopes have been analysed by thermal ionisation mass spectrometry (TIMS) (e.g., Bullen and Chadwick, 2016; Hsieh and Henderson, 2017; Lin et al., 2020; Yobregat et al., 2017) and MC-ICP-MS (e.g., Böttcher et al., 2012; Cao et al., 2016; Horner et al., 2015; Miyazaki et al., 2014; Nan et al., 2018; Tian et al., 2019; van Zuilen et al., 2016a; von Allmen et

al., 2010; Zeng et al., 2019). In contrast to TIMS, MC-ICP-MS allows for a significantly higher sample throughput. However, a major concern in MC-ICP-MS is the large instrumental mass fractionation (IMF) affecting isotope measurements in the percent range compared to the per mil range observed in TIMS measurements (Albarède et al., 2015). The causes of this phenomenon are still not fully understood. One concept assumes the IMF is caused by “space charge effects” (Albarède and Beard, 2004 and references therein). This effect would result in ions with lower kinetic energy (e.g., lower mass to charge ratio) to be more strongly repulsed from the positively charged ion beam than heavier ions and preferential loss of these lighter ions in the expansion chamber and/or interface. In addition, Maréchal et al. (1999) have suggested that IMF also can originate from the plasma itself.

In brief, the very high temperature of the plasma allows for high ionisation efficiency and rapid sample throughput. However, it also generates ions with different initial energies and therefore with complex trajectories in the mass spectrometer (Albarède et al., 2004). Most of these processes favour transmission of the heavier isotopes into the mass spectrometer and therefore lead to different transmission efficiencies for ions of different mass-to-charge ratio and yield non-uniform response across the mass interval (Heumann et al., 1998). Accordingly, correction of the IMF is crucial to obtain accurate and precise isotopic compositions by MC-ICP-MS.

The IMF can vary in the course of an analytical session on MC-ICPMS. Consequently, corrections for the IMF are made for each individual sample using three principal techniques: standard-sample bracketing, double spiking and internal standard normalisation (Albarède and Beard, 2004 and references therein). Theoretically, all three correction methods should result in accurate isotope ratios and indeed, standard-sample bracketing as well as double spiking have been used to correct for IMF during Ba isotope analysis (e.g., Cao et al., 2020b, 2016; Horner et al., 2015; Nan et al., 2018). However, it has been observed that non-spectral matrix effects (i.e. matrix elements in the sample solution that can interfere with the ionisation and transmission of analyte elements) can have a significant effect on the accuracy and precision of the IMF corrections (Barling and Weis, 2008; Cao et al., 2020b; Fietzke and Frische, 2016; Nan et al., 2015; van Zuilen et al., 2016b). In the case of Ba isotopes, Nan et al. (2015) tested for the impact of non-spectral matrix effects by adding a number of elements (Ca, Mg, Na, Sr, K, Al and Fe) to

a NIST SRM 3104a Ba solution on a Thermo Fisher Scientific Neptune Plus equipped with a CETAC Aridus II desolvating nebuliser system, applying a standard-sample bracketing correction method. They found that relatively low mass fraction ratios of particular matrix elements ($[Ca]/[Ba]$ and $[Mg]/[Ba] \leq 1.0$, $[Na]/[Ba]$ and $[Sr]/[Ba] \leq 0.5$, $[K]/[Ba] \leq 0.1$) already shifted the measured Ba isotope compositions. In another study, van Zuilen et al. (2016b) also tested for non-spectral matrix effects by adding major cations (Ca, Na and Sr) to aliquots of the NIST SRM 3104a Ba solution on a Nu Plasma MC-ICP-MS equipped with a ESI Apex Q sample introduction system and applying the ^{130}Ba - ^{135}Ba double spiking. They found that the tolerable amounts of these matrix elements are up to a factor of 200 higher than previously reported by Nan et al. (2015). No non-spectral matrix effects were detected for mass fraction ratios of $[Ca]/[Ba]$, $[Na]/[Ba]$ and $[Sr]/[Ba] \leq 100$. These experiments suggest that the amount of tolerable matrix for accurate Ba isotope measurements is at least partly dependent on the methods used for the IMF correction and probably even the instrumental equipment used.

However, the causal connection between IMF and non-spectral matrix effects is poorly understood (e.g., Albarède and Beard, 2004; Barling and Weis, 2008; Fietzke and Frische, 2016). It is common that non-spectral matrix effects can result in highly precise stable isotope measurements that are not accurate. This makes it difficult to detect these effects when analysing unknown samples. It is therefore crucial to better understand the processes involved and to establish a quantitative protocol to minimise non-spectral matrix effects. In addition, it is essential that the set mass-spectrometric conditions are comparable and quantifiable for different measurement sessions as well as cross-platform comparisons.

The ICP is a quite flexible ion source: different combinations of operating conditions (e.g., RF power, gas flows, cone geometry) result in particular thermal conditions of the plasma at the region where it is sampled for mass-spectrometric analysis (Fietzke and Frische, 2016). In Ba isotope measurements, the large range of operating conditions and instrumental setups that were used in previous studies poses a challenge to assessing the behaviour of matrix-induced IMF (e.g. Böttcher et al., 2012; Nan et al., 2015; van Zuilen et al., 2016b). Recently, Fietzke and Frische (2016) showed that instrumental fractionation and analytical accuracy are strongly controlled by plasma conditions during laser ablation ICP-MS. This study points towards the need for a careful evaluation and

monitoring of isotopic fractionation for individual isotope systems on solution-based MC-ICP-MS. In order to evaluate the ICP operating state, Fietzke and Frische (2016) introduced the Normalised Argon Index (NAI) as a quantitative indicator of the plasma conditions:

$$NAI = 2 \times {}^{38}\text{Ar}^+ / {}^{40}\text{Ar}_2^+ \quad (3.1)$$

The ${}^{38}\text{Ar}^+$ ions and ${}^{40}\text{Ar}_2^+$ dimer ions gain for a given setup of the mass spectrometer are both influenced by plasma temperature. On the one hand, the degree of Ar ionisation primarily depends on temperature. On the other hand, the abundance of the ${}^{40}\text{Ar}_2^+$ dimer ions decreases with increasing plasma temperature as the Ar-Ar bond is more effectively broken up with higher temperature. However, the plasma particle density also decreases with increasing plasma temperature, which impacts both the ${}^{38}\text{Ar}^+$ and ${}^{40}\text{Ar}_2^+$ intensities. By normalising the ${}^{38}\text{Ar}^+$ intensity to the ${}^{40}\text{Ar}_2^+$ intensity not only accounts for this temperature induced plasma density effect as it impacts both ionic species, but also enhances the monitoring sensitivity to plasma temperature. Thus, the NAI is based on the actual thermal conditions of the plasma at the site of ion sampling regardless of how this state has been achieved by a complex combination of e.g. RF power and gas flows. Additionally, the NAI is a generally applicable parameter and easily transferable from one instrument to the other, providing a measure for plasma conditions independent of the actual particular tuning and instrumental equipment used (e.g., cone type, interface pressure, slit setting, detector efficiency). Most importantly, it is possible to systematically investigate the response of matrix-induced IMF to various plasma conditions by adjusting these conditions to a range of NAIs.

In this study we systematically investigate the effect of matrix on the accuracy and precision of Ba isotope measurements under different but quantified plasma conditions. A NIST SRM 3104a Ba standard solution was doped with various amounts of major matrix elements (Ca and Sr) and analysed under six different NAIs. The results provide an improved understanding of the matrix-induced IMF and define a matrix tolerance plasma state for Ba isotope analysis. Although these experiments were performed and calibrated for Ba isotopes, they are considered to be applicable for a wide variety of isotope measurements routinely performed on MC-ICP-MS.

3.2 Experimental setup

3.2.1 Instrumental setups and data reduction

The data of this study were acquired using a Neptune Plus MC-ICPMS (Thermo Scientific, Bremen, Germany) at GEOMAR Helmholtz Centre for Ocean Research Kiel. The analyte was introduced as a dry aerosol using an Aridus II desolvating system (CETAC Technologies, Omaha, NE, USA) and an Aspire PFA micro-concentric nebuliser (uptake rate of $\sim 50 \mu\text{L min}^{-1}$). Ba isotope ratios were measured under six different NAIs. Relatively cold plasma conditions (NAI = 0.14, 0.07 and 0.02) were obtained by a gradual increase of sweep gas flow rate and corresponding reduction of the N_2 gas flow rate. In contrast, relatively hot plasma conditions (NAI = 0.55, 0.86 and 1.01) were achieved by a gradual decrease of sweep gas flow rate and compensating increase of the N_2 gas flow rate. Each plasma state applied during the experiment required the zoom optics, torch positions and source lenses to be tuned for maximum Ba ion transmission. The achieved conditions were then kept constant for Ba isotope analysis. It is worth noting that the Ba peak shape was mainly adjusted by tuning the sweep gas flow rate and N_2 gas flow rate from session to session. The NAI values were monitored by measuring mass 38 (i.e. $^{38}\text{Ar}^+$) and mass 80 (i.e. $^{40}\text{Ar}_2^+$) on the H4 Faraday cup using a $10^{10} \Omega$ amplifier at the beginning and the end of each measurement session. Alternatively, the $^{38}\text{Ar}^+$ ions and $^{40}\text{Ar}_2^+$ dimer ions can be determined on the centre cup in medium/high mass resolution mode by using a $10^{11} \Omega$ amplifier.

For the experiments of this study different Neptune specific interface cones were used, namely a “Jet” sampler cone combined with either a “X” skimmer or an “H” skimmer cone. Application of the “X” skimmer cone results in an increase in the analytical sensitivity (Weyer and Schwieters, 2003). In order to maximise Ba sensitivity and optimise Ba peak shape for a given NAI, the combination of “X” skimmer cone and “Jet” sampler cone was applied under relatively cold plasma conditions (NAI = 0.02, 0.07 and 0.14) and the combination of “H” skimmer cone and “Jet” sampler cone was applied under relatively hot plasma conditions (NAI = 0.55, 0.86 and 1.01). It is important to note that with the combination of “Jet” sampler cone and high sensitivity “X” skimmer cone it was easy to tune the ion optics for an acceptable low resolution peak shape with

relatively cold plasma conditions (i.e. $NAI < 0.5$). In contrast, the combination of “Jet” sampler cone and “H” skimmer cone was necessary to achieve relatively hot plasma conditions (i.e. $NAI > 0.5$). Details of instrumental operating parameters and collector configurations are summarised in Table 3.1.

Table 3.1: Instrumental parameters for Ba isotope measurements

Instrumental parameters	Thermo Fisher Scientific, Neptune plus (GEOMAR)							
RF power	1200 W							
Guard electrode	On							
Cooling Ar gas flow	~16 L min ⁻¹							
Auxiliary Ar gas flow	~0.80 L min ⁻¹							
Nebulizer Ar gas flow	~0.80 L min ⁻¹							
Extraction voltage	-2000 V							
Mass resolution	Low resolution							
Sampler cone	Jet-sampler (Ni)							
Skimmer cones	X-skimmer (Ni) and H-skimmer (Ni)							
Desolvator	Aridus II							
Ar sweep gas flow	2-7 L min ⁻¹							
N2 gas flow	3-15 mL min ⁻¹							
Spray chamber temperature	110 °C							
Desolvator temperature	160 °C							
Solution uptake rate	~ 50 µL min ⁻¹							
Detector mode	Faraday cup static mode							
	L4	L3	L2	C	H1	H2	H3	H4
Amplifier resistor (Ω)	10 ¹¹	10 ¹¹	10 ¹¹	10 ¹¹	10 ¹¹	10 ¹¹	10 ¹¹	10 ¹⁰
	¹³⁰ Ba	¹³¹ Xe	¹³² Ba	¹³⁴ Ba	¹³⁵ Ba	¹³⁶ Ba	¹³⁷ Ba	¹³⁸ Ba

Ba isotope compositions are reported in the δ -notation in per mil (‰) relative to the NIST SRM 3104a Ba solution:

$$\delta^{138}Ba = \frac{{}^{138/134}Ba_{sample}}{{}^{138/134}Ba_{NIST\ SRM\ 3104a}} - 1 \quad (3.2)$$

A ^{130}Ba - ^{135}Ba double spike was applied to correct for IMF as well as isotope fractionation during chemical purification (Cao et al., 2016; Siebert et al., 2001). The double spike was prepared and calibrated relative to the NIST SRM 3104a Ba solution. A three-dimensional data reduction procedure following Siebert et al. (2001) is used, in which an exponential fractionation law is applied to correct for both instrumental and natural mass-dependent isotope fractionation. External reproducibility is given as 2 standard deviation (2 s.d.) of the average $\delta^{138}\text{Ba}$ value obtained from repeated measurements of single sample aliquots. The long-term external reproducibility of the $\delta^{138}\text{Ba}$ measurements of the NIST SRM 3104a Ba solution in this study is 0.03‰ (2 s.d.), based on $n \approx 200$ measurements.

3.2.2 The NIST SRM 3014a Ba solutions doped with matrix elements

The purpose of our experiments was to quantify the influence of a range of different matrix conditions under varying NAIs on the accuracy and precision of Ba isotope measurements. Ca and Sr were identified as the dominant inorganic matrix elements in Ba samples after purification by ion exchange chromatography and are therefore the focus of the standard doping experiments in this study (Horner et al., 2015; Nan et al., 2015; van Zuilen et al., 2016b; Zeng et al., 2019). A large batch of the NIST SRM 3104a Ba solution was spiked with the ^{130}Ba - ^{135}Ba double spike and equilibrated for 24 h. Subsamples of the spiked Ba solution were subsequently doped with different amounts of Ca and Sr standard solutions ($[\text{Ca}]/[\text{Ba}]$ and $[\text{Sr}]/[\text{Ba}]$ of up to 400; Inorganic Ventures ICP standard solutions). Ba sensitivity, BaO^+ formation rate and non-spectral matrix effects were analysed and evaluated on a Neptune Plus MC-ICP-MS under six different NAIs. Each measurement session was comprised of a pre-experiment reference sequence of undoped NIST Ba standards followed by doped standard runs alternating with undoped standards.

3.2.3 Seawater reference sample and chemical purification

The seawater reference water SAFe D2 (1000 m depth) was chosen in this study for Ba isotope analysis. The SAFe D2 sample was collected at the SAFe (Sampling and Analysis of Fe) GEOTRACES station (30°N 140°W) at 1000 m depth with multiple four-bottle casts using Teflon™ coated, 30 L GO-Flo samplers deployed on the Kevlar™ hydroline

to prevent contamination (Bruland et al., 1979). The seawater reference samples were subsequently filtered through 0.45 μm and then 0.2 μm polycarbonate filters and acidified to a pH of ~ 2 using distilled concentrated HCl. All filtrations, acidifications and bottling of the SAFe samples were performed inside of Class-100 clean benches.

The chemical purification procedures for seawater sample were modified from the methods described in (Cao et al., 2016; Horner et al., 2015; Hsieh and Henderson, 2017) and are summarised briefly here. An aliquot of 20 mL of seawater was weighed and spiked with the ^{130}Ba - ^{135}Ba double spike. After an equilibration period of 24 h, Ba was co-precipitated with CaCO_3 by dropwise adding 1 M Ba-free Na_2CO_3 solution. The resulting precipitate was centrifuged and dissolved in 2 mL 1 M HCl in preparation for ion chromatography.

Ion exchange chromatography was performed using cation exchange resin (AG50W-X8, 200–400 mesh, 1.4 mL volume) to purify Ba from residual matrix elements. The cation resin was pre-cleaned with 10 mL of 6 M HNO_3 and 10 mL of 6 M HCl before conditioning with 5 mL 1 M HCl. Samples were loaded in 2 mL of 1 M HCl, then matrix elements were subsequently eluted with 7.5 mL of 1 M HCl and 7.5 mL of 3 M HCl. Finally, Ba cuts were collected with 10 mL of 2 M HNO_3 . This ion exchange chromatography procedure was repeated in full. Finally, the Ba cut was dried down and converted to the NO_3^- form via concentrated HNO_3 refluxing and dissolved in 2% (v/v) HNO_3 for Ba isotope analysis.

3.2.4 Carbonate sample preparation and chemical purification

The carbonate standard JCp-1 was chosen for Ba isotope analysis. It was prepared from a *Porites* coral collected from Ishigaki Island (24°N 124°E) and issued by the Geological Survey of Japan (GSJ). The preparation of JCp-1 powder employed here was described in detail in Okai et al. (2002). Ba and Ca concentrations and Ba isotope compositions of JCp-1 have previously been reported in a number of studies (e.g., Hathorne et al., 2013; Hemsing et al., 2018; Horner et al., 2015; Inoue et al., 2004; Liu et al., 2019; Pretet et al., 2015).

Carbonate dissolution was performed by submerging the coral powder in 18.2 M Ω -cm Milli-Q water and adding drops of 1 M acetic acid with brief sonication until no bubbles could be seen around the aragonite. Following centrifugation, the supernatants were transferred into pre-cleaned Savillex™ vials and converted to Cl⁻ form via concentrated HCl refluxing. A small aliquot of this solution was taken for Ba concentration analysis by ICP-MS using the ¹³⁵Ba isotope dilution method (Freydier et al., 1995). A further aliquot corresponding to 300 ng of Ba was taken for isotopic analysis and the ¹³⁰Ba-¹³⁵Ba double spike was added before chemical purification. After an equilibration period of 24 h, the samples passed through columns only once following the same chemical procedure as mentioned above. Finally, the Ba cuts were dried down and converted to NO₃⁻ form via concentrated HNO₃ refluxing and dissolved in 2% (v/v) HNO₃ for Ba isotope analysis.

3.3 Results and discussion

3.3.1 Sensitivity

The relative sensitivities of Ba measurements were determined using pure as well as matrix-doped NIST Ba solutions and are expressed as ¹³⁸Ba⁺ V per $\mu\text{g L}^{-1}$ of analyte. As shown in Fig. 3.1, a large and systematic increase in Ba sensitivity is observed for all analytes with decreasing NAI from 1.01 to 0.02 (typically 8 to 10-fold depending on the [matrix]/[Ba] ratios). Solutions doped with Ca and Sr show sensitivity variations similar to pure standard solutions. At each given NAI, matrix element addition enhances the sensitivities to some extent for [matrix]/[Ba] \leq 10. However, under relatively low NAIs (0.02 and 0.07), Ba sensitivities reach plateau values at [matrix]/[Ba] = 10, after which signal suppressions are observed with increasing matrix. In contrast, higher NAIs (0.14, 0.55, 0.86 and 1.01) are accompanied by higher tolerance against matrix-induced Ba sensitivity suppressions (Fig. 3.1).

In general, a negative correlation between Ba sensitivity and NAI is observed for either matrix-free or matrix-doped NIST Ba solutions in our study. Higher NAIs (0.55, 0.86 and 1.01) are more easily achieved by using the “Jet” sampler cone in combination with an “H” skimmer cone, which results in relatively low Ba sensitivities. Typical sensitivities under these relatively “hot” plasma conditions are 0.09 to 0.25 V per $\mu\text{g L}^{-1}$. In contrast, the combination of “Jet” sampler cone and “X” skimmer cone enhances Ba sensitivities

significantly, but allows for relatively low NAIs. Typical sensitivities under these relatively “cold” plasma conditions are 0.29 to 1.80 V per $\mu\text{g L}^{-1}$. A variety of studies have suggested that relative elemental sensitivity enhancements can be attributed to different sampler and skimmer cone combinations (e.g., Makishima and Nakamura, 2010; Newman, 2012; Newman et al., 2009). Our experiments confirm these findings and suggest that analyte sensitivity is mainly a function of the NAI that can be achieved with different types of cone geometries. The observed Ba sensitivity enhancements with decreasing NAI are likely due to the higher Ba ion density at colder plasma conditions.

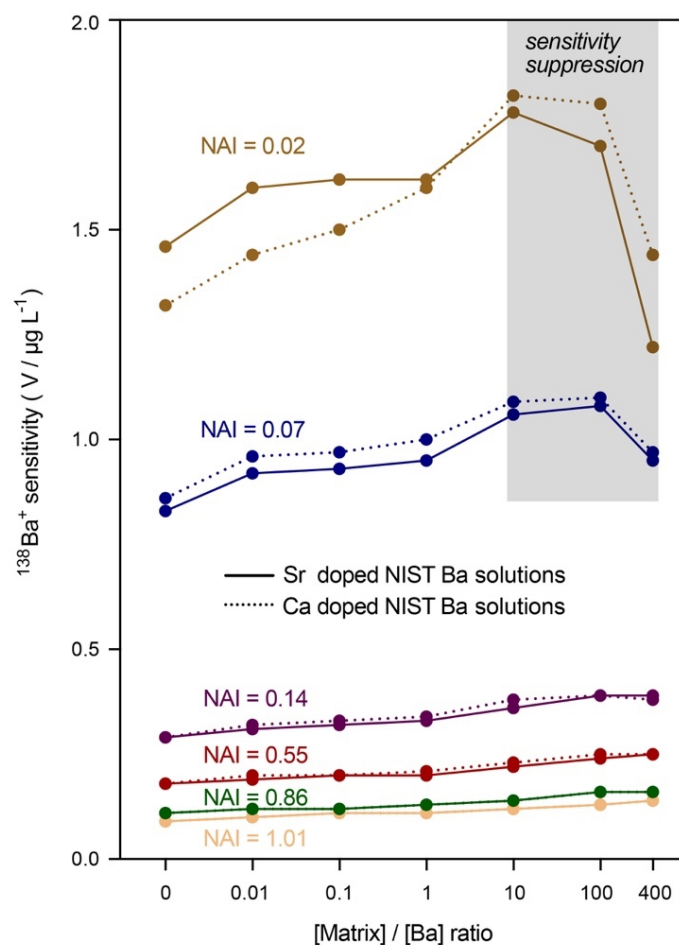


Fig. 3.1: The analytical Ba sensitivity variations in the measured NIST Ba solutions with various amounts of matrix elements under different NAIs. The Ba sensitivity generally increases with decreasing NAI values. At each given NAI, the introduction of large amounts of matrix causes sensitivity suppression at NAI values of 0.02 and 0.07. In contrast, higher NAIs (0.14, 0.55, 0.86 and 1.01) are accompanied by higher tolerance against matrix induced Ba sensitivity suppressions.

In terms of the matrix-induced sensitivity variations, both sensitivity enhancement and suppression are observed with increasing [matrix]/ [Ba] ratios under relatively low NAIs. The increase in Ba sensitivity may be associated with higher collision efficiency in the plasma that results from ionisation of Ca or Sr and therefore an increase in electron density (Hanselman et al., 1994). Another explanation is that the introduction of less matrix results in a cooler plasma, which in turn increases the formation of single-charged ions at the cost of double-charged ions (Barling and Weis, 2008). Barling and Weis (2008) further suggested that the presence of matrix reduces the Ar charge density allowing a higher proportion of analyte ions to reach the centre of the ion beam.

In contrast to the observations described above, the introduction of large amounts of matrix causes sensitivity suppressions at NAI values of 0.02 and 0.07. The suppression of the analyte signal may be caused by the deposition of salt on the sampler and/or skimmer cones, thereby clogging the orifices and substantially affecting the sampling process (Evans and Giglio, 1993). Alternatively, the large amount of Ca or Sr ions may cool the plasma further and shift the onset of Ba atomisation and/or ionisation downstream and shorten the interaction time with the hot regions of the plasma resulting in low efficiency of Ba atomisation and/or ionisation (Aghaei and Bogaerts, 2016).

Previous studies have shown that matrix-induced IMF (i.e. non-spectral matrix effects) are largely associated with changes in sensitivity of the analyte related to the presence of matrix elements (e.g., Barling and Weis, 2008; Olivares and Houk, 1986). Whatever the exact causes for Ba sensitivity increase or suppression are, the changes in sensitivity correspond to changes in the IMF, which in turn can have a significant impact on the accuracy and precision of isotope measurements. More details about non-spectral matrix effects based on our results are discussed in section 3.3.3.

3.3.2 Oxide formation rate

The BaO^+ formation rate was determined using pure as well as matrix-doped NIST Ba solutions over a range of NAIs and calculated by $^{138}\text{BaO}^+ \text{V} / ^{138}\text{Ba}^+ \text{V}$. Our results show that $^{138}\text{BaO}^+ / ^{138}\text{Ba}^+$ ratios of the pure NIST Ba analyte decrease from 0.15% at NAI = 0.02 to 0.004% at NAI = 0.55 and then slightly rise again to 0.006% at NAI = 1.01 (Fig. 3.2). Addition of matrix elements slightly changes the BaO^+ formation rates at each

corresponding NAI, which is considered to be negligible in our study. As expected from the increasing plasma temperatures, Ba oxide formation rates systematically decrease with increasing NAI. However, the slight increase of Ba oxide formation rates at NAIs > 0.55 may be caused by reduced $^{138}\text{Ba}^+$ sensitivity as the absolute $^{138}\text{BaO}^+$ voltage is as low as 0.0003 V.

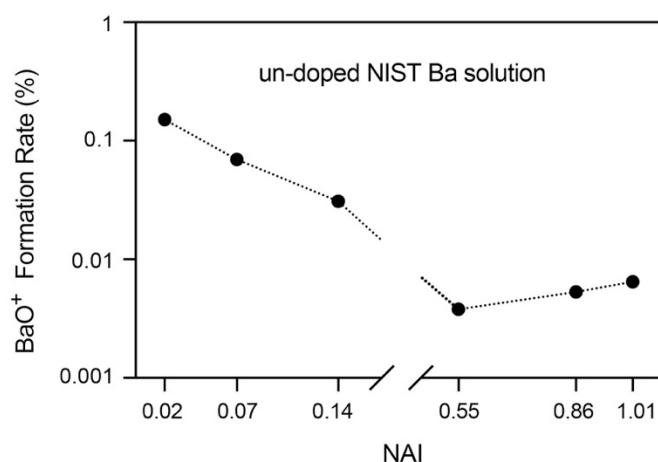


Fig. 3.2: The BaO^+ formation rate variations in the measured un-doped NSIT Ba solutions under different NAIs. The BaO^+ formation rate declines from 0.15% at $\text{NAI} = 0.02$ to 0.004% at $\text{NAI} = 0.55$ and then slightly rises to 0.006% at $\text{NAI} = 1.01$. The relatively low NAIs (0.02, 0.07 and 0.14) were obtained by using the combination of “X” skimmer cone and “Jet” sampler cone. The relatively high NAIs (0.55, 0.86 and 1.01) were obtained by using the combination of “H” skimmer cone and “Jet” sampler cone.

The oxide formation rate has been characterised by a number of studies and has also been used as an indicator for ICP operating conditions (e.g., Evans and Giglio, 1993; Kent and Ungerer, 2005; Tan and Horlick, 1986; Vaughan and Horlick, 1986). These studies suggested that the oxide formation rate is essentially a function of three factors: 1) availability of oxygen within the gas supply system; 2) the strength of the molecular-oxygen (M-O) bond in the MO^+ ion; 3) conditions within the plasma. The impact of the latter two has been demonstrated for solution-based ICP-MS (Kent and Ungerer, 2005). However, for a specific isotope system, the correlation between oxide production and plasma conditions has not been studied systematically given that plasma conditions were difficult to quantify. By taking advantage of NAI, our experiments confirm that the oxide formation rate is strongly dependent on the NAI. As shown above, Ba oxide formation rates are generally reduced with increasing NAI. Moreover, the oxide

formation rates can reach a threshold at a particular NAI, after which no further reductions are seen with increasing NAI (Fig. 3.2). Although this threshold is most likely due to the low BaO^+ intensity and the subsequently poor counting statistics, it suggests that the oxide formation rate itself may not be a sufficiently robust indicator of the plasma conditions if compared to the NAI.

The effect of analyte oxide species on isotope analysis by MC-ICPMS has been investigated in many studies. For example, Newman (2012) reported that neodymium (Nd) isotope ratios measured with high Nd oxide formation rates displayed large deviations from a reference value. Similar deviations have been reported previously when using high sensitivity skimmer cone geometries on a Nu Instrument MC-ICP-MS (Newman et al., 2009). Both studies indicated that the deviations in the measured radiogenic Nd isotope ratios are associated with an increase in the Nd oxide formation rate (Newman, 2012). In this study, a co-variation is observed between the NAI, Ba oxide formation rates and the deviations in the measured Ba isotope ratios. We believe that these serious analytical deviations are mainly caused by the variable NAI that at the same time caused altered oxide formation rates. This is further discussed and confirmed in the following section.

3.3.3 Non-spectral matrix effects

Matrix effects are typically divided into spectral (isobaric) and non-spectral types (Albarède and Beard, 2004; Evans and Giglio, 1993; Tan and Horlick, 1987). Spectral matrix effects are caused by atomic or molecular ions having the same nominal mass as the isotope of interest (Evans and Giglio, 1993). Non-spectral matrix effects in MC-ICP-MS are caused by matrix elements affecting the ionisation and transmission of analyte elements, which may lead to systematic deviations and errors in isotope analysis (Barling and Weis, 2008; Evans and Giglio, 1993; Gillson et al., 1988; Tan and Horlick, 1987).

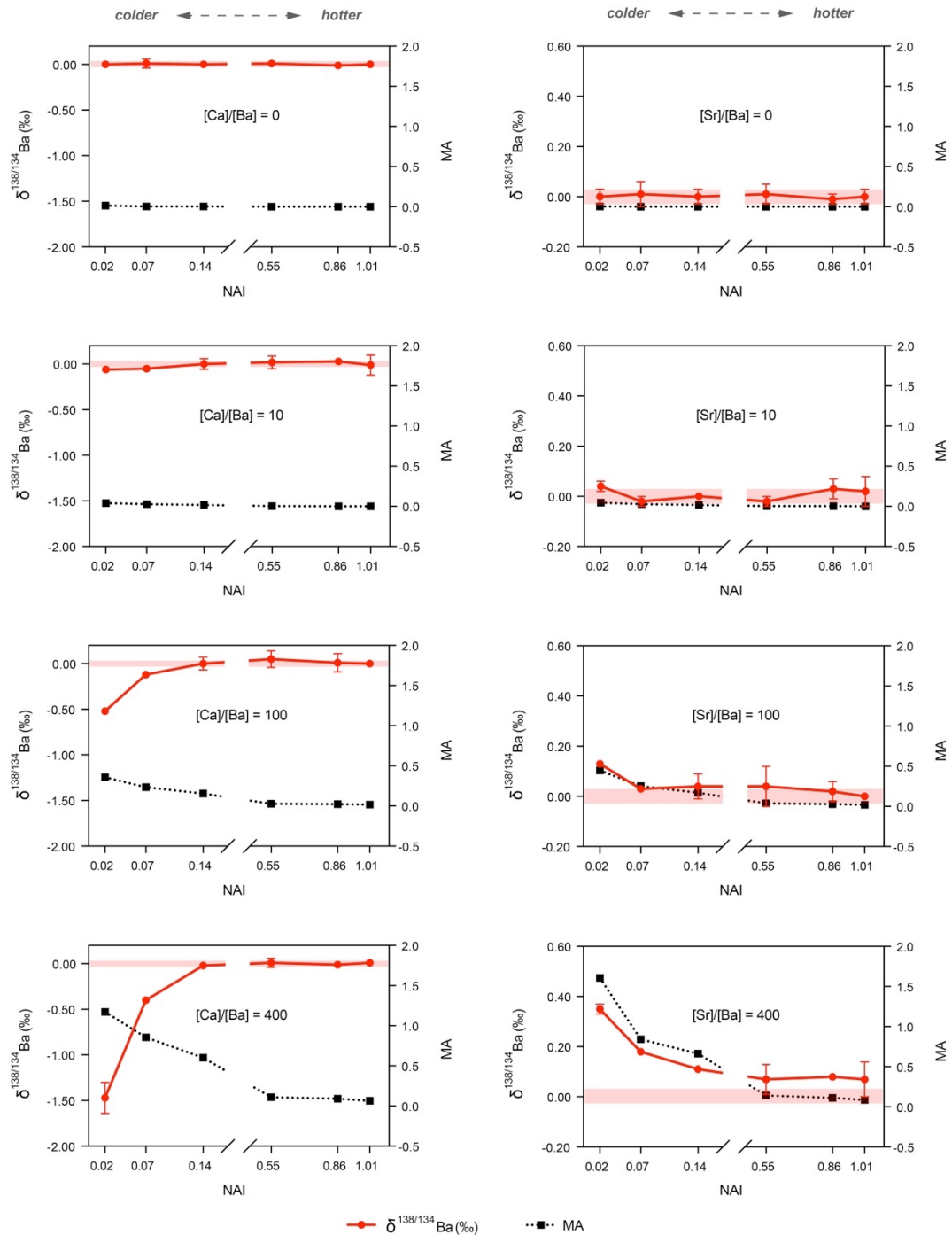


Fig. 3.3: Test for non-spectral matrix effects using NIST Ba solutions with increasing amount of matrix elements under different NAIs. The left column is Ca-doped NIST Ba solutions and the right column is Sr-doped NIST Ba solutions. The NAIs are presented on the horizontal axes against the double spike corrected $\delta^{138/134}\text{Ba}$ values on the left vertical axes and matrix-Ar index (MA) values on the right vertical axes. The long-term 2 s.d. of the $\delta^{138/134}\text{Ba}$ values is ± 0.03 (red shaded area, $n \approx 200$).

The $\delta^{138}\text{Ba}$ values of the NIST Ba solutions (corrected for IMF via the double spike method) for a range of matrix/analyte ratios are plotted against NAI in Fig. 3.3. It is immediately obvious that none of the $\delta^{138}\text{Ba}$ values deviate from the pure NIST Ba reference value within the average measurement precision of 0.03‰ (2 s.d.) when $[\text{Matrix}]/[\text{Ba}] \leq 10$. The addition of Ca causes an increasingly light bias that becomes significant when $[\text{Ca}]/[\text{Ba}]$ ratio reaches 100 and NAI is lower than 0.07. Amongst those, the presence of Ca at a $[\text{Ca}]/[\text{Ba}]$ ratio of 400 results in the maximum light bias of -1.47‰ at the lowest NAI value of 0.02. By tuning the plasma to higher NAIs, the $\delta^{138}\text{Ba}$ value deviations are systematically attenuated even at $[\text{Ca}]/[\text{Ba}]$ ratios of up to 400. The addition of Sr, in contrast, leads to heavy offsets but to a lesser degree when $[\text{Sr}]/[\text{Ba}]$ ratio reaches 100 and NAI is lower than 0.14. Particularly, the presence of Sr at a $[\text{Sr}]/[\text{Ba}]$ ratio of 400 results in the maximum heavy bias of $+0.35\text{‰}$ at the lowest NAI value of 0.02. Similar to the observations with Ca, the $\delta^{138}\text{Ba}$ offsets systematically decrease with increasing NAI. In brief, the presence of Ca causes light offsets whereas Sr leads to heavy offsets when $[\text{matrix}]/[\text{Ba}]$ ratios reach 100 and NAI is relatively low. High NAIs result in greater tolerance for matrix-induced offsets in $\delta^{138}\text{Ba}$ values. Our experiments demonstrate that non-spectral matrix effects caused by addition of Ca or Sr can result in inaccuracies of double spike corrected $\delta^{138}\text{Ba}$ values measured by MC-ICP-MS. These non-spectral matrix effects are primarily controlled by the NAI and vary as a function of matrix/analyte ratio.

In order to get insights into the underlying mechanisms controlling these plasma-related non-spectral matrix effects, a mass load criterion matrix-Ar index (MA) following Fietzke and Frische (2016) is used in this study:

$$MA = \text{sum}(I_{\text{matrix}}) / I_{\text{Ar}} \quad (3.3)$$

where MA denotes the ratio between the integrated intensities of matrix ions (including both matrix and analyte ions) and Ar ions. The measured isotope intensities (i.e. ^{43}Ca , ^{84}Sr , ^{138}Ba and ^{38}Ar) were converted to the total amount of each element using corresponding relative isotope abundances (Berglund and Wieser, 2011). As an example, a $MA = 0.1$ means that during the time of data collection the plasma consisted of 90% Ar ions and 10% ions generated from the introduced material (Fietzke and Frische, 2016).

Our results for the observed MA values calculated from matrix-doped NIST Ba solutions are plotted on the right vertical axes against NAI in Fig. 3.3. In general, the MA values are extremely low when $[\text{Matrix}]/[\text{Ba}] \leq 10$, which indicates that the mass load is negligible compared to that of the Ar ions. When $[\text{Matrix}]/[\text{Ba}] \geq 100$, the MA values are increased markedly at relatively low NAIs and gradually decrease towards higher NAIs. At the lowest NAI value of 0.02, the MA ($[\text{Ca}]/[\text{Ba}] = 400$) shows the maximum value of 1.17 where $\delta^{138}\text{Ba}$ shows the most extreme negative analytical bias. Similarly, the MA ($[\text{Sr}]/[\text{Ba}] = 400$) shows the maximum value of 1.61 at NAI = 0.02, for which $\delta^{138}\text{Ba}$ shows the most extreme positive analytical bias.

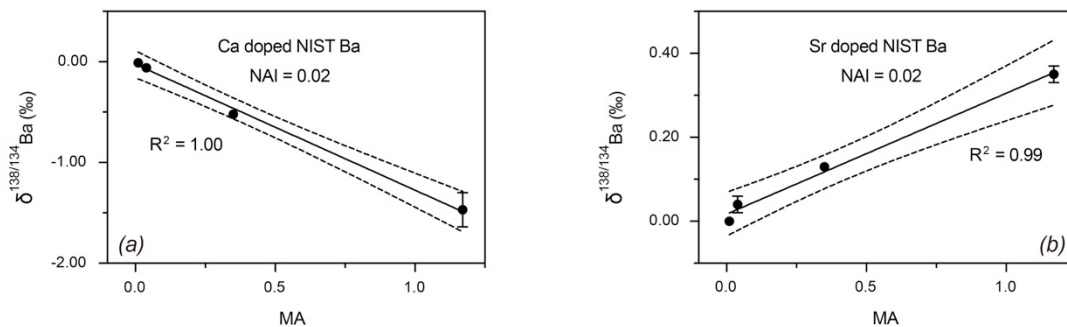


Fig. 3.4: The relationship between the double spike corrected $\delta^{138/134}\text{Ba}$ values and matrix-Ar index (MA) under NAI = 0.02. (a) Ca-doped NIST Ba standard solutions; (b) Sr-doped NIST Ba standard solutions. Note that higher NAIs cannot yield this obvious linear correlation as the deviations in $\delta^{138/134}\text{Ba}$ values are attenuated by increasing NAI.

As proposed by Fietzke and Frische (2016), gradually increasing the MA values above 0.01 can be interpreted as progressively “over-loading” the plasma, challenging its robustness and increasing the risk of non-spectral matrix effects. Indeed, the correlation between MA values and the deviations in $\delta^{138}\text{Ba}$ values is clearly demonstrated in Fig. 3.4. At the lowest NAI value of 0.02, the $\delta^{138}\text{Ba}$ values deviate from the NIST Ba reference value as a linear function of MA values from both Ca and Sr doped NIST Ba solutions. This demonstrates that the MA is a robust indicator of non-spectral matrix effects during isotope analysis.

In summary, we show that the addition of matrix elements can lead to “over-loading” of the plasma resulting in systematic deviations. The non-spectral matrix effects can be attenuated by increasing the NAI thereby minimising the risk of plasma “over-loading”, which can be monitored by the MA.

3.3.4 Effects on instrumental mass fractionation correction methods

From mass balance considerations, no IMF would exist for a given element if it is ionised and transmitted through the mass spectrometer with 100% efficiency (Albarède and Beard, 2004; Teng et al., 2017). However, isotope analysis by MC-ICP-MS is always accompanied by the IMF. Meanwhile, the presence of matrix can affect the ionisation and transmission process of analyte elements, which can lead to over- or underestimation of the IMF correction (Barling and Weis, 2008; Evans and Giglio, 1993; Gillson et al., 1988; Tan and Horlick, 1987). In order to improve our understanding of the effects of matrix on the IMF correction, three different correction methods are discussed below.

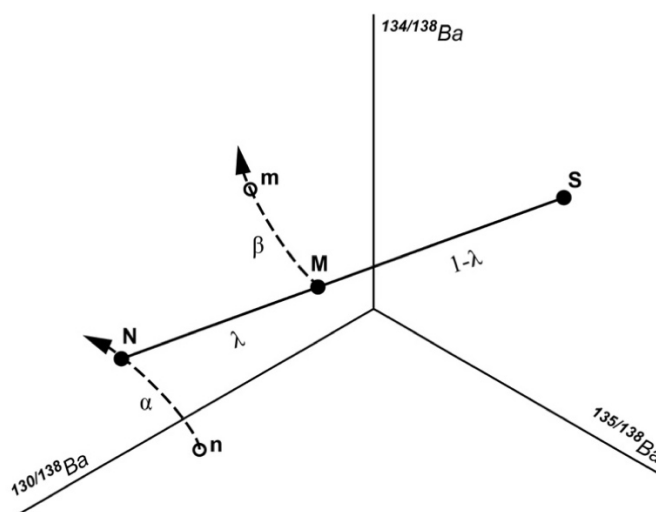


Fig. 3.5: Schematic diagram showing the principle of the double spike technique. In four-isotope space, the double spike (S) is added to a natural sample (N) and the resulting mixture (M) is only dependent on the mixing proportion (λ). As a consequence of the IMF, the measured mixture (m) is displaced along the IMF vector $M-m$ with the instrumental fractionation factor (β). The natural sample (N) is displaced along mass dependent natural fractionation vector $N-n$ with the natural fractionation factor (α). Since the isotopic compositions of S and n are known, a single measurement of m is sufficient to calculate other three unknown variables α , β and N .

The most commonly used correction methods for instrumental mass-dependent isotope fractionation during MC-ICP-MS measurements are double spiking, standard-sample bracketing and internal standard normalisation. The double spike technique was first proposed by Dodson, (1963) and can only be applied to elements of interest with at least four stable isotopes. The principles and applications of the double spike technique have been presented extensively in the literatures (e.g., Galer, 1999; Rudge et al., 2009; Siebert et al., 2001) and hence only a brief summary is presented here. As shown in Fig. 3.5, the double spike (S) is added to a natural sample (N) and the resulting mixture (M) is only dependent on the mixing proportion (λ). As a consequence of the IMF, the measured mixture (m) is displaced along the IMF vector $M-m$ with the instrumental fractionation factor (β). In contrast to radiogenic isotope systems (e.g., Nd), for stable isotope systems which undergo mass dependent natural fractionation, the additional measurements of unspiked sample (n) is not necessary as n is the composition of a standard or a reference. The natural sample (N) is displaced along mass dependent natural fractionation vector $N-n$ with the natural fractionation factor (α). Since the isotopic compositions of S and n are known, a single measurement of m is sufficient to calculate the other three unknown variables α , β and N . As long as the effects of sample matrix are mass dependent and follow the assumed fractionation law, the double spike method should account for these effects, because the IMF correction happens within run and with the same element (Albarède and Beard, 2004 and references therein). However, our experiments show that this is not always the case. Similar problems have been observed before (e.g., Hopp et al., 2016; Miyazaki et al., 2014; Schmitt et al., 2009). Therefore, the influence of matrix elements on double spike data reduction process, using measured Ca-doped NIST Ba solutions data ($\text{NAI} = 0.02$) as an example, is discussed in detail here.

For illustration purposes, the three-dimensional isotopic ratio space is projected onto a two-dimensional plane in Fig. 3.6a with ^{130}Ba representing the spike and ^{134}Ba representing the natural Ba isotope. For the sake of clarity, only three N - M - S mixing lines with $[\text{Ca}]/[\text{Ba}]$ ratios of ≤ 10 , 100 and 400 are shown, because the doped solutions with $[\text{Ca}]/[\text{Ba}]$ ratios ≤ 10 are indistinguishable from the pure NIST Ba solution. The corresponding three vectors of N - n “natural fractionation” and M - m instrumental fractionation are also shown in Fig. 3.6a. The double spike data reduction starts from the directly measured isotopic ratios of m (Fig. 3.6d). The presence of Ca with $[\text{Ca}]/[\text{Ba}]$ ratios ≤ 10 leads to a mass-dependent fractionation (MDF) line whereas increasing

[Ca]/[Ba] ratios to 100 and 400 results in a clear shift of the measured raw ratios off this MDF line. These deviations give rise to three individually calculated IMF correction lines as shown in Fig. 3.6b. As a result of the IMF correction, in terms of M (Fig. 3.6e), the presence of Ca with [Ca]/[Ba] ratios of 100 and 400 leads to positive shifts in $^{134/138}\text{Ba}$ and negative shifts in $^{130/138}\text{Ba}$. Since N , M and S are required to be colinear, the biased M changes the slope of the N - M - S mixing line given that S is fixed (Fig. 3.6a). As a consequence, with respect to N (Fig. 3.6c), the double spike data reduction yields positive deviations of both $^{134/138}\text{Ba}$ and $^{130/138}\text{Ba}$, which increase systematically with increasing [Ca]/[Ba] ratios and become significant when the ratios are higher than 100. It is worth noting that the calculated N and M ratios are still following MDF, although they are both shifted away from the “true” values.

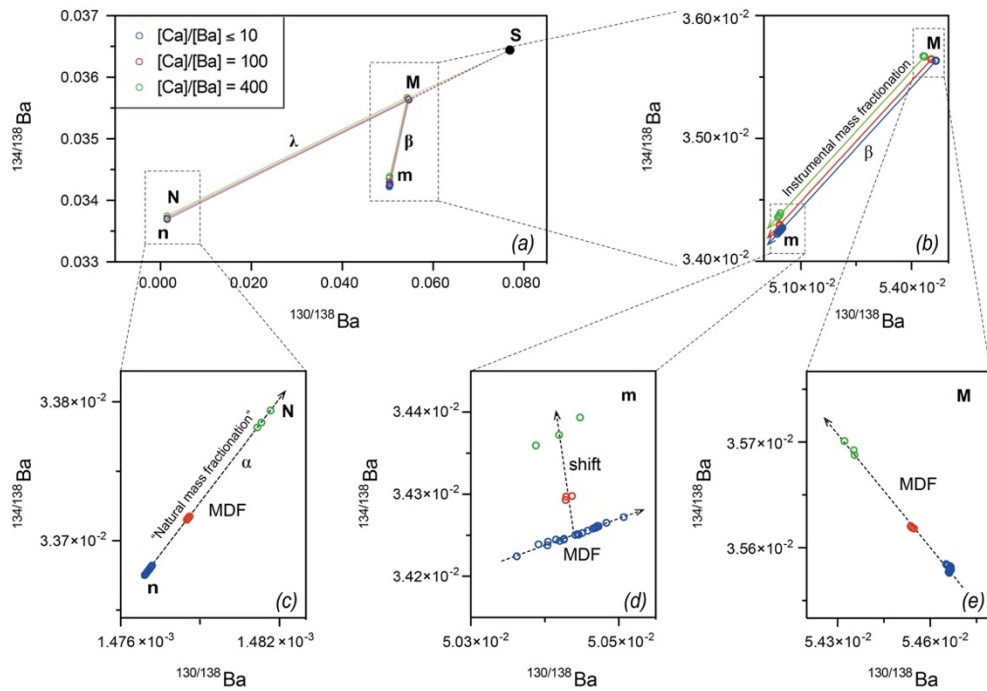


Fig. 3.6: A two dimensional isotopic ratios plane projected by the three-dimensional isotopic ratios space, showing the double spike data reduction procedure by using measured Ca-doped NIST Ba solutions (NAI = 0.02). (a) overview of the double spike data reduction using $^{134/138}\text{Ba}$ ratios and $^{130/138}\text{Ba}$ ratios (b) instrumental mass fractionation correction vectors M - m showing mass-dependent fractionation; (c) natural mass fractionation vectors N - n showing mass-dependent fractionation; (d) measured Ba isotope ratios (m) showing deviations from the mass-dependent fractionation line; (e) instrumental mass fractionation corrected ratios (M) showing mass-dependent fractionation.

As shown above, the unaccounted-for bias in double spike data reduction is most likely due to the clear shifts of the measured raw ratios (m) off the MDF line. In order to further investigate the fractionation behaviour of m , a factor Δm is defined and reported in per mil (‰) using the same raw data without double spike data reduction and calculated applying the standard-sample bracketing method:

$$\Delta_m = \frac{{}^{x/138}\text{Ba}_{\text{matrix-doped NIST}}}{{}^{x/138}\text{Ba}_{\text{bracketing un-doped NIST}}} - 1 \quad (3.4)$$

where x represents 130, 134 and 135, respectively. This approach will allow us to directly address the influence of matrix on the measured ratios. As can be seen in Fig. 3.7a, at $\text{NAI} = 0.02$, $[\text{Ca}]/[\text{Ba}]$ ratios of 100 and 400 result in obvious isotopic anomalies on mass 134, which do not follow MDF. In contrast, an increased NAI of 0.14 results in MDF independent from matrix concentrations (Fig. 3.7b).

One possible reason for the observed isotopic anomalies on mass 134 is the occurrence of Xe isobaric interferences. The argon gas that supplies the plasma always contains a certain amount of Xe, which causes isobaric interferences of ${}^{130}\text{Xe}$ on ${}^{130}\text{Ba}$ and of ${}^{134}\text{Xe}$ on ${}^{134}\text{Ba}$. The most commonly employed method to correct for Xe interferences is the measurement of on-peak zero baseline prior to sample analysis, incorporating the ${}^{130}\text{Xe}$ and ${}^{134}\text{Xe}$ correction in the baseline subtraction (e.g., Cao et al., 2016; Miyazaki et al., 2014; Nan et al., 2015). However, as shown in Fig. 3.7a, this method does not remove the isotopic anomalies on mass 134. Alternatively, interference-free Xe can be monitored simultaneously during sample analysis to correct the interferences of ${}^{130}\text{Xe}$ on ${}^{130}\text{Ba}$ and of ${}^{134}\text{Xe}$ on ${}^{134}\text{Ba}$. Based on the measured ${}^{131}\text{Xe}$ intensity, the ${}^{130}\text{Xe}/{}^{131}\text{Xe}$ and ${}^{134}\text{Xe}/{}^{131}\text{Xe}$ ratios were calculated using the IUPAC isotopic abundances (Berglund and Wieser, 2011) and fractionation corrected using the exponential mass fractionation law. The resulting two ratios were subsequently used to calculate the isobaric interferences of ${}^{130}\text{Xe}$ and ${}^{134}\text{Xe}$, respectively. However, this approach resulted in even more severe isotopic anomalies on mass 134. Therefore, our results suggest that the significant isotopic anomalies on mass 134 cannot solely be the result of Xe interferences correction. Another potential cause for isobaric interferences in MC-ICP-MS measurements is the increased formation of hydrates under low NAIs. Although Ba hydrides would not cause a direct isobaric interference on mass 134 because there is no ${}^{133}\text{Ba}$, the ${}^{130}\text{BaH}^+$ could interfere

with the ^{131}Xe signal and thus make the Xe correction unreliable. Additionally, the observed general suppression effect could be another possible reason. As shown in Fig. 3.1, the presence of large amounts of matrix elements results in a strong suppression of the Ba signal. This means that the intensity of the Ba background and/or Xe should also be suppressed though perhaps to a different degree, which could result in additional problems because the isobaric contributions from the background and/or Xe may be over- or underestimated.

Whatever the exact reasons for the observed mass 134 deviations in the measurements, our results clearly demonstrate that these anomalies on mass 134 can be attenuated by tuning the plasma for higher NAI. Given that the double spike data reduction relies on the assumption of MDF, it cannot provide correct values if m does not follow MDF. A future study is proposed to explore this analytical deviation and additional care should be taken when applying the double spike technique.

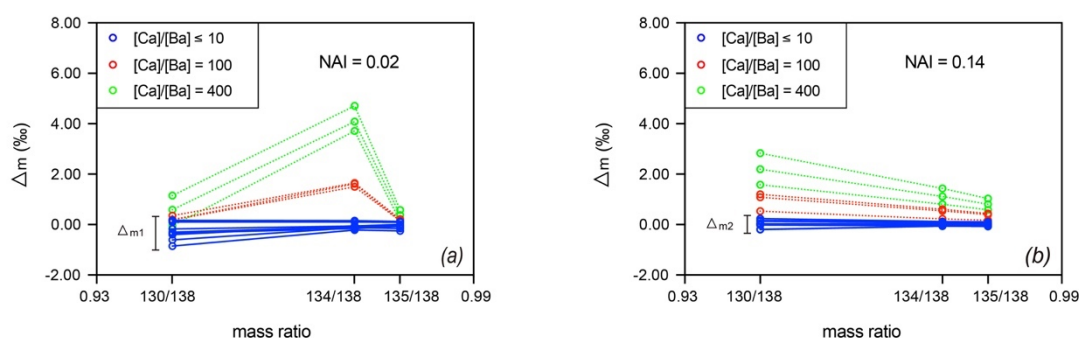


Fig. 3.7: The Ba isotopic variations (Δ_m) from Ca-doped NIST Ba solutions applying standard-sample bracketing method. (a) measurements conducted under NAI = 0.02; (b) measurements conducted under NAI = 0.14.

Standard-sample bracketing is another IMF correction method. It is based on the interpolation of the instrumental mass bias of an unknown sample via the biases inferred from bracketing standard runs (e.g., Albarède and Beard, 2004 and references therein). Because the NIST Ba solutions were spiked and well-equilibrated, the impact of matrix elements on standard-sample bracketing method was evaluated using the same measured Ca-doped NIST Ba solutions as before. The factor β is also used here as a IMF factor for standard-sample bracketing method. A requirement of this approach is that the value of β

remains near constant when alternating between standards and samples. Multiple factors, including matrix mismatching, varying analyte concentrations and acid strength between sample solutions and bracketing standards can result in changes of β (e.g., Hu and Teng, 2019). From our experiments (Fig. 3.7), the range of the Ba isotopic variations under $\text{NAI} = 0.14$ (Δ_{m2}) is obviously smaller than Δ_{m1} obtained under $\text{NAI} = 0.02$, which indicates that higher NAI results in smaller variations of β . This decreased Δ_m value leads to improved accuracy and precision in defining the value of β , which suggests temporal changes in β upon alternating between bracketing standards and samples can be attenuated by increasing NAI. Therefore, performing standard-sample bracketing measurements at high and comparable NAI should increase precision and accuracy of stable isotope measurements.

The third approach for IMF correction is an internal standard normalisation based on internal normalisation to a defined isotope ratio of an element standard that has been added to the sample before the analysis (e.g., Belshaw et al., 1998; Maréchal et al., 1999; Pichat et al., 2003). The main advantage of this approach is that, similar to the double spike method, temporal changes in the IMF during measurement of each sample are corrected for (Yang et al., 2018). However, Maréchal et al. (1999) and White et al. (2000) showed that addition of a standard solution of an element different from the one to be analysed for its isotopic composition might show different IMF behaviour with respect to the element of interest. Thus, they suggested that this problem could be overcome using empirical relationships between isotope ratios. Woodhead (2002) further suggested that by running standards with variable amounts of matrix, much greater variations in mass discrimination can be generated and empirical mass bias slopes can be much more precisely defined. Due to the complexity of this method it is usually only employed where other options are limited, for example for measurement of radiogenic lead isotope compositions. Therefore, we did not test the internal standard normalisation method in this study. However, based on our results it is most likely that the addition of another element or variable amounts of matrix increases the risk of plasma “over-loading”, which can lead to a significant error in the IMF correction. Therefore, we suggest that a higher NAI will provide a more robust measuring condition when applying this correction method.

Overall, the precision and accuracy of isotope measurements by MC-ICP-MS is limited by the IMF correction. Although in principle, all of the above methods are suitable for the IMF correction, our results show that a better control of plasma conditions in solution-based MC-ICP-MS is necessary to avoid any mass bias which cannot easily be resolved numerically. We strongly suggest that running MC-ICP-MS under high NAI provides more robust analytical conditions and minimises the risk of generating bias no matter which IMF correction method is applied. This is of particular importance, because in most cases instruments are simply tuned to the highest sensitivity which will in general be accompanied by relatively low NAI. Our data clearly show that the latter approach will result in the largest potential problems with matrix effects and plasma overload.

3.3.5 Ba isotopic compositions of SAFe D2 and JcP-1

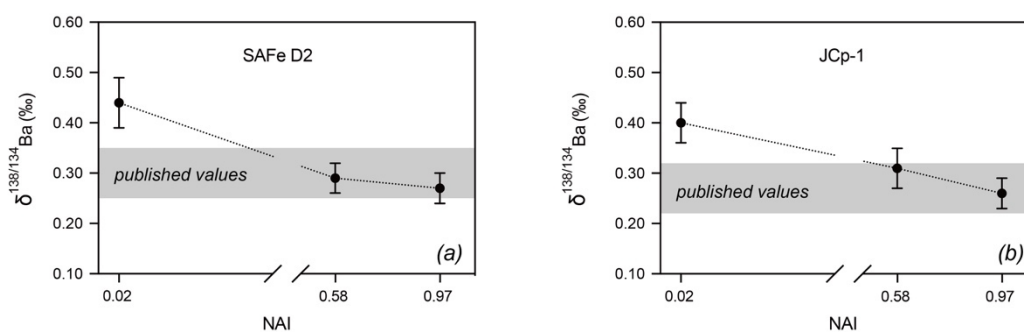


Fig. 3.8: The Ba isotopic compositions of (a) seawater reference sample SAFe D2 and (b) carbonate reference material JcP-1. The $\delta^{138/134}\text{Ba}$ values obtained under NAI = 0.97 agree well with reported values. The $\delta^{138/134}\text{Ba}$ values obtained under NAI = 0.58 show slightly positive shifts, which become significant under NAI = 0.02. The low NAI (0.02) was obtained by using the combination of “X” skimmer cone and “Jet” sampler cone. The high NAIs (0.58 and 0.97) were obtained by using the combination of “H” skimmer cone and “Jet” sampler cone.

In order to further test the effectiveness of tuning for high NAI, one seawater reference sample and one carbonate reference material have been analysed under three different NAIs (0.02, 0.58 and 0.97). All Ba isotope data are shown in Table 3.2 and Fig. 3.8. When NAI = 0.97, the GEOTRACES seawater reference sample SAFe D2 yields a $\delta^{138}\text{Ba}$ value of $+0.27 \pm 0.03\%$, which is consistent with reported values of $+0.27 \pm 0.02\%$ obtained by TIMS measurements (Hsieh and Henderson, 2017) and $+0.32 \pm 0.03\%$ by MC-ICP-

MS measurements (Geyman et al., 2019), respectively. The carbonate reference material JCp-1 yields a $\delta^{138}\text{Ba}$ value of $+0.26 \pm 0.03\text{‰}$, which agrees well with reported values of $+0.25 \pm 0.03\text{‰}$ by TIMS measurements (Hemsing et al., 2018) and $+0.29 \pm 0.03\text{‰}$, $+0.26 \pm 0.10\text{‰}$ and $+0.28 \pm 0.04\text{‰}$ by MC-ICP-MS measurements (Horner et al., 2015; Pretet et al., 2015; Zeng et al., 2019), respectively. The $\delta^{138}\text{Ba}$ values obtained under $\text{NAI} = 0.58$ slightly increase to $+0.29 \pm 0.03\text{‰}$ and $+0.31 \pm 0.04\text{‰}$ for SAFe D2 and JCp-1, respectively. These offsets, however, become significant when the NAI is as low as 0.02. The $\delta^{138}\text{Ba}$ values are shifted to $+0.44 \pm 0.05\text{‰}$ and $+0.40 \pm 0.04\text{‰}$ for SAFe D2 and JCp-1, respectively.

Table 3.2: Ba isotope compositions of reference materials.

References	Reference materials	NAI	$\delta^{138}\text{Ba}(\text{‰})$	2s	n	Method
This study	SAFe D2 (1000 m)	0.02	0.44	0.05	3	MC-ICP-MS
		0.58	0.29	0.03	3	
		0.97	0.27	0.03	3	
(Hsieh and Henderson, 2017)	SAFe D1 (1000 m)		0.27	0.02		TIMS
(Geyman et al., 2019)	SAFe D1 (1000 m)		0.31	0.03		MC-ICP-MS
	SAFe D2 (1000 m)		0.32	0.03		
(Cao et al., 2020b)	SAFe D2 (1000 m)	0.87	0.29	0.02	4	MC-ICP-MS
		0.82	0.32	0.05	5	
This study	JCp-1	0.02	0.40	0.04	3	MC-ICP-MS
		0.58	0.31	0.04	3	
		0.97	0.26	0.03	3	
(Horner et al., 2015)	JCp-1		0.29	0.03		MC-ICP-MS
(Pretet et al., 2015)	JCp-1		0.26 ^{a,b}	0.10		MC-ICP-MS
(Hemsing et al., 2018)	JCp-1		0.25	0.03	3	TIMS
(Zeng et al., 2019)	JCp-1		0.28 ^b	0.04	16	MC-ICP-MS

n is the number of repeated measurements of the same solution.

2s = 2 standard deviations of n repeated measurements.

^a Converted to NIST SRM 3104a scale using $\Delta^{137/134}\text{Ba}$ Fluka-SRM 3104a = $0.015 \pm 0.072\text{‰}$ (van Zuilen et al., 2016b).

^b $\delta^{138}\text{Ba}$ values were calculated based on mass-dependent fractionation of $\delta^{137}\text{Ba}$ using an exponential fractionation law.

In brief, the $\delta^{138}\text{Ba}$ values for seawater and carbonate obtained under high NAIs agree well with published values. The serious offsets in $\delta^{138}\text{Ba}$ values of these reference materials with decreasing NAI emphasise the vital impact of plasma conditions on the accuracy of stable isotope measurements with MC-ICP-MS.

3.4 Conclusion

A systematic investigation of non-spectral matrix effects on the accuracy and precision of stable Ba isotope measurements has been carried out under six distinct plasma conditions quantified by the Normalised Argon Index (NAI). From the results of our experiment, we conclude that Ba sensitivity and Ba oxide formation rate vary significantly with NAI. The addition of matrix elements can result in “overloading” of the plasma and lead to isotopic anomalies that cannot be resolved by the double spike technique. A new approach is presented how these matrix effects can be attenuated by increasing NAI thereby minimising and stabilising the instrumental mass fractionation (IMF) during isotope analysis. The accuracy of the approach is further verified by analyses of two well-studied reference materials with our suggested analytical protocol. Analyses of seawater reference SAFe D2 and coral aragonite standard JCp-1 yield $\delta^{138}\text{Ba}$ value of $+0.27 \pm 0.03\text{‰}$ and $+0.26 \pm 0.03\text{‰}$, respectively, consistent with published values. However, the $\delta^{138}\text{Ba}$ values of these two reference materials are shifted significantly with decreased NAI. We therefore suggest that stable isotope measurements on MC-ICP-MS should be performed at a high NAI and that the combination of the cones should also be chosen based on this consideration. Of course, the NAI achievable will be dependent on the sensitivity needed to perform isotope measurements of specific samples with good counting statistics. In addition, we suggest that the NAI should be consistently tuned to the same value during different measurement session to make the measurement conditions comparable and therefore increase accuracy and precision. It is expected that our proposed approach will also enable improved determination of other stable isotope systems with MC-ICP-MS.

4 Scientific Chapter II

High-latitude controls on dissolved barium isotope distributions in the Atlantic Meridional Overturning Circulation

To be submitted as: Yu, Y., Xie, R.C., Gutjahr, M., Laukert, G., Cao, Z., Hathorne, E., Siebert, C., Patton, G. and Frank, M.: High-latitude controls on dissolved barium isotope distributions in the Atlantic Meridional Overturning Circulation.

Abstract

The high-latitude oceans play a key role in regulating the biogeochemical Ba cycling and the preformed Ba isotope compositions in the global ocean. In this study, we present full-depth dissolved Ba concentrations ([Ba]) and isotope compositions ($\delta^{138}\text{Ba}$) from the Fram Strait (Nordic Seas), the Labrador Sea and the Weddell Sea. These study sites are key locations for deep water formation and circulation of the Atlantic Ocean and thus exert an important control on the spatial variability of $\delta^{138}\text{Ba}$ signatures in the global ocean. The Ba isotope signature of Northern Overflow Water (NOW, $+0.52 \pm 0.07\text{‰}$) at the Fram Strait is clearly modified along its southward transport before contributing to the production of North Atlantic Deep Water (NADW), which displays a uniform $\delta^{138}\text{Ba}$ value of $+0.48 \pm 0.05\text{‰}$ in the Labrador Sea. In contrast, we find that Antarctic Bottom Water (AABW) in the Weddell Sea is characterised by a relatively light $\delta^{138}\text{Ba}$ value of $+0.26 \pm 0.03\text{‰}$ in agreement with the previously estimated southern-sourced water endmember. The well-defined relationship between $\delta^{138}\text{Ba}$ and $1/[\text{Ba}]$ and the distinct $\delta^{138}\text{Ba}$ signatures of deep waters originating in the polar regions constrain the meridional gradient of $\delta^{138}\text{Ba}$ and [Ba] in the deep ocean. With regard to the upper ocean, compiled global datasets show that either an open system steady-state fractionation model or a closed system Rayleigh fractionation model can explain the Ba isotope fractionation due to barite formation and particle adsorption. Regardless of which model is applied, there is a clear shift in source water [Ba] and $\delta^{138}\text{Ba}$ from the North Atlantic via the South Atlantic to the North Pacific. The systematic variation in $\delta^{138}\text{Ba}$ signatures provides valuable insights into the biogeochemical cycling of Ba in the modern ocean and into potential applications of stable Ba isotopes in palaeoceanography.

4.1 Introduction

The marine barium (Ba) budget is controlled by inputs from land and hydrothermal vents and by the removal of Ba from seawater via accumulation in marine sediments primarily in the form of mineral barite (BaSO_4 , Horner and Crockford, 2021 and references therein). Water column concentrations of dissolved Ba ([Ba]) show a nutrient-like depth profile in the oceans, with [Ba] depletion in surface waters resulting from removal with biogenic particles and [Ba] enrichment at depth due to particulate matter decomposition and remineralisation (Bacon and Edmond, 1972; Lea and Boyle, 1989). In addition, although the vast majority of the oceans are undersaturated with respect to barite, marine barite can precipitate from seawater within micro-environments where bacteria facilitate the bioaccumulation of Ba, primarily in the mesopelagic zone (Bishop, 1988; Horner et al., 2015; Martinez-Ruiz et al., 2018). Given that barite formation is largely associated with organic matter decomposition, its accumulation in sediments provides a direct link to palaeo-productivity (Nürnberg et al., 1997; Paytan and Kastner, 1996). Since barite sinks and dissolves in the water column, dissolved [Ba] values in deep waters greatly exceed those of surface and subsurface waters where concentration maxima are observed at the depth of maximum organic matter remineralisation (Carter et al., 2020).

Given that the oceanic residence time of dissolved Ba (7–21 kyr, Horner and Crockford, 2021) is comparable to the global ocean mixing time, stable Ba isotopes ($\delta^{138}\text{Ba}$) have recently been introduced as a novel tool to investigate the biogeochemical cycling of Ba in the world ocean despite the fact that dissolved seawater $\delta^{138}\text{Ba}$ data are still scarce (e.g., Cao et al., 2020b; Horner et al., 2015; Hsieh and Henderson, 2017). In the uppermost water column, Ba isotope fractionation is largely induced by preferential adsorption of the light isotopes onto biogenic particles (Cao et al., 2020a, 2016). During particle sinking and subsequent decomposition at depth, barite formation, with a preference for the assimilation of light isotopes, leads to heavy dissolved $\delta^{138}\text{Ba}$ values in subsurface seawater (Bates et al., 2017; Horner et al., 2015). As a consequence, there is an increase in dissolved $\delta^{138}\text{Ba}$ values between ~ 200 and ~ 600 m water depth supporting earlier findings that barite precipitation mostly occurs at these depths (Bates et al., 2017; Horner et al., 2015). In contrast to the mechanisms causing surface and subsurface Ba isotope fractionation, $\delta^{138}\text{Ba}$ values of deep waters appear to be mainly controlled by large-scale ocean circulation and barite dissolution (Bates et al., 2017; Cao et al., 2016; Hsieh and

Henderson, 2017). Globally, deep water (> 2000 m) $\delta^{138}\text{Ba}$ signatures range from +0.32 to +0.46‰ in the North Atlantic (Bates et al., 2017; Hsieh and Henderson, 2017), from +0.24 to +0.43‰ in the South Atlantic (Bates et al., 2017; Bridgestock et al., 2018; Horner et al., 2015; Hsieh and Henderson, 2017) and from +0.22 to +0.26‰ in the North Pacific (Geyman et al., 2019; Hsieh and Henderson, 2017).

Recent interest has been focused on the cycling of dissolved Ba isotope compositions within individual water masses involved in the deep Atlantic Meridional Overturning Circulation (AMOC, Bates et al., 2017; Hsieh and Henderson, 2017), where the distribution of $\delta^{138}\text{Ba}$ generally follows two endmember mixing between North Atlantic Deep Water (NADW) and Antarctic Bottom Water (AABW). The Ba isotope compositions for these northern and southern-sourced deep water endmembers were estimated at $\delta^{138}\text{Ba} = +0.45\text{‰}$ for NADW and +0.26‰ for AABW, respectively (Bates et al., 2017). However, the lack of $\delta^{138}\text{Ba}$ data from high-latitude regions contributing to these two endmembers results in large uncertainties, especially in light of the recently discovered Ba contributions to the deep oceans originating from hydrothermal vent fluids that result in an apparent non-conservative Ba isotope behaviour (Hsieh et al., 2021).

In this study we examine the spatial and vertical distribution of $\delta^{138}\text{Ba}$ and [Ba] in 12 full water depth profiles from the Fram Strait (Nordic Seas), the Labrador Sea and the Weddell Sea. These data allow us to investigate how NADW and AABW acquire their respective Ba isotope signatures in the polar and subpolar regions. In combination with the previously reported low and mid-latitude $\delta^{138}\text{Ba}$ profiles (Bates et al., 2017; Bridgestock et al., 2018; Horner et al., 2015; Hsieh and Henderson, 2017), we are able to better constrain the meridional Ba transport and mixing processes across the entire Atlantic Ocean. This study not only quantifies the endmember Ba isotope compositions of NADW and AABW, but also explores the mechanisms governing marine Ba isotope fractionation in the upper ocean.

4.2 Materials and methods

4.2.1 Hydrography

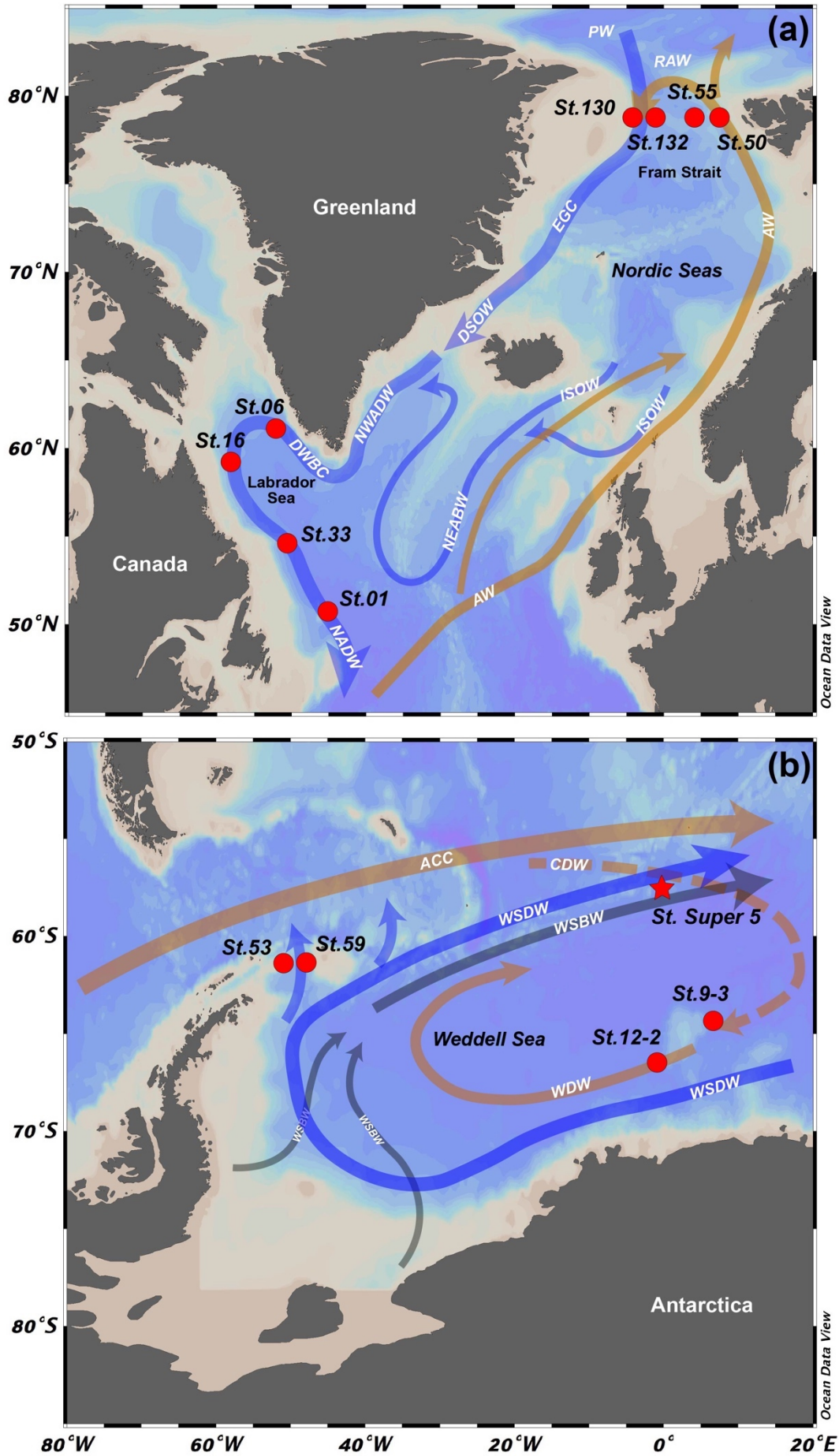


Fig. 4.1 → *page up*: **Locations of seawater profile stations included in this study (red dots) and the literature (St. Super5, red star, Hsieh and Henderson, 2017) in the Fram Strait, the Labrador Sea and the Weddell Sea. Light blue arrows denote cold deep currents and light red arrows represent warm surface and intermediate depth currents. (a) Map of the Nordic Seas and subpolar North Atlantic with schematic circulation. AW: Atlantic Water; RAW: Recirculating Atlantic Water; EGC: East Greenland Current; DSOW: Denmark Strait Overflow Water; ISOW: Iceland-Scotland Overflow Water; NWADW: North West Atlantic Deep Water; NEABW: North East Atlantic Bottom Water; NADW: North Atlantic Deep Water; (b) Map of the Weddell Sea and subpolar South Atlantic with schematic circulation. ACC: Antarctic Circumpolar Current; CDW: Circumpolar Deep Water; WDW: Warm Deep Water; WSDW: Weddell Sea Deep Water; WSBW: Weddell Sea Bottom Water; AABW: Antarctic Bottom Water. Maps were created using Ocean Data View software (ODV, Schlitzer, 2014)**

Table 4.1: Abbreviations for water masses and currents used in the text.

AABW	Antarctic Bottom Water
AAIW	Antarctic Intermediated Water
ACC	Antarctic Circumpolar Current
AW	Atlantic Water
CDW	Circumpolar Deep Water
DSOW	Denmark Strait Overflow Water
DWBC	Deep Western Boundary Current
EGR	East Greenland Current
ISOW	Iceland Scotland Overflow Water
LDW	Lower Deep Water
LSW	Labrador Sea Water
NADW	North Atlantic Deep Water
NEADW	North East Atlantic Deep Water
NOW	Northern Overflow Water
NPIW	North Pacific Intermediate Water
NWABW	North West Atlantic Bottom Water
RAW	Recirculating Atlantic Water
SPMW	Subpolar Mode Water
WDW	Warm Deep Water
WSBW	Weddell Sea Bottom Water
WSDW	Weddell Sea Deep Water
WG	Weddell Gyre

NADW and AABW are formed by the sinking of dense waters from two high-latitude sources: Waters overflowing the Greenland-Scotland Ridge (GSR) in the Nordic Seas (NADW precursor), and the outflow of dense waters formed at various sites on the continental shelf of Antarctica (AABW precursor), a large fraction of which is sourced in the Weddell Sea (Fig. 4.1, Dickson et al., 1990; Orsi et al., 1999).

In the Nordic Seas, the East Greenland Current (EGC) transports cold and fresh shallow waters exiting the Arctic Ocean and Atlantic Water (AW) re-circulating in the Fram Strait or in the Arctic Ocean across the GSR forming a part of the Nordic Seas overflows (Fig. 4.1a, Dickson et al., 1990). Once the Northern Overflow Water (NOW) has crossed the GSR as the Denmark Strait Overflow Water (DSOW) and the Iceland Scotland Overflow Water (ISOW), they descend and subsequently entrain intermediate waters present in the Irminger and Iceland Basins, such as Labrador Sea Water (LSW) and Subpolar Mode Water (SPMW). This process forms North West Atlantic Bottom Water (NWABW) and North East Atlantic Deep Water (NEADW, Dickson and Brown, 1994). Thereafter, NWABW and NEADW merge south of the Denmark Strait forming the upper and lower branches of the Deep Western Boundary Current (DWBC) when reaching Cape Farewell. The DWBC subsequently flows into the Labrador Basin and mixes with LSW thereby forming NADW, which constitutes the northern-deep limb of the AMOC (Dickson and Brown, 1994; Yashayaev, 2007).

In the Southern Ocean, the circulation regime is dominated by the eastward flowing Antarctic Circumpolar Current (ACC) and the cyclonically circulating Weddell Gyre (WG) that is located between the southern boundary of the ACC and the Antarctic shelf of the Weddell Sea (Fig. 4.1b, Fahrbach et al., 1994; Nowlin and Klinck, 1986). The two major source waters that contribute to the formation of AABW are warm remnants of the regional Circumpolar Deep Water (CDW) that have been imported from the ACC, and the extremely cold and dense shelf waters resulting from brine rejection during sea-ice formation (Orsi et al., 1999). Part of this mixture that is dense enough to reach the bottom forms Weddell Sea Bottom Water (WSBW), which is, however, too dense to escape from the Weddell Basin (Carmack and Foster, 1975; Stichel et al., 2012). Only the less dense part of the mixture can feed into Weddell Sea Deep Water (WSDW), which leaves the Weddell Basin via deep gaps across the South Scotia Ridge and becomes the major

contributor to AABW constituting the southern-deep limb of the AMOC (Carmack and Foster, 1975; Orsi et al., 1999).

4.2.2 Sampling and pre-treatment

The seawater samples analysed in this study were collected from the Fram Strait (Nordic Seas), the Labrador Sea, and the Weddell Sea (Fig. 4.1, red dots). The Fram Strait seawater samples were acquired along the 78.8°N meridional transect during the expedition PS80 of the German research vessel FS Polarstern between 15 June and 15 July 2012 (Beszczynska-Möller and Wisotzki, 2012). For Ba concentration and isotope measurements, aliquots of the filtered (0.45 µm, filtration with Millipore® cellulose acetate filters) and acidified (pH ~ 2, on board acidification with concentrated distilled HCl) samples were selected from four full water column stations down to a maximum depth of 2668 m. More information on sample collection, hydrography and CTD (conductivity, temperature, depth) profiles is available from Laukert et al., (2017, and references therein). Aliquots of filtered (0.2 µm, direct filtration with PALL filters) and acidified (same pH and procedure as for the Fram Strait samples) seawater samples from the Labrador Sea were chosen from four stations conducted during the cruise PULSE (Paleoclimate Understanding Labrador Sea) of the German research vessel Maria S. Merian (MSM45) in August 2015. Aliquots of the Weddell Sea samples (filtered and acidified in the same manner as the Labrador Sea samples) were picked from four full depth profiles in the southern and western Weddell Sea during the two expeditions PS111 and PS118 of the German research vessel FS Polarstern in 2018 and 2019. Further details on sampling and hydrographic conditions are available from the cruise reports of PS111 and PS118 (Schröder, 2018; Dorschel, 2019).

Seawater reference samples were collected at the SAFe (Sampling and Analysis of Fe) GEOTRACES station in the North Pacific (30°N 140°W) at the surface and at 1000 m depth, respectively (Bruland et al., 1979). The SAFe samples were filtered through 0.2 µm polycarbonate filters and acidified to a pH of ~ 2 using concentrated distilled HCl.

4.2.3 Ba concentration analyses

The dissolved seawater Ba concentrations ([Ba]) were analysed applying an isotope dilution technique with an Agilent 7500ce inductively coupled plasma mass spectrometer (ICP-MS) at GEOMAR, Kiel. Briefly, an aliquot (50 μL) of acidified seawater was accurately weighed and mixed with defined amounts of an ^{135}Ba single spike to achieve a $^{138}\text{Ba}/^{135}\text{Ba}$ ratio near 0.64. The spike-equilibrated samples were then diluted to about 500 μL with 2% HNO_3 before the $^{138}\text{Ba}/^{135}\text{Ba}$ ratios were measured and mass bias corrected by bracketing analyses of a natural Ba standard solution. Repeated analyses of the two seawater reference materials (SAFe surface and SAFe 1000m) resulted in [Ba] values of $34.3 \pm 0.4 \text{ nmol kg}^{-1}$ (2SD, $N = 3$) and $99.5 \pm 0.7 \text{ nmol kg}^{-1}$ (2SD, $N = 5$), respectively, which are within uncertainty identical to the SAFe values reported by Cao et al. (2020b) and Hsieh and Henderson (2017).

4.2.4 Stable Ba isotope analyses

The method of Ba purification used in this study is adopted from Yu et al. (2020) and is hence only summarised briefly here. Depending on Ba concentration, aliquots of 5 ($> 60 \text{ nmol kg}^{-1}$) or 10 ($< 60 \text{ nmol kg}^{-1}$) mL of the seawater samples were appropriately spiked with an ^{130}Ba - ^{135}Ba double spike. After an equilibration period of 24 hours, Ba was co-precipitated with CaCO_3 and the resulting precipitates were centrifuged and dissolved in 2 mL of 1M HCl in preparation for cation exchange chromatography. Samples were twice passed through columns containing 1.4 mL of Bio-Rad AG 50W-X8 (200-400 mesh size) resin. Matrix elements were subsequently eluted with 8 mL of 1 M HCl and 8 mL of 3 M HCl, respectively. The Ba cuts were then collected with 10 mL of 2 M HNO_3 , dried and re-dissolved in 2% (v/v) HNO_3 for Ba isotope analyses.

Stable Ba isotope measurements were performed with a Thermo Fisher Neptune Plus MC-ICP-MS at GEOMAR, Kiel. The analyte was introduced as a dry aerosol using an Aridus II desolvating system (CETAC Technologies, Omaha, NE, USA) and an Aspire PFA micro-concentric nebuliser (uptake rate of $\sim 50 \mu\text{L min}^{-1}$). The MC-ICP-MS was tuned to a matrix tolerance state defined by a high Normalised Argon Index value (NAI, an index of plasma temperature, Yu et al. 2020). A three-dimensional data reduction procedure following Siebert et al. (2001) was used to correct for both instrumental and

natural mass-dependent isotope fractionation. The Ba isotope compositions are reported in per mil (‰) relative to the National Institute of Standards and Technology (NIST) SRM 3014a Ba standard ($\delta^{138}\text{Ba} = \frac{^{138}\text{Ba}_{\text{sample}}}{^{138}\text{Ba}_{\text{NIST}}} - 1$). Repeated analyses of SAFe surface yielded a $\delta^{138}\text{Ba}$ value of $+0.61 \pm 0.04\text{‰}$ (2SD, N = 4), which agrees well with the reported values of $+0.62 \pm 0.02\text{‰}$ (Hsieh and Henderson, 2017), $+0.63 \pm 0.04\text{‰}$ (Geyman et al., 2019), and $+0.62 \pm 0.04\text{‰}$ (Cao et al., 2020a). Repeated measurements of SAFe 1000 m yielded a $\delta^{138}\text{Ba}$ values of $+0.29 \pm 0.04\text{‰}$ (2SD, N = 12), which is consistent with reported values of $+0.27 \pm 0.02\text{‰}$ (Hsieh and Henderson, 2017), $+0.32 \pm 0.03\text{‰}$ (Geyman et al., 2019), and $+0.28 \pm 0.09\text{‰}$ (Cao et al., 2020a). The uncertainty is reported as the larger of either the internal 2 standard errors (2SE) of repeated sample measurements or the long-term 2SD reproducibility ($\pm 0.04\text{‰}$) of repeated SAFe 1000 m measurements.

4.3 Results

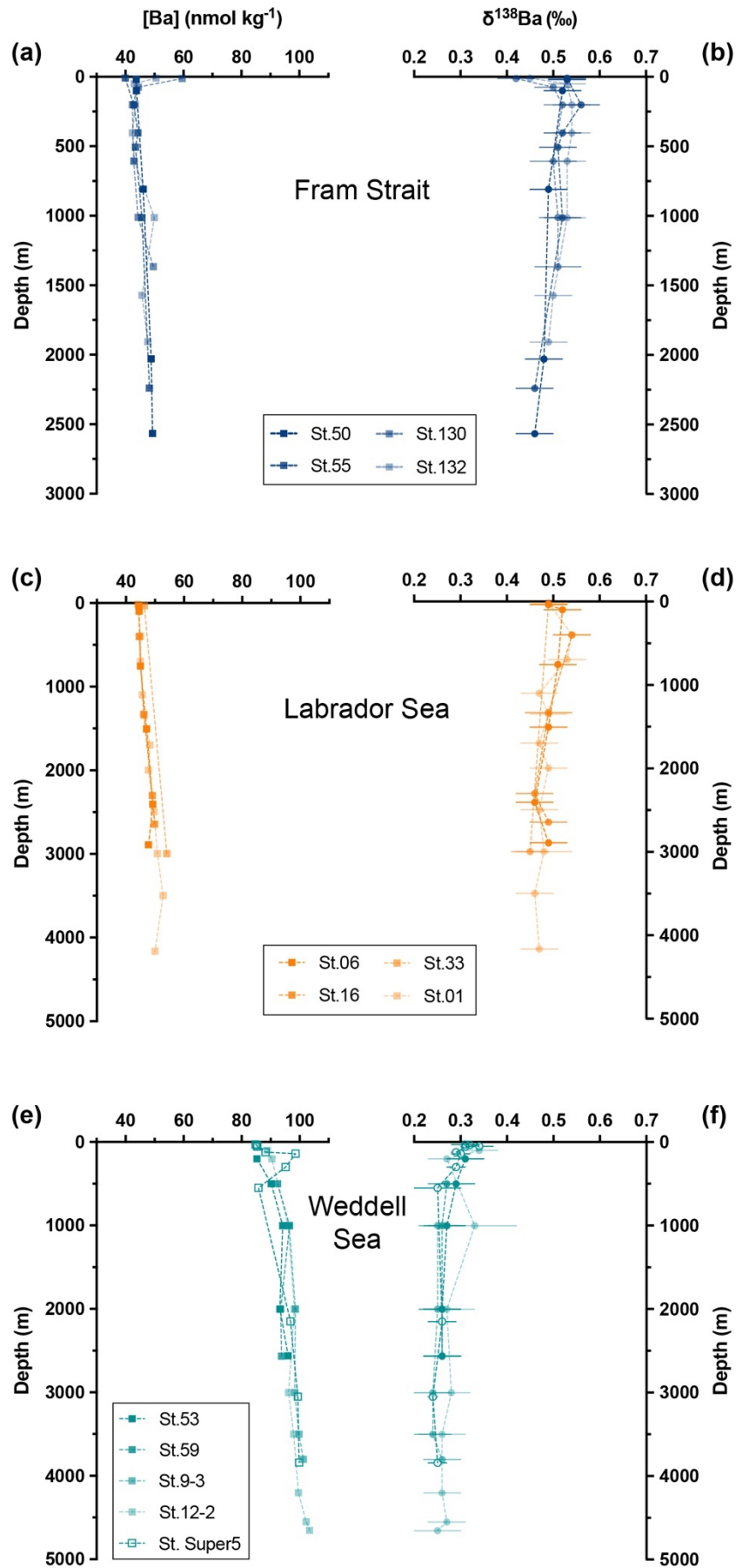
Dissolved Ba concentrations and isotope compositions for all stations are presented in Appendix Table A.2 along with potential temperature and salinity data. The data are also shown as depth profiles for the Fram Strait, the Labrador Sea and the Weddell Sea, respectively (Fig. 4.2).

In the Fram Strait (Figs. 4.2a & b), the depth profiles of [Ba] and $\delta^{138}\text{Ba}$ are similar for all four stations in that Ba is modestly depleted in surface waters associated with relatively heavy $\delta^{138}\text{Ba}$ values of $+0.52\text{‰}$. With increasing depth from 200 m to the bottom, [Ba] generally increases from 43 to 49 nmol kg^{-1} and $\delta^{138}\text{Ba}$ values slightly decrease from $+0.52$ to $+0.46\text{‰}$. An exception to this pattern are surface waters at St. 130 and St. 132, located close to the east Greenland shelf, which have the highest [Ba] and lightest $\delta^{138}\text{Ba}$ values of 59.6 nmol kg^{-1} and $+0.42\text{‰}$ at 15 m (St. 130), respectively. These waters are also marked by low salinities (Table A.2) and constitute cold and fresh Polar Water (PW) exiting the Arctic Ocean through Fram Strait (Laukert et al., 2017). The upper water column between 50 and 500 m water depth in the eastern (St. 50 and St. 55) and western Fram Strait (St. 130 and St. 132) has similar $\delta^{138}\text{Ba}$ and [Ba] signatures.

In the Labrador Sea (Figs 4.2c & d), the vertical distributions of $\delta^{138}\text{Ba}$ and $[\text{Ba}]$ are similar to those of the Fram Strait and only display little variability along the cyclonic circulation within the Labrador Basin. Dissolved $[\text{Ba}]$ exhibits moderate depletion at the surface and relative enrichment at depth, resembling nutrient-type depth profiles and mirroring the $\delta^{138}\text{Ba}$ profiles. All depth profile samples below 1000 m water depth, where NADW dominates (Dickson and Brown, 1994; Talley and McCartney, 1982), feature a homogenous $\delta^{138}\text{Ba}$ value of $+0.48\text{‰} \pm 0.05\text{‰}$, while $[\text{Ba}]$ values slightly increase towards the bottom.

In the Weddell Sea (Figs. 4.2e & f), the depth profiles show slight enrichments towards heavy isotopic compositions in the surface layer relative to deeper waters, which are associated with lower $[\text{Ba}]$ values. A marked $[\text{Ba}]$ enrichment of up to $103.4 \text{ nmol kg}^{-1}$ is observed at St. 12-2 at bottom depth and corresponds to a light $\delta^{138}\text{Ba}$ value of $+0.25\text{‰}$. The nature of the vertical gradient in $\delta^{138}\text{Ba}$ and its relationship to $[\text{Ba}]$ varies insignificantly with sampling sites along the WG, as well as with water depth. Such a vertical distribution is also consistent with the pattern reported for St. Super5 at the north rim of the WG (Hsieh and Henderson, 2017). At depths between 2000 and 4000 m, where the water masses are dominated by WSDW (Orsi et al., 1999), dissolved $[\text{Ba}]$ and $\delta^{138}\text{Ba}$ are tightly constrained to average values of $98.8 \text{ nmol kg}^{-1}$ and $+0.26 \pm 0.03\text{‰}$, respectively.

Fig. 4.2 → page down: Depth profiles of the dissolved Ba concentrations (a, c & e) and isotope compositions (b, d & f) in the Fram Strait (a & b), the Labrador Sea (c & d) and the Weddell Sea (e & f). The error bars for $\delta^{138}\text{Ba}$ are the larger of either the internal 2 standard errors (2SE) of repeated sample measurements or the long-term 2SD reproducibility ($\pm 0.04\text{‰}$) of repeated SAFe (1000 m) measurements. Data for St. Super5 are from Hsieh and Henderson, (2017).



4.4 Discussion

4.4.1 Origin of the $\delta^{138}\text{Ba}$ signature of NADW

North Atlantic Deep Water (NADW) refers to intermediate to deep waters once they leave the mixing area of the north subpolar gyre, notably the Labrador Sea, and that advected south as part of the deep western boundary current (Dickson and Brown, 1994). In the Labrador Sea, NADW is comprised of three main components (LSW, NEADW and NWABW) and occupies the depth below 1000 m (Talley and McCartney, 1982). The mixing and combination of these three components result in the formation of the core of NADW (Dickson and Brown, 1994). As shown in Fig. 4.2d, LSW, NEADW and NWABW have essentially invariant $\delta^{138}\text{Ba}$ values throughout the water column and the average $\delta^{138}\text{Ba}$ value below 1000 m is determined as $+0.48 \pm 0.05\text{‰}$. This $\delta^{138}\text{Ba}$ signature thus defines the endmember Ba isotope composition of NADW, which is within error identical to the previously estimated value for the northern-sourced water endmember ($+0.45 \pm 0.03\text{‰}$, Bates et al., 2017).

The lack of variability in Ba isotope compositions with water depth below 1000 m in the Labrador Sea might be a result of efficient vertical mixing in this region. However, dissolved [Ba] gradually increases with water depth, which is in contrast to the essentially uniform $\delta^{138}\text{Ba}$ values (Figs. 4.2c & d). This suggests that intermediate and deep water masses (i.e., LSW, NEADW and NWABW) advected into the Labrador Sea might be characterised by a uniform Ba isotope composition but different Ba concentrations. Admixture of these waters would thus result in a relatively homogenous $\delta^{138}\text{Ba}$ signature in the Labrador Basin. Although none of our stations are located close to the actual formation areas of NEADW and NWABW, our new data from the Fram Strait provide the opportunity to assess the signatures of the distant contributors to NADW in terms of $\delta^{138}\text{Ba}$ and [Ba].

Strong surface cooling during winter combined with advection of relatively warm AW and cold and fresh PW results in deep convection and the formation of dense waters in the Fram Strait and the Greenland Sea (Dickson and Brown, 1994). These water masses flow southwards at the mid-depth between ~ 400 and ~ 1000 m via the shallow East Greenland Current (EGC) as NOW in agreement with previous nomenclature (Dickson

and Brown, 1994; Lacan and Jeandel, 2004). Depth profiles in the Fram Strait display an essentially constant $\delta^{138}\text{Ba}$ signature between 400 and 1000 m with an average value of $+0.52 \pm 0.07\text{‰}$ for NOW (Fig. 4.2b). While this $\delta^{138}\text{Ba}$ value is within uncertainty identical to the NADW $\delta^{138}\text{Ba}$ signature ($+0.48 \pm 0.05\text{‰}$) in the Labrador Sea, a clear mixing relationship (Fig. 4.3) can be observed between NOW (400-1000 m, Fram Strait), NADW (> 1000 m, Labrador Sea) and the waters from the deep subtropical North Atlantic (> 4000 m, Bates et al., 2017). This suggests that the Ba signature of NOW originating from Fram Strait is modified along its pathway to production sites of NADW.

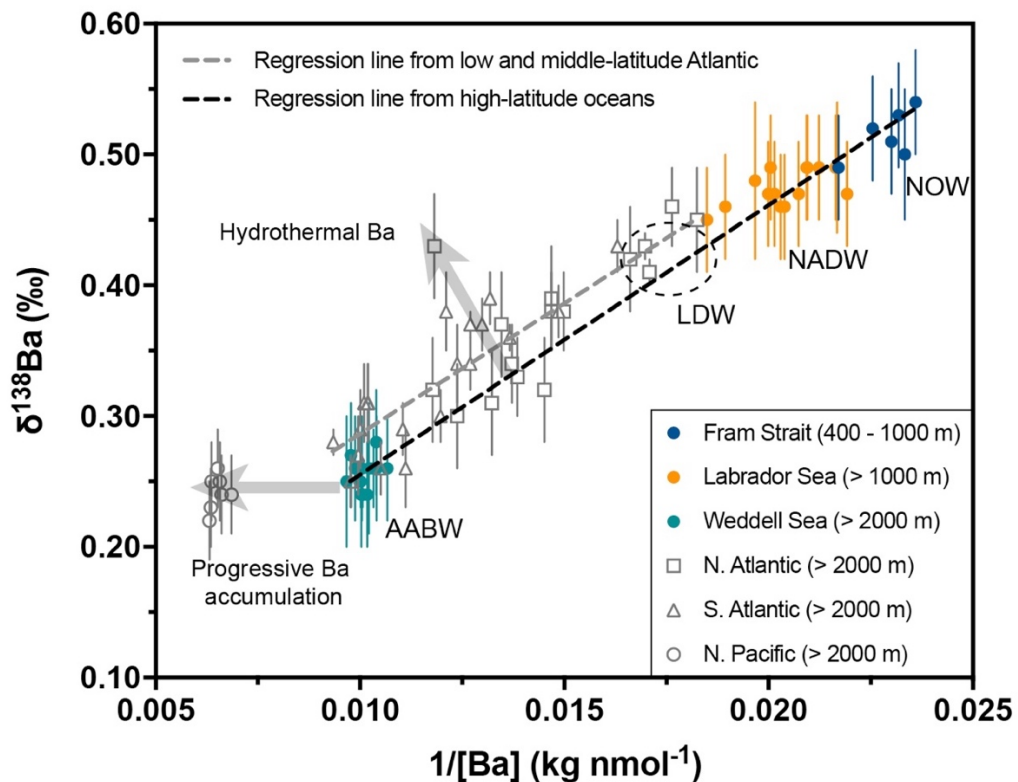


Fig. 4.3: Deep ocean mixing (regression) lines of $\delta^{138}\text{Ba}$ against $1/[\text{Ba}]$ for the seawater samples from the high-latitude oceans (dark dashed line; data from this study) and the low and middle-latitude Atlantic Ocean (grey dashed line; data from Bates et al. 2017, Horner et al. 2015, and Hsieh and Henderson, 2017). The impact of hydrothermal Ba input and progressive Ba accumulation are labelled by bold light grey arrows (Hsieh et al., 2021). NOW: Northern Overflow Water; NADW: North Atlantic Deep Water; LDW: Lower Deep Water; AABW: Antarctic Bottom Water.

The prevailing view on the formation of NADW is that the recirculating component of Lower Deep Water (LDW), which is derived from northward spreading modified AABW,

mixes with the NOW at the head of the Western Basin (McCartney, 1992). This abyssal water mass, LDW, is characterised by a near bottom salinity minimum and a silica maximum in the North Atlantic (McCartney, 1992). Under the assumption that the water masses below ~ 4000 m in the equatorial North Atlantic represent the Ba signatures of LDW, the entrainment of this AABW derivative (LDW), characterised by relatively light $\delta^{138}\text{Ba}$ and high [Ba] signals (Bates et al., 2017), is consistent with our mixing model (Fig. 4.3). This scenario for NADW formation is also consistent with the general oceanography of this region outlined in earlier studies (Dickson and Brown, 1994; McCartney, 1992). Alternatively, the modifications of $\delta^{138}\text{Ba}$ and [Ba] of the NOW may also occur within the Nordic Seas by mixing with local waters along its route to the GSR. Although our $\delta^{138}\text{Ba}$ and [Ba] data are only available for the Fram Strait transect, previously reported dissolved [Ba] data along the EGC in the vicinity of the Denmark Strait Taylor et al. (2003) can be used to determine the possible Ba budget modifications within the Nordic Seas. As shown in Fig. S1, no distinct modifications in the [Ba] profiles are observed along the EGC advection, suggesting that the NOW likely retains its initial Ba characteristics of the water masses from the Fram Strait. This is also in line with distributions of dissolved radiogenic neodymium isotopes, which at these water depths remain relatively constant downstream the EGC, apart from a few minor modifications through particle-seawater interactions at the Denmark Strait (Lacan and Jeandel, 2004; Laukert et al., 2017). Both observations again support the suggestion that the NOW is mainly modified in the North Atlantic subpolar gyre due to the entrainment of LDW at greater depth. The preformed $\delta^{138}\text{Ba}$ signatures of the waters in the Fram Strait thus are a consistent mixing endmember for the Ba isotope compositions of NADW encountered in the Labrador Sea.

4.4.2 Origin of the $\delta^{138}\text{Ba}$ signature of AABW

One of the major pathways by which the interior of the Weddell Sea gains significant amounts of dissolved Ba is the inflow of warm and saline CDW, which is fed by the admixture of NADW to the ACC (Vernet et al., 2019 and references therein). Due to the relatively low productivity in the WG (Orsi et al., 1999), the rising intrusion of CDW onto the Antarctic continental shelves experiences little Ba depletion and isotope fractionation. Therefore, the surface and subsurface Weddell Sea have relatively high Ba concentrations (~ 90 nmol kg^{-1}) and light isotope compositions ($\sim +0.30\text{‰}$) as shown in

Figs. 4.2e & f. The resultant mixing with cold shelf waters and the subsequent dense water formation (i.e., WSDW and WSBW) transfer these surface Ba signals to the abyssal Weddell Basin, resulting in the highest [Ba] and the lightest $\delta^{138}\text{Ba}$ in the Southern Ocean. Within the reported analytical uncertainty ($\pm 0.04\%$), four depth profiles in the southern and western WG are indistinguishable in the Ba isotope compositions of WSDW and WSBW (Fig. 4.2f). The $\delta^{138}\text{Ba}$ values between 2000 and 4000 m water depths reflect the isotope composition of WSDW/AABW and the average $\delta^{138}\text{Ba}$ value (2000 - 4000 m) is calculated as $+0.26 \pm 0.03\%$, which is identical to the previously estimated value of $+0.26 \pm 0.03\%$ for the southern-source water endmember (Bates et al., 2017).

Combination of the present data with another profile from the northern WG (Hsieh and Henderson, 2017) reveals that vertical distributions of [Ba] and $\delta^{138}\text{Ba}$ along the WG advection have very similar patterns (Figs. 4.2e & f). As a result, the depth profiles of $\delta^{138}\text{Ba}$ in the southern and western WG are indistinguishable from that at the northern WG edge. The lack of spatial variations in the profiles of [Ba] and $\delta^{138}\text{Ba}$ is in contrast with the significant spatial differences in hydrographic prosperities and nutrient concentrations (Vernet et al., 2019). For example, the temperature maximum of the CDW is eroded along its pathway within the main flow path of the gyre (Reeve et al., 2016). Given the complexity of the physical and biogeochemical processes occurring within the WG, such as the intense ocean-ice shelves interaction, some variations in the $\delta^{138}\text{Ba}$ distributions could have been expected. This is, however, not the case and the available Ba isotope data in the WG are, indeed, relatively homogenous. We propose that the rapid circulation of the WG (e.g., the residence time of CDW in the WG is ~ 35 years) is the reason for the invariant $\delta^{138}\text{Ba}$ distributions, considering the relatively long residence time of dissolved Ba in open ocean (7 – 21 kyr, Horner and Crockford, 2021).

4.4.3 High-latitude controls on Ba isotope distributions in the deep ocean

Water mass mixing control on deep water Ba isotope distributions in the low and mid-latitude Atlantic Ocean has recently been estimated by Bates et al. (2017), which is remarkably well supported by our new data from high-latitude oceans. The [Ba] and $\delta^{138}\text{Ba}$ data obtained here are compiled with reported results in a plot of $\delta^{138}\text{Ba}$ against $1/[\text{Ba}]$ (Fig. 4.3). Our AABW data are fully consistent with the previously inferred southern endmember and plot near the low end of the mixing line for the Ba isotope

compositions. In contrast, the data from the Fram Strait and the Labrador Sea samples exhibit significantly heavier $\delta^{138}\text{Ba}$ and lower [Ba] values than previously reported results from the mid-latitude North Atlantic (Fig. 4.3). This observation is very important for our understanding of Atlantic Ba isotope systematics and the AMOC, because these heavy $\delta^{138}\text{Ba}$ and low [Ba] values are far beyond existing results for the northern endmember and it is conceivable that the data from the Fram Strait represent the upper endmember of the deep ocean mixing trend.

These markedly heavy $\delta^{138}\text{Ba}$ signals in the Nordic Seas and the Labrador Sea are most likely the result of the fractionation signatures introduced into the return path of the AMOC in the Southern Ocean. In contrast to the waters brought southward to the surface Weddell Sea by upwelling of CDW, the northward ventilation of CDW that enters the high-productivity ACC undergoes strong Ba isotope fractionation due to enhanced productivity and associated barite precipitation (Horner and Crockford, 2021). As the waters transit northward away from the ACC, surface dissolved $\delta^{138}\text{Ba}$ values increases from $\sim +0.3$ to $\sim +0.5\%$ (Bates et al., 2017; Hsieh and Henderson, 2017). The introduction of this highly fractionated $\delta^{138}\text{Ba}$ signal into the northward flowing Antarctic intermediate Water (AAIW) and Subantarctic Mode Water (SAMW) feeds the low-latitude thermoclines and ultimately results in the significantly heavy $\delta^{138}\text{Ba}$ signatures at high northern latitudes. Therefore, the $\sim 0.3\%$ offset in $\delta^{138}\text{Ba}$ values between the northern and southern endmembers (Fig. 4.3) is largely the result of the $\delta^{138}\text{Ba}$ difference between the water masses of Southern Ocean origin (i.e., AABW and AAIW/SAMW), which is similar to the mechanism that govern the oceanic $\delta^{30}\text{Si}$ distributions in the deep Atlantic Ocean (De Souza et al., 2012). In addition, we cannot rule out the potential contribution of heavy Ba isotopes from the Arctic Ocean, which needs to be tested in future studies.

The distinctive Ba isotope signatures of deep waters originating in the Weddell Sea and those in the high-latitude North Atlantic (i.e., Nordic Seas and Labrador Sea) allow to better constrain the meridional gradient of Ba isotope compositions in the deep Atlantic Ocean. The remarkable linear relationship of our [Ba] and $\delta^{138}\text{Ba}$ data (Fig. 4.3, dark regression line) is clearly indicative of conservative mixing between two dominant distinct reservoirs with no other significant sources and sinks. However, the linear regression line of the published data (Fig. 4.3, grey dashed line) shows a clear deviation

towards heavier $\delta^{138}\text{Ba}$ values, which indicates a third mixing endmember (Fig. 4.3). This deviation clearly reflects special conditions at the respective depths and locations, which are not controlled by major deep water mass mixing and are likely associated with the influence of hydrothermal Ba inputs. Hsieh and Henderson (2017) first identified evidence for non-conservative behaviour in the deep Atlantic, while Bates et al. (2017) suggested that Ba isotopes in Atlantic deep waters overall behave conservatively during mixing. More recently, Hsieh et al. (2021) presented Ba isotope measurements in several hydrothermal vent fluids and suggested that the inputs of hydrothermal Ba contribute heavy $\delta^{138}\text{Ba}$ to the deep ocean, which results in the apparent non-conservative behaviour of Ba in deep oceans. Their calculated effective hydrothermal Ba isotope composition of the hydrothermal fluids ($\delta^{138}\text{Ba} = +1.7 \pm 0.7\text{‰}$) accounts for around 3–9% of the Ba in some Atlantic deep waters, which not only causes a deviation from the high-latitude endmember trend line but also results in a similar parallel mixing line. Our high-latitude seawater Ba data thus corroborate the conclusions by Hsieh et al. (2021) on the impact of hydrothermal Ba inputs on the Ba isotope composition of Atlantic deep waters.

In a global context, the water masses from the deep North Pacific are characterised by Ba isotope compositions indistinguishable from those of the deep Weddell Sea, but they have significantly higher Ba concentrations (Fig. 4.3). The nutrient-like behaviour of Ba is expressed by Ba removal and scavenging from surface and subsurface waters and released in deep waters. In this case, a systematic increase (decrease) in deep water [Ba] ($\delta^{138}\text{Ba}$) from the North Atlantic via the Southern Ocean to the North Pacific is expected. However, while [Ba] does appear to increase systematically in deep waters along this deep ocean conveyor belt, the $\delta^{138}\text{Ba}$ signature does not completely follow this pattern. The uniformity of deep water $\delta^{138}\text{Ba}$ signatures between the Southern Ocean and the North Pacific indicates little or no Ba isotope fractionation but progressive accumulation of Ba along the conveyor belt in the deep Pacific. Additional dissolved Ba isotope profiles from the Pacific Ocean are required to test this hypothesis.

4.4.4 Ba isotope fractionation in the upper ocean

Ba is primarily removed from the surface ocean via particle adsorption, while barite formation in association with organic matter decomposition largely controls the biogeochemical cycling of Ba in the mesopelagic zone (e.g., Cao et al., 2020a; Horner et

al., 2015). Figs. 4.4a & b show that Ba signatures in seawater samples in the upper ocean (< 800 m) are consistent with linear $\delta^{138}\text{Ba}$ versus $[\text{Ba}]$ trends regardless of whether the Ba concentrations are plotted in $[\text{Ba}]$ or $\text{Ln}([\text{Ba}])$ scale. This observation indicates that Ba isotope fractionation in the upper ocean is, in principle, compatible with both an open system steady-state fractionation model and a closed system Rayleigh fractionation model.

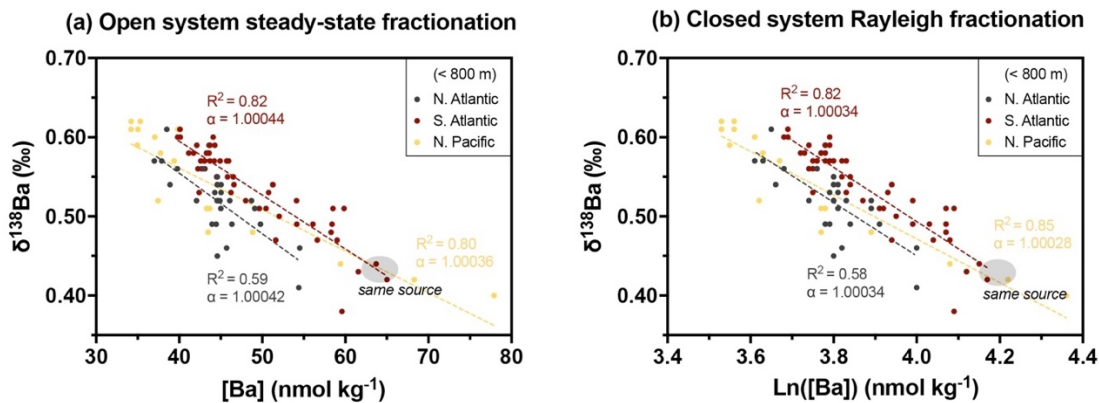


Fig. 4.4: Upper ocean Ba isotope fractionation plots of $\delta^{138}\text{Ba}$ against $[\text{Ba}]$ and $\text{Ln}([\text{Ba}])$ for seawater samples (< 800 m) from the North Atlantic (black), the South Atlantic (red) and the North Pacific (yellow). (a) an open system steady-state fractionation model defines three fractionation factors (α) of 1.00042 (North Atlantic), 1.00044 (South Atlantic) and 1.00036 (North Pacific), respectively; (b) closed system Rayleigh fractionation model defines three fractionation factors (α) of 1.00034 (North Atlantic), 1.00034 (South Atlantic) and 1.00028 (North Pacific), respectively. Regardless of which model is applied, the regression lines from the North Atlantic and the South Atlantic have very similar slopes, but they are offset by $\delta^{138}\text{Ba} = \sim 0.06\text{‰}$, indicating differences in source water compositions. The North Pacific has the lowest fractionation factors (slopes) in both models but similar source water compositions to the South Atlantic. Data sources: Bates et al. (2017); Bridgestock et al. (2018); Geyman et al. (2019); Horner et al. (2015); Hsieh and Henderson (2017) and this study.

The steady-state model has generally been applied to explain the relationship between dissolved $\delta^{138}\text{Ba}$ and $[\text{Ba}]$ in the seawater (e.g., Cao et al., 2016; Horner et al., 2015; Hsieh and Henderson, 2017). In a steady-state model, the continuous supply of Ba balances the export of Ba due to barite formation and particle adsorption. In this case, the following equation can be applied to describe Ba isotope fractionation:

$$\delta^{138}Ba_r = \delta^{138}Ba_i - 1000 \times (1/\alpha - 1) \times (1 - [Ba]_r / [Ba]_i) \quad (4.1)$$

where $\delta^{138}Ba_r$ and $\delta^{138}Ba_i$ denote the Ba isotope composition of the remaining seawater and the initial seawater, respectively. $[Ba]_r$ and $[Ba]_i$ denote the Ba concentration of the remaining seawater and the initial seawater, respectively. The fractionation factor α is defined as $\alpha = \delta^{138}Ba_{SW} / \delta^{138}Ba_{particle}$, whereby $\delta^{138}Ba_{SW}$ and $\delta^{138}Ba_{particle}$ refer to the $\delta^{138}Ba$ values of seawater and the removed particulate phases. If assuming the maximum $[Ba]$ value of water masses around 800 m represents the starting $[Ba]_i$ from three different oceans, the slopes of three linear regression lines in plots of $\delta^{138}Ba$ against $[Ba]$ define three fractionation factors (α_{open}) of 1.00042, 1.00044 and 1.00036 for the North Atlantic, the South Atlantic and the North Pacific, respectively (Fig. 4.4).

On the other hand, Ba isotope fractionation can also be explained by a closed system Rayleigh fractionation model due to the well-defined linear trends in plots of $\delta^{138}Ba$ against $\ln([Ba])$. In a Rayleigh model, light Ba isotopes are progressively removed from a finite dissolved Ba pool, driving the remaining pool towards heavier $\delta^{138}Ba$ values. In this case, the following equation can be applied to describe Ba isotope fractionation:

$$\delta^{138}Ba_r = \delta^{138}Ba_i + 1000 \times (1/\alpha - 1) \times \ln([Ba]_r / [Ba]_i) \quad (4.2)$$

The fractionation factors (α_{closed}) can be directly determined from the slopes of three regression lines in plots of $\delta^{138}Ba$ against $\ln([Ba])$ without assumptions with regard to $[Ba]_i$. This method yields three fractionation factors (α_{closed}) of 1.00034, 1.00034 and 1.00028 for the North Atlantic, the South Atlantic and the North Pacific, respectively.

A clear difference between the open and closed models is that the steady-state model requires larger isotope fractionation factors to account for the correlations seen in Fig. 4.4a than the Rayleigh model of Fig. 4.4b. In principle, the two different Ba isotope fractionation conditions (i.e., open versus closed system) can be assessed by independent estimates of α from culturing experiments. Laboratory precipitation of barite has indicated a fractionation factor of 1.00032 ± 0.00005 (von Allmen et al., 2010), which supports the closed system Rayleigh model to better explain the Ba isotope fractionation in the upper ocean. However, due to the undersaturated conditions with respect to barite

formation in the vast majority of the upper ocean, barite precipitation fundamentally requires a process to incorporate Ba into micro-environments to reach an oversaturated condition, mainly associated with decomposition of sinking biogenic particles (Dehairs et al., 1980). Based on field measurements, particle adsorption in the uppermost water column leads to a larger fractionation factor of 1.00046 ± 0.00011 than observed in laboratory barite precipitation experiments (Cao et al., 2020a). Therefore, these “two-stage” fractionations would result in a combined fractionation factor for Ba removal larger than that of barite precipitation alone, which may reflect a condition that is more consistent with a steady-state model with larger fractionation factors.

While it is unclear which fractionation model is realistic for the interpretation of Ba isotope fractionation in the upper ocean, nor the mechanisms causing the compatibility of the data with both models, there is a clear shift in source water Ba signatures from the North Atlantic to the South Atlantic and the North Pacific (Figs. 4.4a & b). This observation is important because similar scenarios are obtained from both models. Regardless of which model is applied, data from the North Atlantic and those from the South Atlantic show very similar slopes, but they are offset by a $\delta^{138}\text{Ba}$ value of $\sim 0.06\%$. The small but significant offset between these two nearly parallel trends (Figs. 4.4a & b) can be explained by a difference in the Ba isotope compositions of the source water masses. In the North Atlantic, the LSW mainly occupies the mid-depth circulation, while Antarctic Intermediate Water (AAIW) is the major water mass supplying the intermediate depth ocean in the South Atlantic (Dickson and Brown, 1994; Talley, 2013). The observed differences in the Ba isotope compositions between LSW and AAIW (Bates et al., 2017) are consistent with the clear offsets between two regression lines from both models, thereby supporting our proposed explanation. In contrast, the North Pacific has the distinct and the lowest fractionation factors in both models but the source water compositions are similar to the South Atlantic (Figs. 4.4a & b). The mid-depth water masses in the North Pacific are primarily occupied by AAIW and North Pacific Intermediate Water (NPIW, Talley, 2013). Therefore, it is conceivable that the AAIW can at least partially impart its isotope signatures to the intermediate waters supplying the upper ocean in the North Pacific. The observed low fractionation factors are likely caused by the progressive accumulation of remineralised Ba without introducing further isotope fractionations. Overall, the statistical assessment suggests that the data from the upper ocean can be explained by both fractionation models given the small dynamic range of

the endmember Ba isotope signatures and the relatively large analytical uncertainties. The differences between the regression lines of three different ocean basins in both models is likely a consequence of differences in source water Ba isotope compositions and changes in mechanisms governing isotope fractionations in the upper ocean.

4.4.5 Palaeoceanographic prospects

The close to conservative behaviour of Ba documented in the high-latitude oceans, along with the distinctive Ba isotope signatures consistent with conservative mixing between northern and southern deep waters, suggest that Ba isotopes, like Ba/Ca ratios in benthic foraminifera and cold-water corals, may potentially be a useful tracer of deep-ocean circulation in the past. Recent work conducted on Ba isotope signatures of cold-water corals suggested that coral aragonite preferentially incorporates the light Ba isotopes and the isotope fractionation between coral skeletons and seawater is likely independent from temperature and other environmental variables (Geyman et al., 2019; Hemsing et al., 2018). Independent constraints on glacial-interglacial deep-ocean circulation patterns might be provided by stable Ba isotope compositions of cold-water corals or benthic foraminifera. In addition, Ba isotope signatures in shallow-water corals have a great potential to provide a long-term record of freshwater inputs and precipitation on land beyond the instrumental record (Liu et al., 2019), given that river runoff is characterised by relatively light Ba isotope compositions and can significantly modify the $\delta^{138}\text{Ba}$ values of coastal surface seawaters. The direct calibration of Ba isotope fractionation between shallow-water coral skeletons and contemporaneous seawater at high temporal resolution is currently still lacking to fully understand the mechanisms governing Ba/Ca distributions and Ba isotope fractionation during coral calcification. Last but not least, the $\delta^{138}\text{Ba}$ values of deep-sea sediments in the open ocean could reflect variations in dissolved Ba removal by marine barite precipitates originating from the upper ocean, which in turn might help to constrain the related export production during the period of climate change (Bridgestock et al., 2019). Combination with other stable isotope systems (e.g., Cd, Ni, Zn) in deep-sea sediments might help to distinguish the sources of similar Ba isotope signatures observed in detrital and authigenic Ba (Bridgestock et al., 2018).

4.5 Conclusions

We present dissolved Ba concentrations and isotope compositions in the water columns from the high-latitude oceans including the Fram Strait (Nordic Seas), the Labrador Sea, and the Weddell Sea. Given the lack of variability in Ba isotope compositions ($\delta^{138}\text{Ba}$) with water depth in the deep Atlantic Ocean below 1000 m, our data yield an average $\delta^{138}\text{Ba}$ value of $+0.48 \pm 0.05\text{‰}$ for North Atlantic Deep Water (NADW) in the Labrador Sea. Within analytical uncertainty ($\pm 0.04\text{‰}$), depth profiles in the Weddell Sea show no evidence for vertical differences in $\delta^{138}\text{Ba}$ values of Weddell Sea Deep Water (WSDW) and Weddell Sea Bottom Water (WSBW), and the average $\delta^{138}\text{Ba}$ value (2000 – 4000 m) is calculated as $+0.26 \pm 0.03\text{‰}$ for Antarctic Bottom Water (AABW). In combination with the results from the Fram Strait, deep water Ba concentrations and isotope compositions define a close correlation between [Ba] and $\delta^{138}\text{Ba}$, suggesting a predominately conservative behaviour of Ba in these high-latitude oceans. In terms of the upper ocean (< 800 m), the Ba isotope fractionation closely corresponds to variations in [Ba] regardless of whether a linear or a logarithmic relationship is employed, thereby matching either an open system steady-state fractionation model or a closed system Rayleigh fractionation model. Regardless of which model is applied, the regression lines from the North Atlantic and the South Atlantic have very similar slopes, but they are offset by $\sim 0.06\text{‰}$ in $\delta^{138}\text{Ba}$, indicating that changes in Ba isotope compositions of the source waters dominate the upper ocean. The observed low fractionation factors in the North Pacific are likely a result of progressive accumulation of remineralised Ba with no further isotope fractionation. Overall, our results underscore the high-latitude controls on dissolved Ba isotope budget in the global ocean and enhance our current understanding of the mechanisms governing marine Ba isotope fractionation in the upper ocean.

5 Scientific Chapter III

Monthly resolved coral $\delta^{138}\text{Ba}$ record of increased riverine inputs during the South Asian Summer Monsoon at the Andaman Islands, NE Indian Ocean

Submitted to Geochimica et Cosmochimica Acta as: Yu, Y., Hathorne, E., Siebert, C., Felis, T., Rajendran, C. P. and Frank, M.: Monthly resolved coral $\delta^{138}\text{Ba}$ record of increased riverine inputs during the South Asian Summer Monsoon at the Andaman Islands, NE Indian Ocean.

Abstract

We present a monthly resolved stable Ba isotope record ($\delta^{138}\text{Ba}_{\text{coral}}$) of a young fossil coral (*Porites*) from the eastern side of the Andaman Islands, India (Andaman Sea, NE Indian Ocean), which grew prior to the 19th century. This $\delta^{138}\text{Ba}_{\text{coral}}$ record complements 19-year records of $\text{Ba}/\text{Ca}_{\text{coral}}$, $\text{Sr}/\text{Ca}_{\text{coral}}$, $\text{U}/\text{Ca}_{\text{coral}}$, $\delta^{18}\text{O}_{\text{coral}}$ and $\delta^{13}\text{O}_{\text{coral}}$ from the same coral that can serve as a baseline of environmental variability before the industrialised era. The $\delta^{138}\text{Ba}_{\text{coral}}$ record exhibits small but significant seasonal variability ranging from $+0.16 \pm 0.03\text{‰}$ (2SD) to $+0.27 \pm 0.03\text{‰}$ (2SD) over two continuous years. The $\delta^{138}\text{Ba}_{\text{coral}}$ signature is generally light during the South Asian Summer Monsoon (SAM, June-September) and post-SAM season (October-January), which are characterised by enhanced rainfall and regional river discharge. The $\text{Ba}/\text{Ca}_{\text{coral}}$ signal follows the seasonal cycles in $\delta^{138}\text{Ba}_{\text{coral}}$ with elevated $\text{Ba}/\text{Ca}_{\text{coral}}$ accompanying low $\delta^{138}\text{Ba}_{\text{coral}}$. We suggest that Ba desorption from the floodplain-stored sediments of the Myanmar continental shelves followed by lateral advection are the main causes of the light $\delta^{138}\text{Ba}_{\text{coral}}$ and elevated $\text{Ba}/\text{Ca}_{\text{coral}}$ values during the SAM and post-SAM seasons. In addition, pronounced spikes of light $\delta^{138}\text{Ba}_{\text{coral}}$ and high $\text{Ba}/\text{Ca}_{\text{coral}}$ are observed during the pre-SAM season (February-May). Possible explanations for these spikes that occur throughout the 19-year record are (1) barite formation as a consequence of phytoplankton blooms or (2) Ba release from sediments trapped by local fringing mangroves. Andaman Islands surface seawater sampled over an annual cycle exhibits a wide range of $\delta^{138}\text{Ba}_{\text{sw}}$ and $[\text{Ba}]_{\text{sw}}$ values, with significantly light $\delta^{138}\text{Ba}_{\text{sw}}$ of $+0.29 \pm 0.04\text{‰}$ (2SD) and high

[Ba]_{sw} of 66.03 nmol/kg during the SAM, which is broadly consistent with the coral skeletal signals. The $\delta^{138}\text{Ba}_{\text{coral}}$ values may indicate a tendency to overall lighter values than those of ambient seawater ($\Delta^{138}\text{Ba}_{\text{coral-seawater}}$ between -0.07‰ and -0.23‰). Our results suggest that seawater Ba isotope compositions likely dominate the seasonal changes in the signals recorded by coral skeletons, while Rayleigh fractionation and/or mineral growth kinetics may exert additional control on $\delta^{138}\text{Ba}_{\text{coral}}$ and $\text{Ba}/\text{Ca}_{\text{coral}}$ during coral calcification.

5.1 Introduction

Coral skeletons archive a wealth of past climate and environmental information with unrivalled temporal resolution in the tropical and subtropical ocean for times when instrumental data are limited (Beck et al., 1992; Felis, 2020; Gagan et al., 1998; Hendy et al., 2002; McCulloch et al., 2003). A number of geochemical tracers in coral skeletons have been widely applied to reconstruct ambient seawater properties such as temperature and salinity as well as site-specific features including river runoff and upwelling intensity (Cole et al., 1993; Felis et al., 2004; Gagan et al., 2000; Hathorne et al., 2013a; Lea and Boyle, 1989; Smith et al., 1979). In coastal regions, coral-based reconstructions of riverine inputs are critical for understanding changes in local and global elemental budgets in the context of climate change and anthropogenic land use (McCulloch et al., 2003; Moyer et al., 2012; Saha et al., 2016). One elemental tracer broadly used as a proxy for river runoff is the barium to calcium ratio in coral skeletons ($\text{Ba}/\text{Ca}_{\text{coral}}$, e.g., Alibert et al., 2003; Chen et al., 2020; Lewis et al., 2007; McCulloch et al., 2003). In estuarine mixing zones, Ba is desorbed/released from fluvial particles and/or re-suspended sediments by ion-exchange at low salinities and subsequently shows a conservative mixing line along the freshwater-seawater salinity gradient (Coffey et al., 1997; Joung and Shiller, 2014; Singh et al., 2013). As a result, Ba incorporated into coral skeleton has been used to reconstruct riverine inputs to coastal surface waters (Alibert et al., 2003; Grove et al., 2012; McCulloch et al., 2003; Prouty et al., 2010). However, a number of studies reported “anomalous” signals of $\text{Ba}/\text{Ca}_{\text{coral}}$ that are decoupled from recorded peak river discharge suggesting that this proxy is not solely controlled by river discharge (e.g., Jupiter et al., 2008; Lewis et al., 2007; Sinclair, 2005). Other factors, such as coastal upwelling, barite inclusions and productivity can potentially have a significant effect on the temporal variability of the $\text{Ba}/\text{Ca}_{\text{coral}}$ proxy (Saha et al., 2016 and references therein).

Furthermore, the incorporation of ambient seawater Ba signals into coral skeletons can be strongly modulated by differences in partitioning between coral and seawater and by vital effects potentially limiting the interpretation of this proxy (e.g., Gaetani and Cohen, 2006). As a consequence, the use of Ba/Ca_{coral} as a quantitative proxy of riverine inputs is complex and other geochemical indicators are needed to complement and groundtruth the existing Ba/Ca_{coral} proxy.

Recently, stable Ba isotopes ($\delta^{138}\text{Ba}$) have been proposed as a novel proxy for various palaeoenvironmental conditions (e.g., Bridgestock et al., 2019; Cao et al., 2016; Geyman et al., 2019; Hemsing et al., 2018; Horner et al., 2015). It has been shown that river runoff is characterised by light Ba isotope compositions and can significantly modify the Ba isotope compositions of coastal surface seawaters (Cao et al., 2020b; Hsieh and Henderson, 2017). Therefore, Ba isotope signatures in shallow-water corals ($\delta^{138}\text{Ba}_{\text{coral}}$) may reflect the ambient seawater Ba isotope composition ($\delta^{138}\text{Ba}_{\text{sw}}$) and have great potential to provide a long-term record of runoff and precipitation on land beyond the instrumental record (Liu et al., 2019). So far, few studies have systematically investigated this application of the $\delta^{138}\text{Ba}_{\text{coral}}$ proxy. A culture experiment conducted by Pretet et al. (2015) showed that $\delta^{138}\text{Ba}_{\text{coral}}$ values of bulk samples are isotopically identical or lighter than those of ambient waters. Another study suggested that the annually-resolved $\delta^{138}\text{Ba}_{\text{coral}}$ records from diverse oceanic settings also display negative offsets from typical Pacific surface seawater values but are largely unaffected by biomineralization processes and temperature (Liu et al., 2019).

We propose that seasonal variations in monsoon circulation and related changes in river runoff are expected to result in significant Ba isotope variability of surface waters and thus in sub-annually resolved variations of Ba isotopes in shallow-water coral skeletons. However, such data have not been reported as yet and therefore, we will test the utility of $\delta^{138}\text{Ba}_{\text{coral}}$ as a proxy for riverine inputs at seasonal timescales against other proxies in corals and external environmental drivers. Here, we recovered cores from two dead coral colonies (*Porites* sp.) at the middle Andaman Islands (NE Indian Ocean). This region is subject to extensive seasonal freshening events during the South Asian Summer Monsoon (SAM) making it ideal for studying past monsoon variability and reconstructing changes in monsoon-driven runoff. A multiproxy record of monthly resolved $\delta^{138}\text{Ba}_{\text{coral}}$, Ba/Ca , Sr/Ca , U/Ca , $\delta^{18}\text{O}$ and $\delta^{13}\text{C}$ data has been obtained from a fossil *Porites* coral (AND-3-

A II), which is complemented by monthly resolved data of a recently uplifted *Porites* coral for which we know the date it was killed by emergence (AND-2-B). We use coral skeletal Sr/Ca ($\text{Sr}/\text{Ca}_{\text{coral}}$) data to reconstruct past sea surface temperature (SST) at our sampling location. By subtracting this reconstructed SST component from coral skeletal $\delta^{18}\text{O}$ signal ($\delta^{18}\text{O}_{\text{coral}}$), we are able to reconstruct the $\delta^{18}\text{O}$ compositions of ambient seawater ($\delta^{18}\text{O}_{\text{sw}}$) and to estimate sea surface salinity (SSS) variations. The latter should reflect past patterns of evaporation, precipitation and freshwater input in the area, which are potentially related to coral-derived $\delta^{138}\text{Ba}_{\text{coral}}$ and $\text{Ba}/\text{Ca}_{\text{coral}}$ signatures. We discuss the integrity and limitations of these coral-based proxies, provide new insights into their interpretations related to the reconstruction of riverine inputs in monsoonal regions, allowing us to better constrain the seasonal changes of the SAM intensity prior to instrumental observations in this understudied region of the Indian Ocean.

5.2 Materials and Methods

5.2.1 Study area

The Andaman Islands (India) are a narrow-broken island chain between 10°N and 14°N in the NE Indian ocean bounded by the Bay of Bengal (BoB) in the west and by the Andaman Sea (AnS) in the east (Fig. 5.1a). The climate of this region is controlled by the seasonally reversing SAM (Davis and Farley, 2001). The SAM is active during June-September and 80 – 90% of the annual rainfall, runoff and sediment discharge occur during this period in the BoB and AnS (Ramaswamy et al., 2004; Rodolfo, 1969). Observed SSTs show a strong annual cycle with pronounced cooling during winter and prominent warming during summer. Superimposed on this annual cycle is a semi-annual cycle characterised by cooling during winter and mid-summer and warming during spring and fall (e.g., Ashin et al., 2019). This bimodal SST pattern generally shows strong asymmetry with relatively higher SST occurring during the pre-SAM period warming in spring and relatively lower SST during the post-SAM period warming in fall. The net annual surface water exchange (i.e., precipitation plus runoff minus evaporation) is primarily driven by intense freshening events during the SAM, which leads to a pronounced annual SSS cycle in the AnS, with relatively low SSS during the SAM and relatively high SSS during the pre-SAM period (Varkey et al., 1996). In response to the SAM, the surface currents in the AnS change direction twice a year and show a cyclonic

flow during the SAM and an anti-cyclonic pattern during the post-SAM period (Potemra et al., 1991).

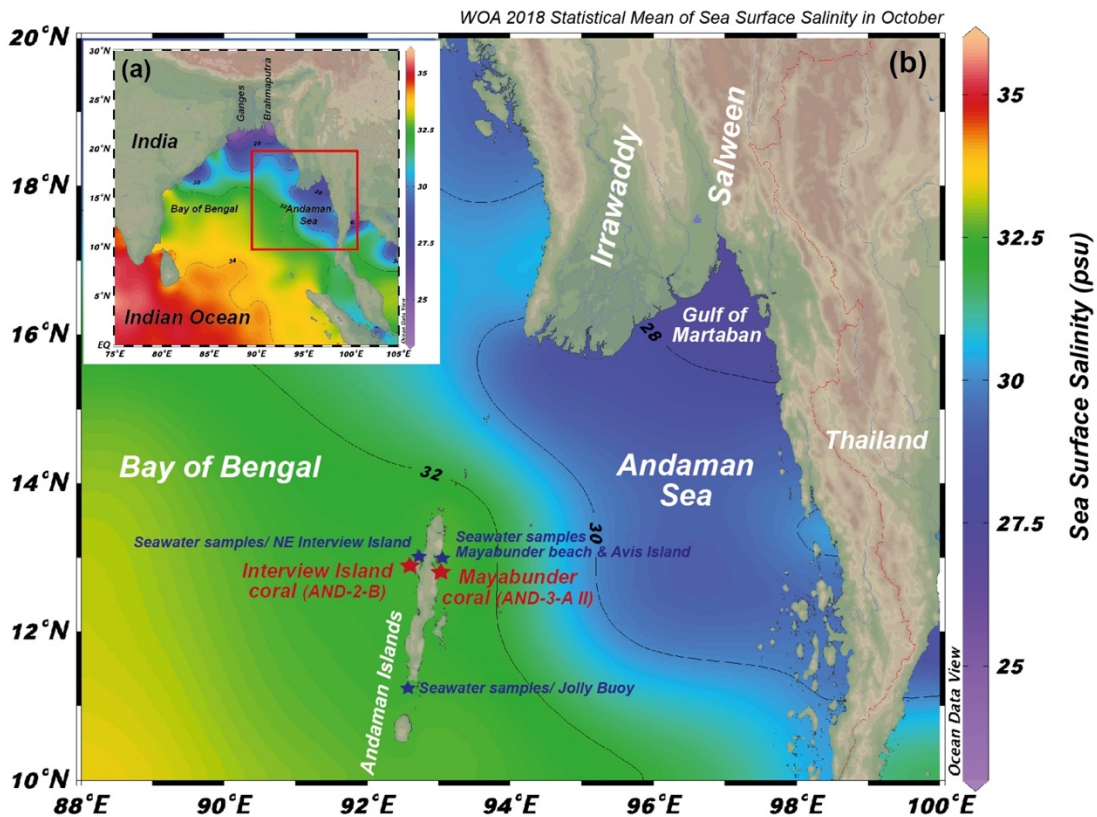


Fig. 5.1: (a) Map of the Bay of Bengal and the Andaman Sea including the major river systems (Ganges-Brahmaputra and Irrawaddy-Salween), which was produced using the Ocean Data View software (Schlitzer, 2009). (b) Two *Porites* coral cores (red stars) were recovered from the Andaman Islands (India): the Interview Island coral (AND-2-B) and the Mayabunder coral (AND-3-A II). Surface seawater samples (blue stars) were collected from the Jolly Buoy, Mayabunder beach, the Avis Island and the NE Interview Island in March, July, and November 2011, and in February and March 2012, and again in March 2013.

The main sources of freshwater runoff and suspended sediment to the AnS are the Irrawaddy and Salween Rivers that have a length of ~2000 and ~2800 km, respectively (Fig. 5.1b, Ramaswamy et al., 2008). The Irrawaddy annual freshwater discharge is $411 \pm 53 \text{ km}^3$ and transports ~350 million tons (MT) of suspended sediments with more than 90% of the freshwater and sediment load delivered during the SAM (Robinson et al., 2007). The annual freshwater flux of the Salween is 211 km^3 , which transports ~200 MT of suspended load (Robinson et al., 2007). Due to the macro-tidal setting, high suspended

sediment concentration is a perennial feature in the Gulf of Martaban and Irrawaddy/Salween continental shelf (Ramaswamy et al., 2008).

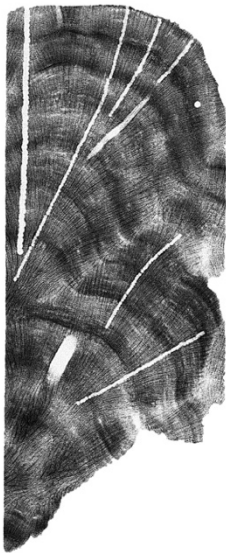
5.2.2 Coral and seawater samples collection and preparation

We recovered cores from two dead coral colonies (*Porites* sp.) at the Andaman Islands (India) in October 2011. One core was drilled from a young fossil coral colony (AND-3-A II) at the beach of Mayabunder on the east coast of the Middle Andaman Island facing the AnS (Fig. 5.1b). The large coral boulder, along with many others, was most likely deposited on the rocky shore during a storm. The second core was drilled from a dead microatoll (AND-2-B) on the west coast of Interview Island facing the open BoB (Fig. 5.1b), which was uplifted and killed as consequence of the Sumatra-Andaman earthquake in December 2004 (Rajendran et al., 2007). These cores were sliced into 3- to 5-mm-thick slabs parallel to the axis of coral growth. Growth rates were 1.0 to 1.6 cm/yr as estimated from X-radiograph images of the slabbed cores (Fig. 5.2), which revealed clear pairs of high- and low- density bands that likely represent annual growth increments (e.g., Felis, 2020). Sub-samples were collected by low-speed drilling using a dental tool with a 1.4-mm-diameter bit in order to obtain a monthly resolution by continuous spot-sampling along a single transect (Fig. 5.2). Sub-sample dissolution was conducted by submerging the coral powder in 18.2 M Ω -cm water (Milli-Q) and adding drops of 1M acetic acid with brief sonication until no bubbles could be observed any more around the aragonite. This method of digestion was chosen to avoid dissolving Ba likely associated with accessory phases like barite, silicates, oxides and organics. Previous studies of Ba/Ca have targeted such phases with aggressive chemical cleaning (e.g., Lea and Boyle, 1989), but our cleaning tests showed this was not necessary and the DTPA and EDTA reagents significantly influenced the stable Ba isotope results. Following centrifugation, the supernatants were transferred into pre-cleaned SavillexTM vials and converted to NO₃⁻ form via concentrated HNO₃ refluxing.

Surface seawater samples were collected from the Jolly Buoy, Avis Island, Mayabunder beach, and NE Interview Island, respectively (Fig. 5.1b). All seawater samples were collected in March, July, and November 2011, and in February and March 2012, and again in March 2013 in pre-cleaned 1-liter PE bottles. Seawater samples were filtered within a few hours of sampling using 0.22 or 0.45 μ m cellulose acetate membranes. The

samples were acidified within 12h of collection with distilled HCl. Field blanks (Milli-Q water) were collected to quantify any potential contamination. Further details of the surface seawater sample collection are given in Hathorne et al. (2020).

(a) Interview Coral



(b) Mayabunder Coral

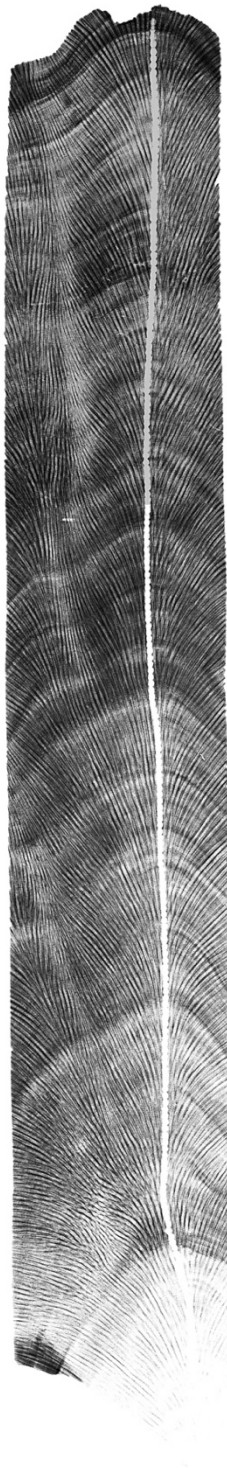


Fig. 5.2: X-radiographs of the (a) Interview Island (AND-2-B) and (b) Mayabunder (AND-3-A II) coral cores. Alternating bands of high (dark colour) and low skeletal density (light colour) are visible. A high-density low-density band pair represents one year.

5.2.3 Geochemical analysis

5.2.3.1 Coral $\delta^{13}\text{C}$ and $\delta^{18}\text{O}$ analysis

Coral skeletal $\delta^{13}\text{C}$ and $\delta^{18}\text{O}$ analysis were performed at GEOMAR using a Finnigan MAT 253 mass spectrometer coupled with a Kiel IV Carbonate device system (Thermo Scientific). Aragonite samples weighing $\sim 200 \mu\text{g}$ were reacted with anhydrous 105% H_3PO_4 under vacuum at 70°C to liberate CO_2 for isotopic analysis. Isotopic compositions are reported in δ notation as per mil deviation from the Vienna Pee Dee Belemnite (VPDB) standard. Calibration to the VPDB scale was performed via the National Bureau of Standards (NBS) 19 and an in-house standard. Analytical precision was better than 0.04% for $\delta^{13}\text{C}$ ($\pm 1\text{SD}$, $N = 62$) and 0.07% for $\delta^{18}\text{O}$ ($\pm 1\text{SD}$, $N = 62$).

5.2.3.2 Trace element analysis

Coral trace element analysis was carried out on an Agilent 7500ce inductively coupled plasma mass spectrometer (ICP-MS) at GEOMAR. Two methods were used to correct the instrumental mass fractionation and matrix effects. The Interview Island coral (AND-2-B) samples were measured using the multi-element isotope dilution (ID) method. This method is based on simultaneous addition of known amounts of four enriched isotope spikes (^{42}Ca , ^{84}Sr , ^{135}Ba and ^{236}U) to a known amount of sample. By measuring the ratios of four pairs of element isotopes in the sample-spike mixture via ICP-MS, the concentration of each element was determined by the classical ID equation:

$$[X]_{sam} = [X]_{spk} \frac{W_{spk}}{W_{sam}} \frac{M_{nat}}{M_{spk}} \frac{A2_{spk}}{A2_{nat}} \frac{\left(\frac{A1_{spk}}{A2_{spk}} - R_{mix} \right)}{\left(R_{mix} - \frac{A1_{nat}}{A2_{nat}} \right)} \quad (5.1)$$

$[X]_{sam}, [X]_{spk}$: sample and spike concentration of a given element.

W_{spk}, W_{sam} : mass in g of the spike and the sample.

M_{nat}, M_{spk} : sample “natural” atomic mass and spike atomic mass.

$A1_{nat}, A2_{nat}, A1_{spk}, A2_{spk}$: natural and spike relative abundances of isotope 1 and 2.

R_{mix} : mass bias corrected measured ratios of isotope1/isotope2 in the sample-spike mixture.

To minimise the sample preparation procedure, single spike solutions were combined into one multi-element spike solution. Each single spike concentration was adjusted to cover the element concentration interval that is commonly encountered in coral samples. The isotopes monitored during this multi-element ID method were ^{42}Ca , ^{43}Ca , ^{84}Sr , ^{87}Sr , ^{135}Ba , ^{138}Ba , ^{233}U , ^{236}U and ^{238}U . Raw intensities were blank corrected and treated offline. The well-characterised JCp-1 coral reference material was analysed as an unknown to assess long-term reproducibility of our results. The mean values of replicate analyses of JCp-1 (1SD, $n = 7$) using this method are 8.84 ± 0.02 mmol/mol for Sr/Ca, 7.29 ± 0.06 $\mu\text{mol/mol}$ for Ba/Ca and 1.19 ± 0.01 $\mu\text{mol/mol}$ for U/Ca, which are within uncertainty of the means of the inter-laboratory consensus values (Hathorne et al., 2013b).

Trace element/Ca ratios in the Mayabunder coral (AND-3-A II) samples were determined using the external standard calibration method. A matrix-matched standard solution was prepared from single-element solutions to achieve known element/Ca ratios (e.g., Sr/Ca, Ba/Ca and U/Ca) similar to the samples and used as an external standard for instrumental mass bias and matrix effects corrections. Measured intensities were blank corrected and normalised to ^{43}Ca before element/Ca ratios were calculated using the technique of Rosenthal et al. (1999). The same solution of the JCp-1 coral reference material was also measured as an unknown to ensure consistency between different methods and sessions. The mean values of replicate analyses of JCp-1 (1SD, $n = 22$) using external standard calibration are 8.80 ± 0.04 mmol/mol for Sr/Ca, 7.25 ± 0.28 $\mu\text{mol/mol}$ for Ba/Ca and 1.20 ± 0.03 $\mu\text{mol/mol}$ for U/Ca, which are within uncertainty of the means of these element/Ca ratios reported above and in Hathorne et al. (2013b).

Surface seawater samples were analysed for dissolved Ba concentration ($[\text{Ba}]_{\text{sw}}$) using isotope dilution. Briefly, aliquots (50 μL) of acidified seawater were accurately weighed and mixed with defined amounts of ^{135}Ba enriched spike to achieve a $^{138}\text{Ba}/^{135}\text{Ba}$ ratio of 0.64. The spike-equilibrated samples were then diluted to 500 μL with 2% (v/v) HNO_3 before $^{138}\text{Ba}/^{135}\text{Ba}$ ratios were measured and mass bias corrected by bracketing analyses of a natural Ba standard solution. Repeated analyses of two GEOTRACES seawater reference materials (SAFe surface and SAFe 1000m) resulted in $[\text{Ba}]_{\text{sw}}$ values of $34.3 \pm$

0.2 nmol/kg (1SD, N = 5) and 99.6 ± 0.2 nmol/kg (1SD, N = 8), respectively, which are within uncertainty of the reported SAFe values in Hsieh and Henderson (2017).

5.2.3.3 Stable Ba isotope analysis

Stable Ba isotope measurements of coral and surface seawater samples were performed with a Thermo Fisher Neptune Plus MC-ICP-MS at GEOMAR. The analyte was introduced as a dry aerosol using an Aridus II desolvator system (CETAC Technologies, Omaha, NE, USA) and ESI PFA micro-concentric nebuliser (uptake rate of ~ 60 $\mu\text{L}/\text{min}$). The ^{130}Ba - ^{135}Ba double spike was added and applied to correct for instrumental mass fractionation as well as potential isotope fractionation during chemical purification (Cao et al., 2020b; Yu et al., 2020). Aliquots of 5 mL seawater samples were spiked, co-precipitated with CaCO_3 (Horner et al., 2015), and the resulting precipitates were centrifuged and dissolved in 2 mL of 1M HCl in preparation for cation-exchange chromatography. Seawater and coral samples were twice passed through cation-exchange columns containing 1.4 mL of Bio-Rad AG 50W-X8 resin. Matrix elements were subsequently eluted with 7.5 mL of 1M HCl and 7.5 mL of 3M HCl. Ba cuts were collected with 10 mL of 2M HNO_3 and dissolved in 2% (v/v) HNO_3 for Ba isotope analysis (Yu et al., 2020). The total procedural Ba blank was on average $< 0.5\%$ of the Ba processed in the samples. Stable Ba isotope measurements were conducted under a matrix tolerance state defined by a high Normalised Ar Index value (NAI, an index of plasma temperature, Fietzke and Frische, 2016; Yu et al., 2020). A three-dimensional data reduction procedure following Siebert et al. (2001) was used, in which an exponential fractionation law was applied to correct for both instrumental and natural mass-dependent isotope fractionation. Ba isotope compositions are reported in per mil (‰) relative to the National Institute of Standards and Technology (NIST) SRM 3014a Ba standard: $\delta^{138}\text{Ba} = ({}^{138}/{}^{134}\text{Ba}_{\text{sample}}/{}^{138}/{}^{134}\text{Ba}_{\text{NIST}} - 1)$.

Repeated analyses of coral reference material JCp-1 yielded a $\delta^{138}\text{Ba}$ value of $+0.28 \pm 0.03\%$ (2SD, N = 22), which agrees well with reported value of $+0.29 \pm 0.03\%$ (Horner et al., 2015), $+0.26 \pm 0.10\%$ (Pretet et al., 2015), $+0.26 \pm 0.03\%$ (Hemsing et al., 2018) and $+0.28 \pm 0.04\%$ (Zeng et al., 2019). Repeated measurements of GEOTRACES seawater reference sample SAFe (surface) yielded a $\delta^{138}\text{Ba}$ value of $+0.61 \pm 0.04\%$ (2SD, N = 4), which is consistent with the reported value of $+0.62 \pm 0.02\%$ (Hsieh and

Henderson, 2017), $+0.63 \pm 0.04\text{‰}$ (Geyman et al., 2019), $+0.64 \pm 0.08\text{‰}$ (Cao et al., 2020b) and $+0.62 \pm 0.04\text{‰}$ (Cao et al., 2020a). Repeated measurements of GEOTRACES seawater reference sample SAFe (1000 m) yielded a $\delta^{138}\text{Ba}$ value of $+0.29 \pm 0.04\text{‰}$ (2SD, $N = 12$), which is consistent with the reported value of $+0.27 \pm 0.02\text{‰}$ (Hsieh and Henderson, 2017), $+0.32 \pm 0.03\text{‰}$ (Geyman et al., 2019), $+0.29 \pm 0.02\text{‰}$ (Cao et al., 2020b) and $+0.28 \pm 0.09\text{‰}$ (Cao et al., 2020a). The uncertainty is reported as the larger of either the internal 2SE of repeated sample measurements or the long-term 2SD, which in this study was $\pm 0.03\text{‰}$ for coral samples and $\pm 0.04\text{‰}$ for seawater samples.

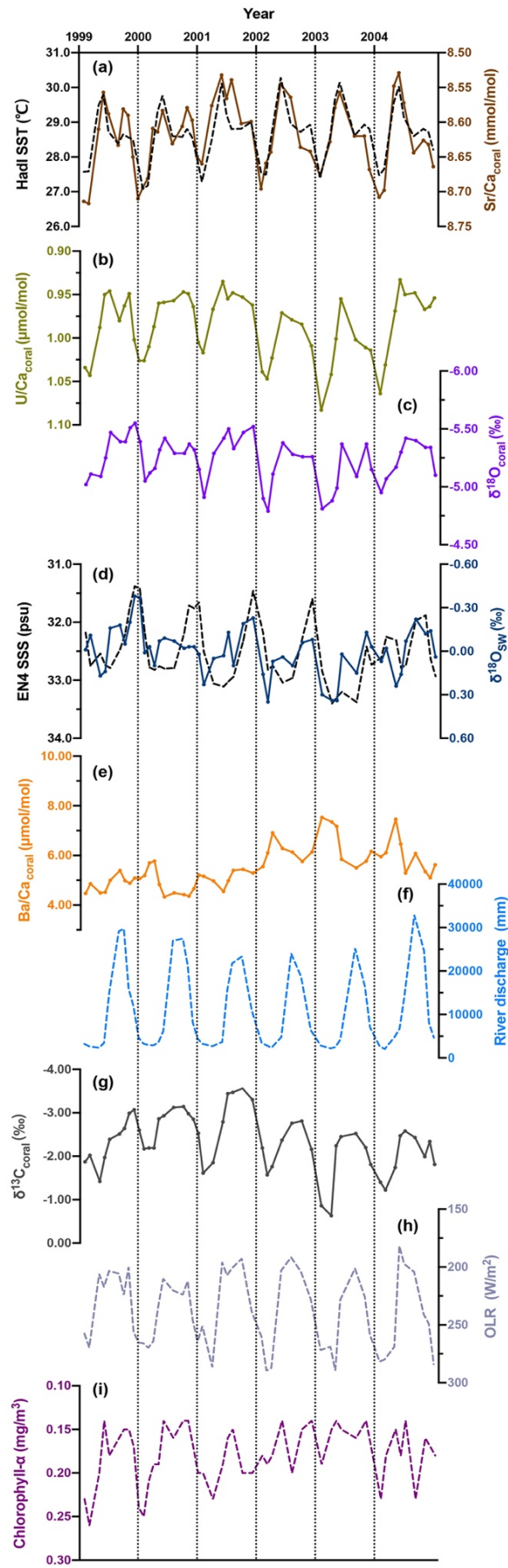
5.2.4 Coral age model

The chronology of the Interview Island coral (AND-2-B) was constructed by counting annual density band pairs visible in the X-radiograph backwards (Fig. 5.2) from the year of coral death (December 2004, Sumatra-Andaman earthquake and tsunami) with subsequent refinement by adjusting the clear annual cycles in the skeletal $\text{Sr}/\text{Ca}_{\text{coral}}$ SST proxy data to monthly Hadley Centre Global Sea Ice and Sea Surface Temperature (HadISST, Rayner et al., 2003) for the 1-degree latitude-longitude grid that includes Interview Island. The seasonal maxima and minima in the $\text{Sr}/\text{Ca}_{\text{coral}}$ data were tied to the corresponding seasonal extreme values in the monthly record of HadISST (Fig. 5.3a). This combined method produced an age model for the Interview Island coral extending from 2004 back to 1999, and followed common procedures for the establishment of chronologies for modern annually-banded corals (e.g., Felis et al., 2018, 2009).

Fig. 5.3 → *page down*: **Monthly resolved geochemical data for the Interview Island coral (AND-2-B, India) and environmental parameters.**

(a) $\text{Sr}/\text{Ca}_{\text{coral}}$ vs. the U.K. Meteorological Office Hadley Centre Global Sea Ice and Sea Surface Temperature (HadISST, Rayner et al., 2003);

(b) $\text{U}/\text{Ca}_{\text{coral}}$; (c) $\delta^{18}\text{O}_{\text{coral}}$; (d) coral $\delta^{18}\text{O}_{\text{sw}}$ vs. the U.K. Meteorological Office EN4 database (Good et al., 2013); (e) $\text{Ba}/\text{Ca}_{\text{coral}}$; (f) river discharge of the Irrawaddy River (<http://grdc.bafg.de>); (g) $\delta^{13}\text{C}_{\text{coral}}$; (h) satellite-based outgoing longwave radiation (OLR, Liebmann and Smith, 1996); (i) Chlorophyll- α concentrations.



The age of the fossil coral from Mayabunder (AND-3-A II) was obtained by radiocarbon dating at the Poznań Radiocarbon Laboratory (Poland). An accelerator mass spectrometry (AMS) ^{14}C age of 505 ± 30 yr before present (BP) was determined on coral sample AND-3-A II / D1 (Poz-70614). The ^{14}C age was converted to calendar age using the CALIB 8.2 radiocarbon calibration program (Stuiver et al., 2020) and the Marine20 marine radiocarbon age calibration curve (Heaton et al., 2020), yielding a median probability age of calibrated yr AD 1771 (1σ range: cal. yr AD 1675 - 1889). This suggests that the Mayerbunder coral grew prior to the 19th century. A weighted mean ΔR value of -211.0 ± 86.0 yr was used to correct for regional differences in reservoir age, based on regional data ($n = 8$) from the Marine Reservoir Correction Database. The internal chronology of the Mayabunder coral was constructed by combining the annual density banding pattern (Fig. 5.2) and the annual cycles in geochemical proxies. Because annual cycles in the $\text{Sr}/\text{Ca}_{\text{coral}}$ SST proxy record are less pronounced compared to the Interview Island coral, the identification of annual cycles and seasonal extreme values was further supported by the corresponding $\text{U}/\text{Ca}_{\text{coral}}$, $\delta^{18}\text{O}_{\text{coral}}$ and $\delta^{13}\text{C}_{\text{coral}}$ records. Seasonal $\text{Sr}/\text{Ca}_{\text{coral}}$ values identified in this way were tied to the average seasonal maxima and minima values observed in the monthly mean record of HadISST, similar to the chronology construction for the Interview Island coral. This combined method produced an internal chronology for the Mayabunder coral over a 19-year time window, and followed common procedures for the establishment of chronologies for fossil annually-banded corals with absolute radiometrically derived ages (e.g., Felis et al., 2015, 2004). Finally, the $\text{Sr}/\text{Ca}_{\text{coral}}$ time series and corresponding proxy data of the two corals from Interview Island and Mayabunder were linearly interpolated and tuned to a monthly resolution using the AnalySeries software package (Paillard et al., 1996).

5.2.5 Methodology of seawater $\delta^{18}\text{O}$ ($\delta^{18}\text{O}_{\text{SW}}$) reconstruction

$\delta^{18}\text{O}_{\text{SW}}$ was calculated by removing the SST component from paired $\delta^{18}\text{O}_{\text{coral}}$ and $\text{Sr}/\text{Ca}_{\text{coral}}$ measurements following the method of Cahyarini et al. (2008):

$$\delta^{18}\text{O}_{\text{SW}} = \left(\delta^{18}\text{O}_{\text{coral}} - \overline{\delta^{18}\text{O}_{\text{coral}}} \right) - \gamma / \beta \left(\text{Sr} / \text{Ca}_{\text{coral}} - \overline{\text{Sr} / \text{Ca}_{\text{coral}}} \right) \quad (5.2)$$

where $\delta^{18}\text{O}_{\text{coral}}$ is the measured coral $\delta^{18}\text{O}$, $\overline{\delta^{18}\text{O}_{\text{coral}}}$ is the mean value of measured coral $\delta^{18}\text{O}$, $\text{Sr}/\text{Ca}_{\text{coral}}$ is the measured coral Sr/Ca, $\overline{\text{Sr}/\text{Ca}_{\text{coral}}}$ is the mean value of measured coral Sr/Ca, γ is the regression slope of Interview Island $\delta^{18}\text{O}_{\text{coral}}$ versus HadISST, and β is the regression slope of Interview Island Sr/Ca_{coral} versus HadISST.

5.2.6 Environmental data sources and statistical analysis

For the period from January 1999 to December 2004, instrumental monthly SST data were obtained from the U.K. Meteorological Office Hadley Centre Global Sea Ice and Sea Surface Temperature (HadISST, Rayner et al., 2003). Instrumental monthly SSS data were obtained from the U.K. Meteorological Office EN4 database (Good et al., 2013). Monthly Chlorophyll- α concentrations (mg/m^3) were acquired from the Level 3 (monthly, 9 km resolution) Sea-Viewing Wide Field-of-View Sensor (SeaWiFS) via the NASA Goddard Earth Sciences Data and Information Services Center (GES DISC) Interactive On-line Visualization and ANalysis Infrastructure (GIOVANNI) web interface. Observed monthly rainfall data were obtained from the Department of Meteorology and Hydrology of Myanmar for 35 stations spanning the period of time from 1999 to 2004. Observed monthly river discharge data of the Irrawaddy over the time period of 1999-2004 were obtained from the Global Runoff Data Centre (<http://grdc.bafg.de>). Monthly satellite-based outgoing longwave radiation (OLR) data, a proxy for atmospheric convection/rainfall, were obtained from the National Oceanic and Atmospheric Administration (NOAA) Interpolated OLR dataset (Liebmann and Smith, 1996). Correlations of coral geochemical records with environmental drivers were determined using Pearson correlation analysis.

5.3 Results

5.3.1 Interview Island coral (AND-2-B) time series

The monthly Interview Island modern coral skeletal Sr/Ca, U/Ca, Ba/Ca, $\delta^{18}\text{O}$ and $\delta^{13}\text{C}$ records as well as the reconstructed $\delta^{18}\text{O}_{\text{sw}}$ are shown in Fig. 5.3. Because instrumental records of environmental data are available for the period from 1999 to 2004 for the

sampling site, we can make direct comparisons between coral geochemical proxies and instrumental records.

The Sr/Ca_{coral} record of SST exhibits well-defined cyclic fluctuations on a seasonal timescale and agrees well with the HadISST data set over the time period between 1999 and 2004 (Fig. 5.3a). The performance of the Sr/Ca_{coral} record in capturing the semiannual cycle in regional SST with its pronounced warming peak during spring and its second, less pronounced warming peak in fall, is remarkable. Regression analysis reveals a significant and strong correlation ($R^2 = 0.72$, $p < 0.05$) between Sr/Ca_{coral} and HadISST (Fig. 5.4a). The Sr/Ca_{coral}-SST slope (-0.05 mmol/mol per 1°C) is consistent with reported estimates that range from -0.04 to -0.08 mmol/mol per 1°C (Corrège, 2006). The U/Ca_{coral} data displays similarly pronounced seasonal variations that also correlate well with HadISST as well as with the Sr/Ca_{coral} time series with the exception of the uppermost portion of the coral head that shows anomalously lower U/Ca_{coral} ratios (Fig. 5.3b). A linear regression of U/Ca_{coral} versus HadISST for the time period 1999-2004 shows a moderate but significant correlation ($R^2 = 0.48$, $p < 0.05$) and yields a slope value of -0.03 $\mu\text{mol/mol}$ per 1°C (Fig. 5.4b), which is consistent with reported values (Felis et al., 2009). Ba/Ca_{coral} data show less pronounced cyclic patterns with more frequent peaks that occurred during the pre-SAM period (Fig. 5.3e). There is no clear correlation between Ba/Ca_{coral} and river discharge of the Irrawaddy (Fig. 5.4c, $p > 0.05$) and HadISST (Fig. 5.4d, $p > 0.05$), which suggests that factors other than river discharge and SST have been involved in driving the Ba/Ca_{coral} seasonality. The $\delta^{13}\text{C}_{\text{coral}}$ data clearly exhibit distinct seasonal cycles with broad $\delta^{13}\text{C}_{\text{coral}}$ -depleted peaks during the SAM (Fig. 5.3g). Regression analysis reveals a moderate and significant correlation ($R^2 = 0.37$, $p < 0.05$) between $\delta^{13}\text{C}_{\text{coral}}$ and the OLR (Fig. 5.4e), which can be explained by decreased availability of light for photosynthesis of the coral's endosymbiotic algae during the cloudy SAM season (e.g., Felis et al., 1998). In addition, a weak but significant ($R^2 = 0.27$, $p < 0.05$) linear correlation is found between $\delta^{13}\text{C}_{\text{coral}}$ and Ba/Ca_{coral} (Fig. 5.4f), suggesting that a common factor may have been involved in controlling these two proxies during growth of the coral skeleton. The $\delta^{18}\text{O}_{\text{coral}}$ variations exhibit a clear seasonal cycle (Fig. 5.3c) and are significantly ($p < 0.05$), but not strongly ($R^2 = 0.30$), correlated with HadISST (Fig. 5.4g). A linear regression of $\delta^{18}\text{O}_{\text{coral}}$ and HadISST yields a slope value of -0.13‰ per 1°C , which is slightly lower than reported relationships between -0.15‰ and -0.23‰ per 1°C (Corrège, 2006; Gagan et al., 2000).

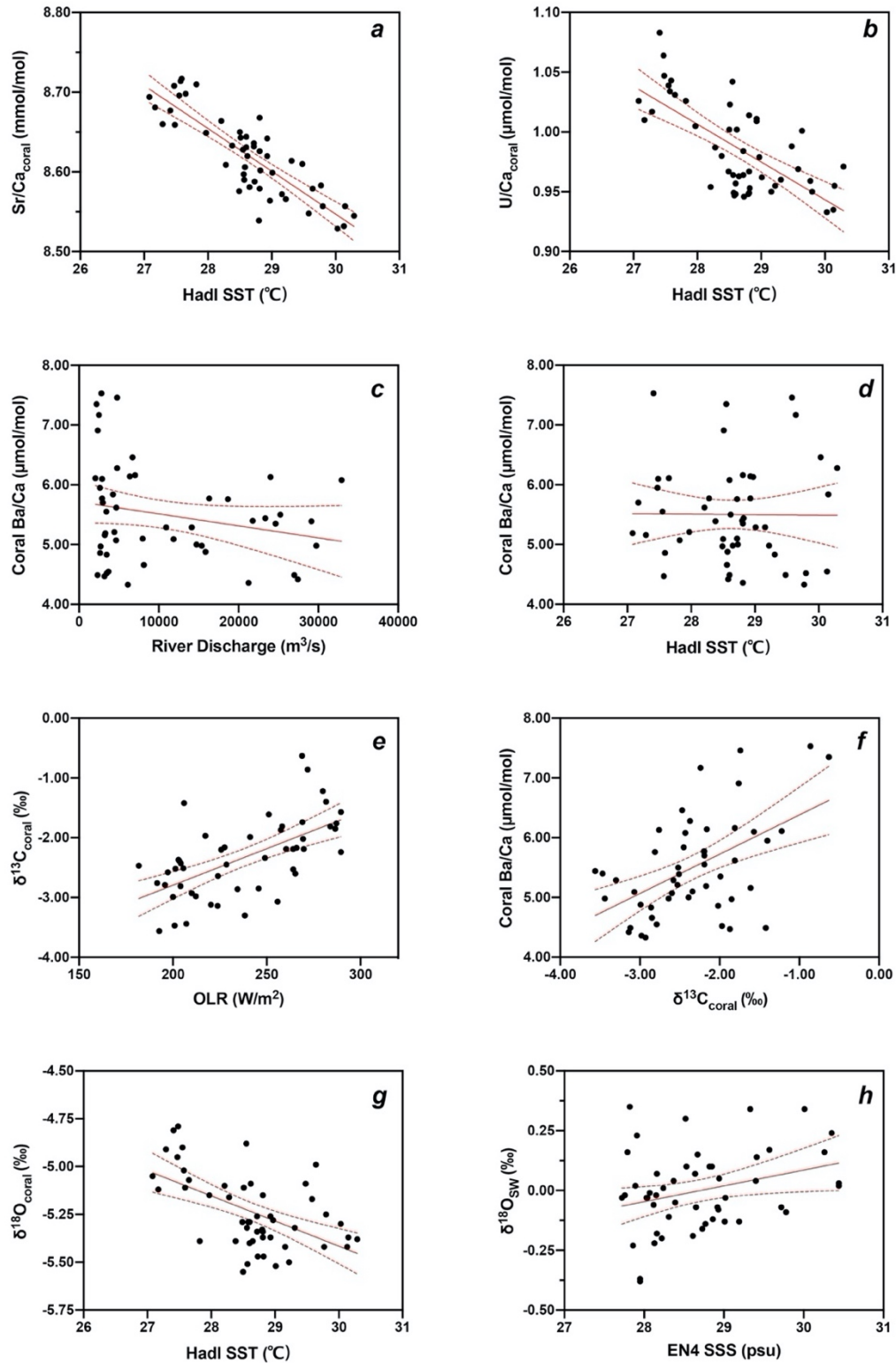


Fig. 5.4: The relationships of (a) Sr/Ca_{coral} versus HadISST; (b) U/Ca_{coral} versus HadISST; (c) Ba/Ca_{coral} versus river discharge; (d) Ba/Ca_{coral} versus HadISST; (e) δ¹³C_{coral} versus OLR; (f) Ba/Ca_{coral} versus δ¹³C_{coral}; (g) δ¹⁸O_{coral} versus HadISST; (h) δ¹⁸O_{SW} versus EN4 SSS for Interview Island coral (AND-2-B).

Importantly, this Interview Island coral $\delta^{18}\text{O}_{\text{coral}}$ pattern is consistent with previously reported $\delta^{18}\text{O}_{\text{coral}}$ data during the same period (1999 – 2004) from a coral colony (*Porites* sp.) growing south of Port Blair, about 100 km south from our sampling site (Fig. 5.5, Rixen et al., 2011). The Sr/Ca_{coral}-based $\delta^{18}\text{O}_{\text{SW}}$ reconstructions show an obvious seasonal cyclicality and a weak but significant ($R^2 = 0.09$, $p < 0.05$) correlation with EN4 SSS (Fig. 5.4h). The shift toward more depleted $\delta^{18}\text{O}_{\text{SW}}$ values occurred during the onset of the SAM, with the exception of the year of 2000 (Fig. 5.3d). The timing of these $\delta^{18}\text{O}_{\text{SW}}$ shifts clearly coincides with decreases of the EN4 SSS values (Fig. 5.3d).

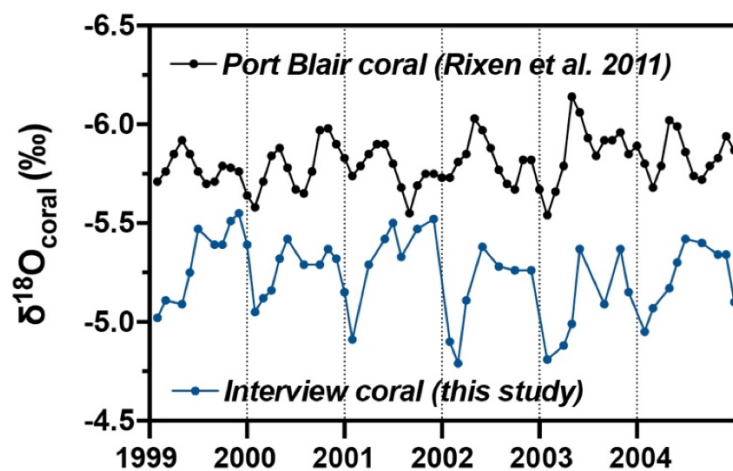


Fig. 5.5: A comparison between our measured $\delta^{18}\text{O}_{\text{coral}}$ values from Interview Island coral (AND-2-B, black points) and previously reported $\delta^{18}\text{O}_{\text{coral}}$ data (blue points) during the same period (1999 – 2004) from a coral colony (*Porites* spp.) growing south of Port Blair, about 100 km south from our sampling site (Rixen et al., 2011)

5.3.2 Mayabunder coral (AND-3-A II) time series

The monthly Mayabunder fossil coral skeletal Sr/Ca, U/Ca, Ba/Ca, $\delta^{18}\text{O}$ and $\delta^{13}\text{C}$ records as well as the reconstructed $\delta^{18}\text{O}_{\text{SW}}$ are shown in Fig. 5.6. In addition, a two-year record of coral skeletal Ba isotope compositions ($\delta^{138}\text{Ba}_{\text{coral}}$) is plotted with Ba/Ca_{coral} as well as other proxies in Fig. 5.6 and Fig. 5.7.

Time series data for $\delta^{138}\text{Ba}_{\text{coral}}$ (Fig. 5.7a) show pronounced seasonal cyclicality over a continuous two-year record within a narrow range from $+0.16 \pm 0.03\text{‰}$ (2SD) to $+0.27 \pm 0.03\text{‰}$ (2SD). $\delta^{138}\text{Ba}_{\text{coral}}$ values are generally lighter during the SAM (June-September)

characterised by enhanced rainfall and river discharge and the post-SAM season (October-January). The Ba/Ca_{coral} variability generally follows the seasonal cycles displayed by coral $\delta^{138}Ba_{\text{coral}}$ values, with higher Ba/Ca_{coral} ratios accompanying lower $\delta^{138}Ba_{\text{coral}}$ values (Fig. 5.7b). In addition to the light $\delta^{138}Ba_{\text{coral}}$ and higher Ba/Ca_{coral} values during the SAM, light $\delta^{138}Ba_{\text{coral}}$ values are also observed during the pre-SAM and are associated with sharp Ba/Ca_{coral} spikes (Figs. 5.7a & b). Sr/Ca_{coral} and U/Ca_{coral} time series all display synchronous and clearly bimodal seasonal cycles over the 19 years of coral growth, with two peaks in March-May and October-November associated with higher SST, respectively (Figs. 5.6c & d). Similarly, the seasonal variations of $\delta^{18}O_{\text{coral}}$ are also characterised by a bimodal pattern, with two peaks in May-June and October-December, respectively (Fig. 5.6e). In contrast, the reconstructed $\delta^{18}O_{\text{sw}}$ peaks typically occurred in the latter half of each year from July to January (Fig. 5.6f). Lastly, seasonal variations of $\delta^{13}C_{\text{coral}}$ are clearly evident and peak negative values mainly occur during the SAM period (Fig. 5.6g).

5.3.3 Surface seawater Ba concentrations ($[Ba]_{\text{sw}}$) and isotope compositions ($\delta^{138}Ba_{\text{sw}}$)

Surface seawater collected around the Andaman Island (Fig. 5.1b) in March, July, and November 2011, and in February and March 2012, and again in March 2013 displays a range of $[Ba]_{\text{sw}}$ values with a maximum value of 66.03 nmol/kg in July 2011 and a minimum value of 51.93 nmol/kg in March 2013. A relatively wide range of $\delta^{138}Ba_{\text{sw}}$ values between +0.29‰ and +0.49‰ are also encountered in these samples and they show a clear correlation with seawater Ba concentrations (Fig. 5.10a). The average $\delta^{138}Ba_{\text{sw}}$ values are +0.46‰ during the pre-SAM period (March 2011, February and March 2012 and March 2013), +0.29‰ during the SAM (July 2011), and +0.41‰ during the post-SAM period (November 2011), respectively (Fig. 5.10b).

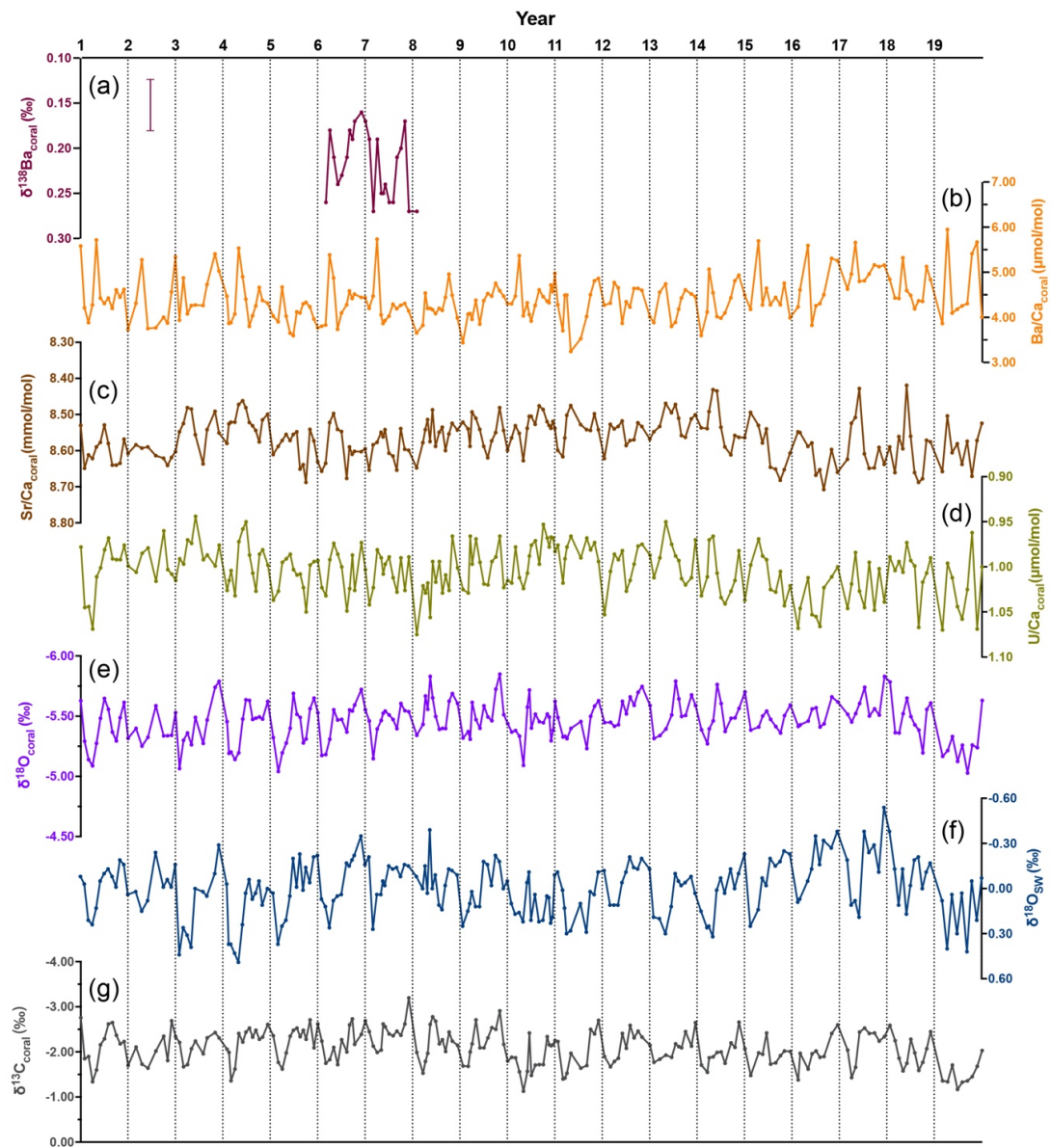


Fig. 5.6: Monthly resolved geochemical time series data for the Mayabunder coral (AND-3-A II, India).

- (a) $\delta^{138}\text{Ba}_{\text{coral}}$, error bar $\pm 2\text{SD}$ analytical uncertainty for JCp-1;**
- (b) $\text{Ba}/\text{Ca}_{\text{coral}}$;**
- (c) $\text{Sr}/\text{Ca}_{\text{coral}}$;**
- (d) $\text{U}/\text{Ca}_{\text{coral}}$;**
- (e) $\delta^{18}\text{O}_{\text{coral}}$;**
- (f) $\text{Sr}/\text{Ca}_{\text{coral}}$ - and $\delta^{18}\text{O}_{\text{coral}}$ -reconstructed $\delta^{18}\text{O}_{\text{sw}}$;**
- (g) $\delta^{13}\text{C}_{\text{coral}}$.**

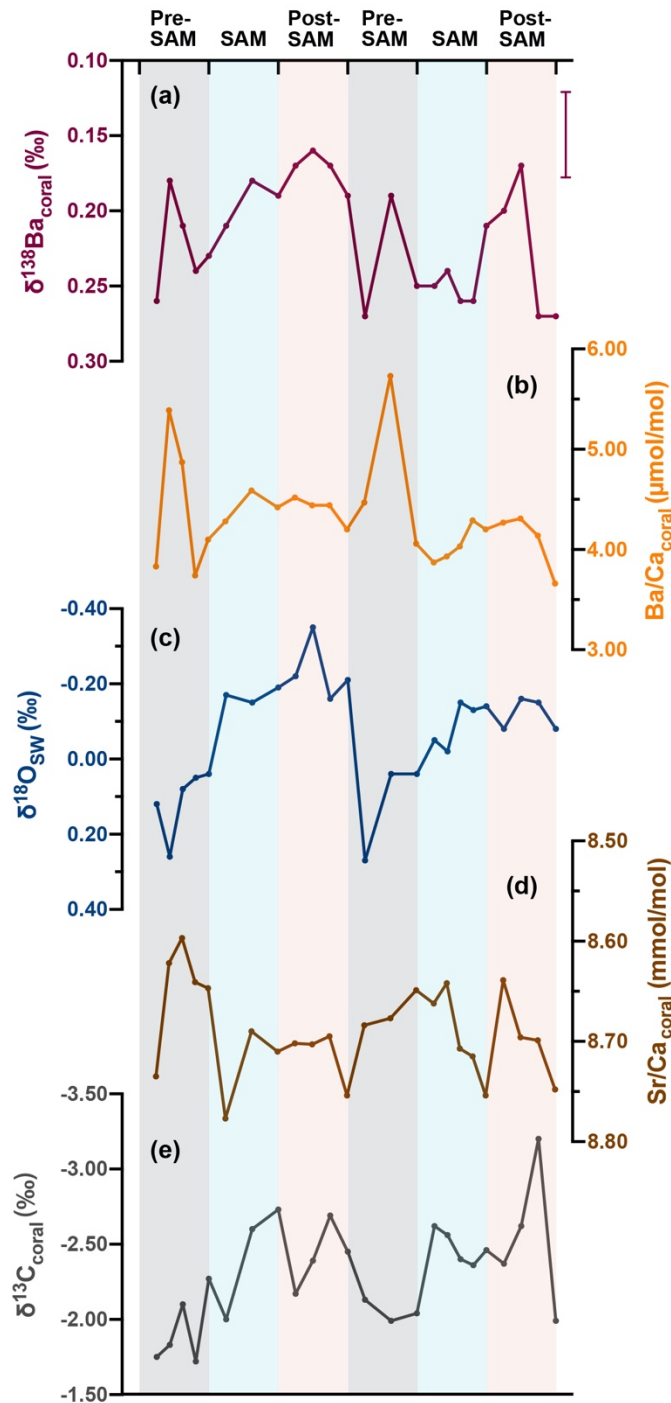


Fig. 5.7: A continuous two-year geochemical record of the Mayabunder coral (AND-3-A II, India).

(a) $\delta^{138}\text{Ba}_{\text{coral}}$, error bar $\pm 2\text{SD}$ analytical uncertainty for JCp-1;

(b) $\text{Ba}/\text{Ca}_{\text{coral}}$;

(c) $\text{Sr}/\text{Ca}_{\text{coral}}$ - and $\delta^{18}\text{O}_{\text{coral}}$ -reconstructed $\delta^{18}\text{O}_{\text{sw}}$;

(d) $\text{Sr}/\text{Ca}_{\text{coral}}$;

(e) $\delta^{13}\text{C}_{\text{coral}}$.

The grey, blue and red shaded bars mark the period of pre-SAM, SAM and post-SAM, respectively.

5.4 Discussion

5.4.1 Monthly variations in $\delta^{18}\text{O}_{\text{SW}}$ and palaeosalinity estimates

The $\delta^{18}\text{O}$ signatures of surface seawater ($\delta^{18}\text{O}_{\text{SW}}$) and their relation to sea surface salinity (SSS) are driven by several processes including evaporation, precipitation, river runoff and internal ocean dynamics such as circulation and upwelling (e.g. Rao and Sivakumar, 2003). Specifically, $\delta^{18}\text{O}_{\text{SW}}$ and SSS both increase with evaporation and decrease with higher precipitation and/or freshwater input and vary by mixing due to lateral advection of water masses and/or upwelling. Given the scarcity of long time series of SSS variations in the AnS, our Sr/Ca_{coral}- and $\delta^{18}\text{O}_{\text{coral}}$ -based $\delta^{18}\text{O}_{\text{SW}}$ reconstructions from two corals present a unique opportunity to evaluate the relationship between $\delta^{18}\text{O}_{\text{SW}}$ and SSS as well as variations in riverine inputs.

Our modern Interview Island Sr/Ca_{coral}- and $\delta^{18}\text{O}_{\text{coral}}$ -based $\delta^{18}\text{O}_{\text{SW}}$ reconstructions show clear shifts towards more depleted values at the onset of the SAM, which is broadly consistent with the EN4 SSS record (Fig. 5.3d). Similar temporal variations of reconstructed $\delta^{18}\text{O}_{\text{SW}}$ are also observed in the Mayabunder fossil coral record that displays clear reductions in $\delta^{18}\text{O}_{\text{SW}}$ values from June to January (Fig. 5.6f). The more depleted $\delta^{18}\text{O}_{\text{SW}}$ values and associated low salinity during the SAM (June-September) reflect enhanced freshwater input from monsoon rainfall, which also coincides with excess precipitation over evaporation (e.g. Rao and Sivakumar, 2003). The less depleted $\delta^{18}\text{O}_{\text{SW}}$ values and associated high salinity during the pre-SAM period are likely a consequence of the dominant effect of evaporation over all other processes. In the months following the SAM (October-January), the more depleted $\delta^{18}\text{O}_{\text{SW}}$ values are still sustained in both coral records (Figs. 5.3d & 5.6f). We suggest that lateral advection of low-salinity surface water accounts for these extended freshening events. In line with our findings, earlier mooring observations in the AnS also demonstrate that the SSS experiences a strong decreasing trend from July to January as a result of high runoff and its redistribution by the basin-scale circulation (Ashin et al., 2019; Sree Lekha et al., 2018). Overall, the signatures of the prominently depleted $\delta^{18}\text{O}_{\text{SW}}$ values and associated low salinity persist for several months from June to January, which can be attributed to the freshwater input originating from summer monsoon rainfall as well as the subsequent basin-scale lateral advection of these fresh waters. The good agreement in the patterns of

$\delta^{18}\text{O}_{\text{SW}}$ variations between two reconstructed $\delta^{18}\text{O}_{\text{SW}}$ and the EN4 SSS records lends support to the notion that coupled measurements of SST proxies (e.g., $\text{Sr}/\text{Ca}_{\text{coral}}$) and $\delta^{18}\text{O}_{\text{coral}}$ can be used to reconstruct high-resolution temporal variations in SSS in this region.

5.4.2 $\delta^{138}\text{Ba}_{\text{coral}}$ as a novel proxy for riverine inputs

The measured $\delta^{138}\text{Ba}_{\text{coral}}$ and $\text{Ba}/\text{Ca}_{\text{coral}}$ values of the Mayabunder fossil coral (AND-3-A II) display synchronous and bimodal seasonal cyclicality in a continuous two-year record including a relatively sharp $\text{Ba}/\text{Ca}_{\text{coral}}$ peak accompanied by lighter $\delta^{138}\text{Ba}_{\text{coral}}$ values during the pre-SAM period, a minimum at the beginning of the SAM and a broader peak developing during the SAM followed by a plateau that continues into post-SAM times (Figs. 5.7a & b).

5.4.2.1 SAM seasons (June-September)

Ba rapidly desorbs from suspended sediment in low-salinity estuarine environments and is advected with the river plumes into coastal regions, where it is incorporated into coral skeletons as a function of $[\text{Ba}]_{\text{SW}}$ (Hanor and Chan, 1977; McCulloch et al., 2003). In the absence of data for seasonal variations in river runoff, the reconstructed $\delta^{18}\text{O}_{\text{SW}}$ signal has been adopted as a runoff proxy in agreement with the strong correlation between $\delta^{18}\text{O}_{\text{SW}}$ and SSS shown above. In addition, $\delta^{13}\text{C}$ -depleted riverine dissolved inorganic carbon (DIC) carried by runoff can reduce the carbon isotopic composition of seawater (Sackett et al., 1997). More depleted $\delta^{13}\text{C}_{\text{coral}}$ values are observed during the SAM along with more negative $\delta^{18}\text{O}_{\text{SW}}$ signatures (Figs. 5.7c & e). A previous study conducted by Rixen et al. (2011) in the south Andaman Islands (India) also suggested that the monthly resolved coral $\delta^{13}\text{C}$ records reveal a strong seasonality, which seems to be caused by the SAM-driven runoff. Although we cannot rule out additional influence of metabolic effects on the depleted $\delta^{13}\text{C}_{\text{coral}}$ signatures (Felis et al., 1998; McConnaughey et al., 1997; Swart et al., 1996), overall a distinct runoff signal is observed during the SAM seasons. Our results clearly show that both broad peaks of the $\delta^{138}\text{Ba}_{\text{coral}}$ and $\text{Ba}/\text{Ca}_{\text{coral}}$ annual cycle correspond to more depleted $\delta^{18}\text{O}_{\text{SW}}$ values (Fig. 5.7) supporting the hypothesis that $\delta^{138}\text{Ba}_{\text{coral}}$ and $\text{Ba}/\text{Ca}_{\text{coral}}$ are largely affected by river runoff during the SAM seasons.

5.4.2.2 Post-SAM seasons (October-January)

In the first year of our record, $\delta^{138}\text{Ba}_{\text{coral}}$ ($\text{Ba}/\text{Ca}_{\text{coral}}$) clearly show a tendency to decrease (increase) with the onset of summer monsoon and are followed by a plateau that persists for several months, which suggests an additional flux of Ba (Fig. 5.7a & b). Similarly, extended periods of elevated $\text{Ba}/\text{Ca}_{\text{coral}}$ signatures have been observed previously in different regions (e.g., Alibert et al., 2003; Chen et al., 2020; Moyer et al., 2012). Alibert et al. (2003) proposed that increased precipitation and a consequently larger volume of freshwater could serve to dilute the limited supply of Ba in rivers originating from weathering. Under such conditions, $\text{Ba}/\text{Ca}_{\text{coral}}$ may be more representative of cumulative rather than instantaneous river discharge and associated terrestrial Ba fluxes. However, the covariation of $\delta^{138}\text{Ba}_{\text{coral}}$, $\text{Ba}/\text{Ca}_{\text{coral}}$, and $\delta^{18}\text{O}_{\text{SW}}$ (SSS) suggests that such dilution effects cannot explain the periods of Ba tailings observed in our studies (Fig. 5.7).

Another possible mechanism proposed by Moyer et al. (2012) is the desorption of Ba from estuarine and/or floodplain-stored sediment. In this region, Ba may desorb from floodplain-stored sediment along the Myanmar continental shelves and be advected seaward (Carroll et al., 1993). In response to the prevailing north-easterly winds during winter monsoon, the surface currents in the AnS can transport this newly desorbed Ba as well as freshwater plumes south-westward towards our coral sampling sites. In support of this mechanism the temporal evolution of SSS ($\delta^{18}\text{O}_{\text{SW}}$) shows reasonably good agreement with the variations in wind-induced horizontal advection (Fig. 5.7c).

In addition, the discrepancies in $\text{Ba}/\text{Ca}_{\text{coral}}$ signatures from Interview Island and Mayabunder are noteworthy. The coral from Interview Island shows less clear $\text{Ba}/\text{Ca}_{\text{coral}}$ peaks during post-SAM periods (Fig. 5.3e & 5.6b). We propose that the more distal location of the Interview Island from the sediment Ba source on the floodplains of the Myanmar continental shelves, facing the open BoB to the west, is likely the main reason for the observed $\text{Ba}/\text{Ca}_{\text{coral}}$ discrepancies (Fig. 5.1b). This observation further highlights the significance of the floodplain-stored Ba supply by the westward propagating surface currents in the AnS. Therefore, we suggest that the floodplain-stored sediment Ba desorption from the Myanmar continental shelves, together with lateral advection, most likely contributes to the sustained light $\delta^{138}\text{Ba}_{\text{coral}}$ and elevated $\text{Ba}/\text{Ca}_{\text{coral}}$ values that continue for several months after the summer monsoon.

5.4.2.3 Pre-SAM seasons (February - May)

During pre-SAM seasons, the $\delta^{138}\text{Ba}_{\text{coral}}$ sharply decreases in March and rises in May of each year (Fig. 5.7a). The $\text{Ba}/\text{Ca}_{\text{coral}}$ appear to follow the seasonal cycles displayed by the $\delta^{138}\text{Ba}_{\text{coral}}$ values, with the highest $\text{Ba}/\text{Ca}_{\text{coral}}$ ratios accompanying the lowest $\delta^{138}\text{Ba}_{\text{coral}}$ values (Fig. 5.7b). A comparison between the pattern of $\delta^{138}\text{Ba}_{\text{coral}}$, $\text{Ba}/\text{Ca}_{\text{coral}}$ and $\delta^{18}\text{O}_{\text{SW}}$ shows that coral skeletal Ba proxies appear to be decoupled from peak river discharge given the reconstructed $\delta^{18}\text{O}_{\text{SW}}$ (SSS) values are less depleted (high) during pre-SAM (Fig. 5.7c). This indicates that factors aside from riverine inputs are driving the unexpected light $\delta^{138}\text{Ba}_{\text{coral}}$ and elevated $\text{Ba}/\text{Ca}_{\text{coral}}$ spikes during the pre-SAM periods. The $\text{Ba}/\text{Ca}_{\text{coral}}$ spikes occur consistently during the same season over the entire 19-year record (Fig. 5.6b), which implies that these Ba spikes are caused by a seasonal environmental driver. Similar episodic and sharp $\text{Ba}/\text{Ca}_{\text{coral}}$ spikes have been reported during dry seasons in other studies (e.g., Moyer et al., 2012; Sinclair, 2005), and a number of possibilities have been proposed as potential causes: (1) Ba enrichment associated with enhanced coastal upwelling, (2) Ba solubilization in association with reductive dissolution of Fe-Mn oxides/(oxy)hydroxides, (3) barite formation in association with phytoplankton blooms and the resulting decaying organic matter, (4) Ba release associated with the fringing mangrove sediments. These possible mechanisms are discussed below.

(1) In the AnS, the vertical salinity structure is characterised by the presence of relatively fresh surface waters above more saline waters of the subsurface layer, which results in the persistent occurrence of strong stratification in the near-surface layer similar to the BoB (Ashin et al., 2019; Rao and Sivakumar, 2003; Sprintall and Tomczak, 1992). In addition, recent observations suggest that the wind speed regime in the AnS is weaker during pre-SAM seasons (Ashin et al., 2019; Sree Lekha et al., 2018). The consistent presence of a halocline along with low wind speeds consequently provide unfavourable conditions for coastal upwelling in the AnS during pre-SAM seasons and can thus be ruled out as the cause for the observed Ba spikes.

(2) The reductive dissolution of Fe-Mn oxides/(oxy)hydroxides is another potential source of Ba in the estuaries. It is well documented that increased solar insolation can enhance the photoactivated reduction of Fe-Mn oxides and/or (oxy)hydroxides under

experimental conditions and might contribute to the sharp increase in Fe and Mn concentrations in surface seawater (e.g., Sunda et al., 1983; Wells et al., 1991). Thus, the contribution of Ba to the dissolved phase via reduction of Fe-Mn oxides/(oxy)hydroxides could be another important driver for elevated Ba/Ca_{coral} . However, the variations of Mn/Ca_{coral} in this study do not show any significant correlation with $\delta^{138}\text{Ba}_{\text{coral}}$ and Ba/Ca_{coral} signatures, in particular during pre-SAM seasons (Fig. 5.8c). Therefore, the reductive dissolution of Fe-Mn oxides/(oxy)hydroxides is unlikely to be responsible for these sharp $\delta^{138}\text{Ba}_{\text{coral}}$ and Ba/Ca_{coral} spikes.

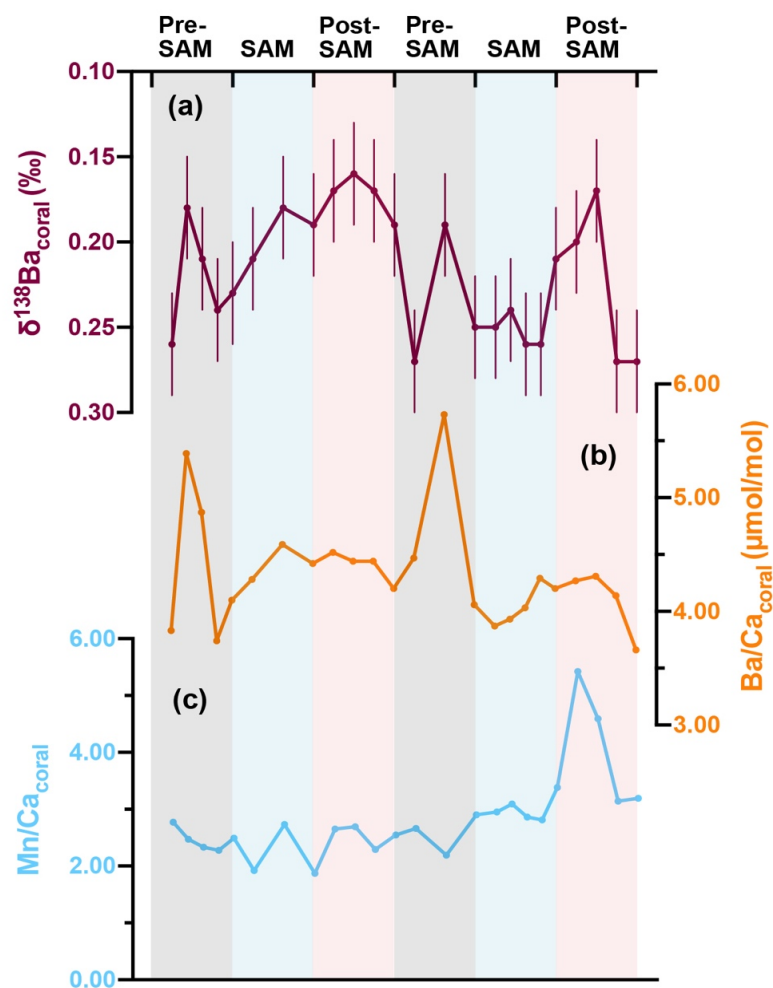


Fig. 5.8: A continuous two-year geochemical record of Mayabunder coral (AND-3-A II). (a) $\delta^{138}\text{Ba}_{\text{coral}}$; (b) Ba/Ca_{coral} ; (c) Mn/Ca_{coral} . The grey, blue and red shaded bars mark the period of pre-SAM, SAM and post-SAM, respectively.

(3) The observed Ba/Ca_{coral} spikes could be related to barite formation in association with local phytoplankton blooms and subsequent decay of the organic matter. Incorporation of these barite particles into the coral may be responsible for the steeply elevated Ba/Ca_{coral} ratios and the lighter $\delta^{138}\text{Ba}_{\text{coral}}$ values given that the light Ba isotopes are preferentially incorporated into barite during precipitation (von Allmen et al., 2010). During the pre-SAM seasons, coastal salinities reach maximum values accompanied by less depleted $\delta^{18}\text{O}_{\text{SW}}$ values, SST is beginning to rise, wind speed is low and solar radiation has been increasing for several months (Fig. 5.3). These conditions favour the formation of phytoplankton blooms. In addition, the less depleted $\delta^{13}\text{C}_{\text{coral}}$ values during pre-SAM period may be another indicator for phytoplankton blooms (Fig. 5.3g). Although $\delta^{13}\text{C}_{\text{coral}}$ may be affected by a number of vital and kinetic effects (e.g., light availability, pH, skeletal architecture), enhanced photosynthesis processes due to phytoplankton blooms can result in an increase in $\delta^{13}\text{C}_{\text{coral}}$ values due to the preferential consumption of $^{12}\text{CO}_2$, but this skeletal signal could also reflect an increased availability of light for photosynthesis of the coral's endosymbiotic algae during the less cloudy pre-SAM season (e.g., Felis et al., 1998). Besides, the high chlorophyll- α concentrations during this period (Fig. 5.3i) also suggest that the incorporation of barite associated with phytoplankton blooms and subsequent decay of organic matters may be a possible driver of the observed Ba spikes in this study. However, to our knowledge, barite precipitation at such shallow water depth has not been reported in the literature. Despite this lack of published data, the incorporation of barite caused by the above precipitation conditions cannot be excluded.

(4) In addition to the Ba desorption from the sediments of the Myanmar continental shelves, the fringing mangroves in the local Mayabunder area are also capable of exporting accumulated Ba into adjacent surface waters via solute-particle/sediment interaction. The desorption of Ba is largely dependent of the ionic strength of the solution such that the magnitude of desorption is higher at higher ionic strength and salinity (Li et al., 1984). This characteristic would explain higher degree of Ba desorption in pre-SAM waters that exhibit the highest salinity. Hence the mangrove-trapped Ba in sediments and/or particles could provide a source of soluble Ba by ion-exchange reactions with seawaters encroaching on the local Mayabunder mangrove areas during spring tides. This is similar to the mechanism proposed by Carroll et al. (1993) to account for high Ba fluxes in the BoB coastal waters during February-March for the Ganges-Brahmaputra system. In addition, the Interview Island coral time series reveals similar Ba/Ca_{coral} spikes during

the pre-SAM seasons (Fig. 5.3e). The consistency of our elevated Ba/Ca_{coral} records from both corals during the pre-SAM period suggests that local external export likely represents a direct source of dissolved Ba to the adjacent surface waters without further dilutions by freshwater input, while the magnitude of these Ba fluxes remain largely unknown.

5.4.3 Constraints on coral Ba isotope compositions

5.4.3.1 Temporal variations in $\delta^{138}\text{Ba}_{\text{SW}}$ and the Ba isotope fractionations between coral and seawater ($\Delta^{138}\text{Ba}_{\text{coral-SW}}$)

We find a significant correlation between reconstructed $\delta^{18}\text{O}_{\text{SW}}$ (SSS), $\delta^{138}\text{Ba}_{\text{coral}}$ and Ba/Ca_{coral} during the SAM and post-SAM seasons (Fig. 5.9a & b). In contrast, no statistically significant correlation between $\delta^{18}\text{O}_{\text{SW}}$ (SSS), $\delta^{138}\text{Ba}_{\text{coral}}$ and Ba/Ca_{coral} is observed during the pre-SAM period (Fig. 5.9a & b). Along with the discussion above, this suggests that riverine inputs and associated variations in surface seawater $\delta^{138}\text{Ba}_{\text{SW}}$ signatures might be the dominant driver for changes in $\delta^{138}\text{Ba}_{\text{coral}}$ values, especially during the SAM and post-SAM seasons.

Seawater exhibits a light $\delta^{138}\text{Ba}_{\text{SW}}$ value of $+0.29 \pm 0.04\text{‰}$ during the SAM in July 2011, when the dissolved [Ba]_{SW} value reached a maximum of 66.03 nmol/kg and the SSS was the lowest (Fig. 5.10a). This observation is in line with the interpretation that river runoff is the major driver for the light Ba isotope signatures observed during the SAM. In comparison to the light $\delta^{138}\text{Ba}_{\text{SW}}$ value in the SAM, heavier $\delta^{138}\text{Ba}_{\text{SW}}$ accompanied by lower [Ba]_{SW} signatures are observed during the pre- and post-SAM periods (Fig. 5.10a). The similarity between the pre- and post-SAM signals may be a result of the relatively coarse temporal resolution of our seawater sampling that is insufficient to capture the additional Ba fluxes, e.g., the Ba spikes observed in the coral during the pre-SAM periods. Nevertheless, the seasonal variations in $\delta^{138}\text{Ba}_{\text{SW}}$ signatures allow us to estimate the temporal variations in $\Delta^{138}\text{Ba}_{\text{coral-SW}}$ by taking the $\delta^{138}\text{Ba}_{\text{SW}}$ value of the SAM and adopting the average of $\delta^{138}\text{Ba}_{\text{SW}}$ values of the pre-SAM and post-SAM, respectively (Fig. 5.10b).

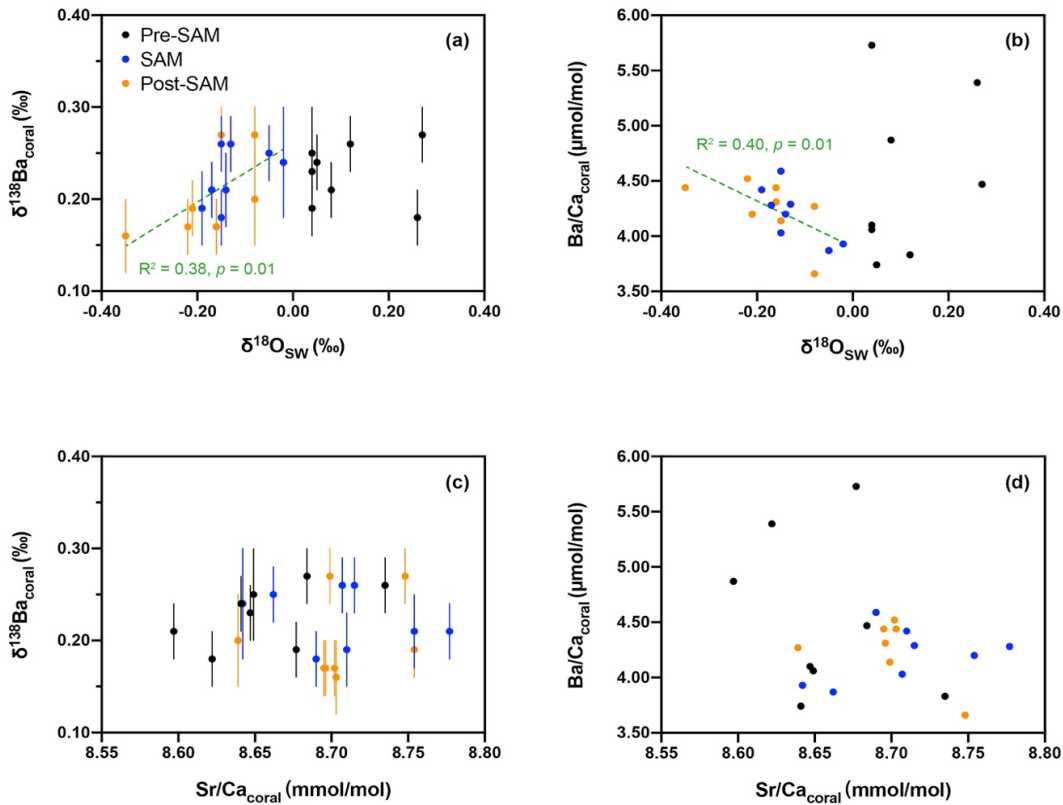


Fig. 5.9: Correlations between $\delta^{138}\text{Ba}_{\text{coral}}$ and $\text{Ba}/\text{Ca}_{\text{coral}}$ values with $\delta^{18}\text{O}_{\text{sw}}$ (SSS) and $\text{Sr}/\text{Ca}_{\text{coral}}$ (SST) from Mayabunder coral (AND-3-A II) for the pre-SAM, SAM and post-SAM periods. (a) $\delta^{138}\text{Ba}_{\text{coral}}$ versus $\delta^{18}\text{O}_{\text{sw}}$; (b) $\text{Ba}/\text{Ca}_{\text{coral}}$ versus $\delta^{18}\text{O}_{\text{sw}}$; (c) $\delta^{138}\text{Ba}_{\text{coral}}$ versus $\text{Sr}/\text{Ca}_{\text{coral}}$; (d) $\text{Ba}/\text{Ca}_{\text{coral}}$ versus $\text{Sr}/\text{Ca}_{\text{coral}}$.

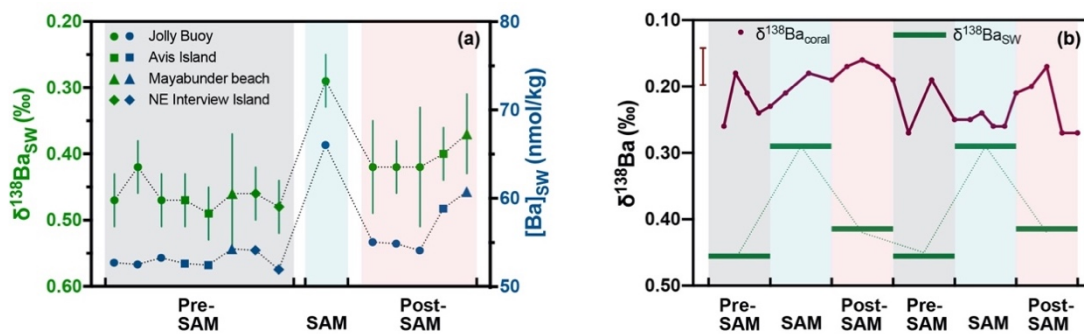


Fig. 5.10: (a) Temporal variations in surface seawater $[\text{Ba}]$ (blue) and $\delta^{138}\text{Ba}_{\text{sw}}$ (green); (b) Temporal variations in coral Ba isotope compositions (maroon, error bar $\pm 2\text{SD}$ analytical uncertainty for JCp-1) and averaged surface seawater Ba isotope compositions (green dash). The averaged pre-SAM $\delta^{138}\text{Ba}_{\text{sw}}$ value was calculated by eight measured $\delta^{138}\text{Ba}_{\text{sw}}$ values from March 2011, February and March 2012 and March 2013. The SAM $\delta^{138}\text{Ba}_{\text{sw}}$ value was directly from one measured seawater sample from July 2011. The averaged post-SAM $\delta^{138}\text{Ba}_{\text{sw}}$ value was calculated by five measured seawater samples from November 2011. The same $\delta^{138}\text{Ba}_{\text{sw}}$ values are used twice for pre-SAM, SAM, and post-SAM, respectively.

Generally, all coral samples analysed in this study are enriched in lighter Ba isotopes compared to ambient seawater (Fig. 5.10b). The preferential incorporation of lighter isotopes during biogenic carbonate precipitation is consistent with previous studies (Hemsing et al., 2018; Liu et al., 2019; Pretet et al., 2015). However, in contrast to a consistent Ba isotopic fractionation factor of -0.30‰ for $\Delta^{138}\text{Ba}_{\text{coral-SW}}$ that has been recently reported by Liu et al. (2019), our estimated $\Delta^{138}\text{Ba}_{\text{coral-SW}}$ seems to indicate a variable fractionation factor between different monsoon seasons (Fig. 5.10b). The average values of $\Delta^{138}\text{Ba}_{\text{coral-SW}}$ are -0.23‰ , -0.07‰ and -0.21‰ for the pre-SAM, SAM and post-SAM, respectively, if the unexpected $\delta^{138}\text{Ba}_{\text{coral}}$ spikes during the pre-SAM seasons are excluded. The magnitude of Ba isotope fractionation is generally comparable with reported values for cultured tropical aragonitic corals, varying between -0.02‰ (*Porites* sp. and *Acropora* sp.) and -0.38‰ (*Stylophora* sp. and *Montipora* sp., Pretet et al., 2015). Previous inorganic precipitation experiments of BaSO_4 and $\text{BaMn}(\text{CO}_3)_2$ showed a similar preference for incorporation of lighter isotopes, with a fractionation of $-0.33 \pm 0.04\text{‰}$ and $-0.17 \pm 0.03\text{‰}$, respectively (Böttcher et al., 2012; von Allmen et al., 2010). In addition, the reported Ba isotope fractionation during BaCO_3 precipitation is between $-0.25 \pm 0.03\text{‰}$ and $-0.07 \pm 0.04\text{‰}$, respectively (Mavromatis et al., 2016; von Allmen et al., 2010). Unfortunately, the limited time resolution of the surface seawater sampling and the fact that the analysed seawater samples were taken during different years than the coral samples, do not allow us to conclude if the $\Delta^{138}\text{Ba}_{\text{coral-SW}}$ is indeed variable depending on environmental factors. However, based on the discussion in section 5.4.2 and the pattern of Ba isotope fractionation discussed above we can conclude that temporal variations in $\delta^{138}\text{Ba}_{\text{SW}}$ is likely the major control on the coral Ba isotope compositions, while the variable $\Delta^{138}\text{Ba}_{\text{coral-SW}}$ may exert additional control on the $\delta^{138}\text{Ba}_{\text{coral}}$ record presented in this study.

5.4.3.2 Equilibrium vs. kinetic processes

Recently, two studies on first-principal calculations indicated that aragonite will be enriched in heavy Ba isotopes if in thermodynamic equilibrium with the aqueous solution (Mavromatis et al., 2020; Wang et al., 2021). Based on the density functional theory (DFT), Wang et al. (2021) predicted that the equilibrium Ba isotope fractionation factor between aragonite and aqueous solution ($\Delta^{138/134}\text{Ba}_{\text{aragonite-solution}}$) is $+0.48\text{‰}$ at 300K, which is consistent with a previously reported value of $+0.36\text{‰}$ at 298K using a

simplified model of Transition State Theory (TST, Mavromatis et al., 2020), if the uncertainty of model fitting ($\sim 0.20\text{‰}$) is considered. This positive fractionation can be well explained by a shorter average Ba-O bond length and a larger Ba coordination number in the newly formed aragonite structure (Mavromatis et al., 2020; Wang et al., 2021). However, $\Delta^{138}\text{Ba}_{\text{coral-SW}}$ values based on this study (between -0.07‰ and -0.23‰) suggest an enrichment of light Ba isotopes in coral aragonite compared with seawater. Clearly, the thermodynamic equilibrium processes cannot explain the observed negative Ba isotope fractionation given that the isotopic exchange equilibrium is unlikely to be reached during coral growth at such low temperatures. Therefore, kinetic processes likely play an additional role in Ba isotope fractionation during coral calcification. For instance, Mavromatis et al. (2020) conducted an abiogenic aragonite precipitation experiment and suggested that isotopic fractionation of Ba ($\Delta^{138}\text{Ba}_{\text{aragonite-solution}}$) during incorporation exhibits a systematic decrease as a function of increasing aragonite growth rate. The precipitated aragonite that is formed at low growth rates ($\leq 10^{-8.1}$ mol/m²/s) is enriched in heavier Ba isotopes, while the newly formed aragonite becomes progressively enriched in lighter Ba isotopes when growth rates exceed $10^{-8.0}$ mol/m²/s. Therefore, the observed negative Ba isotope fractionation may result from the relatively fast growth rate of the coral aragonite. Moreover, the linear relationship between $\Delta^{138}\text{Ba}_{\text{aragonite-solution}}$ and growth rate ($\Delta^{138}\text{Ba}_{\text{aragonite-solution}} = -0.2439 \text{LogRate} - 1.9701$) defined in Mavromatis et al., 2020) may account for the observed variations in $\Delta^{138}\text{Ba}_{\text{coral-SW}}$ values as a consequence of a seasonally variable coral skeletal growth rate.

Sea surface temperature (SST) has been recognised to exert important control on coral growth rate (e.g., Lough and Barnes, 2000) and may affect changes in Ba isotope fractionation between corals and seawater ($\Delta^{138}\text{Ba}_{\text{coral-SW}}$), although other factors, e.g., light, heterotrophy, have also been found to influence skeletal growth (e.g., Wellington, 1982). No significant correlations between either $\delta^{138}\text{Ba}_{\text{coral}}$ or $\text{Ba}/\text{Ca}_{\text{coral}}$ and $\text{Sr}/\text{Ca}_{\text{coral}}$ (SST) are observed in our continuous two-year coral record during any season (Figs. 5.9c & d) suggesting that stable Ba isotope fractionation is not influenced by SST and may thus also be independent from SST-induced variations in growth rate. This is consistent with a recent study by Liu et al. (2019), in which the annual coral records appear to show no correlation of $\delta^{138}\text{Ba}_{\text{coral}}$ signatures with changes in temperature ranging from 25°C to 29°C. In addition, the results of abiotic precipitation experiments have shown that stable Ba isotope fractionation is barely influenced by temperature (Böttcher et al., 2018; von

Allmen et al., 2010). However, the degree to which growth rate affects $\Delta^{138}\text{Ba}_{\text{coral-SW}}$ cannot be derived conclusively from existing data, given that temperature is not the only factor controlling skeletal calcification. Despite the fact that mineral growth rate may significantly affect the Ba isotope compositions of the inorganic aragonite (Mavromatis et al., 2020), direct application of this calibration in natural samples has to be considered with caution. This is because the precipitation experiment was performed under a chemical steady-state condition, which is unlikely to occur during natural coral calcification.

5.4.3.3 Rayleigh fractionation

In contrast to the abiogenic precipitation experiments, previous studies have demonstrated that element fractionation during coral biomineralization can be described by a Rayleigh process, consistent with the hypothesis that aragonite precipitation occurs in an isolated or at least semi-isolated calcifying micro-environment (Gaetani et al., 2011; Gaetani and Cohen, 2006; Gagnon et al., 2012). To better understand the biomineralization processes based on our new data from the AnS, we modelled the Rayleigh fractionation effects on both $\delta^{138}\text{Ba}_{\text{coral}}$ and $\text{Ba}/\text{Ca}_{\text{coral}}$ following the method from Liu et al. (2019) and equations from Inoue et al. (2015).

$$\delta^{138}\text{Ba}_{\text{coral Rayleigh}} = \left(\delta^{138}\text{Ba}_{\text{SW}} + 1000 \right) \times \left(1 - f \right)^{\alpha} / \left(1 - f \right) - 1000 \quad (5.3)$$

and

$$\delta^{138}\text{Ba}_{\text{coral Rayleigh}} = \text{Ba} / \text{Ca}_{\text{SW}} \times \left(1 - f^{K_D^{\text{Ba/Ca}}} \right) / \left(1 - f \right) \quad (5.4)$$

where $\delta^{138}\text{Ba}_{\text{coral Rayleigh}}$ is the predicted Ba isotope compositions of the coral skeleton, $\text{Ba}/\text{Ca}_{\text{coral Rayleigh}}$ is the predicted Ba/Ca ratio of the coral skeleton and f is the fraction of Ba remaining in the calcifying fluid after precipitation has ended. A value of +0.46‰ is used as initial $\delta^{138}\text{Ba}_{\text{SW}}$ value which corresponds to the Ba isotope compositions of the AnS surface seawater during the pre-SAM period. The $\text{Ba}/\text{Ca}_{\text{SW}}$ is set to the value of 2.60 $\mu\text{mol}/\text{mol}$ in order to fit the range of measured $\text{Ba}/\text{Ca}_{\text{coral}}$ ratios and this value is very similar with the used minimum value of 2.43 $\mu\text{mol}/\text{mol}$ in Liu et al. (2019). Because our data do not allow us to define a single fractionation factor between coral and seawater

($\Delta^{138}\text{Ba}_{\text{coral-SW}}$ between -0.07‰ and -0.23‰), we adopted the fractionation factor (α) value of 0.9997 from Liu et al. (2019). Values of 2.09 and 1.78 are used for $K_D^{\text{Ba/Ca}}$ at 26°C and 31°C , respectively (Gaetani and Cohen, 2006).

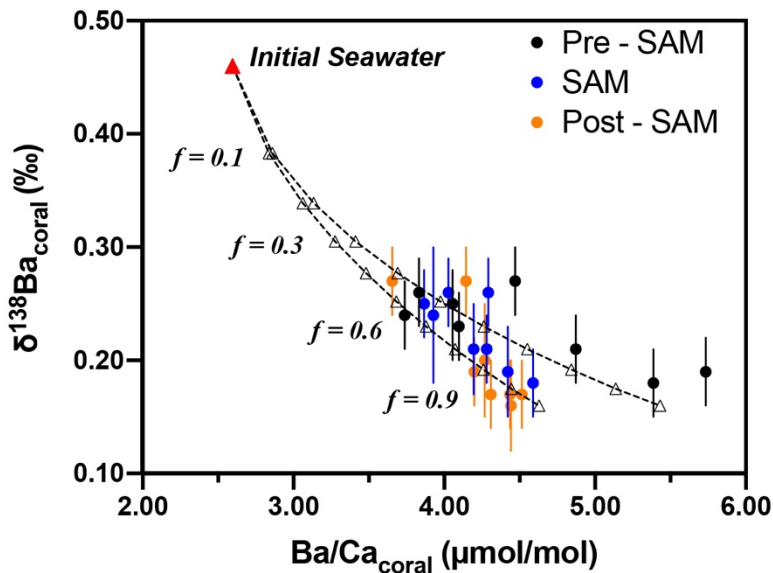


Fig. 5.11: Modelled Rayleigh fractionation (black dash lines) of $\delta^{138}\text{Ba}_{\text{coral}}$ and $\text{Ba}/\text{Ca}_{\text{coral}}$ during coral aragonite precipitation. The red triangle indicates the initial seawater Ba isotope compositions and Ba/Ca ratios. The fractionation factor (α) between coral and seawater used here is 0.9997, which is taken from Liu et al. (2019). Values of 2.09 and 1.78 are used for $K_D^{\text{Ba/Ca}}$ at 26°C and 31°C , respectively (Gaetani and Cohen, 2006). The factor (f) is the proportion of Ba remaining in the calcifying fluid.

As shown in Fig. 5.11, the Rayleigh fractionation model can explain the co-variation in $\delta^{138}\text{B}_{\text{coral}}$ and $\text{Ba}/\text{Ca}_{\text{coral}}$, supporting the assumption that aragonite precipitation occurs in an enclosed calcifying fluid. However, some measured $\delta^{138}\text{B}_{\text{coral}}$ and $\text{Ba}/\text{Ca}_{\text{coral}}$ values apparently do not fall within the limits of the Rayleigh model with constant initial $\delta^{138}\text{B}_{\text{sw}}$ and $\text{Ba}/\text{Ca}_{\text{sw}}$ values (Fig. 5.11). An important assumption underlying the Rayleigh model is that seasonal variations in $\delta^{138}\text{B}_{\text{sw}}$ and $\text{Ba}/\text{Ca}_{\text{sw}}$ of the calcifying fluid are negligible, which apparently has not been the case in our study as indicated by the discussion in section 5.4.3.1. Therefore, temporal variations in the initial seawater Ba isotope compositions must not be neglected, while Rayleigh fractionation may act as an additional control on $\delta^{138}\text{B}_{\text{coral}}$ and $\text{Ba}/\text{Ca}_{\text{coral}}$ signatures. Further work that compares

measured $\Delta^{138}\text{Ba}_{\text{coral-SW}}$ in natural corals with contemporaneous seawater samples will provide additional constraints on how Rayleigh fractionation affects Ba isotope fractionation during biogenic calcification.

5.5 Conclusions

Our study suggests that coral stable Ba isotope compositions ($\delta^{138}\text{Ba}_{\text{coral}}$) are a promising new tool for investigating palaeo-river discharge and biogeochemical processes in the coastal marine environment of tropical monsoon regions. Several lines of observations based on the seasonal variations in $\delta^{138}\text{Ba}_{\text{coral}}$ and $\text{Ba}/\text{Ca}_{\text{coral}}$ support the contention that riverine inputs associated with Ba desorption followed by lateral advection are the main processes supplying Ba during the SAM and post-SAM periods. In contrast, two possible mechanisms, (1) barite formation in association with phytoplankton blooms and (2) Ba release from fringing mangroves-trapped sediments may account for the anomalous Ba behaviour observed during the pre-SAM seasons. With respect to the Ba isotope fractionation between corals and seawater ($\Delta^{138}\text{Ba}_{\text{coral-SW}}$), the enrichment of light Ba isotopes in coral aragonite cannot be explained by equilibrium processes. In contrast, the $\Delta^{138}\text{Ba}_{\text{coral-SW}}$ appears to be largely controlled by *in-situ* seawater Ba isotope compositions, while processes such as Rayleigh fractionation and/or mineral growth kinetics may exert additional control on $\delta^{138}\text{Ba}_{\text{coral}}$ and Ba/Ca during coral calcification. Overall, our study demonstrates that the combined use of seasonal-resolution $\delta^{138}\text{Ba}_{\text{coral}}$, $\text{Ba}/\text{Ca}_{\text{coral}}$, $\text{Sr}/\text{Ca}_{\text{coral}}$, $\delta^{18}\text{O}_{\text{coral}}$ and $\delta^{13}\text{C}_{\text{coral}}$ can provide important constraints on seasonal changes in riverine inputs and environmental conditions prior to instrumental observations in this understudied part of the Indian Ocean.

6 Summary, Conclusions and Outlook

6.1 Summary and Conclusions

To summarise, the following conclusions address the three scientific questions outlined in the Introduction of this thesis.

(1) How to measure stable Ba isotopes with MC-ICP-MS precisely and accurately?

In chapter 3, a systematic investigation of non-spectral matrix effects on the precision and accuracy of stable Ba isotope measurements with MC-ICP-MS has been carried out. The results provide an improved understanding of the matrix-induced instrumental mass fractionation and define a matrix tolerance plasma state for Ba isotope analysis. Although this experiment was performed and calibrated for stable Ba isotopes, it is considered applicable to a wide range of other stable isotope measurements with MC-ICP-MS. The major conclusions are summarised as follows:

- The Normalised Argon Index (NAI) is a generally applicable and quantitative indicator of the plasma thermal conditions, which is independent of the particular tuning and instrumental setup.
- The effect of matrix elements on the instrumental mass fractionation is closely linked to the NAI and behaves as a linear function of the plasma mass loading.
- The addition of matrix elements can result in “over-loading” of the plasma and lead to isotopic anomalies that cannot be resolved by the double spike technique.
- The non-spectral matrix effects can be significantly attenuated by increasing the NAI thereby minimising the risk of plasma “over-loading” and stabilising the instrumental mass fractionation during isotope analysis with MC-ICP-MS.

(2) What are the exact mechanisms controlling the dissolved Ba isotope distributions in the modern ocean?

In chapter 4, we examine the spatial and vertical distribution of $\delta^{138}\text{Ba}$ and $[\text{Ba}]$ in 12 full water column profiles from the high-latitude oceans. These data allow us to investigate how NADW and AABW acquire their respective Ba isotope signatures in the polar and subpolar regions. In combination with the previously reported low and mid-latitude $\delta^{138}\text{Ba}$ profiles, we are able not only to better constrain the meridional Ba transport and mixing processes across the entire Atlantic, but also to explore the mechanisms governing marine Ba isotope fractionation in the upper ocean. The major conclusions are summarised as follows:

- The Ba isotope signature of Northern Overflow Water ($\delta^{138}\text{Ba}$, $+0.52 \pm 0.07\text{‰}$) in the Nordic Seas is clearly modified along its pathway before it contributes to the production of NADW, which displays a uniform $\delta^{138}\text{Ba}$ value of $+0.48 \pm 0.05\text{‰}$ in the Labrador Sea.
- We find that AABW in the Weddell Sea is characterised by an average $\delta^{138}\text{Ba}$ value of $+0.26 \pm 0.03\text{‰}$, which is identical to the previously estimated value of $+0.26 \pm 0.03\text{‰}$ for the southern-sourced water endmember of the AMOC.
- The well-defined relationship between $\delta^{138}\text{Ba}$ and $1/[\text{Ba}]$ and distinct Ba isotope signatures of deep waters originating in the polar regions predominately constrain the meridional gradient of Ba isotope compositions and concentrations in the deep Atlantic Ocean.
- The compiled global datasets show that either an open system steady-state fractionation model or a closed system Rayleigh fractionation model can explain the Ba isotope fractionation due to barite formation and particle adsorption in the upper ocean.

(3) Can stable Ba isotopes in shallow-water corals be used to reconstruct riverine inputs?

In chapter 5, we test the applicability of $\delta^{138}\text{Ba}$ in shallow-water corals as a proxy for past riverine inputs on seasonal timescales against other proxies (Sr/Ca, U/Ca, Ba/Ca, $\delta^{13}\text{C}$, and $\delta^{18}\text{O}$) in corals and in comparison with external environmental drivers. We discuss the integrity and limitations of these coral-based proxies, provide new insights into their interpretations related to the reconstruction of riverine inputs, and explore the mechanisms controlling Ba isotope fractionation during coral skeleton calcification. The major conclusions are summarised as follows:

- Our results of a monthly resolved coral record from the Andaman Islands (India) show that coral $\delta^{138}\text{Ba}$ is generally isotopically lighter during the South Asian Summer Monsoon characterised by enhanced rainfall and regional river discharge, suggesting that coral $\delta^{138}\text{Ba}$ can serve as a novel runoff proxy.
- This is supported by the stable Ba isotope compositions of local seawater samples, which show a significantly lighter $\delta^{138}\text{Ba}$ value of $+0.29 \pm 0.04\text{‰}$ (2SD) during the South Asian Summer Monsoon.
- With respect to the Ba isotope fractionation between the corals and seawater ($\Delta^{138}\text{Ba}_{\text{coral-SW}}$), an enrichment of light Ba isotopes in coral aragonite is observed that cannot be explained by equilibrium processes.
- The seasonal changes in seawater $\delta^{138}\text{Ba}$ likely dominate the seasonal changes in the Ba signals recorded by coral skeletons, while Rayleigh fractionation and/or mineral growth kinetics may exert additional control on coral $\delta^{138}\text{Ba}$ and Ba/Ca during aragonite calcification.

6.2 Outlook

The results regarding the impact of plasma conditions on stable Ba isotope analysis will have important implications for the accurate measurement of other isotope systems with MC-ICP-MS. In comparison to TIMS, MC-ICP-MS allows for high ionisation efficiency and rapid sample throughput. However, the accuracy and precision of MC-ICP-MS measurements are still perceived as insufficiently validated, in particular with reference to TIMS (Albarède and Beard, 2004), mainly due to its significantly larger instrumental mass fractionation. This large mass discrimination is primarily due to the very high temperature of the plasma, which generates ions with different initial energies and therefore with complex trajectories in the mass spectrometer (e.g., Albarède and Beard, 2004). Therefore, careful control of plasma operating conditions is indispensable no matter which instrumental mass bias correction method is applied. This is of particular importance because in most cases the instruments are simply tuned to the highest sensitivity, which can be accompanied by unaccountable matrix effects. In this context, a wide variety of isotope systems (e.g., stable Li, Si, and Mo isotopes; radiogenic Nd and Pb isotopes) need to be investigated under different but quantified plasma conditions to improve the accuracy and precision of the isotope analyses with MC-ICP-MS.

With respect to stable Ba isotopes in the modern ocean, a more comprehensive isotopic characterisation of different Ba sources to the ocean is necessary to better constrain the marine budget of Ba and its isotopes. The main inputs of Ba to the open ocean are riverine and groundwater discharge that carry weathered silicate minerals, while barite precipitation and subsequent sedimentation constitute the major sink of Ba from seawater (e.g., Paytan and Kastner, 1996). The $\delta^{138}\text{Ba}$ signatures in both rivers (between +0.2 and +0.3‰, Cao et al., 2020b; Charbonnier et al., 2020; Gou et al., 2020; Hsieh and Henderson, 2017) and groundwater (\sim +0.1‰, (Mayfield et al., 2021)) are isotopically heavier than that of sedimentary barite (between 0.0 and +0.1‰, (Bridgestock et al., 2018; Crockford et al., 2019)). Therefore, the marine Ba budget is either not in steady state, or is missing at least one major input with $\delta^{138}\text{Ba} \leq +0.1\text{‰}$ (Horner and Crockford, 2021). The determination of the Ba isotope composition of other sources (e.g., estuaries, cold seeps, and dust inputs) and sinks (e.g., Fe-Mn oxides and oxyhydroxides) is needed to close this gap.

Extending the application of stable Ba isotopes into the past offers a number of interesting applications but also raises questions. Firstly, Ba isotope signatures in shallow-water corals have great potential to provide a long-term record of terrestrial inputs and precipitation on land beyond the instrumental record (Liu et al., 2019; Pretet et al., 2015). This proposal is based on the fact that river runoff is characterised by relatively light Ba isotope compositions and can significantly modify the $\delta^{138}\text{Ba}$ values of coastal surface seawaters (Cao et al., 2020b; Hsieh and Henderson, 2017). However, the direct calibration of Ba isotope fractionation between shallow-water coral skeletons and *in-situ* seawater at high temporal resolution is currently still lacking to fully understand the mechanisms governing Ba/Ca distributions and Ba isotope fractionation during shallow-water coral calcification. Secondly, recent work carried out on Ba isotope signatures of cold-water corals suggested that coral aragonite preferentially incorporates the light Ba isotopes and the isotope fractionation between coral skeletons and seawater is likely independent of temperature and other environmental variables (Geyman et al., 2019; Hemsing et al., 2018). Although the temporal changes in skeletal $\delta^{138}\text{Ba}$ are likely related to ambient seawater Ba isotope signatures, the general absence of interior skeletal variability in measured coral $\delta^{138}\text{Ba}$ values requires high temporal resolution studies of deep-sea corals in the future. Thirdly, the $\delta^{138}\text{Ba}$ values of pelagic barites in deep-sea sediments could reflect the balance between Ba input via terrestrial sources and Ba output by authigenic barite sedimentation, which in turn might help to constrain export production as a function of climate change (Bridgestock et al., 2019, 2018). However, early diagenesis in sulphate-depleted sediments and exchange at the sediment-water interface can promote Ba remobilisation and thus compromise the integrity of barite-based $\delta^{138}\text{Ba}$ records (Horner and Crockford, 2021). A better understanding of early diagenetic Ba cycling in deep-sea sediments is thus required for a confident interpretation of Ba isotope compositions of barite for palaeoceanographic reconstructions.

Acknowledgements

First and foremost I would like to thank Martin for being (one of) the best supervisor ever! Without your continued guidance and support the work presented in this thesis would not have been possible, in particular during the coronavirus crisis. You are more than just a supervisor, you are truly an inspiration. Your enthusiasm and dedication have inspired me since the moment I first joined the group. I really appreciate the role you played in helping me get here and will never forget the special Hauptbahnhof pick-up on a Sunday morning in Kiel.

Ed, a supervisor and a friend, two in one. Thank you for sharing your family and friends with me, which means a lot to me! You and your family are such a huge part of my life in Kiel. I cannot wait to see what the years ahead of us bring. Sasha, thank you for your wonderful hospitality and every lovely evenings with delicious food in a beautiful home! It was fantastic to do so many fun things together with the kids. Aurora and Luka, I love watching you grow up. If you get a chance to see this thesis in two decades, please think twice before you decide to start a doctoral project.

Chris, you are so patient with me! I greatly appreciate that when training me you took the time to break things down to a level that I could understand and then build upon systematically. Thank you for your trust in my analytical skills and your willingness to let me follow my own ideas while at the same time helping me to stay focused. I always enjoyed the fruitful discussions of our “spikes” in your office and also thank you for helping me to prepare the German abstract of this thesis.

Georgi, it is my great pleasure to share the office with you for more than two years and you showed me how to work scientifically with a high standard. I really enjoyed the “wine seminars” with you in Hamburg even though I have not found out which wine suits my personal taste. Marcus, Eleni, Tyler and Huang, I will miss the Kieler Woche party with you guys and thank you for making my life more enjoyable in Kiel! Many thanks to my friends and colleagues, Anastasia, Anna, Anne, An-tao, Daniel, Guillaume, Jacky, J.C., Jiang-nan, Jing, Katriina, Ke-chen, Kirsten, Kristin, Lara, Lisa, Patricia, Peer, Sarina, Sebastian, Sonja, Steffen, Te, Xue-chao, Xun-chi, Zhi-fang, Zhou-ling for supporting and putting up with me over the years.

This thesis could not have been completed without the assistance of Jutta, Marcus, Jan, Ana, Tyler, Nadine, Sebastian, and Martina, who helped me greatly in dealing with lab work, instrumental operations and travel paperwork etc. I would like to thank Rui-fang and Ed for the constructive proofreading of this thesis. Many thanks to all my co-authors, who supported me significantly in the preparation of the manuscripts.

I am particularly grateful to Thomas for providing the coral samples from the Andaman Sea and giving me the opportunity to work at MARUM for a short time. Many thanks to Dirk for providing me with a great opportunity to participate the SONNE 264 cruise to the Pacific where the scenery is marvellous. I am also very thankful for the great experiences I have been offered by Zhi-mian in terms of a research visit in Xiamen University.

I would like to thank the China Scholarship Council (CSC) for financing my doctorate.

Last but certainly not least, I owe my deepest gratitude to my parents and family, who have always been there loving and supporting me!

References

- Aghaei, M., Bogaerts, A., 2016. Particle transport through an inductively coupled plasma torch: Elemental droplet evaporation. *J. Anal. At. Spectrom.* 31, 631–641. <https://doi.org/10.1039/c5ja00162e>
- Albarède, F., Albalat, E., Télouk, P., 2015. Instrumental isotope fractionation in multiple-collector icp-ms. *J. Anal. At. Spectrom.* 30, 1736–1742. <https://doi.org/10.1039/c5ja00188a>
- Albarède, F., Beard, B., 2004. Analytical methods for non-traditional isotopes. *Rev. Mineral. Geochemistry.* <https://doi.org/10.2138/gsrng.55.1.113>
- Albarède, F., Telouk, P., Blichert-Toft, J., Boyet, M., Agranier, A., Nelson, B., 2004. Precise and accurate isotopic measurements using multiple-collector ICPMS. *Geochim. Cosmochim. Acta* 68, 2725–2744. <https://doi.org/10.1016/j.gca.2003.11.024>
- Alibert, C., Kinsley, L., Fallon, S.J., McCulloch, M.T., Berkelmans, R., McAllister, F., 2003. Source of trace element variability in Great Barrier Reef corals affected by the Burdekin flood plumes. *Geochim. Cosmochim. Acta* 67, 231–246. [https://doi.org/10.1016/S0016-7037\(02\)01055-4](https://doi.org/10.1016/S0016-7037(02)01055-4)
- Ashin, K., Girishkumar, M.S., Suprit, K., Thangaprakash, V.P., 2019. Observed Upper Ocean Seasonal and Intraseasonal Variability in the Andaman Sea. *J. Geophys. Res. Ocean.* 124, 6760–6786. <https://doi.org/10.1029/2019JC014938>
- Bacon, M.P., Edmond, J.M., 1972. Barium at Geosecs III in the southwest Pacific. *Earth Planet. Sci. Lett.* 16, 66–74. [https://doi.org/10.1016/0012-821X\(72\)90237-3](https://doi.org/10.1016/0012-821X(72)90237-3)
- Barling, J., Weis, D., 2008. Influence of non-spectral matrix effects on the accuracy of Pb isotope ratio measurement by MC-ICP-MS: implications for the external normalization method of instrumental mass bias correction. *J. Anal. At. Spectrom.* 23, 1017–1025. <https://doi.org/10.1039/b717418g>
- Bates, S.L., Hendry, K.R., Pryer, H. V., Kinsley, C.W., Pyle, K.M., Woodward, E.M.S., Horner, T.J., 2017. Barium isotopes reveal role of ocean circulation on barium cycling in the Atlantic. *Geochim. Cosmochim. Acta* 204, 286–299. <https://doi.org/10.1016/j.gca.2017.01.043>
- Beck, J.W., Edwards, R.L., Ito, E., Taylor, F.W., Recy, J., Rougerie, F., Joannot, P., Henin, C., 1992. Sea-surface temperature from coral skeletal strontium/calcium ratios. *Science (80-.)*. 257, 644–647. <https://doi.org/10.1126/science.257.5070.644>
- Belshaw, N.S., Freedman, P.A., O’Nions, R.K., Frank, M., Guo, Y., 1998. A new variable dispersion double-focusing plasma mass spectrometer with performance illustrated for Pb isotopes. *Int. J. Mass Spectrom.* 181, 51–58. [https://doi.org/10.1016/s1387-3806\(98\)14150-7](https://doi.org/10.1016/s1387-3806(98)14150-7)
- Berglund, M., Wieser, M.E., 2011. Isotopic compositions of the elements 2009 (IUPAC

- technical report), in: Pure and Applied Chemistry. pp. 397–410.
<https://doi.org/10.1351/PAC-REP-10-06-02>
- Bishop, J.K.B., 1988. The barite-opal-organic carbon association in oceanic particulate matter. *Nature* 332, 341–343. <https://doi.org/10.1038/332341a0>
- Böttcher, M.E., Geprägs, P., Neubert, N., von Allmen, K., Pretet, C., Samankassou, E., Nögler, T.F., 2012. Barium isotope fractionation during experimental formation of the double carbonate BaMn[CO₃]₂ at ambient temperature. *Isotopes Environ. Health Stud.* 48, 457–463. <https://doi.org/10.1080/10256016.2012.673489>
- Böttcher, M.E., Neubert, N., von Allmen, K., Samankassou, E., Nögler, T.F., 2018. Barium isotope fractionation during the experimental transformation of aragonite to witherite and of gypsum to barite, and the effect of ion (de)solvation. *Isotopes Environ. Health Stud.* 54, 324–335. <https://doi.org/10.1080/10256016.2018.1430692>
- Bridgestock, L., Hsieh, Y. Te, Porcelli, D., Henderson, G.M., 2019. Increased export production during recovery from the Paleocene–Eocene thermal maximum constrained by sedimentary Ba isotopes. *Earth Planet. Sci. Lett.* 510, 53–63. <https://doi.org/10.1016/j.epsl.2018.12.036>
- Bridgestock, L., Hsieh, Y. Te, Porcelli, D., Homoky, W.B., Bryan, A., Henderson, G.M., 2018. Controls on the barium isotope compositions of marine sediments. *Earth Planet. Sci. Lett.* 481, 101–110. <https://doi.org/10.1016/j.epsl.2017.10.019>
- Bruland, K.W., Franks, R.P., Knauer, G.A., Martin, J.H., 1979. Sampling and analytical methods for the determination of copper, cadmium, zinc, and nickel at the nanogram per liter level in sea water. *Anal. Chim. Acta* 105, 233–245. [https://doi.org/10.1016/S0003-2670\(01\)83754-5](https://doi.org/10.1016/S0003-2670(01)83754-5)
- Bryan, S.P., Hughen, K.A., Karnauskas, K.B., Farrar, J.T., 2019. Two Hundred Fifty Years of Reconstructed South Asian Summer Monsoon Intensity and Decadal-Scale Variability. *Geophys. Res. Lett.* 46, 3927–3935. <https://doi.org/10.1029/2018GL081593>
- Bullen, T., Chadwick, O., 2016. Ca, Sr and Ba stable isotopes reveal the fate of soil nutrients along a tropical climosequence in Hawaii. *Chem. Geol.* 422, 25–45. <https://doi.org/10.1016/j.chemgeo.2015.12.008>
- Cahyarini, S.Y., Pfeiffer, M., Timm, O., Dullo, W.C., Schönberg, D.G., 2008. Reconstructing seawater $\delta^{18}\text{O}$ from paired coral $\delta^{18}\text{O}$ and Sr/Ca ratios: Methods, error analysis and problems, with examples from Tahiti (French Polynesia) and Timor (Indonesia). *Geochim. Cosmochim. Acta* 72, 2841–2853. <https://doi.org/10.1016/j.gca.2008.04.005>
- Cao, Z., Li, Y., Rao, X., Yu, Y., Hathorne, E.C., Siebert, C., Dai, M., Frank, M., 2020a. Constraining barium isotope fractionation in the upper water column of the South China Sea. *Geochim. Cosmochim. Acta* 288, 120–137. <https://doi.org/10.1016/j.gca.2020.08.008>

- Cao, Z., Siebert, C., Hathorne, E.C., Dai, M., Frank, M., 2020b. Corrigendum to “Constraining the oceanic barium cycle with stable barium isotopes” [Earth Planet. Sci. Lett. 434 (2016) 1–9](S0012821X15007219)(10.1016/j.epsl.2015.11.017). Earth Planet. Sci. Lett. <https://doi.org/10.1016/j.epsl.2019.116003>
- Cao, Z., Siebert, C., Hathorne, E.C., Dai, M., Frank, M., 2016. Constraining the oceanic barium cycle with stable barium isotopes. Earth Planet. Sci. Lett. 434, 1–9. <https://doi.org/10.1016/j.epsl.2015.11.017>
- Carmack, E.C., Foster, T.D., 1975. On the flow of water out of the Weddell Sea. Deep. Res. Oceanogr. Abstr. 22, 711–724. [https://doi.org/10.1016/0011-7471\(75\)90077-7](https://doi.org/10.1016/0011-7471(75)90077-7)
- Carroll, J., Falkner, Kelly K., Brown, E.T., Moore, W.S., 1993. The role of the Ganges-Brahmaputra mixing zone in supplying barium and ^{226}Ra to the Bay of Bengal. Geochim. Cosmochim. Acta 57, 2981–2990. [https://doi.org/10.1016/0016-7037\(93\)90287-7](https://doi.org/10.1016/0016-7037(93)90287-7)
- Carter, S.C., Paytan, A., Griffith, E.M., 2020. Toward an improved understanding of the marine barium cycle and the application of marine barite as a paleoproductivity proxy. Minerals. <https://doi.org/10.3390/min10050421>
- Charbonnier, Q., Bouchez, J., Gaillardet, J., Gayer, É., 2020. Barium stable isotopes as a fingerprint of biological cycling in the Amazon River Basin. Biogeosciences Discuss. 1–44. <https://doi.org/10.5194/bg-2020-81>
- Chen, X., Deng, W., Wei, G., McCulloch, M., 2020. Terrestrial Signature in Coral Ba/Ca, $\delta^{18}\text{O}$, and $\delta^{13}\text{C}$ Records From a Macrotide-Dominated Nearshore Reef Environment, Kimberley Region of Northwestern Australia. J. Geophys. Res. Biogeosciences 125. <https://doi.org/10.1029/2019JG005394>
- Coffey, M., Dehairs, F., Collette, O., Luther, G., Church, T., Jickells, T., 1997. The Behaviour of Dissolved Barium in Estuaries. Estuar. Coast. Shelf Sci. 45, 113–121. <https://doi.org/10.1006/ecss.1996.0157>
- Cole, J.E., Fairbanks, R.G., Shen, G.T., 1993. Recent variability in the southern oscillation: Isotopic results from a Tarawa Atoll coral. Science (80-.). 260, 1790–1793. <https://doi.org/10.1126/science.260.5115.1790>
- Corrège, T., 2006. Sea surface temperature and salinity reconstruction from coral geochemical tracers. Palaeogeogr. Palaeoclimatol. Palaeoecol. 232, 408–428. <https://doi.org/10.1016/j.palaeo.2005.10.014>
- Crockford, P.W., Wing, B.A., Paytan, A., Hodgskiss, M.S.W., Mayfield, K.K., Hayles, J.A., Middleton, J.E., Ahm, A.S.C., Johnston, D.T., Caxito, F., Uhlein, G., Halverson, G.P., Eickmann, B., Torres, M., Horner, T.J., 2019. Barium-isotopic constraints on the origin of post-Marinoan barites. Earth Planet. Sci. Lett. 519, 234–244. <https://doi.org/10.1016/j.epsl.2019.05.018>
- Das, A., Krishnaswami, S., 2006. Barium in Deccan Basalt Rivers: Its abundance, relative mobility and flux. Aquat. Geochemistry 12, 221–238. <https://doi.org/10.1007/s10498-005-5856-4>

- Davis, T.L.O., Farley, J.H., 2001. Size distribution of southern bluefin tuna (*Thunnus maccoyii*) by depth on their spawning ground, in: *Fishery Bulletin*. pp. 381–386. https://doi.org/10.1007/978-3-642-65468-8_3
- De Souza, G.F., Reynolds, B.C., Rickli, J., Frank, M., Saito, M.A., Gerringa, L.J.A., Bourdon, B., 2012. Southern Ocean control of silicon stable isotope distribution in the deep Atlantic Ocean. *Global Biogeochem. Cycles* 26. <https://doi.org/10.1029/2011GB004141>
- Dehairs, F., Chesselet, R., Jedwab, J., 1980. Discrete suspended particles of barite and the barium cycle in the open ocean. *Earth Planet. Sci. Lett.* 49, 528–550. [https://doi.org/10.1016/0012-821X\(80\)90094-1](https://doi.org/10.1016/0012-821X(80)90094-1)
- Dickson, R.R., Brown, J., 1994. The production of North Atlantic Deep Water: sources, rates, and pathways. *J. Geophys. Res.* 99. <https://doi.org/10.1029/94jc00530>
- Dickson, R.R., Gmitrowicz, E.M., Watson, A.J., 1990. Deep-water renewal in the northern North Atlantic. *Nature* 344, 848–850. <https://doi.org/10.1038/344848a0>
- Dodson, M.H., 1963. A theoretical study of the use of internal standards for precise isotopic analysis by the surface ionization technique: Part I - General first-order algebraic solutions. *J. Sci. Instrum.* 40, 289–295. <https://doi.org/10.1088/0950-7671/40/6/307>
- Dymond, J., Suess, E., Lyle, M., 1992. Barium in Deep-Sea Sediment: A Geochemical Proxy for Paleoproductivity. *Paleoceanography* 7, 163–181. <https://doi.org/10.1029/92PA00181>
- Eagle, M., Paytan, A., Arrigo, K.R., van Dijken, G., Murray, R.W., 2003. A comparison between excess barium and barite as indicators of carbon export. *Paleoceanography* 18. <https://doi.org/10.1029/2002pa000793>
- EUGSTER O, TERA F, WASSERBURG GJ, 1969. Isotopic Analyses of Barium in Meteorites and in Terrestrial Samples. *J Geophys Res* 74, 3897–3908. <https://doi.org/10.1029/jb074i015p03897>
- Evans, E.H., Giglio, J.J., 1993. Interferences in inductively coupled plasma mass spectrometry. A review. *J. Anal. At. Spectrom.* <https://doi.org/10.1039/ja9930800001>
- Fahrbach, E., Rohardt, G., Schröder, M., Strass, V., 1994. Transport and structure of the weddell gyre. *Ann. Geophys.* 12, 840–855. <https://doi.org/10.1007/s00585-994-0840-7>
- Felis, T., 2020. Extending the instrumental record of ocean-atmosphere variability into the last interglacial using tropical corals. *Oceanography* 33, 69–79. <https://doi.org/10.5670/oceanog.2020.209>
- Felis, T., Giry, C., Scholz, D., Lohmann, G., Pfeiffer, M., Pätzold, J., Kölling, M., Scheffers, S.R., 2015. Tropical Atlantic temperature seasonality at the end of the last interglacial. *Nat. Commun.* 6. <https://doi.org/10.1038/ncomms7159>

- Felis, T., Ionita, M., Rimbu, N., Lohmann, G., Kölling, M., 2018. Mild and Arid Climate in the Eastern Sahara-Arabian Desert During the Late Little Ice Age. *Geophys. Res. Lett.* 45, 7112–7119. <https://doi.org/10.1029/2018GL078617>
- Felis, T., Lohmann, G., Kuhnert, H., Lorenz, S.J., Scholz, D., Pätzold, J., Al-Rousen, S.A., Al-Moghrabl, S.M., 2004. Increased seasonality in Middle East temperatures during the last interglacial period. *Nature* 429, 164–168. <https://doi.org/10.1038/nature02546>
- Felis, T., Pätzold, J., Loya, Y., Wefer, G., 1998. Vertical water mass mixing and plankton blooms recorded in skeletal stable carbon isotopes of a Red Sea coral. *J. Geophys. Res. Ocean.* 103, 30731–30739. <https://doi.org/10.1029/98jc02711>
- Felis, T., Suzuki, A., Kuhnert, H., Dima, M., Lohmann, G., Kawahata, H., 2009. Subtropical coral reveals abrupt early-twentieth-century freshening in the western North Pacific Ocean. *Geology* 37, 527–530. <https://doi.org/10.1130/G25581A.1>
- Fietzke, J., Frische, M., 2016. Experimental evaluation of elemental behavior during LA-ICP-MS: Influences of plasma conditions and limits of plasma robustness. *J. Anal. At. Spectrom.* 31, 234–244. <https://doi.org/10.1039/c5ja00253b>
- Foster, D.A., Staubwasser, M., Henderson, G.M., 2004. ²²⁶Ra and Ba concentrations in the Ross Sea measured with multicollector ICP mass spectrometry. *Mar. Chem.* 87, 59–71. <https://doi.org/10.1016/j.marchem.2004.02.003>
- Freydier, R., Dupre, B., Polve, M., 1995. Analyses by inductively coupled plasma mass spectrometry of Ba concentrations in water and rock samples. Comparison between isotope dilution and external calibration with or without internal standard. *Eur. J. Mass Spectrom.* 1, 283. <https://doi.org/10.1255/ejms.140>
- Gaetani, G.A., Cohen, A.L., 2006. Element partitioning during precipitation of aragonite from seawater: A framework for understanding paleoproxies. *Geochim. Cosmochim. Acta* 70, 4617–4634. <https://doi.org/10.1016/j.gca.2006.07.008>
- Gaetani, G.A., Cohen, A.L., Wang, Z., Crusius, J., 2011. Rayleigh-based, multi-element coral thermometry: A biomineralization approach to developing climate proxies. *Geochim. Cosmochim. Acta* 75, 1920–1932. <https://doi.org/10.1016/j.gca.2011.01.010>
- Gagan, M.K., Ayliffe, L.K., Beck, J.W., Cole, J.E., Druffel, E.R.M., Dunbar, R.B., Schrag, D.P., 2000. New views of tropical paleoclimates from corals, in: *Quaternary Science Reviews*. pp. 45–64. [https://doi.org/10.1016/S0277-3791\(99\)00054-2](https://doi.org/10.1016/S0277-3791(99)00054-2)
- Gagan, M.K., Ayliffe, L.K., Hopley, D., Cali, J.A., Mortimer, G.E., Chappell, J., McCulloch, M.T., Head, M.J., 1998. Temperature and surface-ocean water balance of the mid-Holocene tropical western Pacific. *Science* (80-.). 279, 1014–1017. <https://doi.org/10.1126/science.279.5353.1014>
- Gagnon, A.C., Adkins, J.F., Erez, J., 2012. Seawater transport during coral biomineralization. *Earth Planet. Sci. Lett.* 329–330, 150–161. <https://doi.org/10.1016/j.epsl.2012.03.005>

- Gaillardet, J., Viers, J., Dupré, B., 2003. Trace Elements in River Waters, in: *Treatise on Geochemistry*. pp. 225–272. <https://doi.org/10.1016/B0-08-043751-6/05165-3>
- Galer, S.J.G., 1999. Optimal double and triple spiking for high precision lead isotopic measurement. *Chem. Geol.* 157, 255–274. [https://doi.org/10.1016/S0009-2541\(98\)00203-4](https://doi.org/10.1016/S0009-2541(98)00203-4)
- Geyman, B.M., Ptacek, J.L., LaVigne, M., Horner, T.J., 2019. Barium in deep-sea bamboo corals: Phase associations, barium stable isotopes, & prospects for paleoceanography. *Earth Planet. Sci. Lett.* 525. <https://doi.org/10.1016/j.epsl.2019.115751>
- Gillson, G.R., Douglas, D.J., Fulford, J.E., Halligan, K.W., Tanner, S.D., 1988. Nonspectroscopic Inter-element Interferences in Inductively Coupled Plasma Mass Spectrometry. *Anal. Chem.* <https://doi.org/10.1021/ac00165a024>
- Gong, Y., Zeng, Z., Cheng, W., Lu, Y., Zhang, L., Yu, H., Huang, F., 2020. Barium isotopic fractionation during strong weathering of basalt in a tropical climate. *Environ. Int.* 143. <https://doi.org/10.1016/j.envint.2020.105896>
- Gong, Y., Zeng, Z., Zhou, C., Nan, X., Yu, H., Lu, Y., Li, W., Gou, W., Cheng, W., Huang, F., 2019. Barium isotopic fractionation in latosol developed from strongly weathered basalt. *Sci. Total Environ.* 687, 1295–1304. <https://doi.org/10.1016/j.scitotenv.2019.05.427>
- Good, S.A., Martin, M.J., Rayner, N.A., 2013. EN4: Quality controlled ocean temperature and salinity profiles and monthly objective analyses with uncertainty estimates. *J. Geophys. Res. Ocean.* 118, 6704–6716. <https://doi.org/10.1002/2013JC009067>
- Gou, L.F., Jin, Z., Galy, A., Gong, Y.Z., Nan, X.Y., Jin, C., Wang, X.D., Bouchez, J., Cai, H.M., Chen, J. Bin, Yu, H.M., Huang, F., 2020. Seasonal riverine barium isotopic variation in the middle Yellow River: Sources and fractionation. *Earth Planet. Sci. Lett.* 531. <https://doi.org/10.1016/j.epsl.2019.115990>
- Grove, C.A., Zinke, J., Scheufen, T., Maina, J., Epping, E., Boer, W., Randriamanantsoa, B., Brummer, G.J.A., 2012. Spatial linkages between coral proxies of terrestrial runoff across a large embayment in Madagascar. *Biogeosciences* 9, 3063–3081. <https://doi.org/10.5194/bg-9-3063-2012>
- Guay, C.K., Falkner, K.K., 1997. Barium as a tracer of Arctic halocline and river waters. *Deep. Res. Part II Top. Stud. Oceanogr.* 44. [https://doi.org/10.1016/S0967-0645\(97\)00066-0](https://doi.org/10.1016/S0967-0645(97)00066-0)
- Hanor, J.S., Chan, L.H., 1977. Non-conservative behavior of barium during mixing of Mississippi River and Gulf of Mexico waters. *Earth Planet. Sci. Lett.* 37, 242–250. [https://doi.org/10.1016/0012-821X\(77\)90169-8](https://doi.org/10.1016/0012-821X(77)90169-8)
- Hanselman, D.S., Sesi, N.N., Huang, M., Hieftje, G.M., 1994. The effect of sample matrix on electron density, electron temperature and gas temperature in the argon inductively coupled plasma examined by Thomson and Rayleigh scattering.

- Spectrochim. Acta Part B At. Spectrosc. 49, 495–526. [https://doi.org/10.1016/0584-8547\(94\)80042-1](https://doi.org/10.1016/0584-8547(94)80042-1)
- Hathorne, E.C., Felis, T., Suzuki, A., Kawahata, H., Cabioch, G., 2013a. Lithium in the aragonite skeletons of massive Porites corals: A new tool to reconstruct tropical sea surface temperatures. *Paleoceanography* 28, 143–152. <https://doi.org/10.1029/2012PA002311>
- Hathorne, E.C., Frank, M., Mohan, P.M., 2020. Rare Earth Elements in Andaman Island Surface Seawater: Geochemical Tracers for the Monsoon? *Front. Mar. Sci.* 6. <https://doi.org/10.3389/fmars.2019.00767>
- Hathorne, E.C., Gagnon, A., Felis, T., Adkins, J., Asami, R., Boer, W., Caillon, N., Case, D., Cobb, K.M., Douville, E., Demenocal, P., Eisenhauer, A., Garbe-Schönberg, D., Geibert, W., Goldstein, S., Hughen, K., Inoue, M., Kawahata, H., Kölling, M., Cornec, F.L., Linsley, B.K., McGregor, H. V., Montagna, P., Nurhati, I.S., Quinn, T.M., Raddatz, J., Rebaubier, H., Robinson, L., Sadekov, A., Sherrell, R., Sinclair, D., Tudhope, A.W., Wei, G., Wong, H., Wu, H.C., You, C.F., 2013b. Interlaboratory study for coral Sr/Ca and other element/Ca ratio measurements. *Geochemistry, Geophys. Geosystems* 14, 3730–3750. <https://doi.org/10.1002/ggge.20230>
- Heaton, T.J., Köhler, P., Butzin, M., Bard, E., Reimer, R.W., Austin, W.E.N., Bronk Ramsey, C., Grootes, P.M., Hughen, K.A., Kromer, B., Reimer, P.J., Adkins, J., Burke, A., Cook, M.S., Olsen, J., Skinner, L.C., 2020. Marine20 - The Marine Radiocarbon Age Calibration Curve (0-55,000 cal BP). *Radiocarbon* 62, 779–820. <https://doi.org/10.1017/RDC.2020.68>
- Hemsing, F., Hsieh, Y. Te, Bridgestock, L., Spooner, P.T., Robinson, L.F., Frank, N., Henderson, G.M., 2018. Barium isotopes in cold-water corals. *Earth Planet. Sci. Lett.* 491, 183–192. <https://doi.org/10.1016/j.epsl.2018.03.040>
- Hendy, E.J., Gagan, M.K., Alibert, C.A., McCulloch, M.T., Lough, J.M., Isdale, P.J., 2002. Abrupt decrease in tropical pacific sea surface salinity at end of little ice age. *Science (80-.)*. 295, 1511–1514. <https://doi.org/10.1126/science.1067693>
- Heumann, K.G., 1992. Isotope dilution mass spectrometry (IDMS) of the elements. *Mass Spectrom. Rev.* 11, 41–67. <https://doi.org/10.1002/mas.1280110104>
- Heumann, K.G., Gallus, S.M., Rädlinger, G., Vogl, J., 1998. Precision and accuracy in isotope ratio measurements by plasma source mass spectrometry. *J. Anal. At. Spectrom.* 13, 1001–1008. <https://doi.org/10.1039/a801965g>
- Hopp, T., Fischer-Gödde, M., Kleine, T., 2016. Ruthenium stable isotope measurements by double spike MC-ICPMS. *J. Anal. At. Spectrom.* 31, 1515–1526. <https://doi.org/10.1039/c6ja00041j>
- Horner, T.J., Crockford, P.W., 2021. Barium Isotopes, Barium Isotopes. Cambridge University Press. <https://doi.org/10.1017/9781108865845>
- Horner, T.J., Kinsley, C.W., Nielsen, S.G., 2015. Barium-isotopic fractionation in seawater mediated by barite cycling and oceanic circulation. *Earth Planet. Sci. Lett.*

- 430, 511–522. <https://doi.org/10.1016/j.epsl.2015.07.027>
- Horner, T.J., Pryer, H. V., Nielsen, S.G., Crockford, P.W., Gauglitz, J.M., Wing, B.A., Ricketts, R.D., 2017. Pelagic barite precipitation at micromolar ambient sulfate. *Nat. Commun.* 8. <https://doi.org/10.1038/s41467-017-01229-5>
- Hsieh, Y. Te, Bridgestock, L., Scheuermann, P.P., Seyfried, W.E., Henderson, G.M., 2021. Barium isotopes in mid-ocean ridge hydrothermal vent fluids: A source of isotopically heavy Ba to the ocean. *Geochim. Cosmochim. Acta* 292, 348–363. <https://doi.org/10.1016/j.gca.2020.09.037>
- Hsieh, Y. Te, Henderson, G.M., 2017. Barium stable isotopes in the global ocean: Tracer of Ba inputs and utilization. *Earth Planet. Sci. Lett.* 473, 269–278. <https://doi.org/10.1016/j.epsl.2017.06.024>
- Hu, Y., Teng, F.Z., 2019. Optimization of analytical conditions for precise and accurate isotope analyses of Li, Mg, Fe, Cu, and Zn by MC-ICPMS. *J. Anal. At. Spectrom.* 34, 338–346. <https://doi.org/10.1039/c8ja00335a>
- Inoue, M., Gussone, N., Koga, Y., Iwase, A., Suzuki, A., Sakai, K., Kawahata, H., 2015. Controlling factors of Ca isotope fractionation in scleractinian corals evaluated by temperature, pH and light controlled culture experiments. *Geochim. Cosmochim. Acta* 167, 80–92. <https://doi.org/10.1016/j.gca.2015.06.009>
- Inoue, M., Nohara, M., Okai, T., Suzuki, A., Kawahata, H., 2004. Concentrations of trace elements in carbonate reference materials coral JCp-1 and giant clam JCT-1 by inductively coupled plasma-mass spectrometry. *Geostand. Geoanalytical Res.* 28, 411–416. <https://doi.org/10.1111/j.1751-908X.2004.tb00759.x>
- Joung, D.J., Shiller, A.M., 2014. Dissolved barium behavior in Louisiana Shelf waters affected by the Mississippi/Atchafalaya River mixing zone. *Geochim. Cosmochim. Acta* 141, 303–313. <https://doi.org/10.1016/j.gca.2014.06.021>
- Jupiter, S., Roff, G., Marion, G., Henderson, M., Schrammeyer, V., McCulloch, M., Hoegh-Guldberg, O., 2008. Linkages between coral assemblages and coral proxies of terrestrial exposure along a cross-shelf gradient on the southern Great Barrier Reef. *Coral Reefs* 27, 887–903. <https://doi.org/10.1007/s00338-008-0422-3>
- Kent, A.J.R., Ungerer, C.A., 2005. Production of barium and light rare earth element oxides during LA-ICP-MS microanalysis. *J. Anal. At. Spectrom.* 20, 1256–1262. <https://doi.org/10.1039/b505734e>
- Klinkhammer, G.P., Chan, L.H., 1990. Determination of barium in marine waters by isotope dilution inductively coupled plasma mass spectrometry. *Anal. Chim. Acta* 232, 323–329. [https://doi.org/10.1016/S0003-2670\(00\)81249-0](https://doi.org/10.1016/S0003-2670(00)81249-0)
- Lacan, F., Jeandel, C., 2004. Denmark Strait water circulation traced by heterogeneity in neodymium isotopic compositions. *Deep. Res. Part I Oceanogr. Res. Pap.* 51, 71–82. <https://doi.org/10.1016/j.dsr.2003.09.006>
- Laukert, G., Frank, M., Bauch, D., Hathorne, E.C., Rabe, B., von Appen, W.J., Wegner,

- C., Zieringer, M., Kassens, H., 2017. Ocean circulation and freshwater pathways in the Arctic Mediterranean based on a combined Nd isotope, REE and oxygen isotope section across Fram Strait. *Geochim. Cosmochim. Acta* 202. <https://doi.org/10.1016/j.gca.2016.12.028>
- Lea, D., Boyle, E., 1989. Barium content of benthic foraminifera controlled by bottom-water composition. *Nature* 338, 751–753. <https://doi.org/10.1038/338751a0>
- Lea, D.W., Shen, G.T., Boyle, E.A., 1989. Coralline barium records temporal variability in equatorial Pacific upwelling. *Nature* 340, 373–376. <https://doi.org/10.1038/340373a0>
- Lewis, S.E., Shields, G.A., Kamber, B.S., Lough, J.M., 2007. A multi-trace element coral record of land-use changes in the Burdekin River catchment, NE Australia. *Palaeogeogr. Palaeoclimatol. Palaeoecol.* 246, 471–487. <https://doi.org/10.1016/j.palaeo.2006.10.021>
- Li, W.Y., Yu, H.M., Xu, J., Halama, R., Bell, K., Nan, X.Y., Huang, F., 2020. Barium isotopic composition of the mantle: Constraints from carbonatites. *Geochim. Cosmochim. Acta* 278, 235–243. <https://doi.org/10.1016/j.gca.2019.06.041>
- Li, Y.H., Burkhardt, L., Teraoka, H., 1984. Desorption and coagulation of trace elements during estuarine mixing. *Geochim. Cosmochim. Acta* 48, 1879–1884. [https://doi.org/10.1016/0016-7037\(84\)90371-5](https://doi.org/10.1016/0016-7037(84)90371-5)
- Lin, Y.B., Wei, H.Z., Jiang, S.Y., Hohl, S., Lei, H.L., Liu, X., Dong, G., 2020. Accurate determination of barium isotopic compositions in sequentially leached phases from carbonates by double spike-thermal ionization mass spectrometry (ds-tims). *Anal. Chem.* 92, 2417–2424. <https://doi.org/10.1021/acs.analchem.9b03137>
- Liu, Y., Li, X., Zeng, Z., Yu, H.M., Huang, F., Felis, T., Shen, C.C., 2019. Annually-resolved coral skeletal $\delta^{138}/^{134}\text{Ba}$ records: A new proxy for oceanic Ba cycling. *Geochim. Cosmochim. Acta* 247, 27–39. <https://doi.org/10.1016/j.gca.2018.12.022>
- Lough, J.M., Barnes, D.J., 2000. Environmental controls on growth of the massive coral *Porites*. *J. Exp. Mar. Bio. Ecol.* 245, 225–243. [https://doi.org/10.1016/S0022-0981\(99\)00168-9](https://doi.org/10.1016/S0022-0981(99)00168-9)
- Makishima, A., Nakamura, E., 2010. Precise isotopic determination of Hf and Pb at sub-nano gram levels by MC-ICP-MS employing a newly designed sample cone and a pre-amplifier with a 1012 ohm register. *J. Anal. At. Spectrom.* 25, 1712–1716. <https://doi.org/10.1039/c0ja00015a>
- Maréchal, C.N., Télouk, P., Albarède, F., 1999. Precise analysis of copper and zinc isotopic compositions by plasma-source mass spectrometry. *Chem. Geol.* 156, 251–273. [https://doi.org/10.1016/S0009-2541\(98\)00191-0](https://doi.org/10.1016/S0009-2541(98)00191-0)
- Martinez-Ruiz, F., Jroundi, F., Paytan, A., Guerra-Tschuschke, I., Abad, M.D.M., González-Muñoz, M.T., 2018. Barium bioaccumulation by bacterial biofilms and implications for Ba cycling and use of Ba proxies. *Nat. Commun.* 9. <https://doi.org/10.1038/s41467-018-04069-z>

- Mavromatis, V., van Zuilen, K., Blanchard, M., van Zuilen, M., Dietzel, M., Schott, J., 2020. Experimental and theoretical modelling of kinetic and equilibrium Ba isotope fractionation during calcite and aragonite precipitation. *Geochim. Cosmochim. Acta* 269, 566–580. <https://doi.org/10.1016/j.gca.2019.11.007>
- Mavromatis, V., van Zuilen, K., Purgstaller, B., Baldermann, A., Nögler, T.F., Dietzel, M., 2016. Barium isotope fractionation during witherite (BaCO₃) dissolution, precipitation and at equilibrium. *Geochim. Cosmochim. Acta* 190, 72–84. <https://doi.org/10.1016/j.gca.2016.06.024>
- Mayfield, K.K., Eisenhauer, A., Santiago Ramos, D.P., Higgins, J.A., Horner, T.J., Auro, M., Magna, T., Moosdorf, N., Charette, M.A., Gonnee, M.E., Brady, C.E., Komar, N., Peucker-Ehrenbrink, B., Paytan, A., 2021. Groundwater discharge impacts marine isotope budgets of Li, Mg, Ca, Sr, and Ba. *Nat. Commun.* 12. <https://doi.org/10.1038/s41467-020-20248-3>
- McCartney, M.S., 1992. Recirculating components to the deep boundary current of the northern North Atlantic. *Prog. Oceanogr.* 29, 283–383. [https://doi.org/10.1016/0079-6611\(92\)90006-L](https://doi.org/10.1016/0079-6611(92)90006-L)
- McConnaughey, T.A., Burdett, J., Whelan, J.F., Paull, C.K., 1997. Carbon isotopes in biological carbonates: Respiration and photosynthesis. *Geochim. Cosmochim. Acta* 61, 611–622. [https://doi.org/10.1016/S0016-7037\(96\)00361-4](https://doi.org/10.1016/S0016-7037(96)00361-4)
- McCulloch, M., Fallon, S., Wyndham, T., Hendy, E., Lough, J., Barnes, D., 2003. Coral record of increased sediment flux to the inner Great Barrier Reef since European settlement. *Nature* 421, 727–730. <https://doi.org/10.1038/nature01361>
- McManus, J., Berelson, W.M., Klinkhammer, G.P., Johnson, K.S., Coale, K.H., Anderson, R.F., Kumar, N., Burdige, D.J., Hammond, D.E., Brumsack, H.J., McCorkle, D.C., Rushdi, A., 1998. Geochemistry of barium in marine sediments: Implications for its use as a paleoproxy. *Geochim. Cosmochim. Acta* 62, 3453–3473. [https://doi.org/10.1016/s0016-7037\(98\)00248-8](https://doi.org/10.1016/s0016-7037(98)00248-8)
- Meija, J., Coplen, T.B., Berglund, M., Brand, W.A., De Bièvre, P., Gröning, M., Holden, N.E., Irrgeher, J., Loss, R.D., Walczyk, T., Prohaska, T., 2016. Atomic weights of the elements 2013 (IUPAC Technical Report). *Pure Appl. Chem.* <https://doi.org/10.1515/pac-2015-0305>
- Miyazaki, T., Kimura, J.I., Chang, Q., 2014. Analysis of stable isotope ratios of Ba by double-spike standard-sample bracketing using multiple-collector inductively coupled plasma mass spectrometry. *J. Anal. At. Spectrom.* 29, 483–490. <https://doi.org/10.1039/c3ja50311a>
- Moyer, R.P., Grottoli, A.G., Olesik, J.W., 2012. A multiproxy record of terrestrial inputs to the coastal ocean using minor and trace elements (Ba/Ca, Mn/Ca, Y/Ca) and carbon isotopes (δ¹³C, Δ¹⁴C) in a nearshore coral from Puerto Rico. *Paleoceanography* 27. <https://doi.org/10.1029/2011PA002249>
- Moynier, F., Pringle, E.A., Bouvier, A., Moureau, J., 2015. Barium stable isotope

- composition of the Earth, meteorites, and calcium-aluminum-rich inclusions. *Chem. Geol.* 413, 1–6. <https://doi.org/10.1016/j.chemgeo.2015.08.002>
- Nan, X., Wu, F., Zhang, Z., Hou, Z., Huang, F., Yu, H., 2015. High-precision barium isotope measurements by MC-ICP-MS. *J. Anal. At. Spectrom.* 30, 2307–2315. <https://doi.org/10.1039/c5ja00166h>
- Nan, X.Y., Yu, H.M., Rudnick, R.L., Gaschnig, R.M., Xu, J., Li, W.Y., Zhang, Q., Jin, Z.D., Li, X.H., Huang, F., 2018. Barium isotopic composition of the upper continental crust. *Geochim. Cosmochim. Acta* 233, 33–49. <https://doi.org/10.1016/j.gca.2018.05.004>
- Newman, K., 2012. Effects of the sampling interface in MC-ICP-MS: Relative elemental sensitivities and non-linear mass dependent fractionation of Nd isotopes, in: *Journal of Analytical Atomic Spectrometry*. pp. 63–70. <https://doi.org/10.1039/c1ja10222b>
- Newman, K., Freedman, P.A., Williams, J., Belshaw, N.S., Halliday, A.N., 2009. High sensitivity skimmers and non-linear mass dependent fractionation in ICP-MS. *J. Anal. At. Spectrom.* 24, 742–751. <https://doi.org/10.1039/b819065h>
- Nielsen, S.G., Horner, T.J., Pryer, H. V., Blusztajn, J., Shu, Y., Kurz, M.D., Le Roux, V., 2018. Barium isotope evidence for pervasive sediment recycling in the upper mantle. *Sci. Adv.* 4. <https://doi.org/10.1126/sciadv.aas8675>
- Nielsen, S.G., Shu, Y., Auro, M., Yogodzinski, G., Shinjo, R., Plank, T., Kay, S.M., Horner, T.J., 2020. Barium isotope systematics of subduction zones. *Geochim. Cosmochim. Acta* 275, 1–18. <https://doi.org/10.1016/j.gca.2020.02.006>
- Nier, A.O., 1938. The isotopic constitution of Strontium, Barium, Bismuth, Thallium and Mercury. *Phys. Rev.* 54, 275–278. <https://doi.org/10.1103/PhysRev.54.275>
- Nowlin, W.D., Klinck, J.M., 1986. The physics of the Antarctic Circumpolar Current. *Rev. Geophys.* <https://doi.org/10.1029/RG024i003p00469>
- Nürnberg, C.C., Bohrmann, G., Schlüter, M., Frank, M., 1997. Barium accumulation in the Atlantic sector of the Southern Ocean: Results from 190,000-year records. *Paleoceanography* 12, 594–603. <https://doi.org/10.1029/97PA01130>
- Okai, T., Suzuki, A., Kawahata, H., Terashima, S., Imai, N., 2002. Preparation of a new Geological Survey of Japan geochemical reference material: Coral JCp-1. *Geostand. Newsl.* 26, 95–99. <https://doi.org/10.1111/j.1751-908X.2002.tb00627.x>
- Olivares, J.A., Houk, R.S., 1986. Suppression of Analyte Signal by Various Concomitant Salts in Inductively Coupled Plasma Mass Spectrometry. *Anal. Chem.* 58, 20–25. <https://doi.org/10.1021/ac00292a008>
- Orsi, A.H., Johnson, G.C., Bullister, J.L., 1999. Circulation, mixing, and production of Antarctic Bottom Water. *Prog. Oceanogr.* 43, 55–109. [https://doi.org/10.1016/S0079-6611\(99\)00004-X](https://doi.org/10.1016/S0079-6611(99)00004-X)
- Paillard, D., Labeyrie, L., Yiou, P., 1996. Macintosh Program performs time-series analysis. *Eos, Trans. Am. Geophys. Union* 77, 379–379.

- <https://doi.org/10.1029/96eo00259>
- Paytan, A., Griffith, E.M., 2007. Marine barite: Recorder of variations in ocean export productivity. *Deep. Res. Part II Top. Stud. Oceanogr.* 54, 687–705. <https://doi.org/10.1016/j.dsr2.2007.01.007>
- Paytan, A., Kastner, M., 1996. Benthic Ba fluxes in the central equatorial pacific, implications for the oceanic Ba cycle. *Earth Planet. Sci. Lett.* 142, 439–450. [https://doi.org/10.1016/0012-821x\(96\)00120-3](https://doi.org/10.1016/0012-821x(96)00120-3)
- Paytan, A., Kastner, M., Chavez, F.P., 1996. Glacial to interglacial fluctuations in productivity in the equatorial pacific as indicated by marine barite. *Science (80-)*. 274, 1355–1357. <https://doi.org/10.1126/science.274.5291.1355>
- Pichat, S., Douchet, C., Albarède, F., 2003. Zinc isotope variations in deep-sea carbonates from the eastern equatorial Pacific over the last 175 ka. *Earth Planet. Sci. Lett.* 210, 167–178. [https://doi.org/10.1016/S0012-821X\(03\)00106-7](https://doi.org/10.1016/S0012-821X(03)00106-7)
- Potemra, J.T., Luther, M.E., O'Brien, J.J., 1991. The seasonal circulation of the upper ocean in the Bay of Bengal. *J. Geophys. Res.* 96, 12667. <https://doi.org/10.1029/91jc01045>
- Pretet, C., Zuilen, K., Nägler, T.F., Reynaud, S., Böttcher, M.E., Samankassou, E., 2015. Constraints on barium isotope fractionation during aragonite precipitation by corals. *Depos. Rec.* 1, 118–129. <https://doi.org/10.1002/dep2.8>
- Prouty, N.G., Field, M.E., Stock, J.D., Jupiter, S.D., McCulloch, M., 2010. Coral Ba/Ca records of sediment input to the fringing reef of the southshore of Moloka'i, Hawai'i over the last several decades. *Mar. Pollut. Bull.* 60, 1822–1835. <https://doi.org/10.1016/j.marpolbul.2010.05.024>
- Rajendran, C.P., Rajendran, K., Anu, R., Earnest, A., Machado, T., Mohan, P.M., Freymueller, J., 2007. Crustal deformation and seismic history associated with the 2004 Indian Ocean earthquake: A perspective from the Andaman-Nicobar Islands. *Bull. Seismol. Soc. Am.* 97. <https://doi.org/10.1785/0120050630>
- Ramaswamy, V., Gaye, B., Shirodkar, P. V., Rao, P.S., Chivas, A.R., Wheeler, D., Thwin, S., 2008. Distribution and sources of organic carbon, nitrogen and their isotopic signatures in sediments from the Ayeyarwady (Irrawaddy) continental shelf, northern Andaman Sea. *Mar. Chem.* 111, 137–150. <https://doi.org/10.1016/j.marchem.2008.04.006>
- Ramaswamy, V., Rao, P.S., Rao, K.H., Thwin, S., Rao, N.S., Raiker, V., 2004. Tidal influence on suspended sediment distribution and dispersal in the northern Andaman Sea and Gulf of Martaban. *Mar. Geol.* 208, 33–42. <https://doi.org/10.1016/j.margeo.2004.04.019>
- Rao, R.R., Sivakumar, R., 2003. Seasonal variability of sea surface salinity and salt budget of the mixed layer of the north Indian Ocean. *J. Geophys. Res. Ocean.* 108. <https://doi.org/10.1029/2001jc000907>

- Rayner, N.A., Parker, D.E., Horton, E.B., Folland, C.K., Alexander, L. V., Rowell, D.P., Kent, E.C., Kaplan, A., 2003. Global analyses of sea surface temperature, sea ice, and night marine air temperature since the late nineteenth century. *J. Geophys. Res. Atmos.* 108. <https://doi.org/10.1029/2002jd002670>
- Reeve, K.A., Boebel, O., Kanzow, T., Strass, V., Rohardt, G., Fahrbach, E., 2016. A gridded data set of upper-ocean hydrographic properties in the Weddell Gyre obtained by objective mapping of Argo float measurements. *Earth Syst. Sci. Data* 8, 15–40. <https://doi.org/10.5194/essd-8-15-2016>
- Riedinger, N., Kasten, S., Gröger, J., Franke, C., Pfeifer, K., 2006. Active and buried authigenic barite fronts in sediments from the Eastern Cape Basin. *Earth Planet. Sci. Lett.* 241, 876–887. <https://doi.org/10.1016/j.epsl.2005.10.032>
- Rixen, T., Ramachandran, P., Lehnhoff, L., Dasbach, D., Gaye, B., Urban, B., Ramachandran, R., Ittekkot, V., 2011. Impact of monsoon-driven surface ocean processes on a coral off Port Blair on the Andaman Islands and their link to North Atlantic climate variations. *Glob. Planet. Change* 75, 1–13. <https://doi.org/10.1016/j.gloplacha.2010.09.005>
- Robinson, R.A.J., Bird, M.I., Nay, W.O., Hoey, T.B., Maung, M.A., Higgitt, D.L., Lu, X.X., Aung, S., Tin, T., Swe, L.W., 2007. The irrawaddy river sediment flux to the Indian ocean: The original nineteenth-century data revisited. *J. Geol.* 115, 629–640. <https://doi.org/10.1086/521607>
- Rodolfo, K.S., 1969. Sediments of the Andaman Basin, northeastern Indian Ocean. *Mar. Geol.* 7, 371–402. [https://doi.org/10.1016/0025-3227\(69\)90014-0](https://doi.org/10.1016/0025-3227(69)90014-0)
- Rosenthal, Y., Field, M.P., Sherrell, R.M., 1999. Precise determination of element/calcium ratios in calcareous samples using sector field inductively coupled plasma mass spectrometry. *Anal. Chem.* 71, 3248–3253. <https://doi.org/10.1021/ac981410x>
- Rudge, J.F., Reynolds, B.C., Bourdon, B., 2009. The double spike toolbox. *Chem. Geol.* 265, 420–431. <https://doi.org/10.1016/j.chemgeo.2009.05.010>
- Sackett, W.M., Netratanawong, T., Holmes, M.E., 1997. Carbon-13 variations in the dissolved inorganic carbon in estuarine waters. *Geophys. Res. Lett.* 24, 21–24. <https://doi.org/10.1029/96GL03694>
- Saha, N., Webb, G.E., Zhao, J.X., 2016. Coral skeletal geochemistry as a monitor of inshore water quality. *Sci. Total Environ.* <https://doi.org/10.1016/j.scitotenv.2016.05.066>
- Samanta, S., Dalai, T.K., 2016. Dissolved and particulate Barium in the Ganga (Hooghly) River estuary, India: Solute-particle interactions and the enhanced dissolved flux to the oceans. *Geochim. Cosmochim. Acta* 195. <https://doi.org/10.1016/j.gca.2016.09.005>
- Schmitt, A.D., Galer, S.J.G., Abouchami, W., 2009. High-precision cadmium stable isotope measurements by double spike thermal ionisation mass spectrometry. *J. Anal.*

- At. Spectrom. 24, 1079–1088. <https://doi.org/10.1039/b821576f>
- Siebert, C., Nögler, T.F., Kramers, J.D., 2001. Determination of molybdenum isotope fractionation by double-spike multicollector inductively coupled plasma mass spectrometry. *Geochemistry, Geophys. Geosystems* 2. <https://doi.org/10.1029/2000GC000124>
- Sinclair, D.J., 2005. Non-river flood barium signals in the skeletons of corals from coastal Queensland, Australia. *Earth Planet. Sci. Lett.* 237, 354–369. <https://doi.org/10.1016/j.epsl.2005.06.039>
- Singh, S.P., Singh, S.K., Bhushan, R., 2013. Internal cycling of dissolved barium in water column of the Bay of Bengal. *Mar. Chem.* 154, 12–23. <https://doi.org/10.1016/j.marchem.2013.04.013>
- Smith, S. V., Buddemeier, R.W., Redalje, R.C., Houck, J.E., 1979. Strontium-calcium thermometry in coral skeletons. *Science* (80-). 204, 404–407. <https://doi.org/10.1126/science.204.4391.404>
- Sprintall, J., Tomczak, M., 1992. Evidence of the barrier layer in the surface layer of the tropics. *J. Geophys. Res.* 97, 7305. <https://doi.org/10.1029/92jc00407>
- Sree Lekha, J., Buckley, J.M., Tandon, A., Sengupta, D., 2018. Subseasonal Dispersal of Freshwater in the Northern Bay of Bengal in the 2013 Summer Monsoon Season. *J. Geophys. Res. Ocean.* 123, 6330–6348. <https://doi.org/10.1029/2018JC014181>
- Stichel, T., Frank, M., Rickli, J., Haley, B.A., 2012. The hafnium and neodymium isotope composition of seawater in the Atlantic sector of the Southern Ocean. *Earth Planet. Sci. Lett.* 317–318, 282–294. <https://doi.org/10.1016/j.epsl.2011.11.025>
- Sunda, W.G., Huntsman, S.A., Harvey, G.R., 1983. Photoreduction of manganese oxides in seawater and its geochemical and biological implications. *Nature* 301, 234–236. <https://doi.org/10.1038/301234a0>
- Swart, P.K., Leder, J.J., Szmant, A.M., Dodge, R.E., 1996. The origin of variations in the isotopic record of scleractinian corals: II. Carbon. *Geochim. Cosmochim. Acta* 60, 2871–2885. [https://doi.org/10.1016/0016-7037\(96\)00119-6](https://doi.org/10.1016/0016-7037(96)00119-6)
- Talley, L.D., 2013. Closure of the global overturning circulation through the Indian, Pacific, and southern oceans. *Oceanography* 26, 80–97. <https://doi.org/10.5670/oceanog.2013.07>
- Talley, L.D., McCartney, M.S., 1982. Distribution and Circulation of Labrador Sea Water. *J. Phys. Oceanogr.* 12, 1189–1205. [https://doi.org/10.1175/1520-0485\(1982\)012<1189:dacols>2.0.co;2](https://doi.org/10.1175/1520-0485(1982)012<1189:dacols>2.0.co;2)
- Tan, S.H., Horlick, G., 1987. Matrix-effect observations in inductively coupled plasma mass spectrometry. *J. Anal. At. Spectrom.* 2, 745–763. <https://doi.org/10.1039/ja9870200745>
- Tan, S.H., Horlick, G., 1986. Background Spectral Features in Inductively Coupled Plasma/Mass Spectrometry. *Appl. Spectrosc.* 40, 445–460.

- <https://doi.org/10.1366/0003702864508944>
- Taylor, J.R., Falkner, K.K., Schauer, U., Meredith, M., 2003. Quantitative considerations of dissolved barium as a tracer in the Arctic Ocean. *J. Geophys. Res. Ocean.* 108. <https://doi.org/10.1029/2002jc001635>
- Teng, F.Z., Dauphas, N., Watkins, J.M., 2017. Non-Traditional Stable Isotopes: Retrospective and Prospective, in: *Non-Traditional Stable Isotopes*. pp. 1–26. <https://doi.org/10.2138/rmg.2017.82.1>
- Tian, L.L., Gong, Y.Z., Wei, W., Kang, J.T., Yu, H.M., Huang, F., 2020. Rapid determination of Ba isotope compositions for barites using a H₂O-extraction method and MC-ICP-MS. *J. Anal. At. Spectrom.* 35, 1566–1573. <https://doi.org/10.1039/d0ja00078g>
- Tian, L.L., Zeng, Z., Nan, X.Y., Yu, H.M., Huang, F., 2019. Determining Ba isotopes of barite using the Na₂CO₃ exchange reaction and double-spike method by MC-ICP-MS. *J. Anal. At. Spectrom.* 34, 1459–1467. <https://doi.org/10.1039/c9ja00064j>
- Tieman, Z.G., Stewart, B.W., Capo, R.C., Phan, T.T., Lopano, C.L., Hakala, J.A., 2020. Barium Isotopes Track the Source of Dissolved Solids in Produced Water from the Unconventional Marcellus Shale Gas Play. *Environ. Sci. Technol.* 54, 4275–4285. <https://doi.org/10.1021/acs.est.0c00102>
- Torres, M.E., Brumsack, H.J., Bohrmann, G., Emeis, K.C., 1996. Barite fronts in continental margin sediments: A new look at barium remobilization in the zone of sulfate reduction and formation of heavy barites in diagenetic fronts. *Chem. Geol.* 127, 125–139. [https://doi.org/10.1016/0009-2541\(95\)00090-9](https://doi.org/10.1016/0009-2541(95)00090-9)
- van Zuilen, K., Müller, T., Nägler, T.F., Dietzel, M., Küsters, T., 2016a. Experimental determination of barium isotope fractionation during diffusion and adsorption processes at low temperatures. *Geochim. Cosmochim. Acta* 186, 226–241. <https://doi.org/10.1016/j.gca.2016.04.049>
- van Zuilen, K., Nägler, T.F., Bullen, T.D., 2016b. Barium Isotopic Compositions of Geological Reference Materials. *Geostand. Geoanalytical Res.* 40, 543–558. <https://doi.org/10.1111/ggr.12122>
- Varkey, M.J., Murty, V.S.N., Suryanarayana, A., 1996. Physical oceanography of the Bay of Bengal and Andaman Sea, in: *Oceanography and Marine Biology: An Annual Review*. Vol. 34. pp. 1–70.
- Vaughan, M.A., Horlick, G., 1986. Oxide, Hydroxide, and Doubly Charged Analyte Species in Inductively Coupled Plasma/Mass Spectrometry. *Appl. Spectrosc.* 40, 434–445. <https://doi.org/10.1366/0003702864509006>
- Vernet, M., Geibert, W., Hoppema, M., Brown, P.J., Haas, C., Hellmer, H.H., Jokat, W., Jullion, L., Mazloff, M., Bakker, D.C.E., Brearley, J.A., Croot, P., Hattermann, T., Hauck, J., Hillenbrand, C.D., Hoppe, C.J.M., Huhn, O., Koch, B.P., Lechtenfeld, O.J., Meredith, M.P., Naveira Garabato, A.C., Nöthig, E.M., Peeken, I., Rutgers van der Loeff, M.M., Schmidtke, S., Schröder, M., Strass, V.H., Torres-Valdés, S.,

- Verdy, A., 2019. The Weddell Gyre, Southern Ocean: Present Knowledge and Future Challenges. *Rev. Geophys.* <https://doi.org/10.1029/2018RG000604>
- von Allmen, K., Böttcher, M.E., Samankassou, E., Nägler, T.F., 2010. Barium isotope fractionation in the global barium cycle: First evidence from barium minerals and precipitation experiments. *Chem. Geol.* 277, 70–77. <https://doi.org/10.1016/j.chemgeo.2010.07.011>
- Wang, W., Wu, Z., Huang, F., 2021. Equilibrium barium isotope fractionation between minerals and aqueous solution from first-principles calculations. *Geochim. Cosmochim. Acta* 292, 64–77. <https://doi.org/10.1016/j.gca.2020.09.021>
- Wellington, G.M., 1982. An experimental analysis of the effects of light and zooplankton on coral zonation. *Oecologia* 52, 311–320. <https://doi.org/10.1007/BF00367953>
- Wells, M.L., Mayer, L.M., Donard, O.F.X., De Souza Sierra, M.M., Ackelson, S.G., 1991. The photolysis of colloidal iron in the oceans. *Nature* 353, 248–250. <https://doi.org/10.1038/353248a0>
- Weyer, S., Schwieters, J.B., 2003. High precision Fe isotope measurements with high mass resolution MC-ICPMS. *Int. J. Mass Spectrom.* 226, 355–368. [https://doi.org/10.1016/S1387-3806\(03\)00078-2](https://doi.org/10.1016/S1387-3806(03)00078-2)
- White, W.M., Albarède, F., Télouk, P., 2000. High-precision analysis of Pb isotope ratios by multi-collector ICP-MS. *Chem. Geol.* 167, 257–270. [https://doi.org/10.1016/S0009-2541\(99\)00182-5](https://doi.org/10.1016/S0009-2541(99)00182-5)
- Woodhead, J., 2002. A simple method for obtaining highly accurate Pb isotope data by MC-ICP-MS. *J. Anal. At. Spectrom.* 17, 1381–1385. <https://doi.org/10.1039/b205045e>
- Yang, L., Tong, S., Zhou, L., Hu, Z., Mester, Z., Meija, J., 2018. A critical review on isotopic fractionation correction methods for accurate isotope amount ratio measurements by MC-ICP-MS. *J. Anal. At. Spectrom.* <https://doi.org/10.1039/c8ja00210j>
- Yashayaev, I., 2007. Hydrographic changes in the Labrador Sea, 1960–2005. *Prog. Oceanogr.* 73, 242–276. <https://doi.org/10.1016/j.pocean.2007.04.015>
- Yobregat, E., Fitoussi, C., Bourdon, B., 2017. A new method for TIMS high precision analysis of Ba and Sr isotopes for cosmochemical studies. *J. Anal. At. Spectrom.* 32, 1388–1399. <https://doi.org/10.1039/c7ja00012j>
- Yu, Y., Siebert, C., Fietzke, J., Goepfert, T., Hathorne, E., Cao, Z., Frank, M., 2020. The impact of MC-ICP-MS plasma conditions on the accuracy and precision of stable isotope measurements evaluated for barium isotopes. *Chem. Geol.* 549. <https://doi.org/10.1016/j.chemgeo.2020.119697>
- Zeng, Z., Li, X., Liu, Y., Huang, F., Yu, H.M., 2019. High-Precision Barium Isotope Measurements of Carbonates by MC-ICP-MS. *Geostand. Geoanalytical Res.* 43, 291–300. <https://doi.org/10.1111/ggr.12256>

Appendix

Table A1: A systematic investigation of the impact of MC-ICP-MS plasma conditions on stable Ba isotope analysis

 $NAI = 0.02^{ac}$

[Ca] (ppb)	[Ca]/[Ba]	$\delta^{138}\text{Ba}$	2s.d.	^{43}Ca (V)	^{138}Ba (V)	BaO (V)	BaOH (V)	^{38}Ar (V)	ArAr (V)	MA	NAI
0	0	0.00	0.03	0.04	8.80	0.01	0.01	1.68	145.00	0.01	0.02
0.5	0.01	-0.01	0.01	0.04	10.00	0.01	0.01	1.87	161.00	0.01	0.02
5	0.1	-0.01	0.01	0.04	10.00	0.01	0.01	1.87	163.00	0.01	0.02
50	1	-0.01	0.01	0.05	10.00	0.02	0.01	1.87	164.00	0.02	0.02
500	10	-0.06	0.02	0.16	11.70	0.02	0.01	2.04	178.00	0.04	0.02
5000	100	-0.52	0.03	1.60	11.40	0.01	0.01	2.12	185.00	0.36	0.02
20000	400	-1.47	0.17	4.77	9.80	0.01	0.01	1.91	168.00	1.17	0.02
[Sr] (ppb)	[Sr]/[Ba]	$\delta^{138}\text{Ba}$	2s.d.	^{84}Sr (V)	^{138}Ba (V)	BaO (V)	BaOH (V)	^{38}Ar (V)	ArAr (V)	MA	NAI
0	0	0.00	0.03	0.00	9.20	0.01	0.01	2.10	175.00	0.00	0.02
0.5	0.01	0.00	0.04	0.00	10.40	0.01	0.01	2.10	178.00	0.00	0.02
5	0.1	0.00	0.02	0.01	10.40	0.01	0.01	2.10	179.00	0.00	0.02
50	1	0.00	0.01	0.08	10.60	0.01	0.01	2.10	180.00	0.01	0.02
500	10	0.04	0.02	0.75	11.30	0.02	0.01	2.10	181.00	0.05	0.02
5000	100	0.13	0.00	7.30	11.20	0.02	0.01	1.86	161.00	0.45	0.02
20000	400	0.35	0.02	22.16	8.62	0.01	0.01	1.56	135.00	1.61	0.02

Table A1 (continued): A systematic investigation of the impact of MC-ICP-MS plasma conditions on stable Ba isotope analysis

NAI = 0.07^a

[Ca] (ppb)	[Ca]/[Ba]	$\delta^{138}\text{Ba}$	2s.d.	⁴³ Ca (V)	¹³⁸ Ba (V)	BaO (V)	BaOH (V)	³⁸ Ar (V)	Ar/Ar (V)	MA	NAI
0	0	0.00	0.03	0.09	43.00	0.03	0.04	15.50	465.00	0.01	0.07
0.5	0.01	0.01	0.03	0.10	48.00	0.04	0.05	15.50	465.00	0.01	0.07
5	0.1	0.00	0.02	0.10	48.50	0.04	0.05	15.30	466.00	0.01	0.07
50	1	-0.02	0.02	0.14	50.00	0.04	0.05	15.30	464.00	0.01	0.07
500	10	-0.05	0.01	0.78	54.50	0.05	0.05	15.00	456.00	0.03	0.07
5000	100	-0.12	0.01	6.90	55.00	0.04	0.04	14.00	425.00	0.23	0.07
20000	400	-0.40	0.01	22.20	48.50	0.01	0.02	12.20	371.00	0.86	0.07
[Sr] (ppb)	[Sr]/[Ba]	$\delta^{138}\text{Ba}$	2s.d.	⁸⁴ Sr (V)	¹³⁸ Ba (V)	BaO (V)	BaOH (V)	³⁸ Ar (V)	Ar/Ar (V)	MA	NAI
0	0	0.00	0.03	0.00	41.30	0.03	0.04	14.70	434.00	0.00	0.07
0.5	0.01	0.00	0.04	0.01	46.00	0.04	0.05	14.70	440.00	0.00	0.07
5	0.1	-0.01	0.02	0.03	46.30	0.04	0.05	14.60	445.00	0.00	0.07
50	1	-0.01	0.01	0.30	47.50	0.04	0.04	15.00	448.00	0.01	0.07
500	10	-0.02	0.02	3.26	52.80	0.04	0.05	14.60	450.00	0.03	0.06
5000	100	0.03	0.01	31.77	54.00	0.04	0.04	14.40	435.00	0.25	0.07
20000	400	0.18	0.01	16.58 ^c	6.87 ^c	0.00 ^c	0.00 ^c	2.23 ^c	69.00 ^c	0.84 ^c	0.06 ^c

Table A1 (continued): A systematic investigation of the impact of MC-ICP-MS plasma conditions on stable Ba isotope analysis

 $NAI = 0.14^a$

[Ca] (ppb)	[Ca]/[Ba]	$\delta^{138}\text{Ba}$	2s.d.	^{43}Ca (V)	^{138}Ba (V)	BaO (V)	BaOH (V)	^{38}Ar (V)	ArAr (V)	MA	NAI
0	0	0.00	0.03	0.03	14.50	0.00	0.01	8.90	127.00	0.00	0.14
0.5	0.01	0.01	0.02	0.03	16.00	0.01	0.01	8.90	128.00	0.00	0.14
5	0.1	0.00	0.05	0.03	16.30	0.01	0.01	8.90	128.00	0.00	0.14
50	1	0.00	0.00	0.05	17.00	0.01	0.01	8.80	129.00	0.00	0.14
500	10	0.00	0.06	0.28	19.00	0.01	0.01	8.70	127.00	0.02	0.14
5000	100	0.00	0.07	2.76	19.50	0.01	0.01	8.40	123.00	0.16	0.14
20000	400	-0.02	0.01	9.47	18.90	0.00	0.00	7.40	110.00	0.60	0.13

[Sr] (ppb)	[Sr]/[Ba]	$\delta^{138}\text{Ba}$	2s.d.	^{84}Sr (V)	^{138}Ba (V)	BaO (V)	BaOH (V)	^{38}Ar (V)	ArAr (V)	MA	NAI
0	0	0.00	0.03	0.00	14.50	0.00	0.01	8.20	121.00	0.00	0.14
0.5	0.01	-0.01	0.04	0.00	15.50	0.01	0.01	8.20	122.00	0.00	0.13
5	0.1	0.00	0.02	0.01	15.80	0.01	0.01	8.20	123.00	0.00	0.13
50	1	-0.01	0.01	0.11	16.30	0.01	0.01	8.20	124.00	0.00	0.13
500	10	0.00	0.01	1.18	18.20	0.01	0.01	8.20	124.00	0.02	0.13
5000	100	0.04	0.05	12.30	19.50	0.01	0.01	8.30	127.00	0.17	0.13
20000	400	0.11	0.00	47.00	19.70	0.00	0.00	8.03	123.00	0.66	0.13

Table A1 (continued): A systematic investigation of the impact of MC-ICP-MS plasma conditions on stable Ba isotope analysis

NAI = 0.55^b

[Ca] (ppb)	[Ca]/[Ba]	$\delta^{138}\text{Ba}$	2s.d.	⁴³ Ca (V)	¹³⁸ Ba (V)	BaO (V)	BaOH (V)	³⁸ Ar (V)	Ar/Ar (V)	MA	NAI
0	0	0.00	0.03	0.00	9.20	0.00	0.00	20.60	75.50	0.00	0.55
0.5	0.01	0.03	0.16	0.01	10.00	0.00	0.00	20.60	76.50	0.00	0.54
5	0.1	0.06	0.11	0.01	10.00	0.00	0.00	20.60	76.50	0.00	0.54
50	1	0.02	0.07	0.01	10.35	0.00	0.00	20.60	76.50	0.00	0.54
500	10	0.02	0.07	0.11	11.40	0.00	0.00	20.60	76.50	0.00	0.54
5000	100	0.05	0.09	1.19	12.40	0.00	0.00	20.30	76.00	0.03	0.53
20000	400	0.01	0.05	4.70	12.66	0.00	0.00	20.30	76.00	0.11	0.53
[Sr] (ppb)	[Sr]/[Ba]	$\delta^{138}\text{Ba}$	2s.d.	⁸⁴ Sr (V)	¹³⁸ Ba (V)	BaO (V)	BaOH (V)	³⁸ Ar (V)	Ar/Ar (V)	MA	NAI
0	0	0.00	0.03	0.00	9.20	0.00	0.00	20.30	74.00	0.00	0.55
0.5	0.01	0.00	0.08	0.00	9.70	0.00	0.00	20.30	74.00	0.00	0.55
5	0.1	-0.03	0.02	0.01	9.77	0.00	0.00	20.30	74.00	0.00	0.55
50	1	-0.02	0.02	0.05	10.00	0.00	0.00	20.30	74.50	0.00	0.54
500	10	-0.02	0.02	0.59	11.10	0.00	0.00	20.30	74.50	0.00	0.54
5000	100	0.04	0.12	6.60	12.20	0.00	0.00	20.30	75.00	0.04	0.54
20000	400	0.07	0.06	26.20	12.40	0.00	0.00	20.90	77.00	0.14	0.54

Table A1 (continued): A systematic investigation of the impact of MC-ICP-MS plasma conditions on stable Ba isotope analysis

 $NAI = 0.86^b$

[Ca] (ppb)	[Ca]/[Ba]	$\delta^{138}\text{Ba}$	2s.d.	^{43}Ca (V)	^{138}Ba (V)	BaO (V)	BaOH (V)	^{38}Ar (V)	ArAr (V)	MA	NAI
0	0	0.00	0.03	0.00	5.65	0.00	0.00	18.00	42.00	0.00	0.86
0.5	0.01	-0.01	0.10	0.00	6.20	0.00	0.00	18.00	42.20	0.00	0.85
5	0.1	-0.04	0.02	0.00	6.20	0.00	0.00	18.00	42.50	0.00	0.85
50	1	0.04	0.10	0.01	6.40	0.00	0.00	17.20	40.50	0.00	0.85
500	10	0.03	0.03	0.08	7.03	0.00	0.00	16.60	39.50	0.00	0.84
5000	100	0.01	0.10	0.80	7.76	0.00	0.00	16.60	39.50	0.02	0.84
20000	400	-0.01	0.03	3.20	8.00	0.00	0.00	16.60	39.50	0.09	0.84
[Sr] (ppb)	[Sr]/[Ba]	$\delta^{138}\text{Ba}$	2s.d.	^{84}Sr (V)	^{138}Ba (V)	BaO (V)	BaOH (V)	^{38}Ar (V)	ArAr (V)	MA	NAI
0	0	0.00	0.03	0.00	5.60	0.00	0.00	16.60	38.50	0.00	0.86
0.5	0.01	0.05	0.09	0.00	6.05	0.00	0.00	18.00	42.00	0.00	0.86
5	0.1	0.04	0.01	0.00	6.15	0.00	0.00	18.00	42.20	0.00	0.85
50	1	0.02	0.05	0.04	6.25	0.00	0.00	18.00	42.60	0.00	0.85
500	10	0.03	0.04	0.38	7.02	0.00	0.00	18.00	42.60	0.00	0.85
5000	100	0.02	0.04	4.30	7.76	0.00	0.00	18.00	42.80	0.03	0.84
20000	400	0.08	0.01	17.90	8.05	0.00	0.00	18.20	43.00	0.11	0.85

Table A1 (continued): A systematic investigation of the impact of MC-ICP-MS plasma conditions on stable Ba isotope analysis

NAI = 1.01^b

[Ca] (ppb)	[Ca]/[Ba]	$\delta^{138}\text{Ba}$	2s.d.	^{43}Ca (V)	^{138}Ba (V)	BaO (V)	BaOH (V)	^{38}Ar (V)	ArAr (V)	MA	NAI
0	0	0.00	0.03	0.00	4.63	0.00	0.00	19.00	37.50	0.00	1.01
0.5	0.01	0.00	0.04	0.00	5.12	0.00	0.00	20.00	40.00	0.00	1.00
5	0.1	0.03	0.01	0.00	5.25	0.00	0.00	20.00	40.20	0.00	1.00
50	1	0.02	0.05	0.01	5.41	0.00	0.00	19.50	39.30	0.00	0.99
500	10	-0.01	0.11	0.07	6.00	0.00	0.00	19.50	39.50	0.00	0.99
5000	100	0.00	0.04	0.70	6.70	0.00	0.00	19.50	41.20	0.02	0.95
20000	400	0.01	0.03	2.80	6.95	0.00	0.00	20.00	41.20	0.07	0.97
[Sr] (ppb)	[Sr]/[Ba]	$\delta^{138}\text{Ba}$	2s.d.	^{84}Sr (V)	^{138}Ba (V)	BaO (V)	BaOH (V)	^{38}Ar (V)	ArAr (V)	MA	NAI
0	0	0.00	0.03	0.00	4.63	0.00	0.00	19.00	37.50	0.00	1.01
0.5	0.01	0.00	0.06	0.00	5.20	0.00	0.00	19.50	38.80	0.00	1.01
5	0.1	-0.01	0.00	0.00	5.25	0.00	0.00	20.00	39.80	0.00	1.01
50	1	0.02	0.06	0.03	5.40	0.00	0.00	20.00	40.00	0.00	1.00
500	10	0.02	0.06	0.33	6.10	0.00	0.00	20.00	40.20	0.00	1.00
5000	100	0.00	0.00	3.70	6.60	0.00	0.00	20.20	40.50	0.02	1.00
20000	400	0.07	0.07	15.50	6.90	0.00	0.00	20.20	40.50	0.09	1.00

^a experiments conducted by using "X" skimmer cone

^b experiments conducted by using "H" skimmer cone

^c experiments conducted under high resolution

Table A.2: The dissolved Ba concentrations and isotope compositions along with hydrographic parameters.

Sampling site	Cruise	Station	Latitude	Longitude	Depth (m)	Pot. T. (°C)	Salinity (psu)	[Ba]/(nmol kg ⁻¹)	$\delta^{138}\text{Ba}$ (‰)	2SD
Fram Strait	PS80	50	78.83	5.35	20	4.34	35.11	43.71	0.53	0.04
Fram Strait	PS80	50	78.83	5.35	101	2.75	35.08	43.80	0.52	0.04
Fram Strait	PS80	50	78.83	5.35	810	-0.46	34.91	46.06	0.49	0.04
Fram Strait	PS80	50	78.83	5.35	2031	-0.87	34.92	48.87	0.48	0.04
Fram Strait	PS80	50	78.83	5.35	2568	-0.89	34.93	49.37	0.46	0.04
Fram Strait	PS80	55	78.83	3.66	10	0.06	33.90	39.89	0.53	0.04
Fram Strait	PS80	55	78.83	3.66	203	3.07	35.07	42.81	0.56	0.04
Fram Strait	PS80	55	78.83	3.66	405	1.17	34.93	44.35	0.52	0.04
Fram Strait	PS80	55	78.83	3.66	507	1.30	34.98	43.45	0.51	0.04
Fram Strait	PS80	55	78.83	3.66	1014	-0.41	34.91	45.68	0.52	0.04
Fram Strait	PS80	55	78.83	3.66	2241	-0.89	34.92	48.27	0.46	0.04
Fram Strait	PS80	130	78.83	-4.58	14	-1.63	32.30	59.58	0.42	0.04
Fram Strait	PS80	130	78.83	-4.58	76	-1.73	33.97	44.43	0.50	0.04
Fram Strait	PS80	130	78.83	-4.58	203	2.74	34.97	42.34	0.52	0.04
Fram Strait	PS80	130	78.83	-4.58	608	0.74	34.91	42.85	0.50	0.05
Fram Strait	PS80	130	78.83	-4.58	1013	-0.27	34.89	44.35	0.51	0.04
Fram Strait	PS80	130	78.83	-4.58	1368	-0.49	34.91	49.64	0.51	0.05

Table A.2 (continued): The dissolved Ba concentrations and isotope compositions along with hydrographic parameters.

Sampling site	Cruise	Station	Latitude	Longitude	Depth (m)	Pot. T. (°C)	Salinity (psu)	[Ba]/(mmol kg ⁻¹)	$\delta^{138}\text{Ba}$ (‰)	2SD
Fram Strait	PS80	132	78.83	-3.92	10	-1.51	32.74	50.54	0.45	0.04
Fram Strait	PS80	132	78.83	-3.92	51	-1.71	34.01	43.02	0.53	0.04
Fram Strait	PS80	132	78.83	-3.92	202	2.87	35.03	43.43	0.54	0.04
Fram Strait	PS80	132	78.83	-3.92	405	0.80	34.88	42.37	0.54	0.04
Fram Strait	PS80	132	78.83	-3.92	608	0.22	34.87	43.14	0.53	0.04
Fram Strait	PS80	132	78.83	-3.92	1014	-0.27	34.90	49.93	0.53	0.04
Fram Strait	PS80	132	78.83	-3.92	1573	-0.62	34.91	45.69	0.50	0.04
Fram Strait	PS80	132	78.83	-3.92	1908	-0.71	34.92	47.68	0.49	0.04
Labrador Sea	MSM45	06	61.75	-53.50	2894	1.85	34.90	47.78	0.49	0.04
Labrador Sea	MSM45	06	61.75	-53.50	2409	2.72	34.92	49.27	0.46	0.04
Labrador Sea	MSM45	06	61.75	-53.50	1507	3.49	34.93	47.08	0.49	0.04
Labrador Sea	MSM45	06	61.75	-53.50	756	3.71	34.89	45.00	0.51	0.04
Labrador Sea	MSM45	06	61.75	-53.50	99	5.10	34.90	44.56	0.52	0.04
Labrador Sea	MSM45	06	61.75	-53.50	39	3.99	34.53	44.47	0.49	0.04
Labrador Sea	MSM45	16	58.57	-58.01	2646	2.00	-	49.87	0.49	0.04
Labrador Sea	MSM45	16	58.57	-58.01	2302	2.63	-	49.04	0.46	0.04
Labrador Sea	MSM45	16	58.57	-58.01	1332	3.64	34.93	46.13	0.49	0.05
Labrador Sea	MSM45	16	58.57	-58.01	404	3.98	34.87	44.59	0.54	0.04

Table A.2 (continued): The dissolved Ba concentrations and isotope compositions along with hydrographic parameters.

Sampling site	Cruise	Station	Latitude	Longitude	Depth (m)	Pot. T. (°C)	Salinity (psu)	[Ba]/(nmol kg ⁻¹)	$\delta^{138}\text{Ba}$ (‰)	2SD
Labrador Sea	MSM45	33	54.57	-50.68	2998	2.26	-	54.08	0.45	0.04
Labrador Sea	MSM45	33	54.57	-50.68	35	4.78	34.13	46.34	0.49	0.04
Labrador Sea	MSM39	01	50.83	-45.58	15	10.01	33.85	43.96	0.49	0.04
Labrador Sea	MSM39	01	50.83	-45.58	399	4.27	34.82	45.03	0.54	0.04
Labrador Sea	MSM39	01	50.83	-45.58	698	4.16	34.91	45.03	0.53	0.04
Labrador Sea	MSM39	01	50.83	-45.58	1099	3.81	34.91	45.61	0.47	0.04
Labrador Sea	MSM39	01	50.83	-45.58	1349	3.73	34.92	46.21	0.49	0.02
Labrador Sea	MSM39	01	50.83	-45.58	1699	3.43	34.93	48.23	0.47	0.04
Labrador Sea	MSM39	01	50.83	-45.58	1999	3.19	34.92	47.72	0.49	0.04
Labrador Sea	MSM39	01	50.83	-45.58	2498	2.85	34.92	49.66	0.47	0.04
Labrador Sea	MSM39	01	50.83	-45.58	2999	2.36	34.91	50.85	0.48	0.06
Labrador Sea	MSM39	01	50.83	-45.58	3499	1.93	34.90	52.81	0.46	0.04
Labrador Sea	MSM39	01	50.83	-45.58	4167	1.58	34.90	50.04	0.47	0.04
Weddell Sea	PS118	53	-60.84	-49.76	200	-0.76	34.46	85.25	0.31	0.04
Weddell Sea	PS118	53	-60.84	-49.76	500	0.42	34.66	90.21	0.29	0.04
Weddell Sea	PS118	53	-60.84	-49.76	1000	0.13	34.66	94.10	0.27	0.04
Weddell Sea	PS118	53	-60.84	-49.76	2000	-0.40	34.65	93.20	0.26	0.04
Weddell Sea	PS118	53	-60.84	-49.76	2560	-0.57	34.64	96.04	0.26	0.04

Table A.2 (continued): The dissolved Ba concentrations and isotope compositions along with hydrographic parameters.

Sampling site	Cruise	Station	Latitude	Longitude	Depth (m)	Pot. T. (°C)	Salinity (psu)	[Ba] (nmol kg ⁻¹)	δ ¹³⁸ Ba (‰)	2SD
Weddell Sea	PS118	59	-60.84	-48.20	500	0.39	34.66	92.36	0.27	0.04
Weddell Sea	PS118	59	-60.84	-48.20	1000	0.12	34.66	96.50	0.26	0.04
Weddell Sea	PS118	59	-60.84	-48.20	2000	-0.36	34.65	93.44	0.26	0.04
Weddell Sea	PS118	59	-60.84	-48.20	2567	-0.60	34.65	93.73	0.26	0.04
Weddell Sea	PS111	9-3	-64.00	5.00	1000	0.37	34.68	96.38	0.25	0.04
Weddell Sea	PS111	9-3	-64.00	5.00	2000	-0.07	34.67	98.49	0.25	0.04
Weddell Sea	PS111	9-3	-64.00	5.00	3000	-0.37	34.66	98.26	0.24	0.04
Weddell Sea	PS111	9-3	-64.00	5.00	3500	-0.47	34.66	99.71	0.24	0.04
Weddell Sea	PS111	9-3	-64.00	5.00	3800	-0.51	34.65	101.22	0.26	0.04
Weddell Sea	PS111	12-2	-66.74	-0.04	100	-0.32	34.51	88.80	0.34	0.04
Weddell Sea	PS111	12-2	-66.74	-0.04	200	0.89	34.69	90.38	0.27	0.04
Weddell Sea	PS111	12-2	-66.74	-0.04	1000	0.44	34.69	95.98	0.33	0.09
Weddell Sea	PS111	12-2	-66.74	-0.04	2000	-0.03	34.67	98.17	0.27	0.06
Weddell Sea	PS111	12-2	-66.74	-0.04	3000	-0.34	34.66	96.15	0.28	0.04
Weddell Sea	PS111	12-2	-66.74	-0.04	3500	-0.44	34.66	97.90	0.26	0.05
Weddell Sea	PS111	12-2	-66.74	-0.04	4200	-0.55	34.65	99.53	0.26	0.04
Weddell Sea	PS111	12-2	-66.74	-0.04	4550	-0.64	34.65	102.25	0.27	0.04
Weddell Sea	PS111	12-2	-66.74	-0.04	4654	-0.72	34.65	103.40	0.25	0.05

Table A.3: Monthly resolved geochemical records of Interview Island coral.

	$\delta^{13}\text{C}$	$\delta^{18}\text{O}$	$\delta^{18}\text{O}_{\text{sw}}$	Sr/Ca	U/Ca	Ba/Ca
	‰	‰	‰	mmol/mol	$\mu\text{mol/mol}$	$\mu\text{mol/mol}$
AND2B-01	-1.87	-5.02	-0.01	8.71	1.03	4.47
AND2B-02	-2.02	-5.11	-0.11	8.72	1.04	4.86
AND2B-03	-1.42	-5.09	0.17	8.61	0.99	4.49
AND2B-04	-1.97	-5.25	0.14	8.56	0.95	4.52
AND2B-05	-2.39	-5.47	-0.16	8.59	0.95	5.00
AND2B-06	-2.51	-5.39	-0.18	8.63	0.98	5.39
AND2B-07	-2.64	-5.39	-0.05	8.58	0.96	4.98
AND2B-08	-2.99	-5.51	-0.20	8.59	0.95	4.88
AND2B-09	-3.07	-5.55	-0.38	8.65	1.00	5.09
AND2B-10	-2.60	-5.39	-0.37	8.71	1.03	5.07
AND2B-11	-2.17	-5.05	0.01	8.69	1.03	5.19
AND2B-12	-2.19	-5.12	-0.03	8.68	1.01	5.70
AND2B-13	-2.19	-5.16	0.10	8.61	0.99	5.77
AND2B-14	-2.86	-5.32	-0.07	8.61	0.96	4.83
AND2B-15	-2.93	-5.42	-0.09	8.58	0.96	4.33
AND2B-16	-3.12	-5.29	-0.07	8.63	0.96	4.49
AND2B-17	-3.14	-5.29	-0.02	8.61	0.95	4.42
AND2B-18	-2.98	-5.37	-0.03	8.58	0.95	4.36
AND2B-19	-2.85	-5.32	-0.03	8.60	0.96	4.66
AND2B-20	-2.53	-5.15	0.02	8.65	1.01	5.21
AND2B-21	-1.61	-4.91	0.23	8.66	1.02	5.16
AND2B-22	-1.85	-5.29	0.05	8.58	0.97	4.97
AND2B-23	-2.79	-5.42	0.03	8.53	0.94	4.55
AND2B-24	-3.44	-5.50	-0.13	8.57	0.95	4.98
AND2B-25	-3.47	-5.33	0.10	8.54	0.95	5.40
AND2B-26	-3.56	-5.47	-0.19	8.60	0.95	5.44
AND2B-27	-3.30	-5.52	-0.23	8.60	0.96	5.29
AND2B-28	-2.19	-4.90	0.16	8.70	1.04	5.55
AND2B-29	-1.57	-4.79	0.35	8.66	1.05	6.10
AND2B-30	-1.76	-5.11	0.07	8.64	1.02	6.91
AND2B-31	-2.37	-5.38	0.04	8.55	0.97	6.28
AND2B-32	-2.76	-5.28	0.10	8.56	0.98	6.13
AND2B-33	-2.81	-5.26	-0.06	8.64	0.98	5.76
AND2B-34	-2.16	-5.26	-0.08	8.64	1.01	6.14
AND2B-35	-0.86	-4.81	0.30	8.68	1.08	7.53
AND2B-36	-0.63	-4.88	0.34	8.63	1.04	7.35
AND2B-37	-2.24	-4.99	0.34	8.58	1.00	7.17

Table A.3 (continued): Monthly resolved geochemical records of Interview Island coral.

	$\delta^{13}\text{C}$	$\delta^{18}\text{O}$	$\delta^{18}\text{O}_{\text{SW}}$	Sr/Ca	U/Ca	Ba/Ca
	‰	‰	‰	<i>mmol/mol</i>	<i>$\mu\text{mol/mol}$</i>	<i>$\mu\text{mol/mol}$</i>
AND2B-38	-2.45	-5.37	0.02	8.56	0.95	5.84
AND2B-39	-2.52	-5.09	0.15	8.62	1.00	5.50
AND2B-40	-2.20	-5.37	-0.13	8.62	1.01	5.77
AND2B-41	-1.81	-5.15	-0.03	8.67	1.01	6.16
AND2B-42	-1.40	-4.95	0.07	8.71	1.06	5.95
AND2B-43	-1.22	-5.07	-0.02	8.70	1.03	6.11
AND2B-44	-1.74	-5.17	0.24	8.55	0.97	7.46
AND2B-45	-2.47	-5.30	0.16	8.53	0.93	6.46
AND2B-46	-2.58	-5.42	-0.07	8.57	0.95	5.29
AND2B-47	-2.43	-5.40	-0.22	8.64	0.95	6.08
AND2B-48	-1.99	-5.34	-0.12	8.63	0.97	5.35
AND2B-49	-2.34	-5.34	-0.14	8.63	0.96	5.10
AND2B-50	-1.81	-5.10	0.04	8.66	0.95	5.62

Table A.4: Monthly resolved geochemical records of Mayabunder coral.

	$\delta^{13}\text{C}$	$\delta^{18}\text{O}$	$\delta^{18}\text{O}_{\text{sw}}$	Sr/Ca	U/Ca	Ba/Ca	$\delta^{138}\text{Ba}$	2SD
	‰	‰	‰	mmol/mol	$\mu\text{mol/mol}$	$\mu\text{mol/mol}$	‰	
AND3A-01	-2.76	-5.63	-0.08	8.63	0.98	5.58		
AND3A-02	-1.85	-5.29	-0.03	8.75	1.05	4.21		
AND3A-03	-1.90	-5.14	0.21	8.71	1.04	3.89		
AND3A-04	-1.34	-5.09	0.24	8.72	1.07	4.28		
AND3A-05	-1.60	-5.27	0.13	8.69	1.01	5.72		
AND3A-06	-2.16	-5.48	-0.05	8.68	1.00	4.43		
AND3A-07	-2.29	-5.65	-0.10	8.63	0.98	4.31		
AND3A-08	-2.62	-5.56	-0.13	8.68	0.97	4.43		
AND3A-09	-2.65	-5.37	-0.08	8.74	0.99	4.20		
AND3A-10	-2.37	-5.29	-0.01	8.74	0.99	4.61		
AND3A-11	-2.18	-5.49	-0.19	8.73	0.99	4.45		
AND3A-12	-2.23	-5.62	-0.16	8.67	0.98	4.62		
AND3A-13	-1.70	-5.32	0.04	8.71	1.00	3.73		
AND3A-14	-2.11	-5.40	0.02	8.68	1.01	4.31		
AND3A-15	-1.73	-5.25	0.15	8.69	0.99	5.28		
AND3A-16	-1.64	-5.33	0.08	8.69	0.98	3.76		
AND3A-17	-2.02	-5.59	-0.24	8.71	1.02	3.77		
AND3A-18	-2.35	-5.34	-0.01	8.72	0.96	4.00		
AND3A-19	-1.81	-5.34	-0.06	8.74	1.00	3.88		
AND3A-20	-2.69	-5.34	-0.01	8.72	1.01	4.56		
AND3A-21	-2.34	-5.53	-0.16	8.70	1.01	5.34		
AND3A-22	-2.21	-5.06	0.44	8.65	0.99	3.94		
AND3A-23	-1.67	-5.30	0.26	8.62	1.00	4.87		
AND3A-24	-1.72	-5.36	0.31	8.58	0.97	4.08		
AND3A-25	-2.07	-5.26	0.39	8.58	0.97	4.26		
AND3A-26	-2.24	-5.49	0.00	8.66	0.94	4.27		
AND3A-27	-1.96	-5.27	0.02	8.74	0.99	4.27		
AND3A-28	-2.31	-5.47	0.05	8.64	0.99	4.73		
AND3A-29	-2.43	-5.74	-0.10	8.59	1.00	5.41		
AND3A-30	-2.31	-5.79	-0.29	8.65	0.98	5.03		
AND3A-31	-2.06	-5.46	-0.03	8.68	1.03	4.47		
AND3A-32	-1.99	-5.19	0.37	8.63	1.02	3.87		
AND3A-33	-1.36	-5.20	0.37	8.62	1.00	3.88		
AND3A-34	-1.62	-5.14	0.43	8.62	1.03	4.07		
AND3A-35	-2.41	-5.20	0.49	8.57	0.97	5.53		
AND3A-36	-2.22	-5.48	0.24	8.56	0.96	4.90		
AND3A-37	-2.44	-5.64	0.03	8.58	0.95	4.40		

Table A.4 (continued): Monthly resolved geochemical records of Mayabunder coral.

	$\delta^{13}\text{C}$	$\delta^{18}\text{O}$	$\delta^{18}\text{O}_{\text{SW}}$	Sr/Ca	U/Ca	Ba/Ca	$\delta^{138}\text{Ba}$	2SD
	‰	‰	‰	mmol/mol	$\mu\text{mol/mol}$	$\mu\text{mol/mol}$	‰	
AND3A-38	-2.53	-5.63	-0.06	8.62	0.99	3.80		
AND3A-39	-2.33	-5.47	0.07	8.63	1.01	4.03		
AND3A-40	-2.48	-5.48	0.03	8.64	1.03	4.25		
AND3A-41	-2.28	-5.49	-0.05	8.68	0.99	4.66		
AND3A-42	-2.33	-5.48	0.11	8.61	0.98	4.38		
AND3A-43	-2.61	-5.62	0.00	8.60	1.00	4.32		
AND3A-44	-2.36	-5.32	0.03	8.71	1.04	4.03		
AND3A-45	-1.77	-5.04	0.37	8.69	1.03	3.90		
AND3A-46	-1.62	-5.19	0.25	8.67	0.99	4.67		
AND3A-47	-1.98	-5.28	0.21	8.65	0.99	4.03		
AND3A-48	-2.35	-5.40	0.05	8.67	0.99	3.65		
AND3A-49	-2.48	-5.69	-0.20	8.66	1.00	3.60		
AND3A-50	-2.53	-5.52	-0.01	8.65	1.01	4.12		
AND3A-51	-2.34	-5.49	-0.23	8.75	1.01	4.10		
AND3A-52	-2.48	-5.28	0.01	8.74	1.02	4.30		
AND3A-53	-2.28	-5.31	-0.14	8.79	1.05	4.33		
AND3A-54	-2.71	-5.56	-0.04	8.64	1.00	4.23		
AND3A-55	-2.09	-5.65	-0.21	8.67	0.99	3.96		
AND3A-56	-2.62	-5.53	-0.22	8.73	0.99	3.77		
AND3A-57	-2.24	-5.17	0.07	8.76	1.02	3.81		
AND3A-58	-1.75	-5.18	0.12	8.73	1.03	3.83	0.26	0.03
AND3A-59	-1.83	-5.31	0.26	8.62	0.99	5.39	0.18	0.03
AND3A-60	-2.10	-5.55	0.08	8.60	0.97	4.87	0.21	0.03
AND3A-61	-1.72	-5.47	0.05	8.64	0.99	3.74	0.24	0.03
AND3A-62	-2.27	-5.47	0.04	8.65	1.00	4.10	0.23	0.03
AND3A-63	-2.00	-5.37	-0.17	8.78	1.05	4.28	0.21	0.03
AND3A-64	-2.60	-5.55	-0.15	8.69	1.02	4.59	0.18	0.03
AND3A-65	-2.73	-5.54	-0.19	8.71	0.99	4.42	0.19	0.03
AND3A-66	-2.17	-5.59	-0.22	8.70	1.03	4.52	0.17	0.03
AND3A-67	-2.39	-5.72	-0.35	8.70	0.97	4.44	0.16	0.03
AND3A-68	-2.69	-5.55	-0.16	8.69	1.00	4.44	0.17	0.03
AND3A-69	-2.45	-5.46	-0.21	8.75	1.04	4.20	0.19	0.03
AND3A-70	-2.13	-5.15	0.27	8.68	1.02	4.47	0.27	0.03
AND3A-71	-1.99	-5.39	0.04	8.68	0.98	5.73	0.19	0.03
AND3A-72	-2.04	-5.47	0.04	8.65	0.99	4.06	0.25	0.03
AND3A-73	-2.62	-5.52	-0.05	8.66	1.01	3.87	0.25	0.03
AND3A-74	-2.56	-5.54	-0.02	8.64	1.00	3.93	0.24	0.03

Table A.4 (continued): Monthly resolved geochemical records of Mayabunder coral.

	$\delta^{13}\text{C}$	$\delta^{18}\text{O}$	$\delta^{18}\text{O}_{\text{sw}}$	Sr/Ca	U/Ca	Ba/Ca	$\delta^{138}\text{Ba}$	2SD
	‰	‰	‰	mmol/mol	$\mu\text{mol/mol}$	$\mu\text{mol/mol}$	‰	
AND3A-75	-2.40	-5.51	-0.15	8.71	0.99	4.03	0.26	0.03
AND3A-76	-2.36	-5.47	-0.13	8.72	1.01	4.29	0.26	0.03
AND3A-77	-2.46	-5.40	-0.14	8.75	1.03	4.20	0.21	0.03
AND3A-78	-2.37	-5.61	-0.08	8.64	0.99	4.27	0.20	0.03
AND3A-79	-2.62	-5.55	-0.16	8.70	1.03	4.31	0.17	0.03
AND3A-80	-3.20	-5.54	-0.15	8.70	0.99	4.14	0.27	0.03
AND3A-81	-1.99	-5.34	-0.08	8.75	1.07	3.66	0.27	0.03
AND3A-82	-1.53	-5.43	0.00	8.68	1.02	3.83		
AND3A-83	-1.79	-5.67	-0.15	8.64	1.03	4.54		
AND3A-84	-1.97	-5.56	0.03	8.61	1.02	4.20		
AND3A-85	-2.61	-5.83	-0.39	8.68	1.06	4.20		
AND3A-86	-2.78	-5.65	0.00	8.59	0.99	4.17		
AND3A-87	-2.68	-5.50	-0.09	8.69	1.02	4.09		
AND3A-88	-2.18	-5.39	0.11	8.65	0.99	4.20		
AND3A-89	-2.27	-5.40	0.14	8.63	1.03	4.16		
AND3A-90	-2.01	-5.40	-0.02	8.70	1.01	4.44		
AND3A-91	-2.44	-5.62	-0.13	8.65	1.03	4.96		
AND3A-92	-2.24	-5.69	-0.12	8.62	0.97	4.49		
AND3A-93	-2.15	-5.61	-0.09	8.64	1.00	3.99		
AND3A-94	-1.69	-5.32	0.25	8.62	1.03	3.44		
AND3A-95	-1.68	-5.37	0.15	8.64	1.03	4.07		
AND3A-96	-2.00	-5.31	0.10	8.69	0.97	4.09		
AND3A-97	-2.18	-5.61	0.02	8.59	1.00	3.96		
AND3A-98	-2.71	-5.47	0.12	8.61	0.97	4.38		
AND3A-99	-2.09	-5.40	0.12	8.64	0.99	3.85		
AND3A-100	-2.09	-5.59	-0.18	8.69	1.02	4.37		
AND3A-101	-2.31	-5.49	-0.16	8.72	1.02	4.53		
AND3A-102	-2.54	-5.46	-0.02	8.67	0.99	4.47		
AND3A-103	-2.50	-5.73	-0.22	8.65	0.99	4.76		
AND3A-104	-2.91	-5.85	-0.18	8.58	0.97	4.59		
AND3A-105	-2.17	-5.51	0.00	8.64	1.02	4.47		
AND3A-106	-1.80	-5.44	-0.05	8.70	1.01	4.31		
AND3A-107	-1.88	-5.37	0.10	8.66	1.02	4.30		
AND3A-108	-1.87	-5.38	0.17	8.63	0.98	4.47		
AND3A-109	-1.56	-5.33	0.16	8.65	1.01	5.37		
AND3A-110	-1.13	-5.09	0.22	8.73	1.02	4.03		
AND3A-111	-1.57	-5.57	-0.04	8.64	1.01	4.32		

Table A.4 (continued): Monthly resolved geochemical records of Mayabunder coral.

	$\delta^{13}\text{C}$	$\delta^{18}\text{O}$	$\delta^{18}\text{O}_{\text{SW}}$	Sr/Ca	U/Ca	Ba/Ca	$\delta^{138}\text{Ba}$	2SD
	‰	‰	‰	mmol/mol	$\mu\text{mol/mol}$	$\mu\text{mol/mol}$	‰	
AND3A-112	-2.42	-5.72	-0.11	8.60	0.99	4.06		
AND3A-113	-1.48	-5.40	0.21	8.60	0.98	3.92		
AND3A-114	-1.71	-5.52	0.04	8.63	0.97	4.26		
AND3A-115	-1.72	-5.46	0.22	8.58	1.00	4.61		
AND3A-116	-1.72	-5.44	0.21	8.59	0.95	4.46		
AND3A-117	-2.34	-5.52	0.05	8.62	0.97	4.36		
AND3A-118	-2.16	-5.49	0.06	8.63	0.98	4.33		
AND3A-119	-2.14	-5.30	0.23	8.64	0.97	4.72		
AND3A-120	-2.16	-5.38	0.19	8.62	0.97	4.57		
AND3A-121	-2.25	-5.62	-0.09	8.64	0.98	4.98		
AND3A-122	-2.23	-5.49	-0.11	8.70	0.98	4.28		
AND3A-123	-1.40	-5.33	0.01	8.72	1.02	3.71		
AND3A-124	-1.42	-5.33	0.13	8.67	0.99	4.49		
AND3A-125	-1.53	-5.31	0.30	8.60	0.98	4.49		
AND3A-126	-1.97	-5.40	0.28	8.57	0.97	3.25		
AND3A-127	-1.64	-5.46	0.10	8.63	0.99	3.53		
AND3A-128	-1.70	-5.23	0.29	8.64	0.97	4.02		
AND3A-129	-2.50	-5.50	0.02	8.64	0.98	4.50		
AND3A-130	-2.40	-5.58	0.04	8.60	0.97	4.81		
AND3A-131	-2.70	-5.63	-0.11	8.64	0.99	4.86		
AND3A-132	-1.90	-5.45	-0.12	8.72	1.05	4.27		
AND3A-133	-1.67	-5.45	0.11	8.63	1.01	4.32		
AND3A-134	-1.79	-5.42	0.11	8.64	0.99	4.77		
AND3A-135	-1.86	-5.43	0.11	8.63	0.99	4.66		
AND3A-136	-2.41	-5.62	-0.04	8.62	0.98	3.87		
AND3A-137	-2.08	-5.52	-0.11	8.69	1.03	4.34		
AND3A-138	-2.59	-5.66	-0.21	8.67	1.02	4.23		
AND3A-139	-2.31	-5.59	-0.14	8.67	1.00	4.64		
AND3A-140	-2.46	-5.70	-0.13	8.62	0.98	4.65		
AND3A-141	-2.33	-5.75	-0.20	8.63	0.98	4.60		
AND3A-142	-2.15	-5.59	-0.13	8.67	0.99	4.02		
AND3A-143	-1.77	-5.31	0.19	8.65	1.01	3.89		
AND3A-144	-1.84	-5.34	0.20	8.63	0.99	4.56		
AND3A-145	-1.93	-5.39	0.30	8.57	0.95	4.74		
AND3A-146	-1.88	-5.51	0.12	8.59	0.97	3.80		
AND3A-147	-2.18	-5.79	-0.10	8.57	0.99	3.89		
AND3A-148	-2.12	-5.64	-0.05	8.61	0.99	4.18		

Table A.4 (continued): Monthly resolved geochemical records of Mayabunder coral.

	$\delta^{13}\text{C}$	$\delta^{18}\text{O}$	$\delta^{18}\text{O}_{\text{sw}}$	Sr/Ca	U/Ca	Ba/Ca	$\delta^{138}\text{Ba}$	2SD
	‰	‰	‰	mmol/mol	$\mu\text{mol/mol}$	$\mu\text{mol/mol}$	‰	
AND3A-149	-2.09	-5.50	-0.02	8.66	1.01	4.43		
AND3A-150	-2.45	-5.51	-0.04	8.66	1.02	4.61		
AND3A-151	-2.13	-5.68	-0.08	8.61	1.01	4.52		
AND3A-152	-2.65	-5.59	0.03	8.60	0.97	4.46		
AND3A-153	-1.71	-5.39	0.15	8.64	1.03	3.60		
AND3A-154	-1.55	-5.27	0.26	8.64	1.01	4.12		
AND3A-155	-1.87	-5.39	0.25	8.59	0.97	5.07		
AND3A-156	-1.89	-5.46	0.32	8.53	0.97	4.55		
AND3A-157	-1.99	-5.76	0.01	8.53	1.01	4.02		
AND3A-158	-2.00	-5.61	-0.07	8.64	1.03	3.98		
AND3A-159	-1.75	-5.37	0.03	8.69	1.04	4.10		
AND3A-160	-2.20	-5.48	-0.13	8.71	1.03	4.43		
AND3A-161	-2.10	-5.49	0.00	8.66	1.02	4.81		
AND3A-162	-2.66	-5.57	-0.10	8.66	0.98	4.94		
AND3A-163	-2.07	-5.70	-0.23	8.66	1.04	4.50		
AND3A-164	-1.48	-5.38	0.25	8.59	1.00	4.18		
AND3A-165	-1.98	-5.41	0.14	8.63	0.97	5.70		
AND3A-166	-1.95	-5.50	-0.07	8.68	0.99	4.28		
AND3A-167	-2.42	-5.54	-0.02	8.64	0.99	4.65		
AND3A-168	-1.73	-5.47	-0.20	8.75	1.03	4.28		
AND3A-169	-1.76	-5.41	-0.15	8.75	1.03	4.45		
AND3A-170	-1.92	-5.36	-0.18	8.78	1.01	4.28		
AND3A-171	-2.02	-5.51	-0.25	8.75	1.04	4.76		
AND3A-172	-2.01	-5.59	-0.23	8.71	1.02	3.99		
AND3A-173	-1.38	-5.42	0.09	8.65	1.07	4.23		
AND3A-174	-1.97	-5.43	0.07	8.65	1.05	4.61		
AND3A-175	-1.62	-5.46	-0.05	8.69	1.01	5.59		
AND3A-176	-1.96	-5.56	-0.13	8.68	1.05	3.82		
AND3A-177	-2.02	-5.57	-0.35	8.77	1.06	4.26		
AND3A-178	-1.88	-5.41	-0.16	8.75	1.07	4.30		
AND3A-179	-1.90	-5.44	-0.32	8.81	1.02	4.50		
AND3A-180	-2.41	-5.66	-0.27	8.70	1.01	5.31		
AND3A-181	-2.60	-5.62	-0.38	8.76	1.00	5.26		
AND3A-182	-2.04	-5.52	-0.19	8.72	1.05	4.63		
AND3A-183	-1.43	-5.45	0.11	8.62	1.02	4.96		
AND3A-184	-1.66	-5.52	0.08	8.61	0.98	5.66		
AND3A-185	-2.44	-5.60	0.19	8.53	1.03	4.80		

Table A.4 (continued): Monthly resolved geochemical records of Mayabunder coral.

	$\delta^{13}\text{C}$	$\delta^{18}\text{O}$	$\delta^{18}\text{O}_{\text{SW}}$	Sr/Ca	U/Ca	Ba/Ca	$\delta^{138}\text{Ba}$	2SD
	‰	‰	‰	mmol/mol	$\mu\text{mol/mol}$	$\mu\text{mol/mol}$	‰	
AND3A-186	-2.53	-5.74	-0.38	8.71	1.04	4.81		
AND3A-187	-2.41	-5.50	-0.24	8.75	1.00	4.96		
AND3A-188	-2.42	-5.56	-0.29	8.75	1.05	5.16		
AND3A-189	-2.24	-5.51	-0.11	8.69	1.00	5.13		
AND3A-190	-2.34	-5.83	-0.54	8.74	1.04	5.16		
AND3A-191	-2.59	-5.79	-0.38	8.69	0.99	4.85		
AND3A-192	-2.25	-5.36	-0.13	8.76	1.00	4.43		
AND3A-193	-1.86	-5.36	0.11	8.66	0.99	4.42		
AND3A-194	-1.58	-5.52	-0.13	8.70	1.01	5.32		
AND3A-195	-1.75	-5.65	0.17	8.52	0.97	4.59		
AND3A-196	-2.28	-5.50	-0.02	8.66	0.99	4.49		
AND3A-197	-1.98	-5.43	-0.19	8.76	1.00	4.19		
AND3A-198	-1.59	-5.38	-0.21	8.79	1.07	4.37		
AND3A-199	-1.77	-5.20	0.00	8.78	1.02	4.36		
AND3A-200	-2.07	-5.56	-0.11	8.67	1.01	5.13		
AND3A-201	-2.45	-5.61	-0.17	8.68	0.99	4.84		
AND3A-202	-1.36	-5.17	0.08	8.76	1.07	3.87		
AND3A-203	-1.34	-5.22	0.40	8.60	1.00	5.95		
AND3A-204	-1.71	-5.33	0.04	8.71	1.01	4.09		
AND3A-205	-1.17	-5.12	0.30	8.68	1.04	4.18		
AND3A-206	-1.33	-5.26	0.03	8.74	1.06	4.25		
AND3A-207	-1.36	-5.03	0.42	8.67	1.02	4.31		
AND3A-208	-1.45	-5.26	-0.05	8.77	0.96	5.41		
AND3A-209	-1.68	-5.24	0.21	8.67	1.07	5.67		
AND3A-210	-2.03	-5.63	-0.07	8.62	1.00	4.01		

Table A.5: The dissolved Ba concentrations and isotope compositions from the Andaman Sea.

Sample ID	Date taken	Location	Latitude	Longitude	Salinity (psu)	[Ba] (nmol kg ⁻¹)	$\delta^{138}\text{Ba}_{\text{sw}}$	2SD
AN-15	31.03.2011	Jolly Buoy	11.51	92.62	33.36	52.70	0.47	0.04
2012Feb	01.02.2012	Jolly Buoy	11.51	92.62	32.92	52.51	0.42	0.04
2012Mar	01.03.2012	Jolly Buoy	11.51	92.62	33.54	53.25	0.47	0.04
AN-134	02.03.2013	Avis Island	12.92	92.93	33.10	52.61	0.47	0.04
AN-136	02.03.2013	Avis Island	12.92	92.91	32.98	52.43	0.49	0.04
AN-132	01.03.2013	Mayabunder beach	12.92	92.90	33.48	54.29	0.46	0.09
AN-6	21.03.2011	NE Interview Island	12.98	92.72	34.11	54.15	0.46	0.04
AN-138	03.03.2013	NE Interview Island	12.98	92.72	34.33	51.93	0.48	0.04
AN-24	26.07.2011	Jolly Buoy	11.51	92.62	32.98	66.03	0.29	0.04
AN-58a	03.11.2011	Jolly Buoy	11.51	92.62	32.48	55.07	0.42	0.07
AN-58b	03.11.2011	Jolly Buoy	11.51	92.62	32.48	54.89	0.42	0.04
AN-94	12.11.2011	Jolly Buoy	11.51	92.62	32.41	54.12	0.42	0.09
AN-74	07.11.2011	Avis Island	12.92	92.93	30.16	58.83	0.40	0.04
AN-78	07.11.2011	Mayabunder beach	12.92	92.90	31.88	60.76	0.37	0.06